AN ABSTRACT OF THE THESIS OF

Douglas G. Pyle for the degree of Doctor of Philosophy

in Oceanography presented on October 21, 1993

Title: Geochemistry of Mid-Ocean Ridge Basalt Within and Surrounding the Australian-Antarctic Discordance

Redacted for Privacy

Abstract Approved: David M. Christie

The Australian-Antarctic Discordance (AAD) is a unique feature of the global mid-ocean ridge (MOR) spreading system located in the Southern Ocean between Australia and Antarctica. Dramatic changes in MOR morphology and geochemistry, comparable to the contrasts between the slow-spreading Mid-Atlantic Ridge and the fast spreading East Pacific Rise, coincide with an abrupt axial depth transition between the AAD and adjacent sections of the Southeast Indian Ridge (SEIR). A regionally uniform, intermediate spreading rate requires that mantle temperature and melt supply controls the physical and chemical characteristics of the spreading axis.

An isotopically defined boundary (Sr, Nd, and Pb) between Indian Ocean-type and Pacific Ocean-type MORB mantle lies beneath the AAD. The transition between these two upper mantle reservoirs is abrupt, over <40 km along the easternmost AAD spreading axis. West of a ridge-transform intersection at ~126°E, SEIR lavas have Indian Ocean MORB isotopic characteristics, whereas SEIR lavas to the east have Pacific Ocean MORB isotopic characteristics. Mixing of melts from theses two upper mantle reservoirs occurs within 40 km transition zone. Off-axis sampling indicates Indian Ocean MORB mantle has migrated westward beneath the easternmost AAD spreading segment at ~25 mm/yr during the last 3-4 Ma. Migration of the boundary could reflect a large-scale westward outflow of Pacific

Ocean mantle from a shrinking Pacific basin or a small-scale perturbation of a long-term isotopic discontinuity created by the mantle dynamics producing the AAD.

The geochemistry and geochronology of DSDP Legs 28 and 29 basalt samples recovered east of the Kerguelen Plateau and west of the Macquarie Triple Junction show no direct evidence for large-scale flow of Pacific mantle westward, but important regional variations in the isotopic signature of mantle sources through time is observed. All samples west of the AAD are Indian Ocean MORB that display increasing isotopic and trace element enrichment with decreasing age indicating the eastward migration of Kerguelen hot spot material along the SEIR near 110°E. East of the South Tasman Rise, all DSDP basalts are Pacific Ocean MORB indicating this reservoir at the eastern margin of Gondwana before seafloor spreading began in the Tasman Sea (~80 Ma). DSDP samples directly west of the South Tasman Rise have higher $^{87}Sr/^{86}Sr$ and lower $^{206}Pb/^{204}Pb$ than DSDP samples farther east and have elevated $^{208}Pb/^{204}Pb$ and $^{207}Pb/^{204}Pb$ values, characteristics transitional between Pacific Ocean and Indian Ocean MORB.

Geochemistry of Mid-Ocean Ridge Basalt Within and Surrounding the Australian-Antarctic Discordance

by

Douglas G. Pyle

A THESIS
submitted to

Oregon State University

in partial fulfillment of
the requirements for
the degree of

Doctor of Philosophy

Completed (October 21, 1993)

Commencement June (1994)

APPROVED: Redacted for Privacy

Professor of Oceanography in charge of Major

Redacted for Privacy

Dean of College of Oceanography

Redacted for Privacy

Dean of Graduate School

Date thesis is presented October 21, 1993

Assembled by Sue Pullen for Douglas G. Pyle

dedicated to

Heidi

with love

Acknowledgements

It is impossible to remember everyone who provide some form of assistance or encouragement in the completion of this thesis. The Captain and crew of the *R/V Moana Wave* and all the participating scientist - J. Palmer, J.-C. Sempéré, A. Sheehan, C. Ruppel, J. Phipps-Morgan, T. Plank, deserve recognition for their assistance in the collection of samples. J. Palmer, J.-C. Sempéré, and B. West participated in many helpful discussions concerning the AAD and provided made-for-order SeaMARCII bathymetry for this region. The ideas presented here have greatly benefited from discussions with A. Grunder, T. Plank, M. Fisk, D. Graham, E. Klein, R. Kinzler, R. Nielsen, L. Forsyth, R. Duncan, and participation in RIDGE sponsored short courses. We thank C. Langmuir and G. Eberhart for providing major and trace element DCP analysis of glasses samples presented in this study. R. Schmidt and M. Conrady are gratefully acknowledged for allowing access to the OSU Radiation Center counting facilities. R. Collier is greatly acknowledged for providing employment and free rein of his lab prior to and after this work started. Thanks to B. Conard for INAA instruction and A. Ungerer for space and lab assistance. Thanks to R. Keller, C. Sinton, B. Gallahan the IX, K. McKelwee and all the other students I should have known or forgotten. Support for this (and hopefully future) work was graciously provided by the National Science Foundation under grants OCE87-11120, OCE89-01405, and OCE90-00595 and viewers like you. Curation and storage of the MW8801 samples is funded under an NSF grant to the Oregon State University Repository. Allann Brothers is (are?) noted for gallons of coffee which cost plenti-o-money.

A major part of this thesis involves Sr, Nd, and Pb isotope work and J. Mahoney played an instrumental role in making sure that the quality of these results is unsurpassed. I greatly appreciate the enthusiasm, good nature and hospitality extend by Officer Mahoney (and Nancy) on each and every visit to Hawaii. He has taught me the true meaning of

clean. Many thanks to K. Spencer and the mighty Peng for help in the SOEST lab and on the mass spectrometer. The participants of the alternate TGIF are thanked for providing that essential outlet, they are true Rhino Chasers. If their eyes ever scan these lines, may they toss it over the balcony, preferably around sundown (on fire would be a nice effect).

There are a select few that deserve special consideration. None of this would have happened without the support and encouragement of R. Duncan, the only person who saw it all. And then there's '...WHAT...ARE YOU....DOING!' Lew, thanks for teaching me how to burn my fingers intentionally. I'd also like to thank R. Hart for employment even when funding was tight and introducing me to the Archean, peridotites, seafloor alteration, chert, and true geochemistry. And of course, the best for last - I could never adequately convey my gratitude to Dave Christie. He unselfishly allowed me to work through this entire project, offering great advise and a healthy perspective on the business of science. It is undoubtedly rare when a study as interesting as the AAD gets dropped into your lap - truly a case of the right place at the right time. I couldn't have stumbled into a better project or advisor.

Finally, I'd like to thank good ol' mom for that procrastination gene, anything that could be done today can probably be done tomorrow in less time (probably). I'd like to thank P.B. West for providing the means and having the insight to know that I could get this far. But the ONE, most important person who really deserves credit for getting me through this work is Heidi. She has invested as much time as I, but sacrificed more, without gaining any of the satisfaction. I thank her for her companionship, understanding, and most of all, for knowing that nothing should be taken too seriously.

TABLE OF CONTENTS

Table of Contents
(continued)

List of Figures

Chapter 4

List of Tables

Geochemistry of Mid-Ocean Ridge Basalt Within and Surrounding the Australian-Antarctic Discordance

Chapter 1

Introduction and Overview

The global Mid-Ocean Ridge spreading system samples the earth's upper mantle along a continuous volcanic system that stretches across nearly 25,000 km of the earth's surface. Compositional and morphological variations within and between Mid-Ocean Ridge spreading centers convey basic information on the physical processes leading to upper mantle melting and seafloor accretion. In the past decade, physical models of mantle melting and melt extraction have converged with observations from global variations in Mid-Ocean Ridge basalt composition, to show that mantle temperature directly affects both the physical and chemical characteristics of the spreading ridge [McKenzie, 1884; Klein and Langmuir, 1987; McKenzie and Bickle, 1988; Langmuir et al., 1993; Forsyth, 1993 and references therein].

This thesis is a geochemical study of an 800 km section of the Southeast Indian Ridge (SEIR) which includes the Australian-Antarctic Discordance (AAD). Mid-ocean ridge basalts collected for this study were recovered from spreading segments that display a significant range, comparable to the entire global variation, of Mid-Ocean Ridge axial morphologies and basalt compositions. The contrasts in axial morphology in this relatively restricted section of the Southeast Indian Ridge are comparable to differences between the fast-spreading East Pacific Rise and the slow-spreading Mid-Atlantic Ridge, even though they occur at a uniform, intermediate spreading rate of ~74 mm/yr [Weissel and Hayes, 1971; DeMets et al., 1990]. Since spreading rate is not a factor, fundamental differences in

magma supply must be the dominant factor determining the physical and chemical contrasts along the spreading axis in this region.

The Australian-Antarctic Discordance (AAD) is a unique among spreading systems because it encompasses radical changes in axial bathymetry and ridge segmentation that occur over less 50 km along-axis. Spreading segments are generally ~1000 m deeper within the AAD, than along adjacent sections of the SEIR [Hayes and Conolly, 1972; Hayes, 1988; Marks et al., 1991]. Within the AAD, spreading segments are <100 km in length and offset along large transforms, whereas east of the AAD, the spreading axis is continuous for 200-300 km and offset only by propagating rifts. In fact, the AAD is centered on a bathymetric low which spans the entire Southeast Indian Ocean basin between Australia and Antarctic (Fig. I.1) [Veevers, 1982]. Coincident with the AAD bathymetric anomaly is a gravity/geoid low (Fig. I.1) [Weissel and Hayes, 1974; Marks et al., 1990, 1991]. Taken together, the depth and geoid anomalies have been interpreted as reflecting downwelling, convective flow in the upper mantle [Hayes and Conolly, 1972; Weissel and Hayes, 1974]. The arcuate shape of the depth-geoid anomaly suggests that these features have remained centered on the spreading axis and migrated westward through much of the history of the basin. Also, variations in the amplitude of the depth anomaly have been interpreted as fluctuation in the strength of the mantle forces creating the unique geophysical features of the AAD [Marks et al., 1990].

Prior to this investigation, the eastern SEIR between 115°E and 138°E had been sampled at only eleven dredge sites [Anderson et al., 1980; Klein et al., 1988]. Eight of these dredge sites are located east and west of the AAD, but only three lie within the AAD. Aspects of the petrology and geochemistry of the basalts recovered from this 1700 km length of the eastern SEIR have been reported in several investigations [Anderson et al., 1980; Klein and Langmuir, 1987; Klein et al., 1988; Klein et al., 1991] which recognized that the three AAD basalts represent an endmember in the global spectrum of mid-ocean ridge major element compositions. These AAD basalts have had a profound

Figure. I.1 Residual bathymetric anomaly and geoid anomaly of the eastern Southeast Indian Ocean basin [Marks et al., 1991]. The could be interpreted as resulting from downwelling, convective flow in the mantle beneath the AAD [Hayes and Conolly, 1972; Weissel and Hayes, 1974; Klein et al., 1988].

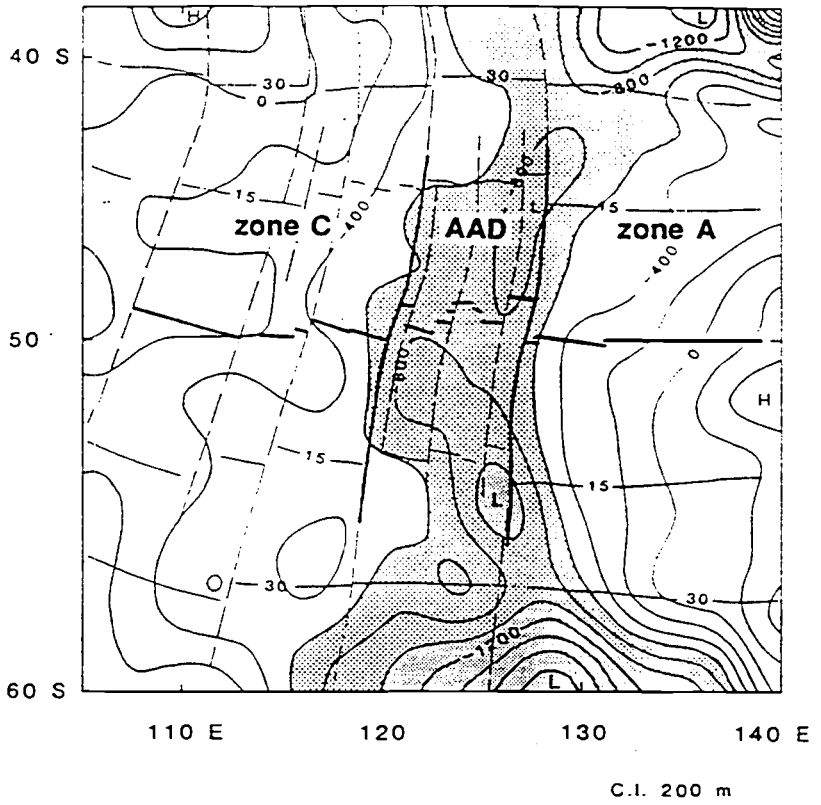

Marks et al., 1991

AAD Residual Depth Anomalies

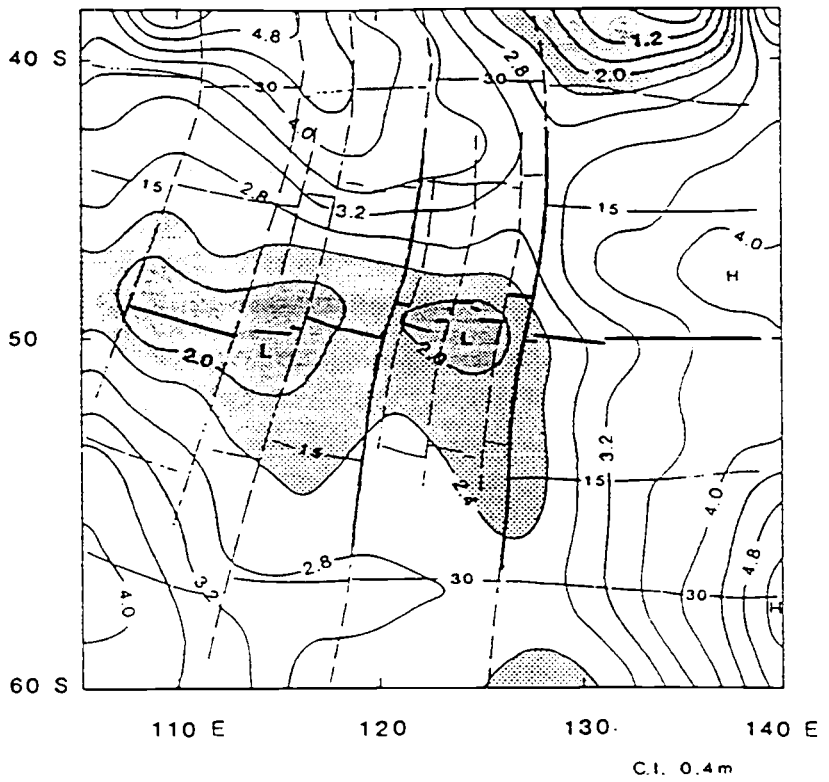

AAD Residual Geoid Anomalies

Figure I.1

impact on the understanding of melt generation and crustal accretion at mid-ocean ridge systems worldwide. The unique compositional characteristics of AAD basalts and the unusually deep axial depth from which they erupted, have suggested that the mantle beneath the AAD is abnormally cold relative to normal MORB mantle [Klein and Langmuir, 1987]. In addition, Klein et al. [1988] discovered that a boundary between isotopically defined Pacific Ocean upper mantle and Indian Ocean upper mantle existed beneath the AAD and that the transition between these two major mantle reservoirs occurred between two AAD dredge sites separated by ~200 km.

A dredging and SeaMARCII mapping investigation of the Southeast Indian Ridge within and east of the AAD was conducted in January and February of 1988 aboard the *R/V Moana Wave*. The objectives of this study were to gain a better understanding of the position and nature of the isotopic boundary, characterize the major and trace element diversity of basalts generated within the AAD and along surrounding spreading segments, and determine how the geochemical diversity in the region relates to the contrasts in axial depth, morphology, and mantle temperature. The geophysical aspects of this study have been discussed by Sempéré et al. [1990], Palmer et al. [1993], and West et al. [1994]. This thesis addresses the geochemical aspects of mid-ocean ridge basalts collected within and surrounding the AAD during the *R/V Moana Wave* cruise MW8801. The body of this work is divided into three papers. The first two papers discuss the major element, trace element and isotopic geochemistry of samples dredged along Southeast Indian Ridge within and east of the AAD. The third paper grew out of the isotopic results presented in the first paper. It expands the compositional characterization of Southeast Indian Ocean seafloor by using additional samples taken from existing core material recovered by the Deep Sea Drilling Program.

Chapter 2, "Resolving an isotopic boundary in the Australian-Antarctic Discordance", was co-authored by D.M. Christie and J.J. Mahoney and published in Earth Planetary Science Letters. This chapter presents the Sr, Nd, and Pb isotope results for a

selected group of basaltic glass samples to determine the position, width and transitional characteristics of the isotopic boundary detected by an earlier regional study of the eastern SEIR [Klein et al., 1988]. our new data show that the isotopic boundary is surprisingly abrupt, only 40 km in width along-axis, and that limited mixing between the Pacific Ocean upper mantle and the Indian Ocean upper mantle may have occurred beneath the easternmost AAD spreading segment. No comparable mantle boundary is known along the worldwide MOR spreading system.

More remarkable, is evidence that the isotopic boundary has migrated westward at a minimum rate of ~25 mm/yr over the last 4 m.y. Assuming a steady migration rate, the position of the boundary can be extrapolated to the eastern margin of Australia and Antarctica prior to the breakup of these two Gondwana continents, suggesting that Pacific upper mantle may have flowed westward in response to the opening of the Southern Ocean Basin (see Chapter 4).

Chapter 3. "Geochemistry and Morphology of the Southeast Indian Ridge in the Vicinity of the Australian-Antarctic Discordance", is co-authored by D.M Christie. This chapter is an examination of the major and trace element variations that accompany the abrupt changes in axial segmentation and morphology between the AAD and spreading segments of the SEIR to the east. Since spreading rate is uniform throughout this region, compositional and morphological variations are most likely related to variations in melt production beneath the spreading axis. The AAD spreading system has a deficient melt supply to the spreading axis and compositional variations appear to be controlled primarily by partial melting in the mantle source. The SEIR east of the AAD has an excess melt supply, and compositional diversity is dominated by shallow-pressure crystal fractionation. Mid-ocean ridge basalt compositions and axial morphology vary systematically between these two regions.

The major element characteristics of AAD basalts indicate that they are derived from low pressures of melting and low average degrees of melting. The major element contrasts

between the AAD basalts and surrounding SEIR basalts are consistent with variations in mantle temperature producing variations in mantle melting. However, trace element systematics show that lavas produced by low degree melting within the AAD and Zone A have very similar characteristics, despite their very different major element compositions. The major and trace element variations cannot be produced by differences in partial melting alone, unless trace element heterogeneity in the source mantle is invoked. An alternative model is presented in which the modal proportion of clinopyroxene (cpx) contributing to melting is varied. This model satisfies the trace element conditions and predicts that the AAD mantle is higher in modal cpx. Therefore, AAD basalts are the product of lower degrees of melting within a more fertile, clinopyroxene-rich source mantle.

Chapter 4. "Geochemistry and Geochronology of Ancient Southeast Indian and Southwest Pacific seafloor", is co-authored by D.M. Christie, J.J. Mahoney and R.A. Duncan. This paper presents a geochemical study of basaltic samples from older Southern Ocean seafloor recovered by Legs 28 and 29 of the Deep Sea Drilling Project (DSDP). This study centered on the development of a regional framework for the distribution of Indian Ocean and Pacific Ocean upper mantle through time in order to constrain a fundamental question concerning the nature history of the isotopic boundary within the AAD. Is the observed small-scale displacement of the isotopic boundary a result of local variations in the position of a boundary that is, in the long term, tied to the AAD, or is it indicative of a large-scale, westward migration of Pacific Ocean upper mantle which began as Australia and Antarctica drifted apart?

The DSDP study documents regional variations in the isotopic composition of the mantle beneath the Southern Ocean Basin that are consistent with, but do not require long-term, westward migration of the Pacific Ocean upper mantle. Isotopic signatures that are intermediate between those of Indian Ocean and Pacific Ocean upper mantle occur close to Tasmania, well to the east of the present isotopic boundary, suggesting that the boundary has not always existed beneath the AAD and therefore, implying large scale migration.

Further sampling, by ocean drilling, of seafloor <40 m.y. and located west of the South Tasman Rise is necessary to determine whether long-term westward flow of Pacific Ocean upper mantle has occurred.

West of the AAD, the compositional influence of the Kerguelen hot spot on basalts formed along the SEIR increases with decreasing seafloor age. The isotopic and trace element trends suggest that a mantle contaminant derived from the Kerguelen plume was carried eastward as seafloor spreading progressed. The enrichment trend of these older SEIR basalts is the opposite of what would be expected if a broad Kerguelen plume head had spread beneath this region.

The co-authors for the chapters provided analytical facilities and valuable instruction. The Sr, Nd, and Pb isotopic analyses were completed at the University of Hawaii with the help of J.J. Mahoney. The ^{40}Ar-^{39}Ar analyses were completed at Oregon State University with the guidance of R.A. Duncan. D.M. Christie provided financial support through grants OCE 87-11120, OCE 90-00595 and OCE 92-17186 from the National Science Foundation for all of this work. Ideas that have evolved from this geochemical study of seafloor basalts from the eastern Southeast Indian Ocean are the result of active participation by all the co-authors.

Chapter 2

Resolving an Isotopic Boundary within the Australian-Antarctic Discordance

D.G. Pyle, D.M. Christie, and J.J. Mahoney

ABSTRACT

New Sr, Nd, and Pb isotopic analyses of MORB glasses from the Australian-Antarctic Discordance (AAD) confirm the presence of an abrupt boundary between 'Indian'-type and 'Pacific'-type MORB mantle. The transition between these two upper mantle reservoirs is gradational along ~40 km of the easternmost AAD spreading center (i.e. segment B5W) and terminates at its western ridge-transform intersection. Axial lavas dredged immediately west of the B4/B5 transform are unequivocally derived from an 'Indian' MORB source, whereas axial lavas dredged east of this transform have a 'Pacific'-type signature with evidence of an 'Indian' MORB imprint. Off-axis sampling of the easternmost AAD spreading segment show these lavas to have been derived from an 'Indian'-type source indicating that the isotopic boundary has migrated westward into the AAD in the last 3-4 Myr. Pacific mantle must flow beneath the B5 spreading axis at a rate of ~25 mm/yr in order for it to displace Indian mantle as the source of melt for this segment. The gradational character of the boundary suggests that as the westward migration of 'Pacific' mantle progresses, an increasing memory of a remnant 'Indian' signature is incorporated into lavas near the leading edge of the boundary zone. At present, approximately equal proportions of 'Pacific' and 'Indian' mantle contribute to the isotopic signature of lavas erupted 10 km east of the B4/B5 spreading axis offset at ~126° E. Migration of the boundary could reflect a continuous, large-scale, westward outflow of upper mantle which has recently arrived beneath the AAD from a shrinking Pacific basin, or alternatively, the displacement may reflect a small-scale perturbation of a long-term isotopic discontinuity, created and maintained by the mantle dynamics producing the AAD.

INTRODUCTION

The Australian-Antarctic Discordance (AAD) is a 500 km section of the Southeast Indian Ridge (SEIR) at the center of a basin-wide, seafloor depression between Australia and Antarctica. This spreading center is one of the deepest of the global mid-ocean ridge system (4000-4500 m) [Cochran, 1986; Marks et al., 1990] and a unique feature of the world's ocean basins. Weissel and Hayes [1971] subdivided this region into zone A, zone B (the AAD) and zone C based on the remarkable contrasts in seafloor morphology that exist between each zone (Fig. II.1). Contrasts in axial morphology, analogous to well-known differences between the fast-spreading East Pacific Rise and the slow-spreading Mid-Atlantic Ridge, occur between zone A and the AAD despite a regionally uniform spreading rate (~74 mm/yr) [Palmer et al., 1991; Sempéré et al., 1991]. The morphological contrasts encompass most of the global variability in accretionary tectonics and appear to reflect fundamental differences in magma supply rates beneath adjacent portions of the SEIR [Palmer et al., 1991; Sempéré et al., 1991; Klein et al., 1991; Christie et al., 1988; Pyle and Christie, 1992].

The unusually deep AAD spreading ridge is centered on a regional geoid low [Weissel and Hayes, 1971, 1974]. Anomalously high upper mantle shear wave velocities also coincide with the depth anomaly, indicating the presence of cooler mantle beneath the AAD [Forsyth et al., 1987]. The depth anomaly appears to have existed beneath this area at least since seafloor spreading began at ~100 Ma, and possibly before continental rifting [Cande and Mutter, 1982; Mutter et al., 1985; Veevers, 1982]. The broad V-shaped pattern of the depth and gravity anomalies on the surrounding seafloor suggests that the "source" of the AAD has migrated westward at ~15 mm/yr [Marks et al., 1990, 1991] and remained centered on the SEIR which is migrating northward at ~40mm/yr (absolute motion) [DeMets et al., 1990]. Therefore, the mantle dynamics producing the AAD cannot be fixed in an absolute reference frame [Marks et al., 1990, 1991].

Figure II.1 Regional bathymetry of the Southeast Indian Ocean modified from a Deep Sea Drilling Project compilation map. Kerguelen plateau bathymetry is from Royer and Sandwell [1989] and spreading axis trace is taken from Cande et al. [1989]. The locations of Vema dredge samples analyzed by Klein et al. [1991] are designated by open circles along the SEIR east and west of the AAD (zone A and zone C, respectively). Active westward propagating rifts are shown schematically as dashed arrows along the zone A spreading axis. The box encompassing part of the AAD and zone A outlines the approximate boundaries of Fig. II.2.

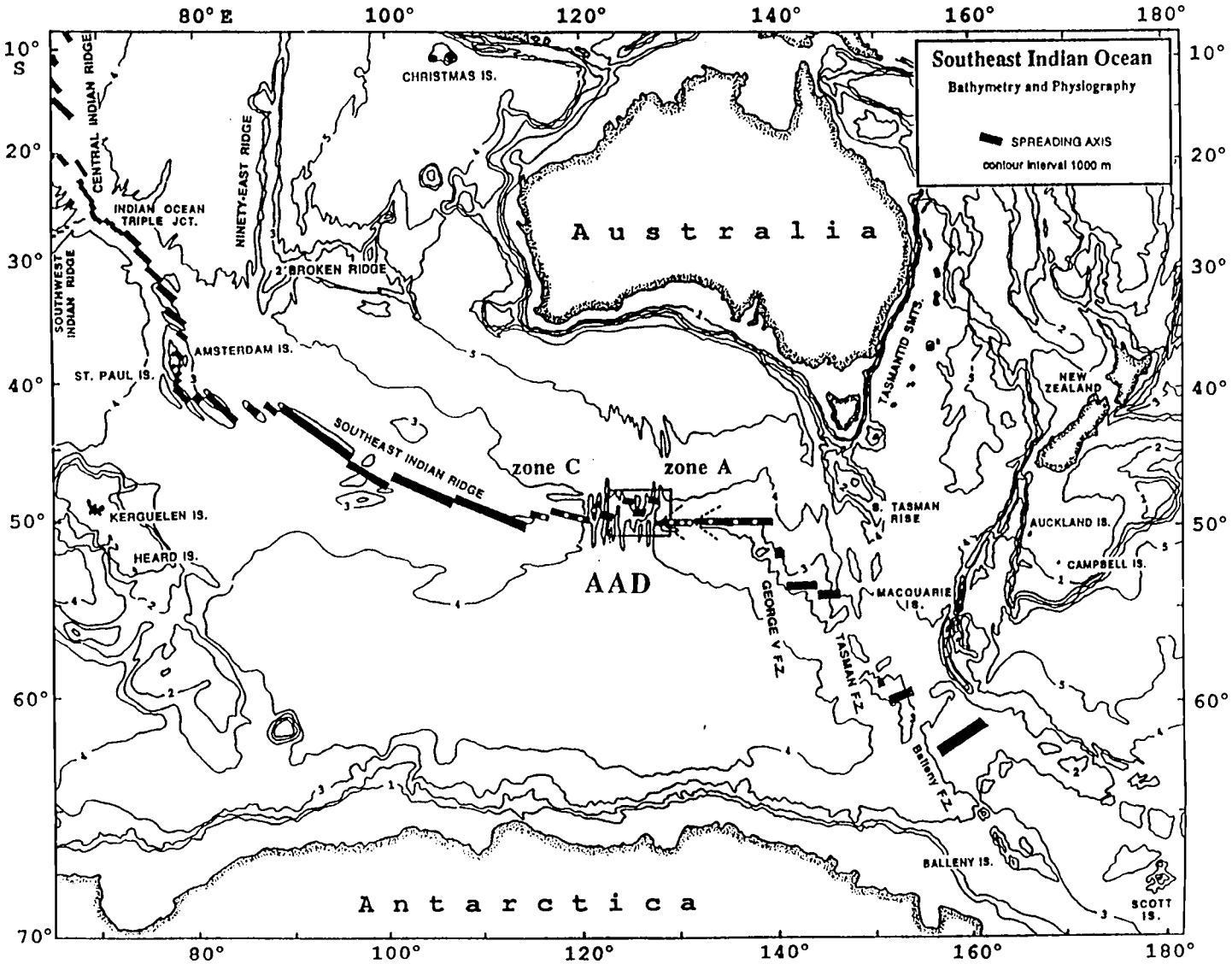
Southeast Indian Ocean
Bathymetry and Physiography
SPREADING AXIS
contour interval 1000 m
80° E
100°
120°
140°
160°
180°
10° S
20°
30°
40°
50°
60°
70°
CENTRAL INDIAN RIDGE
NINETY-EAST RIDGE
CHRISTMAS IS.
INDIAN OCEAN TRIPLE JCT.
SOUTHWEST INDIAN RIDGE
BROKEN RIDGE
Australia
AMSTERDAM IS.
ST. PAUL IS.
TASMANTID SEAMTS.
NEW ZEALAND
SOUTHEAST INDIAN RIDGE
zone C
zone A
KERGUELEN IS.
HEARD IS.
S. TASMAN RISE
AUCKLAND IS.
CAMPBELL IS.
AAD
GEORGE V FZ
MACQUARIE IS.
TASMAN FZ
Balleny FZ
BALLENY IS.
Antarctica
SCOTT IS.

Figure II.1

Petrologically, the AAD lavas constitute one end-member of a broad global correlation between ridge depth and $Na_{8.0}$, $Si_{8.0}$ and $Fe_{8.0}$ values (i.e. Na_2O, SiO_2, FeO contents corrected to 8.0% MgO) [Klein and Langmuir, 1987]. AAD lavas are generally more primitive (i.e. higher MgO), and have higher $Na_{8.0}$, lower $Fe_{8.0}$, and higher $Si_{8.0}$ values relative to zone A, indicating lower extents of partial melting and lower mean pressures of melting beneath the AAD [Klein et al., 1991; Christie et al., 1988; Pyle and Christie 1992; Klein and Langmuir, 1987; Anderson et al., 1980]. Moreover, a major upper mantle boundary between isotopically distinct Indian and Pacific mid-ocean ridge basalt (MORB) occurs beneath the AAD, independent of the morphologic and major element discontinuities associated with zone A-AAD transform fault boundary [Klein et al., 1988]. In this paper we refine the details of the isotopic transition between Indian and Pacific MORB sources beneath the AAD with data from thirteen new dredge sites between 128°-123° E. The data show the isotopic boundary to be unusually abrupt and that it has migrated westward over the last 4 Myr. The nature of the isotopic boundary, its migration history, and its relationship to the AAD are important keys to understanding the mantle dynamics creating the AAD, as well as to understanding the development of the Indian Ocean MORB reservoir.

SAMPLE SELECTION and ANALYTICAL METHODS

Data presented in this paper (Table II.1) are from samples obtained during cruise MW8801 of the R/V Moana Wave in 1988. Dredge sites were selected along ~800 km of the SEIR in zones A and B (AAD) on the basis of SeaMARC II bathymetry and side-scan imagery obtained during the same cruise [Palmer et al., 1991; Sempéré et al., 1991]. Herein, zones A and B are further subdivided into spreading segments (B1-B5 and A1-A3) which are delineated by major transform faults or propagating rifts (Fig. II.2) [Vogt et al., 1983]. The along-axis dredge interval varies from 5 to 80 km, averaging around 40 km. In twenty-five dredge hauls, we recovered over 650 individual samples with quenched

Table II.1 Sr, Nd and Pb isotope ratios of Southeast Indian Ridge MORB (123°E - 130°E).

Sample†	latitude (°S)	longitude (°E)	$^{87}Sr/^{86}Sr$	$^{143}Nd/^{144}Nd$	ε_{Nd}	$^{206}Pb/^{204}Pb$	$^{207}Pb/^{204}Pb$	$^{208}Pb/^{204}Pb$	depth* (m)
Zone A									
MW88-13-47	50.15	128.01	0.70258	0.513076	8.5	18.656	15.485	38.136	3500
MW88-16-1	50.16	127.58	0.70251	0.513088	8.7	18.717	15.466	38.153	3450
MW88-16-12	50.16	127.58	0.70258	0.513064	8.3	18.798	15.504	38.291	3450
MW88-17-26	50.22	127.42	0.70254	0.513054	8.1	18.630	15.475	38.099	3350
AAD									
MW88-4-2	48.76	127.36	0.70248	0.513092	8.8	18.649	15.491	38.154	3900
				0.513087	8.7				
MW88-6-2	48.76	126.88	0.70268	0.513050	8.0	18.398	15.477	38.005	4400
MW88-5-1	48.68	126.52	0.70284	0.513038	7.8	18.226	15.465	37.956	4700
MW88-22-13	49.68	125.89	0.70281	0.513184	10.6	17.764	15.431	37.584	4200
MW88-23-1	49.61	125.66	0.70285	0.513234	11.6	17.805	15.421	37.638	3800
MW88-27-58	49.06	124.96	0.70365	0.512903	5.1	17.888	15.490	37.837	4200
MW88-27-71	49.06	124.96	0.70290			17.843	15.462	37.614	4200
MW88-30-6	48.94	124.28	0.70295	0.513012	7.3	17.926	15.475	37.769	3500
MW88-26-1	49.46	123.23	0.70276	0.513048	8.0	17.894	15.452	37.626	4700
MW88-18-4 ††	50.04	126.74	0.70305	0.513025	7.5	17.903	15.459	37.742	4000
MW88-24-18 ††	49.77	126.17	0.70305	0.512997	7.0	17.965	15.470	37.872	3600

† Sample numbers consist of three elements. MW88-26-1 refers to sample number 1, dredge station 26 of the cruise MW8801 of the R/V Moana Wave. In the text, this sample is referred to as MW26-1.

†† Off-axis samples recovered from ~3-4 Ma seafloor within the B5 spreading segment.

* Depth determined from SeaMarcII bathymetry.

Isotopic fractionation corrections are $^{148}NdO/^{144}NdO=0.242436$, corresponding to $^{148}Nd/^{144}Nd=0.241572$; $^{86}Sr/^{88}Sr=0.1194$. Data are reported relative to U. of Hawaii standard values: for La Jolla Nd, $^{143}Nd/^{144}Nd=0.511855$; for BCR-1, $^{143}Nd/^{144}Nd=0.512630$; for NBS 987 Sr, $^{87}Sr/^{86}Sr=0.71025$; for E & A Sr, $^{87}Sr/^{86}Sr=0.70803$. The total range measured for La Jolla Nd is ±0.000012 (0.2 ε_{Nd} units); for NBS 987 Sr it is ±0.000022. Pb isotopic ratios are corrected for fractionation using the NBS 981 standard values of Todt et al. [1983]; the total ranges measured are ±0.010 for $^{206}Pb/^{204}Pb$, ±0.009 for $^{207}Pb/^{204}Pb$, and ±0.032 for $^{208}Pb/^{204}Pb$. Within-run errors on individual sample measurements are less than or equal to the above external uncertainties on the La Jolla, NBS 987, and NBS 981 standards in all cases.

Total procedural blanks are 5-30 picograms for Pb, <20 picograms for Nd, and <120 picograms for Sr; all are negligible.

ε_{Nd} (0)=0 corresponds to $^{143}Nd/^{144}Nd=0.51264$.

glassy margins. Major element analyses of all the glasses were determined by electron microprobe, and 47 compositionally distinct groups have been identified based on those results [Pyle and Christie, 1992]. The most primitive chemical groups within selected dredge hauls (i.e. highest MgO) were sampled for Pb, Sr, and Nd isotope analysis. Fifteen glasses were analyzed (Table II.1), including thirteen "zero-age" samples from 11 sites in zones A and B, as well as two off-axis samples collected on 3-4 Ma seafloor within segment B5. Trace element variability at MW16 (propagating rift tip) and MW27 (segment B3) indicate the presence of multiple mantle sources [Pyle and Christie, 1992] which we have investigated by isotopic analyses of two groups from each site.

All samples were crushed in a ceramic mortar, sieved to a 30-mesh size fraction (~0.5-1.0 mm) and hand-picked for glass free of phenocrysts and weathered or altered material. In some cases, microcrystalline phases could not be avoided and it is presumed that they represent incipient crystallization of the host glass. Splits of ~50 mg of fresh glass were sequentially cleaned in acetone, 2N HCl, and 2N HNO_3 for 10-20 minutes in an ultrasonic bath to remove surface contaminants. Pb, Sr, and Nd were separated from a single digestion and analyzed by the VG Sector multicollector mass spectrometer at the University of Hawaii. Chemical and mass spectrometric techniques are described by Mahoney et al. [1991].

RESULTS

Along-axis Isotopic Variations

Our new Sr, Nd, and Pb isotopic data for SEIR MORB glasses from 123° E to 130° E are shown with data of Klein et al. [1988] in figure II.3. The two data sets agree well and confirm the presence of clearly definable 'Indian'-type and 'Pacific'-type isotopic populations (through the remainder of the text, 'Indian' and 'Pacific' refer to lavas from zones A, B, and C while Pacific MORB and Indian MORB refer to the overall reservoir). Indian Ocean MORB are distinct from Pacific (and north Atlantic) MORB in extending to

Figure II.2 Simplified SeaMARC II bathymetry (500 m contours) and tectonics of the AAD and zone A spreading centers surveyed during the MW8801 cruise of the R/V Moana Wave Moana [Palmer et al., 1993]. MW8801 dredge locations are shown as rectangular symbols and prefixed by 'MW'. Vema dredges are shown as filled circles and prefixed by 'V'. Non-transform ridge discontinuities (NTD) separate the AAD spreading centers into east and west segments (e.g. B4E and B4W). Spreading segments A1 and A2 represent a doomed rift-propagating rift system within zone A.

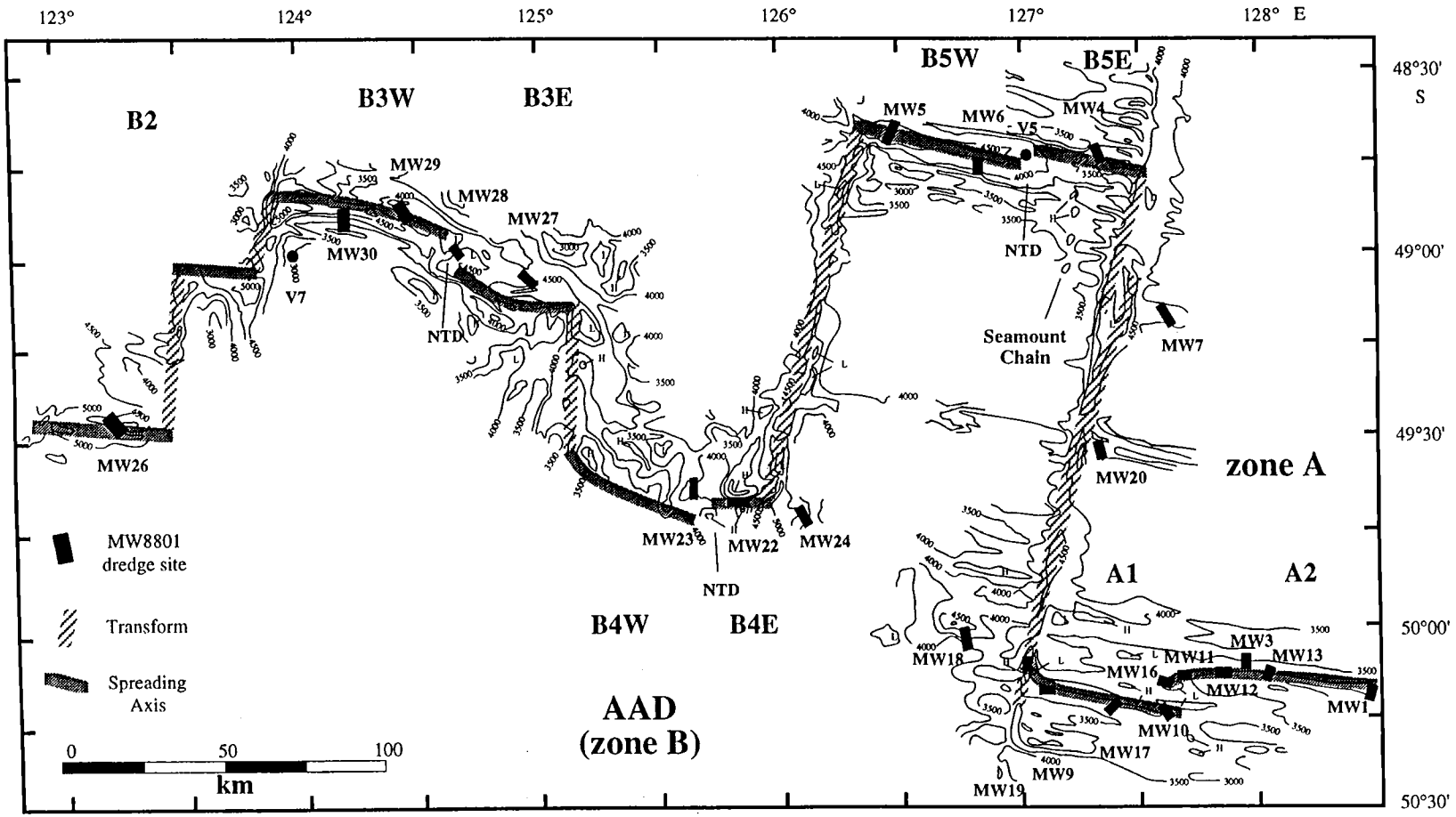
123°
124°
125°
126°
127°
128° E
48°30' S
49°00'
49°30'
50°00'
50°30'
B2
B3W
B3E
B4W
B4E
B5W
B5E
A1
A2
zone A
AAD (zone B)
MW1
MW3
MW4
MW5
MW6
V5
MW7
MW9
MW10
MW11
MW12
MW13
MW16
MW17
MW18
MW19
MW20
MW22
MW23
MW24
MW26
MW27
MW28
MW29
MW30
V7
NTD
NTD
NTD
Seamount Chain
MW8801 dredge site
Transform
Spreading Axis
0
50
100
km

Figure II.2

lower $^{206}Pb/^{204}Pb$ values and having higher $^{87}Sr/^{86}Sr$, lower $^{143}Nd/^{144}Nd$, and higher $^{208}Pb/^{204}Pb$, $^{207}Pb/^{204}Pb$ at a given $^{206}Pb/^{204}Pb$ [Subbarao and Hedge, 1973; Hedge et al., 1973; Dupré and Allègre, 1983; Hamelin and Allègre, 1985; Hamelin et al., 1986; Hart, 1984; Michard et al., 1986; Price et al., 1986; Dosso et al., 1988; Mahoney et al., 1989, 1992]. Consequently, lavas derived from 'Pacific' and 'Indian' MORB sources are readily distinguishable along-axis. The isotopic discontinuity between 'Pacific' and 'Indian' MORB within the AAD is defined by an abrupt westward decrease in $^{206}Pb/^{204}Pb$ and $^{208}Pb/^{204}Pb$, and an increase in $^{87}Sr/^{86}Sr$ along the western 40 km of the B5 spreading axis (Fig. II.3). Contrasts in $^{207}Pb/^{204}Pb$ and $^{143}Nd/^{144}Nd$ between the 'Indian' and 'Pacific' groups are less distinct, but both ratios are systematically lower in lavas dredged west of the isotopic boundary located near the B4/B5 transform at ~126°E (Fig. II.2).

The transition from a 'Pacific' to an 'Indian' MORB source occurs west of a non-transform discontinuity (NTD) that offsets the B5 axis by 2-3 km near 127° E. Lavas from the B5E segment, including those recovered within the NTD (V5), are indistinguishable from the 'Pacific' lavas of zone A despite an ~150 km offset of the B5E-zone A spreading segments. The B5W lavas become progressively more 'Indian'-like toward the B5/B4 transform boundary with sample MW5-1, dredged 10 km from the ridge-transform intersection, having isotopic characteristics which could be considered as Pacific or Indian MORB. By contrast, MW22-13 (B4E) has an unequivocal 'Indian' isotopic signature and lies less than 7 km from the B4/B5 transform. Both MW22-13 and MW5-1 overlap in $^{87}Sr/^{86}Sr$, but abrupt discontinuities in radiogenic Pb and Nd between the B4 and B5 segments suggest that the eastern limit to the Indian Ocean MORB reservoir is near the B4/B5 transform within the AAD. B4E 'Indian' lavas show no gradation toward 'Pacific' isotopic ratios and have maintained a distinctive signature. Thus it appears that the lavas generated from a 'Pacific' MORB source beneath B5W segment interact with increasing amounts of 'Indian' mantle material approaching the B4/B5 transform.

Figure II.3 Along-axis profiles of isotopic ratios from the SEIR between 115° E and 138° E. Open symbols represent 'Pacific' group compositions and filled symbols represent 'Indian' group compositions. Data from this study are shown as squares and the results of Klein et al. [1988] are shown as triangles. Filled squares with open circles are off-axis samples from segment B5. The horizontal axis represents distance (km) from the eastern bounding transform fault of the AAD. Two longitude scales are shown because of the ~.5° eastward offset of the B5 spreading axis at 48°45' S from the termination of the zone A spreading axis at 50°15' S. Vertical solid lines indicate transforms, vertical dashed lines indicate non-transform discontinuities within the AAD and propagating rift tips within zone A. The present location of the leading edge of the isotopic boundary is at or very close to the B4/B5 transform fault. The shaded fields display the isotopic variability within the 'Indian' and 'Pacific' groups excluding unusually high or low values. The axial depth profile is compiled from SeaMARC II bathymetry (solid line) [Palmer et al., 1993], dredge depths (solid circles) [Klein et al., 1988], and best fit subsidence curve to ridge flanks (open circles) [Cochran, pers.comm.].

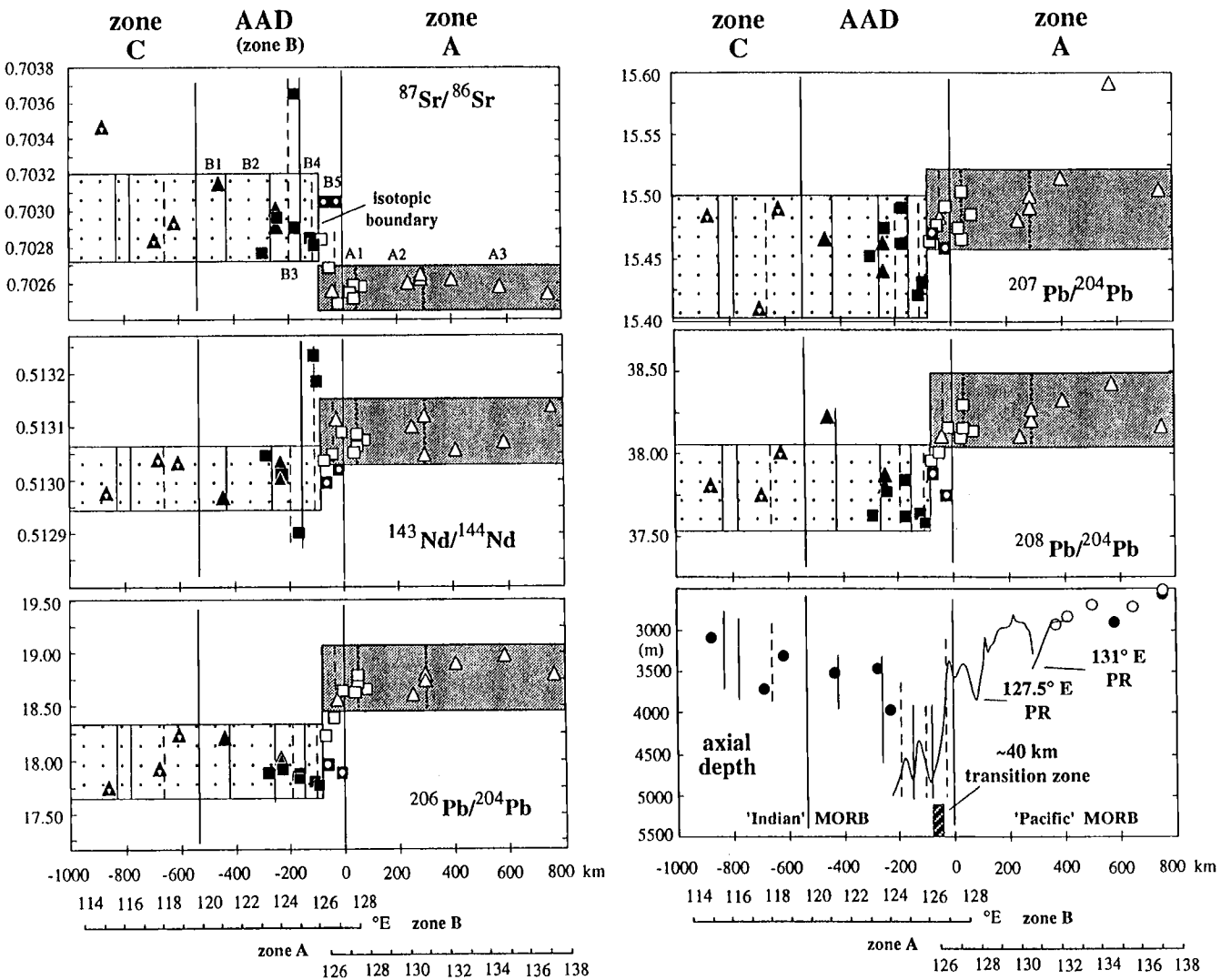
zone C
AAD (zone B)
zone A
$^{87}Sr/^{86}Sr$
B1
B2
B4
B5
B3
isotopic boundary
A1
A2
A3
$^{143}Nd/^{144}Nd$
$^{206}Pb/^{204}Pb$
$^{207}Pb/^{204}Pb$
$^{208}Pb/^{204}Pb$
axial depth
131° E PR
127.5° E PR
~40 km transition zone
'Indian' MORB
'Pacific' MORB
°E
zone B
zone A

Figure II.3

Off-axis Isotopic Variations

Basaltic glasses from dredge sites located on 3-4 Ma seafloor south of the B5 spreading center (MW18, MW24) have Sr, Nd, and Pb isotope ratios that lie well within the range of 'Indian' values (Fig. II.3). This contrasts with the 'Pacific' signature of the B5 axial lavas, implying that the isotopic boundary has migrated ~100 km westward beneath the B5 segment during the last 3-4 Myr. Assuming that the isotopic boundary coincided with the eastern AAD bounding transform circa 4 Ma, and that it now lies at the B4/B5 transform, a 'Pacific' mantle migration rate of approximately 25 mm/yr is required. Despite the rapid westward migration of 'Pacific' mantle, only a very narrow transition zone separates the 'Pacific' and 'Indian' MORB sources. In fact, the B5W isotopic gradients may reflect a 'memory-effect', sampling the last vestiges of Indian mantle left behind the leading edge of a migrating 'Pacific' mantle. The lack of a discernible 'Pacific' mantle signature in 'Indian'-type, off-axis B5 samples and axial B4 samples is consistent with such a memory effect. The isotopic boundary within the AAD is a unique feature separating two large upper mantle reservoirs with very different isotopic histories. It is quite unlike the broad regional geochemical gradients commonly observed along mid-ocean ridges adjacent to hot spots [e.g. Hart et al., 1973; Sun et al., 1975; Schilling et al., 1982; Schilling, 1985] and it also appears to be unlike a more diffuse, gradational Indian-Atlantic boundary along the Southwest Indian Ridge [Schilling et al., 1982].

Isotopic Diversity within MORB Groups

The 'Indian' group is also distinct from the 'Pacific' group in displaying greater isotopic diversity. The contrast in diversity is most pronounced in $^{87}Sr/^{86}Sr$, for which the 'Indian' group range (0.70276-0.70365) is five times greater than the 'Pacific' group range (0.70248-0.70264; Table II.2, Fig. II.3). Although much of the 'Indian' group range is encompassed by two samples from a single dredge (MW27), there is a substantial spread in $^{87}Sr/^{86}Sr$ between samples from other dredge sites in zones B and C [Klein et al., 1988].

Table II.2 Isotopic averages and variability of the MORB sources beneath the eastern SEIR.

	$^{87}Sr/^{86}Sr$	$^{143}Nd/^{144}Nd$	ε_{Nd}	$^{206}Pb/^{204}Pb$	$^{207}Pb/^{204}Pb$	$^{208}Pb/^{204}Pb$
'Pacific' group †						
n=12						
average	0.702568	0.513086	+8.7	18.742	15.498	38.197
sd	0.000044	0.000029	0.6	0.124	0.032	0.102
range	0.000156	0.000089	1.7	0.406	0.124	0.321
SE%	0.0063	0.0057	6.8	0.664	0.206	0.268
'Indian' group						
n=14						
average	0.703036	0.513036	+7.7	17.945	15.458	37.792
sd	0.000251	0.000086	1.7	0.149	0.025	0.167
range	0.000884	0.000331	6.5	0.484	0.081	0.627
SE%	0.0357	0.0168	22	0.831	0.161	0.443

† Excluding samples MW5-1 and MW6-2 from the B5W spreading segment.

In contrast, 'Pacific' group $^{87}Sr/^{86}Sr$ values are remarkably uniform along 800 km of the SEIR east of the isotopic boundary, both within and between dredges, and comparable to the $^{87}Sr/^{86}Sr$ homogeneity of Pacific MORB from the East Pacific Rise [Macdougall and Lugmair, 1985; White et al., 1987; Ito et al., 1987].

In terms of Nd and Pb isotope ratios, the 'Indian' and 'Pacific' groups display broadly similar ranges, but for each isotopic system, individual outliers within the 'Indian' data suggest that the 'Indian' mantle is more heterogeneous on a local scale (Table II.2). For example, lavas with ε_{Nd} values as high as +11.6 ($^{143}Nd/^{144}Nd = 0.513234$) and as low as +5.1 ($^{143}Nd/^{144}Nd = 0.512903$) have been recovered from AAD dredge sites separated by only 60 km along axis. The +11.6 ε_{Nd} value for MW23-1 is the highest value reported for any Indian Ocean MORB and the 6.5 ε_{Nd} unit range in the 'Indian' group lavas covers a large fraction of the entire Indian Ocean MORB range. $^{206}Pb/^{204}Pb$ variations show relatively smooth along-axis profiles in both 'Pacific' and 'Indian' groups but the 'Indian' $^{208}Pb/^{204}Pb$ and $^{207}Pb/^{204}Pb$ values are considerably more scattered, overlapping the 'Pacific' range to a greater extent, particularly within the western AAD and zone C [Klein et al., 1988].

Sr, Nd, and Pb Isotope Systematics

In Figures II.4-II.7, our data and those of Klein et al. [1988] are plotted for comparison with available Indian Ocean MORB and Indian Ocean Island basalt (OIB) data, as well as with Pacific and Atlantic MORB data. In general, Indian Ocean MORB define broadly negative $^{87}Sr/^{86}Sr$-$^{206}Pb/^{204}Pb$ and $^{87}Sr/^{86}Sr$-ε_{Nd} correlations (Fig. II.4 and II.5), and positive $^{208}Pb/^{204}Pb$-$^{206}Pb/^{204}Pb$ and $^{207}Pb/^{204}Pb$-$^{206}Pb/^{204}Pb$ correlations that are parallel to, but offset from the Pb-Pb isotopic trends of the Pacific/Atlantic fields (Fig. II.6 and II.7) [Dupré and Allègre, 1983; Hamelin and Allègre, 1985; Hamelin et al., 1986; Hart, 1984; Michard et al., 1986; Price et al., 1986; Dosso et al., 1988; Mahoney et al., 1989; 1992]. Isotopic differences among individual Indian Ocean spreading centers

Figure II.4 Zone A, zone C and AAD (zone B) $^{87}Sr/^{86}Sr$-$^{206}Pb/^{204}Pb$ variations compared to Atlantic, Pacific, and Indian OIB (inset) and other Indian Ocean spreading centers (CIR-Central Indian Ridge; ITJ-Indian Ocean Triple Junction; CR-Carlsberg Ridge; SWIR-Southwest Indian Ridge; SEIR-Southeast Indian Ridge; SR-Sheba Ridge). The 'Kerguelen' type field includes data from Kerguelen Island, Heard Island, and Ninetyeast Ridge. The 'Reunion' type field includes data from Reunion, Marion-Prince Edward, Rodriguez, Mauritius, Christmas, Crozet, Amsterdam, St. Paul, and Comores Islands. Data sources for Indian Ocean fields include Barling and Goldstein [1990], Baxter et al.[1985], Cohen et al. [1980], Cohen and O'Nions [1982], Dosso et al. [1979; 1980; 1988], Dupre and Allègre [1983], Fisk et al. [1988], Gautier et al. [1990], Hart et al. [1986], Hart [1988], Hamelin et al. [1985], Hamelin and Allègre [1985], Ito et al. [1987], Klein et al. [1988], leRoex et al. [1983; 1985], Mahoney et al. [1983; 1989], McCulloch [1988], Michard et al. [1986], O'Nions et al. [1977], O'Nions and Pankhurst [1974], Price et al. [1986], Storey et al. [1988], Sun [1980], Weis et al. [1989], White et al. [1991], and White [unpub.]. The field labeled Ba represents data from the Balleny hot spot located east of the AAD in the SW Pacific. Mixing curves between mantle components of Zindler and Hart [1986] and between depleted AAD MORB and Indian hot spot melt compositions are also shown with tick marks at 5, 10, 20, and 50 % mixtures (Table II.3). A lava from Heard Island [Storey et al., 1988] has been used to represent a 'Kerguelen'-type composition and an 'average' Amsterdam lava [Michard et al., 1986; Dosso et al., 1988] has been used as a 'Reunion'-type composition in the mixing calculations. A mixing curve between the more depleted 'Indian' and 'Pacific' compositions is also shown. The Inset scale is the same as that of the main figure.

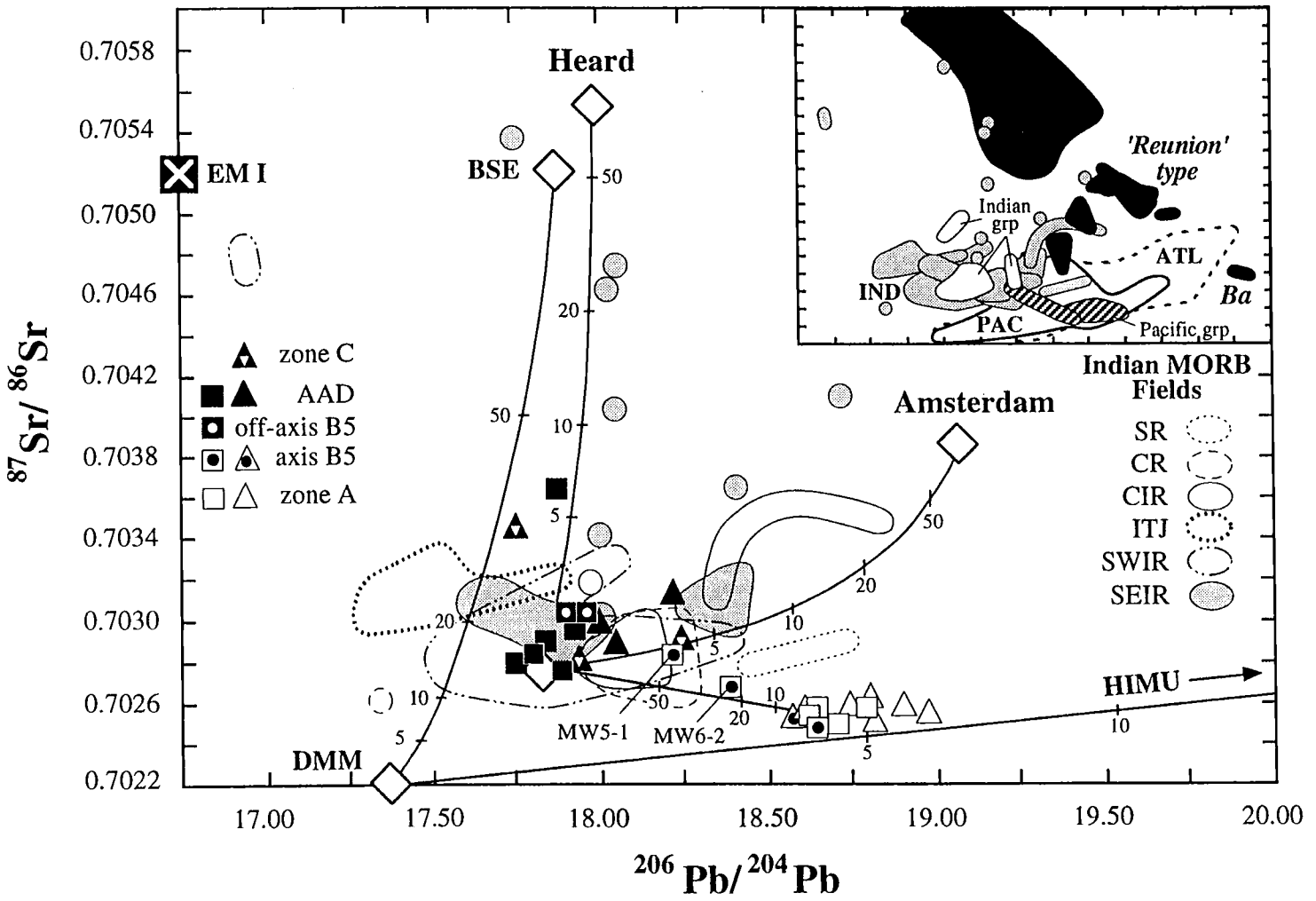
0.7058
0.7054
0.7050
0.7046
0.7042
0.7038
0.7034
0.7030
0.7026
0.7022
87Sr/86Sr
17.00
17.50
18.00
18.50
19.00
19.50
20.00
206Pb/204Pb
Heard
BSE
EM I
DMM
Amsterdam
HIMU
MW5-1
MW6-2
zone C
AAD
off-axis B5
axis B5
zone A
'Reunion' type
Indian grp
ATL
IND
Ba
PAC
Pacific grp
Indian MORB Fields
SR
CR
CIR
ITJ
SWIR
SEIR

Figure II.4

Figure II.5 Zone A, zone C and AAD $^{87}Sr/^{86}Sr$-ε_{Nd} variations compared to Atlantic, Pacific, Indian MORB and Indian OIB (inset scale expanded). Symbols, fields, mixing curves and abbreviations as in Fig. II.4. Christmas Island (Cr) and Comores Island (Co) are 'Reunion'-type OIB that are significantly lower in ε_{Nd}. The Tasmantid Seamounts $^{87}Sr/^{86}Sr$-ε_{Nd} range is also shown.

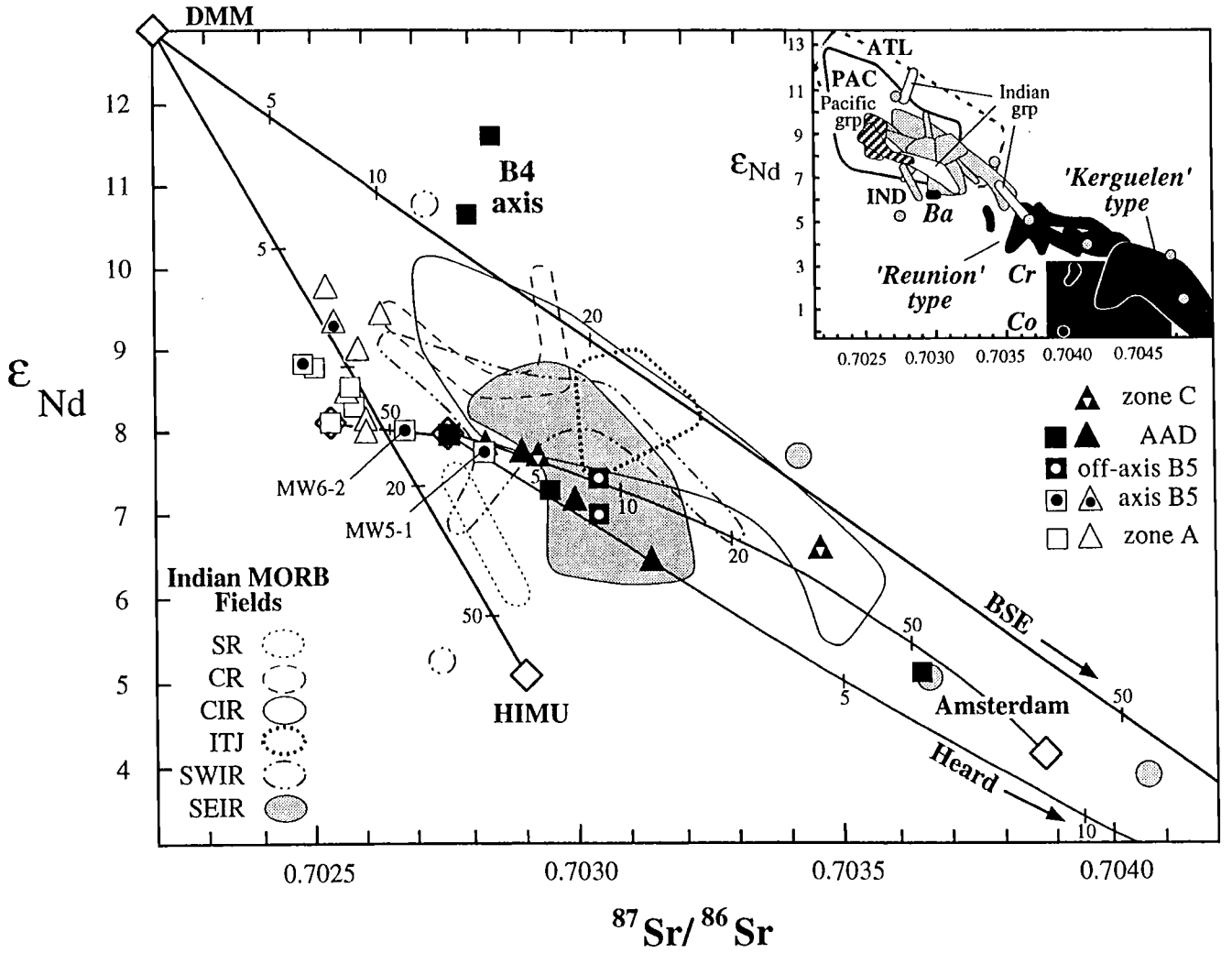
DMM
B4
axis
HIMU
Amsterdam
BSE
Heard
MW6-2
MW5-1
Indian MORB
Fields
SR
CR
CIR
ITJ
SWIR
SEIR
zone C
AAD
off-axis B5
axis B5
zone A
ATL
PAC
Pacific
grp
Indian
grp
IND
Ba
'Kerguelen'
type
'Reunion'
type
Cr
Co
εNd
87Sr/86Sr
0.7025
0.7030
0.7035
0.7040
0.7045

Figure II.5

Figure II.6 Zone A, zone C and AAD $^{208}Pb/^{204}Pb$-$^{206}Pb/^{204}Pb$ variations compared with Atlantic, Pacific, Indian MORB and Indian OIB. Northern Hemisphere reference line (NHRL) is from Hart [1984]. Symbols, fields, mixing curves and abbreviations are the same as previous figures. Inset scale is the same as the main figure.

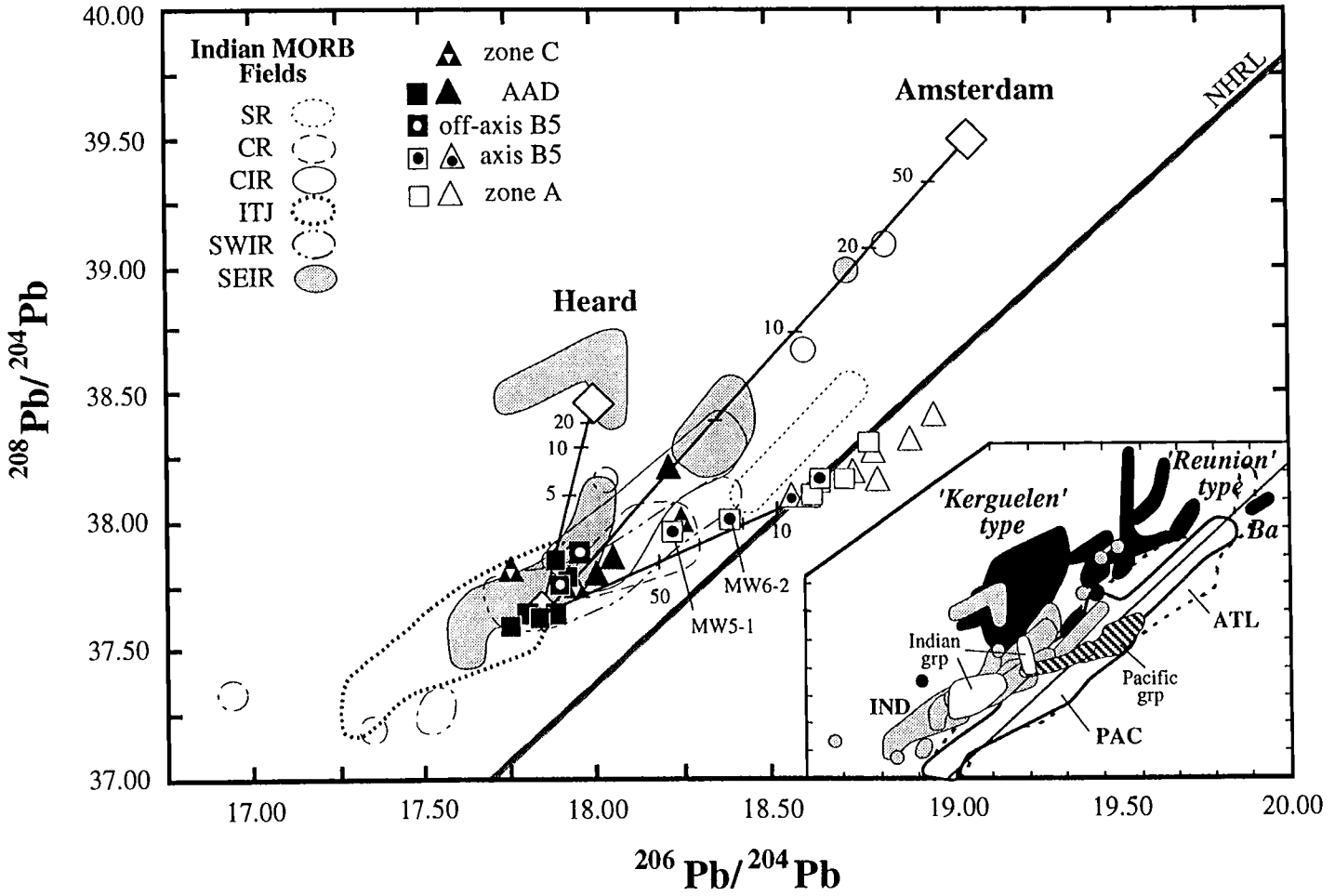
Indian MORB Fields
SR
CR
CIR
ITJ
SWIR
SEIR
zone C
AAD
off-axis B5
axis B5
zone A
Amsterdam
Heard
NHRL
MW6-2
MW5-1
'Kerguelen' type
'Reunion' type
Ba
ATL
Indian grp
Pacific grp
IND
PAC
40.00
39.50
39.00
38.50
38.00
37.50
37.00
17.00
17.50
18.00
18.50
19.00
19.50
20.00
$^{208}Pb/^{204}Pb$
$^{206}Pb/^{204}Pb$

Figure II.6

Figure II.7 Zone A, zone C and AAD $^{207}Pb/^{204}Pb$-$^{206}Pb/^{204}Pb$ variations compared with Atlantic, Pacific and Indian MORB and Indian OIB. Symbols, fields, and abbreviations are the same as previous figures. Inset scale is the same as the main figure.

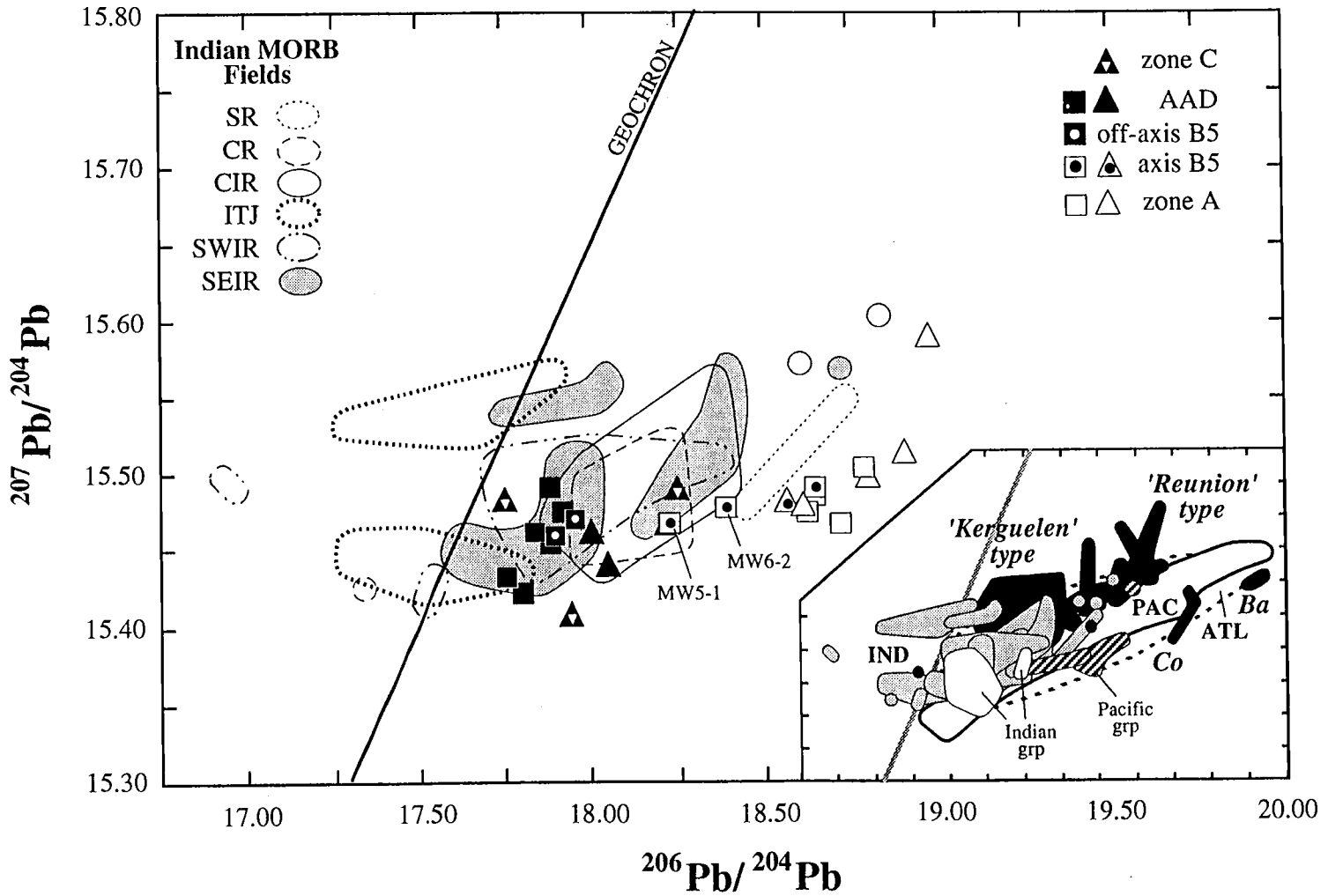
Indian MORB Fields
SR
CR
CIR
ITJ
SWIR
SEIR
GEOCHRON
zone C
AAD
off-axis B5
axis B5
zone A
MW6-2
MW5-1
'Reunion' type
'Kerguelen' type
PAC
Ba
ATL
IND
Co
Pacific grp
Indian grp
15.80
15.70
15.60
15.50
15.40
15.30
17.00
17.50
18.00
18.50
19.00
19.50
20.00
207Pb/204Pb
206Pb/204Pb

Figure II.7

[Michard et al., 1986; Price et al., 1986; Dosso et al., 1988; Mahoney et al., 1989, 1992], as well as between 'Indian' and 'Pacific' MORB from the eastern SEIR are most clearly shown by their Sr-Pb systematics (Fig. II.4). 'Indian' group lavas of the AAD and zone C have $^{87}Sr/^{86}Sr$ and $^{206}Pb/^{204}Pb$ compositions that overlap all other Indian MORB fields except for the Indian Ocean Triple Junction (ITJ) field. Most of the 'Indian' group compositions fall roughly midway between the ITJ field and the 'Pacific' group field, along the negative Sr-Pb isotopic trend of Indian Ocean MORB. Outlying 'Indian' group data points from both the AAD and zone C plot toward either 'Kerguelen'-type OIB (i.e Kerguelen Is., Heard Is., and Ninetyeast Ridge fields) or toward 'Reunion'-type OIB (i.e. Amsterdam-St. Paul, Reunion, Comores, and Crozet Is. fields). In these respects, the 'Indian' group Sr-Pb isotopic variations mimic trends observed in the greater Indian MORB population.

'Pacific' group lavas define two $^{87}Sr/^{86}Sr$-$^{206}Pb/^{204}Pb$ trends. Zone A lavas display wide variations in $^{206}Pb/^{204}Pb$ at essentially constant $^{87}Sr/^{86}Sr$ producing a horizontal field. At the low $^{206}Pb/^{204}Pb$ end of this field, zone A and B5E samples are isotopically indistinguishable (Fig. II.4), but as $^{206}Pb/^{204}Pb$ decreases westward along the B5W segment, $^{87}Sr/^{86}Sr$ progressively increases in samples MW6-2 and MW5-1 resulting in a negative Sr-Pb isotopic trend toward Indian Ocean MORB values. Overall, the $^{87}Sr/^{86}Sr$-$^{206}Pb/^{204}Pb$ systematics of the B5W segment vary within the Pacific Ocean MORB field, however MW5-1 plots a narrow region of overlap between the Pacific Ocean and Indian Ocean MORB fields.

Despite considerable overlap in the ε_{Nd}-$^{87}Sr/^{86}Sr$ fields for Pacific and Indian Ocean MORB, the 'Pacific' and 'Indian' lavas define distinct groups except for the transitional isotopic characteristics of MW6-2 and MW5-1 (Fig. II.5). The distinctiveness of the two MORB groups is accentuated by data trends that reflect differences in the Sr-Nd isotope systematics of their mantle source. 'Indian' group glasses vary along an array that more or less parallels the global trend (B4 glasses being unusually high ε_{Nd} exceptions).

The 'Indian' group $^{87}Sr/^{86}Sr$ values are typical for Indian Ocean spreading centers, but tend to have lower ε_{Nd}, similar to some lavas from the western SEIR. The lowest ε_{Nd} 'Pacific' group glasses plot along an extension of the 'Indian' group array, but the higher ε_{Nd} 'Pacific' data and relatively limited $^{87}Sr/^{86}Sr$ range produces a roughly vertical field that cuts across the mantle array. In contrast to the uniformly low Pb isotopic ratios for B5 axial samples compared to the rest of the 'Pacific' group, the $^{87}Sr/^{86}Sr$-ε_{Nd} variations for this spreading segment spans nearly the entire zone A range.

The 'Indian' group lavas are consistently lower than the 'Pacific' group lavas in $^{206}Pb/^{204}Pb$ (except for MW5-1), but in $^{208}Pb/^{204}Pb$ and, to a greater extent $^{207}Pb/^{204}Pb$, the two groups overlap. The 'Pacific' lavas fall within the overall Pacific MORB $^{208}Pb/^{204}Pb$-$^{206}Pb/^{204}Pb$ trend (Fig. II.6), but their $^{207}Pb/^{204}Pb$ values appear to be lower than all Pacific MORB at comparable $^{206}Pb/^{204}Pb$ (Fig. II.7). The 'Indian' group lavas show typical Indian MORB $^{208}Pb/^{204}Pb$-$^{206}Pb/^{204}Pb$ systematics, but for a few 'Indian' lavas, $^{207}Pb/^{204}Pb$ values are low relative to other Indian Ocean MORB with similar $^{206}Pb/^{204}Pb$ values (Fig. II.6 and II.7).

In summary, the isotopic correlations between Sr-Pb (Fig. 4), Sr-Nd (Fig. II.5), and Pb-Pb (Fig. II.6 and II.7) of the 'Pacific' and 'Indian' groups show that these lavas define distinct compositional fields which follow general trends observed in Pacific Ocean and Indian Ocean MORB. Samples from B5W form an intermediate field in which the westernmost sample, MW5-1, invariably shows isotopic characteristics of both Pacific and Indian MORB sources, whereas farther east, MW6-2 always has a greater 'Pacific' affinity. These relationships are consistent with decreasing entrainment of remnant 'Indian' mantle behind a westward advancing 'Pacific' mantle.

DISCUSSION

'Indian' and 'Pacific' MORB Sources

The 'Indian' and 'Pacific' MORB sources are distinct in both isotopic composition and diversity. None of the variation diagrams or along-axis profiles reveal systematic spatial trends in isotopic composition relative to the isotopic boundary in either the 'Pacific' or 'Indian' groups beyond the localized 'Indian' influence in 'Pacific' lavas from the B5W spreading segment. Lavas of the 'Pacific' group have typical Pacific MORB isotopic ratios with no recognizable contribution from hot spot sources east of zone A (i.e. Balleny or Tasmantid hot spots). The range of 'Indian' lavas from the AAD and zone C encompasses much of the overall variability observed for Indian Ocean MORB. Both 'Kerguelen'- and 'Reunion'-type OIB isotopic signatures are evident within the 'Indian' group suggesting that these contaminants have remained isotopically distinct and have not been homogenized by upper mantle mixing even as far as the eastern Indian Ocean MORB boundary, several thousand kilometers from their presumed sources.

Several mixing curves have been calculated to illustrate that the 'Indian' group isotopic trends are consistent with the presence of dispersed 'Kerguelen'- or 'Reunion'-type hot spot contaminants within a depleted 'Indian' MORB matrix (Fig. II.4, II.5, and II.6). The Heard and Amsterdam Island lavas (representing 'Kerguelen' and 'Reunion'-type OIB, respectively) used to calculate the mixing curves are melt compositions extracted from mantle which is itself a mixture of several 'endmember' mantle components (e.g. depleted MORB mantle, "DMM"; bulk silicate earth, "BSE"; high U/Th, "HIMU"; enriched mantle, "EM I" [Zindler and Hart, 1986]). The 'Indian' group data cannot be reproduced mixing any two proposed mantle components; however, the 'Pacific' samples (excluding MW6-2 and MW5-1) do appear to be a mixture of DMM and HIMU mantle. The 'Indian' data trends are more successfully modeled by the addition of small amounts (<5%) of either 'Kerguelen' or 'Reunion'-type OIB related melts to an 'Indian' MORB melt from the AAD. The main difference between mixing mantle components and mixing melts from OIB and

MORB sources is essentially that of mixing mantle material in the solid-state as opposed to mixing of melts as they move through the upper mantle. The 'Indian' group data suggest that discrete melts of either 'Reunion'- or 'Kerguelen'-like contaminants mix with 'depleted' Indian MORB melts en route to the surface. Similar isolated 'Kerguelen'- and 'Reunion'-type contaminants have also been found in western SEIR lavas (Fig. II.4) [Dosso et al., 1988].

The isotopic diversity of the 'Indian' population suggests that the mantle beneath the AAD and zone C is heterogeneous at the scale of dredging (tens of km) to the scale of a single dredge haul (1-3 km). Moreover, the heterogeneities both within and between the two upper mantle domains are not necessarily on the same scale for all isotopic systems, and correlations, such as high $^{87}Sr/^{86}Sr$ with low $^{143}Nd/^{144}Nd$, are not always observed. The localized, and sometimes extreme, 'Indian' group variations in radiogenic Sr, Nd, and to a lesser extent, Pb, is not present in the 'Pacific' group. 'Pacific' mantle appears to be homogeneous for $^{87}Sr/^{86}Sr$ at the scale of melting beneath the ridge, whereas the 'Indian' mantle is not. Radiogenic Nd and Pb show comparable ranges within each reservoir, although occasional, apparently random, low or high Nd and Pb isotopic ratios occur in the 'Indian' group. Along-axis $^{206}Pb/^{204}Pb$ and $^{208}Pb/^{204}Pb$ tend to correlate with each other but not with $^{207Pb/204Pb}$, and all three Pb isotopic ratios vary independently of both Sr and Nd isotopic ratios. Although lower degrees of melting beneath the AAD [Klein et al., 1991] may promote the selective incorporation of unusually radiogenic (or unradiogenic) material into the 'Indian' lavas, the decoupling of the three isotopic systems reflects the isotopic complexity of Indian Ocean MORB in general.

The Indian MORB Isotopic Province

Models for creating and isolating an isotopically distinct Indian MORB reservoir generally require the contamination of Pacific (or N. Atlantic) Ocean upper mantle asthenosphere with material from one or more sources: (1) Indian Ocean hot spot material(s), (2) lower continental lithosphere, and/or (3) convectively recycled, subducted

altered oceanic crust (plus sediments) [e.g. Dupré and Allègre, 1983; Hamelin and Allègre, 1985; Hamelin et al., 1986; Hart, 1984; Michard et al., 1986; Price et al., 1986; Dosso et al., 1988; Mahoney et al., 1989, 1992; Hoffman and White, 1982; Storey et al., 1988, 1989; Barling and Goldstein, 1990]. Thinning and dispersal of low $^{206}Pb/^{204}Pb$ Gondwanan continental lithosphere by high $^{87}Sr/^{86}Sr$ Kerguelen hot spot mantle has been suggested as a possible mechanism responsible for the Indian MORB isotopic signature [Mahoney et al., 1989, 1992; Storey et al., 1988, 1989; Barling and Goldstein, 1990]. The B5 segment data trends emphasize the significance of the low $^{206}Pb/^{204}Pb$ and a high $^{87}Sr/^{86}Sr$ contaminants (Fig. II.4-II.7). If the isotopic compositions of MW6-2 and MW5-1 are attributed to mixing of melts from a migrating 'Pacific' mantle with a remnant 'Indian' source (Table II.3) beneath B5W, then MW5-1 appears to be composed of approximately equal proportions of both mantle sources. The mixing curve indicates that the 'Indian' composition used in these calculations is too low in $^{87}Sr/^{86}Sr$ (Fig. II.5) and possibly in $^{208}Pb/^{204}Pb$ (Fig. II.6) to be a simple mixture of the most depleted lavas from each group. In fact, the trajectory of the B5W data suggest that the higher $^{87}Sr/^{86}Sr$ and $^{208}Pb/^{204}Pb$ compositions of the B5 off-axis samples would be a more appropriate 'Indian' contaminant to the 'Pacific' lavas beneath this segment.

The mixing trend between the 'Indian' and 'Pacific' groups in the AAD defines one of four trends that emanate from the main body of Indian MORB data on the $^{87}Sr/^{86}Sr$-$^{206}Pb/^{204}Pb$ diagram (Fig. II.4). These trends highlight the variable affect different contaminants have had on individual Indian Ocean spreading centers. Two of these trends are consistent with the presence of 'Kerguelen'- or 'Reunion'-type hot spot material within the depleted Indian MORB mantle. A third trend, defined by Sheba Ridge (Gulf of Aden) data, lies between the Amsterdam mixing curve and the 'Pacific' group field [Dupré et al., 1988; Altherr et al., 1990; Schilling et al., 1992]. The 'Pacific' group samples define a

Table II.3 Hypothetical mantle components and melt end-members used for mixing calculations.

Endmember	Sr (ppm)	$^{87}Sr/^{86}Sr$	Nd (ppm)	$^{143}Nd/^{144}Nd$	Pb (ppm)	$^{206}Pb/^{204}Pb$	$^{207}Pb/Pb^{204}$	$^{208}Pb/^{204}Pb$
DMM A*	12	0.7022	.65	0.51330	.04	17.4	15.40	
HIMU*	120	0.7029	6.5	0.51290	.40	21.5	15.85	
BSE*	18.4	0.7052	1.0	0.51260	.135	17.9	15.62	
Heard**	850	0.70555	54	0.512582	7.0	18.009	15.547	38.461
Amsterdam***	450	0.70387	12	0.512854	4.0	19.082	15.621	39.481
'Indian' grp†	125	0.70276	6.0	0.513048	.30	17.85	15.42	37.630
'Pacific' grp††	105	0.70254	6.6	0.513054	.23	18.630	15.475	38.099

* Zindler and Hart [1986]
** values of Storey et al. [1988] sample BM64986
*** avg. of values of Michard et al. [1986] and Dosso et al. [1988].
† 'depleted' melt endmember for Indian grp. samples
†† 'depleted' melt endmember for Pacific grp. samples (sample MW17-26)

fourth trend of low $^{87}Sr/^{86}Sr$ and high $^{206}Pb/^{204}Pb$ values which merges with the Indian MORB fields due to the remnant 'Indian' source imprint on the 'Pacific' lavas erupted along the B5W spreading segment. Similar relationships are evident in the $^{208}Pb/^{204}Pb$-$^{206}Pb/^{204}Pb$ systematics of these ridges (Fig. II.6). The Sheba Ridge and 'Pacific'-'Indian' data converge near the Carlsberg Ridge field and the high $^{206}Pb/^{204}Pb$ end of the Southwest Indian Ridge field. All of these ridges lie at the periphery of the Indian Ocean basin and their low $^{87}Sr/^{86}Sr$-high $^{206}Pb/^{204}Pb$ trends are distinct from the hot spot-related trends of the central Indian Ocean. These isotopic trends probably represent mixing of Indian MORB with Atlantic MORB or a hot spot contaminant unlike Indian Ocean OIB and may signify the western limits to the Indian MORB mantle. In fact, Mahoney et al. [1992] have recently documented a broad, gradational boundary between Indian and Atlantic MORB sources along the Southwest Indian Ridge.

Mantle Flow toward the AAD

The AAD has been interpreted as a region underlain by cold mantle and characterized by converging, and possibly downwelling, mantle flow. Hypotheses to explain this mantle flow fall into two classes; those which involve driving forces external to the AAD (active flow) and those in which flow is a response to the presence of cold mantle beneath the region (passive flow).

Active Mantle Flow

Convective downwelling: Weissel and Hayes [1974] and Klein et al. [1988] proposed that the AAD overlies downwelling limbs of broad Indian and Pacific upper mantle convection cells which converge beneath the region. The convection boundary between the two cells is conceived as a N-S oriented planar feature that spans the ocean basin between Australia and Antarctica. This hypothesis is appealing because it explains the presence of cold mantle, it provides a mechanism for maintaining the separation of the two isotopic reservoirs, and it could be consistent with the off-axis geometry of the depth anomaly if the convection boundary were migrating westward at ~15 mm/yr.

Nevertheless, this hypothesis is problematic in that the scale of the convection cells and the locations of upwelling regions are undefined. Simple convection cells beneath a narrow Southeast Indian Ocean basin during the early stages of Australia-Antarctica separation seem to require an improbably high aspect ratio, unless the scale of convection was much greater than the depth to the base of the continental lithosphere and existed beneath the continent(s) before rifting.

Hot spot-driven flow: A distinctly different type of active convergence, which neither requires nor precludes downwelling, has been proposed by Vogt and Johnson [1973, 1975] and more recently by Marks et al. [1990, 1991]. These workers have suggested that the AAD marks the convergence of subaxial asthenospheric flow driven by the supply of excess material from hot spots to the east and west. The AAD would, therefore, overlie the coolest, and presumably most incompatible-element depleted, segment of mantle along the SEIR. The principal evidence cited for this type of sub-axial flow lies in the presence of propagating rifts and in the off-axis geometry of the depth anomaly. This hypothesis is attractive in that it is consistent with the geometric constraints recognized by Marks et al. [1990, 1991] and it can allow for apparent fluctuations in both the magnitude of the depth anomaly and the position of the isotopic boundary. A major problem with this hypothesis is the remoteness of the AAD from hot spot sources. The Tasmantid and Balleny hot spots lie about 2000 km to the east and are, in any case, volumetrically insignificant. An unnamed seamount ~1000 km to the east in the George V transform is also of small volume and appears to have formed too recently to have had a significant effect on the formation of the AAD. The Amsterdam-St. Paul and Kerguelen hot spots lie >3000 km west of the AAD. The isotopic influence of these hot spots has been documented southeast of Amsterdam Island along the SEIR [Dosso et al., 1988], but MORB compositions apparently return to 'ambient' values within 150 km, implying a very limited region of influence. The isotopic and topographic effects of large hot spots on spreading centers are well documented in other places, but the most prominent examples

extend only ~1000 km in the case of Iceland and ~500 km in the case of the Galapagos [Hart et al., 1973; Sun et al., 1975; Schilling et al., 1982; Schilling, 1985]. The topographic gradient on either side of the AAD appears to be a consequence of the unusually deep axial bathymetry of the AAD rather than directly related to any hot spot, and as we have shown, the expected isotopic gradients are absent.

Pacific mantle migration: Alvarez [1982, 1990] proposed that Pacific upper mantle must necessarily migrate through gaps between deep continental roots surrounding the Pacific basin as the long-term shrinkage of the Pacific Ocean proceeds. In terms of this hypothesis, the isotopic boundary in the AAD would represent the leading edge of Pacific mantle which began to flow westward when a gap between the continental roots of Australia and Antarctica opened through the South Tasman Rise. Presumably, 'Indian' upper mantle existed beneath the region prior to the inflow of Pacific mantle, having migrated eastward during the early stages of continental rifting which propagated from west to east [Mutter et al., 1985, Royer and Sandwell, 1989; Veevers and Li, 1991]. The westward mantle migration rate of 25 mm/yr estimated from the isotopic data within the AAD would place the opening of the South Tasman Rise to mantle flow at ~50 Ma, broadly consistent with the opening of the circum-Antarctic region to oceanic circulation at 35 to 42 Ma [Royer and Sandwell, 1989; Veevers et al., 1991; Hinz et al., 1991]. This hypothesis implies that the isotopic boundary has only recently arrived beneath the AAD and it is not directly related to the long-lived geophysical and morphologic features of the region.

Passive Mantle Flow

Implicit in each of the active flow hypotheses is the concept that the upper mantle beneath the AAD is cold because it represents the distal regions of a horizontal mantle flow regime. It is also possible that the characteristics of cold mantle beneath the AAD may generate or reinforce a passive lateral mantle flow into the region.

Mantle coldspot: Hayes [1976] and Anderson et al. [1980] suggested that the AAD is associated with a mantle "coldspot". This concept is not clearly defined but it involves,

in some sense, the downwelling inverse of a hot spot. Fluid dynamic modeling of convection in an internally heated mantle [Bercovici, 1989] appears to favor focused upwelling and more diffuse, sheet-like downwelling, suggesting that a down-flowing coldspot is unlikely to be a stable feature. In any case, as Marks et al. [1990, 1991] have shown, the V-shaped trace of the AAD and the northward migration of the SEIR require that the physical processes producing the AAD cannot be associated with a point source or sink fixed in the mantle reference frame.

Passive mantle flow: Forsyth et al. [1987] proposed a self-consistent model on the basis of seismic data that showed the AAD to be underlain by cooler-than-normal mantle and that the lithosphere thickens away from the AAD spreading axis more rapidly than average. Cool mantle, being closer to its solidus, would produce less melt and overall thinner crust. Cooler and/or volatile-depleted asthenosphere beneath the AAD should also be more viscous than usual [Forsyth et al., 1987]. As a result, lateral return flow due to plate separation along the SEIR may draw material along-axis from 'normal' (i.e. less viscous) asthenosphere east and west of the AAD. This model does not require either mantle downwelling beneath the AAD or a specific external driving force for subaxial flow, apart from plate separation. This model is consistent with many of the known features of the AAD and with the presence of propagating rifts [Phipps Morgan and Parmentier, 1985]. It predicts that the isotopic boundary is a long-term (if oscillatory) feature of the AAD, but it does not provide an explanation for the existence of cold mantle in the first place.

Implications for mantle dynamics beneath the AAD

Mantle flow toward the AAD has been inferred from the convergence of propagating rifts from the east and west during the last 25 Ma [Marks et al., 1990, 1991; Vogt et al., 1983] and from the pronounced bathymetric gradients along the SEIR [Weissel and Hayes, 1974; Hayes and Conolly, 1972]. Fundamental questions as to whether mantle flow towards the AAD is active or passive and whether mantle downwelling is occurring

remain unresolved. Tangible evidence for recent mantle flow beneath the AAD is provided by the off-axis data from segment B5.

Whether the migration of the isotopic boundary represents a continuous, long-term westward flow of Pacific mantle or a recent perturbation of the boundary about a mean position beneath the easternmost AAD is not known. If the westward movement of the isotopic boundary across B5 has been a continuous phenomenon, then mantle migration rates between 10 mm/yr and 40 mm/yr are permitted by existing data, depending on the exact ages of off-axis samples and assumptions about present (and past) positions of the isotopic boundary. We have assumed that the isotopic boundary coincided with the eastern AAD bounding transform at 4 Ma and now lies at the B4/B5 transform, requiring Pacific mantle flow of ~25 mm/yr westward beneath the B5 spreading segment. The most interesting implication of steady, westward, Pacific mantle flow is that the isotopic boundary has only recently arrived beneath the AAD and that it is not coupled to, or formed by, the mantle dynamics creating the regional gravity and bathymetric anomalies. Although the timing of the arrival seems fortuitous, the consistency between inferred rates of migration and the likely timing for rifting of the South Tasman Rise allowing upper mantle outflow from a shrinking Pacific basin [Alvarez, 1982, 1990] requires that this hypothesis be carefully considered.

An isotopic boundary that is instead related to the mantle dynamics creating the AAD is equally plausible given the present sampling distribution. Movement of the isotopic boundary may simply reflect small-scale oscillations in mantle flow from the east and west. If small scale fluctuations in the boundary position have occurred throughout the existence of the AAD depth anomaly (over the last 100 Ma), a much wider zone of mixing and isotopic exchange might be expected to have developed between the two MORB sources [Hofmann and McKenzie, 1985], leading to smooth gradients in all isotopic systems on either side of a median boundary position. The only evidence for this type of source mingling is near the leading edge of the 'Pacific' source and, significantly, the B4

segment lavas lie well within the Indian MORB field on all diagrams. Furthermore, sharp discontinuities in Pb and Nd isotope ratios remain between the B4E and B5W segments. At present, we believe that these observations imply that 'Pacific' mantle has not penetrated beyond the B4/B5 transform and that there is a gradually diminishing 'memory' of 'Indian' mantle incorporated into 'Pacific' lavas beneath B5, behind the migrating isotopic boundary.

The present position and the abrupt nature of the eastern Indian MORB boundary at ~126°E is not easily explained by simple dispersion of low $^{206}Pb/^{204}Pb$ and Indian Ocean hot spot contaminants by channelized, sub-axial, hot spot-induced mantle flow, because the AAD is beyond a reasonable distance over which hot spots are likely to have a significant influence. Dispersion of the Indian Ocean upper mantle is more consistent with a regional, eastward flow of mantle towards the AAD in response to the separation of Australia and Antarctica. By this mechanism, isolated 'Kerguelen'- and 'Reunion'-type contaminants could be drawn eastward with depleted Indian MORB mantle until it is halted by the countervailing westward flow of 'Pacific' mantle. The unusually abrupt nature of the eastern Indian MORB boundary may reflect an active, westward Pacific mantle flow, driven by the shrinkage of the Pacific basin [Alvarez, 1982, 1990], which is colliding with a more passive Indian Ocean mantle. The western boundary to the Indian MORB reservoir is not as sharp or well-defined [Mahoney et al., 1992] because both the Atlantic and Indian basins are presently growing and no flow of upper mantle from one basin to another is required to accommodate the continental motions.

SUMMARY

The new results presented here, together with previous data [Klein et al., 1988], show that the isotopic boundary between Pacific and Indian MORB mantle provinces is remarkably abrupt beneath the AAD. No other boundary of comparable abruptness and contrast has been documented anywhere along the global mid-ocean ridge system. The transition between Indian and Pacific MORB sources occurs within a narrow zone (~40 km) beneath the spreading axis of a single segment (B5) within the eastern AAD. Limited off-axis sampling from this segment indicates that the boundary has migrated approximately 100 km westward since 4 Ma. Despite the movement of Pacific mantle beneath the AAD, the 'Indian' and 'Pacific' sources have maintained distinct isotopic signatures, apart from the isotopic gradients along the B5W segment. The characteristics of the Pacific-Indian upper mantle transition suggest that the isotopic boundary is near the B4/B5 transform and that a 'memory' of the displaced 'Indian' mantle signature is incorporated into 'Pacific' lavas behind the leading edge of a migrating Pacific mantle.

Two classes of upper mantle flow towards the AAD can explain the geophysical and isotopic characteristics of the AAD: (1) sub-axial mantle flow in response to spreading over a cool mantle, and perhaps to along-axis topographic gradients; (2) long-range inflow of upper mantle from a shrinking Pacific Ocean in which Pacific mantle is gradually displacing Indian Ocean mantle. In neither case are the origin of the cold mantle beneath the AAD and the depth and gravity anomalies centered on the AAD satisfactorily explained. The first model predicts that the isotopic boundary is linked to the long-lived geophysical anomalies and morphological features which define the AAD, whereas the second model requires that they are independent and that the isotopic boundary has only recently arrived beneath the AAD. The present sample distribution does not allow an unequivocal discrimination between these two models; however, both lead to specific, testable predictions as to the off-axis configuration of the isotopic boundary. The isotopic data are overwhelmingly biased to 'zero-age', spreading axis samples and it is clear from this study

that significant information about mantle flow in the region, and therefore the mantle dynamics beneath the AAD, is to be found off-axis.

Chapter 3

Geochemical and Morphological Contrasts in the Vicinity of the Australian-Antarctic Discordance

D. G. Pyle and D. M. Christie

ABSTRACT

The Southeast Indian Ridge (SEIR) in the vicinity of the Australian-Antarctic Discordance (AAD) is a region of unusually diverse spreading axis morphology and mid-ocean ridge basalt (MORB) geochemistry. Distinct changes in major and trace element composition are shown to coincide with the abrupt change in axial segmentation and morphology that accompanies the transition between the AAD and SEIR spreading segments to the east (i.e., Zone A). Since spreading rate is uniform throughout this region, compositional and morphological variations are most likely related to variations in melt production beneath the spreading axis. The AAD spreading system is melt deficient and compositional variations within the AAD MORB suite are primarily controlled by partial melting of the mantle source. The Zone A spreading system is melt saturated and compositional variations are dominated by shallow pressure, crystal fractionation.

The major element characteristics of the AAD indicate that these basalts are derived from low average pressures of melting and low degrees of melting. The Zone A basalts are derived from higher average pressures and higher average degrees of melting. The major element contrasts between these two MORB suites are consistent with a variations in mantle temperature producing variations in mantle melting. However, trace element systematics show that lavas produced by low degree melting throughout the region (both AAD and Zone A) have very similar source mantle signatures, but retain very different major element compositions. Differences in partial melting alone can not produce these relationships unless trace element heterogeneity in the source mantle is evoked. An alternative model is presented in which the modal proportion of clinopyroxene (cpx) in the source mantle is varied . This model satisfies the trace element conditions and predicts that the AAD mantle is higher in modal cpx. Therefore, AAD compositions result from lower degrees of melting from a more fertile source mantle (i.e., higher proportion of cpx).

INTRODUCTION

The formation of oceanic crust at mid-ocean spreading centers is controlled by the combined effects of spreading rate and mantle upwelling. The interaction between these two processes results in a spectrum of petrogenetic and tectonic conditions along-axis that are recorded by axial morphology and mid-ocean ridge basalt (MORB) composition. In this study, we present major and trace element data for basaltic glass samples dredged along 400 km of the eastern Southeast Indian Ridge (SEIR), an area encompassing the eastern three-quarters of the Australian-Antarctic Discordance and adjacent spreading centers to the east. Along this portion of the SEIR, an unusually diverse suite of MORB compositions has erupted from spreading centers which display, at a uniform, intermediate spreading rate (74 mm/yr full rate) [De Mets et al., 1990], nearly the entire range in axial morphology observed at slow and fast spreading systems. This requires that spreading rate is not the dominant variable for controlling either axial morphology or basalt petrogenesis. More likely, variations in mantle upwelling patterns related to variations in mantle temperature dominate spreading conditions in this region [West et al., 1994; Christie et al., 1988; Christie et al., 1990]. The SEIR within and adjacent to the AAD provides an uncommon opportunity to examine the effect of mantle upwelling on melt production, MORB petrogenesis, and spreading axis morphology independent of spreading rate.

BACKGROUND

The Australian-Antarctic Discordance (AAD) (Hayes and Conolly, 1972) is a 500 km section of the eastern SEIR characterized by a pronounced, along-axis change in segmentation patterns and unusually deep axial bathymetry relative to adjacent SEIR spreading centers to the east and west (commonly referred to as Zone A and Zone C, respectively; Fig. III.1). Within the AAD, spreading centers are relatively short (<100 km) and bounded by large transform fault zones that strike N-S and offset the spreading segments by 80 to 180 km [Palmer et al., 1993; Sempéré et al., 1991]. To the east, Zone

Figure III.1 Regional bathymetric map (500 m contours) and spreading axis traces of the AAD and Zone A surveyed during the MW8801 cruise of the *R.V. Moana Wave*. MW8801 dredge locations are shown as rectangular symbols prefixed by 'MW' and Vema dredge locations are shown are filled circles prefixed by 'V'. Non-transform discontinuities (NTD) separate the AAD spreading axes into east and west segments (e.g., B5E and B5W). AAD specifically refers to zone B and the AAD spreading segments are designated from west to east as B1 through B5 following Hayes and Conolly [1972]. Likewise, Zone A is subdivided into segments A1 (doomed rift), A2 (127.5° E propagating rift), and A3 (131.0° E propagating rift; not shown).

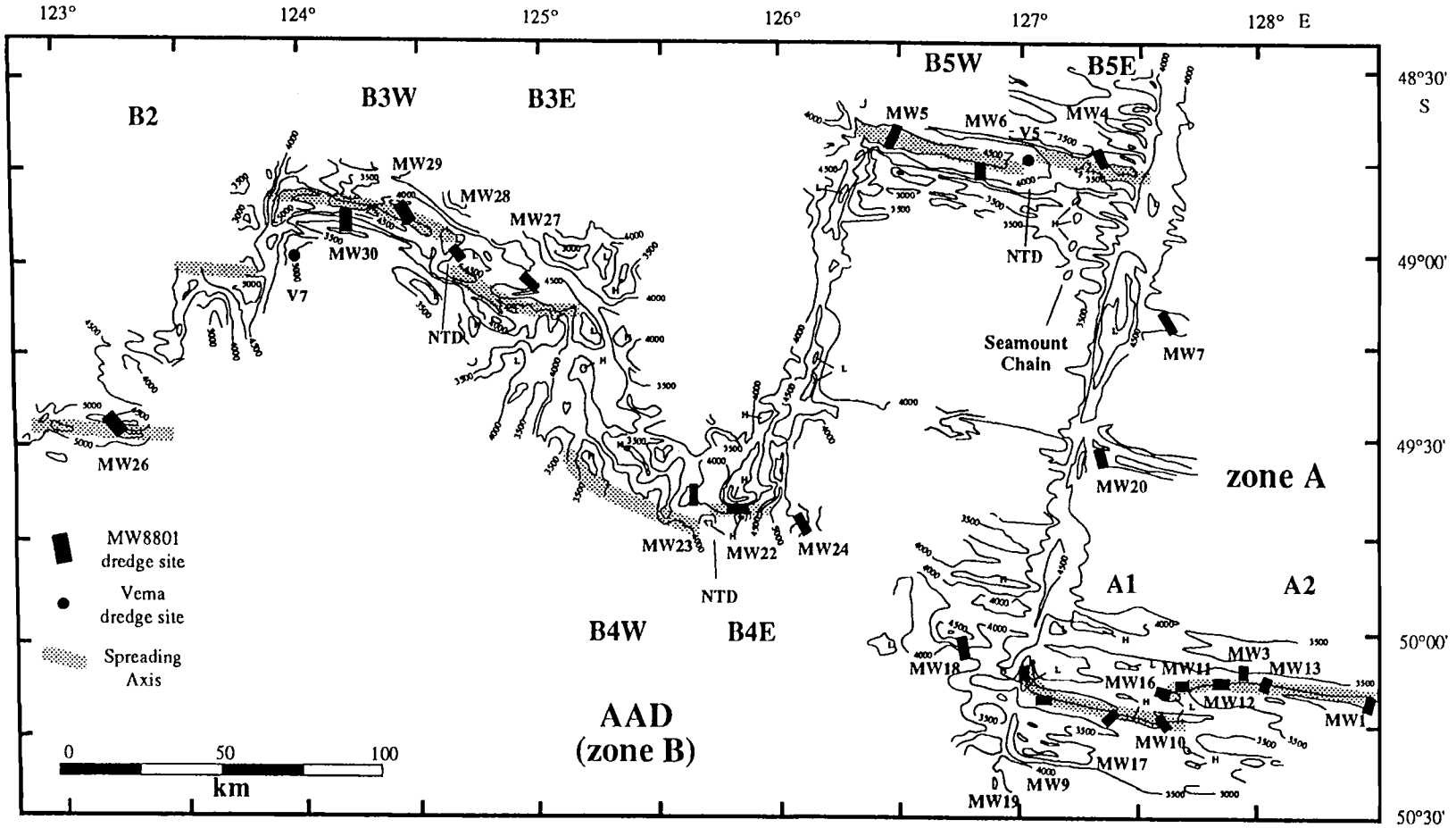
123°
124°
125°
126°
127°
128° E
48°30' S
49°00'
49°30'
50°00'
50°30'
B2
B3W
B3E
B5W
B5E
B4W
B4E
A1
A2
zone A
AAD
(zone B)
MW1
MW3
MW4
MW5
MW6
V5
MW7
MW9
MW10
MW11
MW12
MW13
MW16
MW17
MW18
MW19
MW20
MW22
MW23
MW24
MW26
MW27
MW28
MW29
MW30
V7
NTD
NTD
NTD
Seamount Chain
MW8801 dredge site
Vema dredge site
Spreading Axis
0
50
100
km

Figure III.1

A spreading segments are generally longer than 300 km and the only known axial discontinuities are westward-propagating rifts that offset the neovolcanic zone by less than 10 km. The axial morphology and tectonic configuration of zone C is poorly known, however geochemical similarities between the AAD and zone C lavas suggest that the morphological transition between these regions is not as well defined as between the AAD and Zone A.

In addition to the dramatic change in axial segmentation between Zone A and the AAD, there is an abrupt increase in axial depth within the AAD. Axial depths within Zone A vary between 3100-3400 m and display a broad regional increase toward the Zone A-AAD transform boundary (Fig. III.2). Near the mid-point of easternmost AAD spreading segment (B5), the spreading axis deepens over 1000 m just west of a non-transform discontinuity [Palmer et al., 1993]. West of the B5 non-transform discontinuity, axial depths commonly exceed 4000 m, increasing to 4600 m close to transform fracture zones. The longevity of the AAD bathymetric anomaly is manifested as a regional, U-shaped seafloor depression hat extends across the Southern Ocean to the continental margins of Australia and Antarctica, suggesting that this feature has existed since seafloor spreading began at ~95 Ma [Veevers, 1982; Mutter et al., 1985; Marks et al., 1990].

Regional magnetic anomaly patterns indicate that the depth anomaly pre-dates development of the present segment offset configuration of the AAD plate boundary [Vogt et al., 1984]. Also, the regional depth anomaly cuts the eastern AAD transform boundary at magnetic anomaly 5b (~ 25 Ma), suggesting that the depth anomaly formed before the AAD transform boundaries or that the presently defined AAD and the depth anomaly have not always coincided.

Fundamental differences in the upper mantle velocity structure coincide with the contrasts in seafloor morphology between the deeper AAD and shallower ridge segments further east (e.g., Zone A) [Rouland et al., 1985; Forsyth et al., 1987; Anderson et al., 1992; Woodhouse and Dziewonski, 1984]. Rayleigh phase velocities of sub-AAD mantle

Figure III.2 Axial depth profile and axial morphology of the AAD (zone B) and Zone A (see fig. 2 for locations). Axial depth gradually increases within Zone A approaching the AAD , then abruptly increases by ~1000 m west of the B5 NTD. An axial ridge morphology characterizes Zone A spreading centers and an axial valley morphology characterizes AAD spreading centers. The transition in axial morphology is closely related to deepening of the spreading axis. A longitudinal overlap of the AAD and Zone A spreading segments is caused by the spreading axis offset along the eastern bounding transform of the AAD. The overlap has been removed to facilitate axial depth comparisons (note two longitude scales are shown).

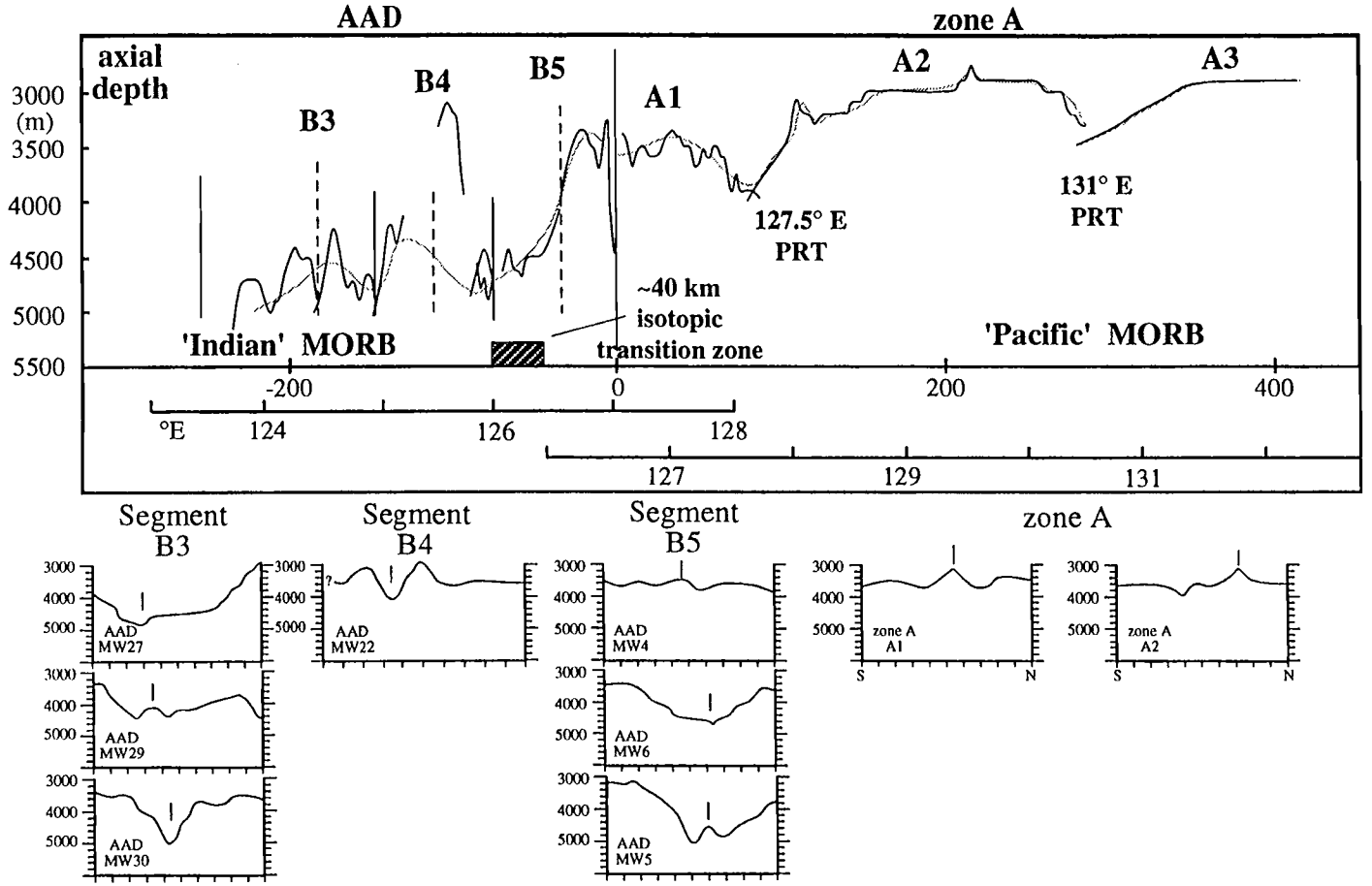
AAD
zone A
axial depth
3000 (m) 3500 4000 4500 5000 5500
B3
B4
B5
A1
A2
A3
127.5° E PRT
131° E PRT
~40 km isotopic transition zone
'Indian' MORB
'Pacific' MORB
-200
0
200
400
°E
124
126
128
127
129
131
Segment B3
Segment B4
Segment B5
zone A
AAD MW27
AAD MW29
AAD MW30
AAD MW22
AAD MW4
AAD MW6
AAD MW5
zone A A1
zone A A2
S
N

Figure III.2

are significantly faster than regions of comparable age in the Pacific. These unusually fast shear wave velocities are most prevalent in the 20-40 km depth range, becoming less pronounced to depths of 150 km [Forsyth et al., 1987]. Depending on melt distribution, the velocity contrast could reflect a complete absence of partial melt within the AAD upper mantle, or the upper mantle may be 100°C cooler and contain 8% less melt by comparison to the EPR upper mantle [Forsyth, 1993; West et al., 1993].

Similarities between the mantle shear wave velocity structure east of the AAD (i.e., Zone A) and the EPR [Rouland et al., 1985] imply that a significant contrast in mantle temperature exists between Zone A and the AAD. The large temperature differential suggests a wide range in the amount of melt delivered to the spreading axis which may, in turn, translate to a diversity of spreading axis morphology and basalt composition. The broad axial rise and active rift propagation of Zone A are characteristics commonly produced by high melt production typically associated with high spreading rates or hot spot influenced spreading centers [Schilling 1985; Christie and Sinton 1981; Sinton et al. 1983; Vogt & Johnson, 1973]. The deep axial valleys and short ridge segmentation found within the AAD are characteristics commonly associated with slow spreading rates and low melt production [Sempéré et al., 1991].

In addition to their unique tectonic context, the AAD basalts are believed to be derived from lower average melting pressures, and lower degrees of mantle melting than any other MORB suite worldwide [Klein and Langmuir, 1987, 1989; Klein et al., 1991]. Therefore, the AAD MORB suite represents the high Na_2O, high SiO_2 and low FeO_t endmember in the global range of MORB major element composition. We examine compositional variations between the AAD and Zone A lavas in the context of their distinct spreading axis morphologies. Southeast Indian Ridge MORB major and trace element compositions change systematically with the abrupt deepening of the spreading axis and development of an axial valley topography. Mantle temperature differences between these regions are most apparent in the major element systematics, however the trace element contrasts could result

from differences in the modal mineralogy of beneath Zone A and the AAD. The isotopic transition from Pacific-type MORB to Indian-type MORB also coincides with the morphological transition along-axis [Pyle et al., 1992]. The close correspondence between the geochemical and geophysical characteristics of the spreading ridge imply that an orderly change in mantle source accompanies the change in the upper mantle thermal regime.

SAMPLE COLLECTION and ANALYSIS

A detailed SeaMARC II mapping and intermediate-scale dredge sampling investigation of the SEIR between 132 °E and 123 °E was conducted in January and February of 1988 aboard the *R/V Moana Wave* . This survey covered ~500 km of the AAD and Zone A plate boundaries (Fig. III.1) [Sempéré et al., 1991; Palmer et al., 1993], including spreading segments A1, A2, B5, B4, B3, and parts of B2 and A3. Dredge sites were selected using SeaMARC II side-scan bathymetry and were spaced 10-40 km apart insuring that most segments were sampled at three or more sites (Table III.1). Several off-axis dredges from 2-4 Ma seafloor within the AAD and Zone A were also successful.

Twenty-six dredges within Zone A and the AAD brought aboard over 650 basaltic samples with quenched glass margins. Major element concentrations were determined for every sample with glassy margins using the Lamont-Doherty Cameca microprobe (Table III.2). Chemical groups within each dredge were visually identified by the clustering of microprobe data on major element variation diagrams. Forty-seven chemically distinct major element compositions were identified and each composition is assumed to represent a single flow and/or magma pulse supplied to the spreading axis at each dredge site.

A representative suite of glass samples was selected for detailed major and trace element analysis by a combination of direct current plasma spectroscopy (DCP) and instrumental neutron activation analysis (INAA) (Table III.3). All analyses are of fresh glass chips that have been crushed to 0.5-1.0 mm in a ceramic mortar and hand-picked to remove phenocryst and alteration material. INAA was performed on ~500 mg splits of

Table III.1 MW8801 cruise dredge summary.

Dredge	Latitude (°S)	Longitude (°E)	depth† (m)	Summary
zone A				
segment A2 (propagting rift)				
MW02	50.31	129.53	3200	Valley along axis, immediately S. of axial ridge.
MW01	50.21	128.54	3200	Near mid-point of segment A2, north side of a high ridge south of the axial ridge.
MW13	50.21	128.01	3400-3200	Graben 3 km N of axis, 30 km behind A2 propagating rift tip.
MW03	50.15	127.96	3600-3400	North slope of a distinctive axial ridge.
MW12	50.11	127.83	3600	1.5 km N. of axial high, 18 km behind A2 propagating rift tip.
MW11	50.15	127.65	3400	Axial valley 5 km behind A2 propagating rift tip.
MW16	50.16	127.58	3600-3500	Bathymetric deep at the A2 propagating rift tip.
segment A1 (doomed rift)				
MW10	50.24	127.59	3200	Along crest of A1 axial ridge, 8 km south of A2 propagating rift tip.
MW17	50.22	127.42	3400-3100	Graben on N. side of A1 axial ridge, 30 km east of zone A-AAD transfrom.
MW09	50.20	127.06	3400-3200	Along S. slope of axial ridge 8 km east of zone A-AAD transform.
MW19	50.15	127.02	3200	Westernmost A1, along axial ridge which turns N. into the zone A-AAD tranform.
MW07	49.22	127.66	3300	Off-axis (~3.5 Ma crust), lower slope of 500m axis-parallel ridge.10 km east of zone A-AAD transform
MW20	49.52	127.59	3300	Off-axis (~2.0 Ma crust), S. slope of an axis-parallel ridge, 17 km east of zone A-AAD transform.
AAD (zone B)				
segment B5				
MW04	48.76	127.36	4000-3600	Central high within a broad axial valley, 7 km west of zone A-AAD transform.
MW06	48.76	126.88	4400	Axial valley, west of the B5 non-transform discontinuity (NTD).
MW05	48.68	126.52	4600-4800	Small axial ridge within a deep axial valley, 8 km east of B4/B5 transform.
MW18	50.04	126.74	4600-4000	Off-axis (~3.5 Ma crust), deep broad valley 18 km west of zone A-AAD transform.
MW24	49.77	126.17	3600-3500	Off-axis (~3.0 Ma crust), S. slope of an axial parallel ridge, 9 km east of B4/B5 transform.
segment B4				
MW22	49.68	125.89	4000	Along axial graben, 8 km west of B4/B5 transform.
MW23	49.61	125.66	4000-3800	Base of transverse axial ridge within the B4E axial valley, near B4 NTD.
segment B3				
MW27	49.06	124.96	4200-4000	Northern side of rift valley up steep, 700 m slope from valley floor to plateau.
MW28	48.99	124.71	4200-4600	Base of small volcanic(?) hill within B3 NTD deep.
MW29	48.91	124.47	4200-4600	Plateau within axial graben, 10 km west of B3 NTD.
MW30	48.94	124.28	4400-3400	Southen wall of B3 axial valley, 20 km east of B2/B3 transform.
MW26	49.46	123.23	4800-5000	Extensional relay axial valley within B2/B3 transform zone.

† Dredge depths have been determined from SeaMARC II bathymetry [Palmer et al., 1992]. Shipboard 'on bottom'/'off bottom' depth estimates showed large variations, particularly within the AAD because of the unusally rough and rapidly changing bathymetry.

Table III.2 Microprobe analyses of natural glass.

Zone A
segment A2 (Propagating Rift)

dredge.grp n	MW02 (n=1)†	MW01.a (n=10)	MW01.b (n=8)	MW01.c (n=2)	MW13.a (n=38)	MW13.b (n=3)	MW03 (n=17)	MW12 (n=1)	MW11 (n=23)	MW16.a (n=2)	MW16.b (n=24)	MW16.c (n=2)	MW16.d (n=1)
SiO2	50.90	50.59 (.17)	50.72 (.57)	50.74 (.29)	50.68 (.40)	55.74 (.47)	50.78 (.27)	51.17	50.94 (.27)	49.32 (.09)	50.42 (.29)	50.45 (.04)	50.22
TiO2	2.00	2.38 (.14)	2.47 (.25)	2.80 (.13)	2.76 (.11)	2.63 (.04)	3.11 (.13)	3.18	1.97 (.04)	1.70 (.01)	1.51 (.06)	1.89 (.02)	2.29
Al2O3	14.50	13.90 (.09)	13.74 (.17)	13.50 (.24)	13.55 (.16)	13.31 (.21)	12.98 (.14)	13.46	14.71 (.26)	16.59 (.05)	15.36 (.24)	15.21 (.05)	14.91
FeOt	10.10	11.41 (.21)	11.97 (.25)	12.69 (.08)	12.62 (.36)	12.30 (.33)	13.73 (.32)	13.83	10.20 (.22)	8.26 (.02)	8.78 (.26)	9.26 (.10)	10.20
MnO	0.18	0.19 (.02)	0.22 (.03)	0.21 (.00)	0.21 (.02)	0.20 (.01)	0.23 (.02)	0.25	0.17 (.02)	0.16 (.00)	0.16 (.02)	0.16 (.01)	0.17
MgO	6.93	6.72 (.13)	6.36 (.20)	5.75 (.12)	6.20 (.14)	4.11 (.08)	5.44 (.12)	5.59	7.20 (.13)	7.99 (.06)	7.84 (.18)	7.37 (.01)	7.16
CaO	11.27	10.88 (.22)	10.52 (.25)	10.14 (.20)	10.27 (.16)	7.83 (.13)	9.40 (.09)	9.70	11.06 (.09)	10.99 (.04)	11.80 (.28)	11.06 (.07)	10.95
Na2O	3.09	2.74 (.07)	2.92 (.13)	3.13 (.09)	2.86 (.10)	3.51 (.39)	2.94 (.10)	2.70	2.95 (.10)	3.05 (.01)	3.01 (.14)	2.93 (.01)	3.02
K2O	0.09	0.12 (.02)	0.13 (.02)	0.14 (.02)	0.11 (.02)	0.31 (.01)	0.14 (.03)	0.17	0.07 (.02)	0.19 (.00)	0.05 (.02)	0.08 (.02)	0.16
P2O5	0.34	0.25 (.02)	0.26 (.02)	0.30 (.01)	0.26 (.03)	0.36 (.09)	0.26 (.02)	0.27	0.20 (.01)	0.23 (.00)	0.19 (.03)	0.229 (.01)	0.26
total	99.41	99.19	99.31	99.40	99.51	100.31	99.02	100.32	99.48	98.48	99.12	98.62	99.33

segment A1 (Doomed Rift)

dredge.grp n	MW10 (n=10)	MW17.a (n=32)	MW17.b (n=10)	MW17.c (n=4)	MW17.d (n=6)	MW17.e (n=10)	MW17.f (n=23)	MW19.a (n=17)	MW19.b (n=23)	MW19.c (n=8)	MW09.a (n=44)	MW09.b (n=3)	MW20 (n=2)	MW07 (n=1)
SiO2	50.86 (.27)	50.64 (.31)	50.77 (.14)	51.36 (.20)	50.99 (.29)	50.70 (.16)	50.84 (.29)	50.61 (.26)	50.75 (.27)	50.79 (.25)	50.82 (.38)	50.44 (.47)	50.87 (.01)	50.14
TiO2	2.62 (.02)	1.35 (.03)	1.38 (.03)	1.40 (.03)	1.58 (.03)	1.90 (.09)	2.31 (.06)	2.30 (.04)	2.52 (.05)	2.70 (.05)	2.06 (.06)	3.09 (.10)	2.03 (.03)	1.89
Al2O3	14.02 (.18)	15.56 (.13)	15.67 (.18)	15.70 (.26)	14.98 (.13)	14.68 (.21)	14.12 (.17)	14.29 (.14)	13.90 (.13)	13.66 (.12)	14.68 (.16)	13.46 (.27)	14.53 (.13)	14.17
FeOt	11.17 (.18)	8.46 (.14)	8.47 (.10)	8.50 (.09)	9.15 (.09)	9.88 (.21)	10.81 (.23)	10.53 (.22)	11.29 (.27)	11.78 (.16)	9.96 (.28)	13.03 (.40)	10.41 (.04)	10.18
MnO	0.20 (.02)	0.15 (.02)	0.15 (.03)	0.17 (.03)	0.18 (.01)	0.16 (.03)	0.19 (.02)	0.18 (.02)	0.20 (.03)	0.22 (.02)	0.17 (.03)	0.22 (.02)	0.17 (.01)	0.17
MgO	6.38 (.07)	8.48 (.10)	8.03 (.11)	7.47 (.23)	7.85 (.10)	7.56 (.15)	6.85 (.13)	6.97 (.07)	6.60 (.06)	6.27 (.04)	7.21 (.13)	5.86 (.21)	7.25 (.25)	7.32
CaO	10.34 (.12)	11.67 (.22)	11.83 (.26)	12.11 (.45)	11.56 (.17)	11.20 (.10)	10.84 (.15)	10.89 (.11)	10.50 (.19)	10.24 (.10)	11.20 (.13)	10.00 (.08)	10.61 (.13)	11.64
Na2O	3.12 (.11)	2.82 (.09)	2.87 (.09)	2.86 (.13)	2.73 (.12)	2.85 (.08)	2.99 (.18)	3.05 (.10)	3.07 (.15)	3.19 (.17)	3.03 (.12)	2.82 (.26)	2.79 (.11)	2.52
K2O	0.13 (.03)	0.04 (.01)	0.03 (.01)	0.03 (.02)	0.04 (.02)	0.10 (.01)	0.12 (.03)	0.17 (.03)	0.14 (.02)	0.12 (.02)	0.08 (.02)	0.11 (.02)	0.11 (.02)	0.09
P2O5	0.26 (.01)	0.16 (.04)	0.17 (.03)	0.19 (.01)	0.19 (.03)	0.23 (.02)	0.24 (.01)	0.25 (.02)	0.24 (.02)	0.28 (.02)	0.23 (.01)	0.28 (.02)	0.22 (.00)	0.14
total	99.31	99.32	99.36	99.79	99.25	99.27	99.31	99.24	99.21	99.23	99.43	99.32	98.99	98.26

† 'n' represents number of individual glass samples within each group average.
All analyses with totals <98.5 or >101.0 have been omitted from the group averages.
Numbers in parenthesis are 1σ variations in the mean of major element oxides for each group.
Microprobe analyses were performed at an accelerating voltage of 15 kV with a beam current of 5 nA for K and Na and 20 nA for Si, Ti, Al, Fe, Mn, Mg, Ca, and P. Counts for all peaks were acquired over a 20 second interval.

Table III.3 Microprobe analyses of natural glass.

AAD
segments B5 & B4

dredge.grp n	MW04.a (n=1)	MW04.b (n=1)	MW05 (n=2)	MW06 (n=6)	MW18.a (n=3)	MW18.b (n=26)	MW18.c (n=6)	MW24 (n=14)	MW22 (n=33)	MW23 (n=7)
SiO2	50.62	50.78	51.61 (.06)	50.96 (.63)	51.72 (.44)	51.94 (.43)	52.99 (.54)	52.06 (.24)	51.11 (.31)	51.12 (.43)
TiO2	1.51	1.57	1.46 (.01)	1.38 (.07)	1.19 (.01)	1.37 (.06)	1.60 (.04)	1.40 (.03)	1.01 (.02)	1.09 (.02)
Al2O3	16.00	16.12	15.88 (.00)	15.68 (.19)	16.29 (.06)	15.97 (.24)	15.45 (.16)	15.87 (.09)	16.58 (.12)	16.19 (.15)
FeOt	8.71	9.31	8.46 (.01)	8.43 (.19)	7.56 (.12)	8.01 (.27)	8.45 (.12)	7.83 (.13)	7.80 (.10)	8.98 (.25)
MnO	0.14	0.18	0.15 (.01)	0.14 (.02)	0.15 (.01)	0.15 (.02)	0.16 (.02)	0.15 (.02)	0.15 (.02)	0.13 (.03)
MgO	7.76	6.94	7.81 (.06)	8.09 (.11)	8.55 (.13)	7.70 (.13)	6.74 (.11)	7.35 (.13)	8.29 (.06)	7.88 (.16)
CaO	11.56	11.21	11.31 (.08)	11.61 (.16)	11.36 (.19)	10.99 (.22)	10.34 (.27)	10.49 (.08)	10.99 (.09)	10.85 (.14)
Na2O	3.47	3.61	3.00 (.03)	3.00 (.15)	2.98 (.08)	3.38 (.17)	3.64 (.17)	3.65 (.12)	3.13 (.10)	2.81 (.07)
K2O	0.06	0.05	0.14 (.02)	0.07 (.01)	0.09 (.02)	0.13 (.02)	0.26 (.02)	0.14 (.01)	0.08 (.02)	0.08 (.02)
P2O5	0.15	0.18	0.17 (.00)	0.14 (.03)	0.13 (.05)	0.16 (.04)	0.19 (.03)	0.19 (.01)	0.17 (.01)	0.15 (.01)
total	99.98	99.95	99.99	99.50	100.01	99.81	99.82	99.10	99.31	99.27

segments B3 & B2

dredge.grp n	MW27.a (n=2)	MW27.b (n=16)	MW27.c (n=7)	MW27.d (n=15)	MW27.e (n=15)	MW28 (n=1)	MW29.a (n=8)	MW29.b (n=1)	MW30 (n=27)	MW26 (n=1)
SiO2	52.52 (.19)	52.42 (.38)	51.96 (.43)	51.83 (.27)	51.12 (.35)	52.39	51.63 (.66)	52.88	51.73 (.39)	51.10
TiO2	1.27 (.09)	1.32 (.05)	1.38 (.06)	1.40 (.04)	1.49 (.04)	1.40	1.21 (.03)	1.40	1.29 (.06)	1.40
Al2O3	16.14 (.14)	15.86 (.25)	15.61 (.22)	16.26 (.25)	16.92 (.28)	15.77	16.39 (.09)	16.22	16.50 (.24)	15.55
FeOt	7.72 (.23)	7.90 (.17)	8.18 (.16)	7.78 (.11)	8.04 (.08)	8.49	7.40 (.07)	7.85	7.58 (.11)	8.52
MnO	0.16 (.02)	0.15 (.02)	0.15 (.02)	0.15 (.02)	0.14 (.02)	0.14	0.10 (.04)	0.14	0.14 (.02)	0.16
MgO	8.03 (.10)	7.65 (.10)	7.53 (.06)	7.46 (.15)	7.40 (.24)	7.35	8.19 (.05)	7.31	7.70 (.12)	7.88
CaO	10.99 (.15)	10.66 (.15)	11.10 (.11)	10.59 (.13)	10.03 (.13)	10.53	10.89 (.08)	10.37	10.85 (.18)	10.95
Na2O	3.37 (.23)	3.46 (.11)	3.39 (.13)	3.70 (.13)	3.66 (.06)	3.30	3.29 (.07)	3.85	3.48 (.13)	2.94
K2O	0.11 (.02)	0.14 (.02)	0.11 (.01)	0.19 (.04)	0.63 (.06)	0.10	0.18 (.01)	0.17	0.17 (.06)	0.07
P2O5	0.13 (.05)	0.18 (.02)	0.19 (.01)	0.19 (.02)	0.24 (.02)	0.18	0.19 (.01)	0.19	0.19 (.02)	0.18
total	100.45	99.73	99.60	99.55	99.68	99.65	99.45	100.37	99.64	98.75

Table III.4 Direct current plasma (DCP) and instrumental neutron activation analyses (INAA) of natural glass.

	Zone A (segment A2)														
Sample	02-1	01-15	01-36	01-37	13-47	13-51	13-7	13-14	03-6	12-1	11-17	16-12	16-1	16-16	16-19
probe grp		a	b	c	a	a	a	b				a	b	c	d
depth (m)	3200		3200				3300		3500	3600	3400			3500	
km†	191		113				76		72	63	50			45	
SiO_2	50.05	49.89	49.68	49.29	49.66	49.64	49.42	54.15	49.81	49.69	49.74	48.85	50.09	49.84	49.42
TiO_2	1.81	2.34	2.85	2.82	2.44	2.46	2.58	2.47	2.86	2.94	1.80	1.57	1.43	1.73	2.07
Al_2O_3	14.61	13.89	13.35	13.18	13.59	13.80	13.54	12.92	12.93	13.25	15.16	16.48	15.37	15.27	15.22
Fe_2O_3	11.46	12.87	14.48	14.47	13.61	13.50	13.87	12.99	15.17	14.64	11.17	9.35	9.68	10.51	11.23
MnO	0.19	0.20	0.22	0.22	0.22	0.22	0.22	0.20	0.23	0.22	0.18	0.16	0.17	0.17	0.18
MgO	7.28	6.87	6.01	5.95	6.49	6.52	6.39	4.08	5.80	5.79	7.62	8.24	7.84	7.76	7.63
CaO	11.23	10.77	9.83	9.72	10.38	10.46	10.25	7.76	9.45	9.40	11.02	11.03	11.64	11.08	10.72
Na_2O	2.92	2.73	3.00	3.00	2.84	2.83	2.81	3.86	2.94	3.05	2.92	3.03	3.12	2.94	2.99
K_2O	0.09	0.13	0.14	0.15	0.12	0.12	0.11	0.32	0.14	0.16	0.07	0.20	0.05	0.14	0.12
P_2O_5	0.19	0.24	0.30	0.30	0.25	0.25	0.26	0.42	0.28	0.33	0.18	0.23	0.13	0.19	0.24
total	99.81	99.93	99.87	99.10	99.59	99.78	99.45	99.17	99.62	99.47	99.86	99.13	99.51	99.63	99.82
mg#††	58.3	54.0	47.7	47.5	51.2	51.5	50.3	40.9	45.7	46.5	60.0	66.0	64.1	61.9	59.9
Ba	5.7	11.3	10.9	11.3	9.9	9.2	8.4	21	10.4	12.3	4.4	8.5	2.8	6.9	8.0
Sr	125	103	107	106	100	101	97	101	103	113	120	231	125	134	144
Th	0.09		0.10		0.08	0.12		0.38	0.16	0.19	0.08	0.10	0.05	0.11	0.08
U	0.14		0.15		0.16	0.12		0.3	0.23	0.20	0.18	0.26	0.06	0.08	0.06
Ta	0.26		0.33		0.20	0.35		0.42	0.36	0.31	0.29	0.28	0.06	0.15	0.16
Zr	142	182	233	228	191	188	201	453	221	257	140	155	105	143	177
Hf	3.43		5.76		4.89	4.79		12.61	5.64	6.48	3.70	3.45	2.67	3.65	4.27
Y	41.8	53.3	65.7	64.7	56.0	55.7	58.0	105.6	60.0	69.1	40.9	31.1	31.3	38.3	46.2
Sc	40.3	40.7	40.4	40.2	40.1	41.1	40.8	29.9	40.0	38.9	36.5	34.2	38.5	36.0	35.6
Ni	78	73	61	58	78	63	75	93	52	63	89	128	95	103	121
Cr	303	177	89	87	119	117	116	44	53	91	297	276	329	302	283
Co	38.4		41.2		41.4	39.5		31.2	42.7	38.1	40.1	40.9	39.7	40.4	40.0
V	326	409	451	450	418	418	422	323	462	456	304	243	251	296	320
Zn	85.8	101.1	117.3	114.9	103.3	107.0	101.7	114.1	116.3	101.6	81.4	64.7	67.3	81.0	88.0
Cu	66.3	56.8	52.1	51.8	58.2	55.8	53.7	42.0	46.3	48.2	61.5	63.6	72.1	62.6	58.1
La	3.75		6.79		5.39	5.27		14.94	6.26	7.61	3.95	6.71	2.81	4.32	5.34
Ce	13.2		19.9		18.3	16.9		47.8	21.4	25.3	14.2	18.7	10.2	13.4	17.3
Nd	13.2		19.6		17.4	18.3		40.6	20.7	28.2	12.6	13.5	11.2	12.0	16.2
Sm	4.52		7.23		5.82	5.98		13.05	7.03	7.89	4.39	3.94	3.54	4.28	5.05
Eu	1.54		2.28		2.00	1.95		3.30	2.28	2.39	1.55	1.50	1.40	1.55	1.76
Tb	1.06		1.68		1.54	1.54		2.99	1.78	1.92	1.17	0.86	0.94	1.08	1.24
Yb	4.29		7.04		6.29	5.92		12.76	6.98	7.36	4.43	3.14	3.18	3.94	4.88
Lu	0.65		1.10		0.86	0.90		1.79	1.02	1.05	0.61	0.45	0.48	0.56	0.66

† Distance (km) from Zone A-AAD transform boundary.
†† mg#=$Mg^{+2}/(Mg^{+2} + Fe^{+2})$ with $Fe^{+2} = .9 * Fe_{(total)}$
DCP analyses: All major elements and Ba, Sr, Zr, Y, Sc, Ni, Cr, V., Zn, Cu.
INAA analyses: Ta, Hf, Co, La, Ce, Nd, Sm, Eu, Tb, Yb, Lu (all trace elements reported as ppm).

Table III.5 Direct current plasma (DCP) and instrumental neutron activation analyses (INAA) of natural glass (cont.).

	Zone A (segment A1)													
Sample	10-1	17-26	17-33	17-13	17-46	17-68	17-48	09-41	09-7	19-2	19-56	19-33	07-1	20-1
probe grp		a	b	c	d	e	f	a	b	a	b	c		
depth (m)	3200			3400				3400			3200		3300	3300
km	46			33				8			5		30	28
SiO_2	50.03	50.17	50.42	49.70	50.34	49.73	50.02	49.95	49.53	50.01	49.67	49.98	49.97	49.83
TiO_2	2.44	1.29	1.32	1.27	1.45	1.81	2.24	1.88	2.74	2.14	2.39	2.53	1.78	1.88
Al_2O_3	14.06	15.61	15.35	15.42	15.46	14.81	14.19	14.63	13.66	14.38	14.23	13.64	14.60	14.60
Fe_2O_3	12.38	9.49	9.52	9.42	10.18	10.96	12.06	11.03	13.70	11.59	12.60	13.20	11.64	11.70
MnO	0.20	0.16	0.16	0.16	0.17	0.18	0.20	0.18	0.21	0.19	0.20	0.21	0.19	0.19
MgO	6.56	8.61	8.57	8.58	8.17	7.54	6.97	7.29	6.30	7.13	6.70	6.38	7.47	7.50
CaO	10.42	11.73	11.75	11.66	11.53	11.25	10.85	11.16	10.10	11.06	10.47	10.28	11.41	10.51
Na_2O	3.10	2.83	2.82	2.82	2.77	2.76	2.96	2.96	2.96	2.95	3.00	3.09	2.59	2.84
K_2O	0.14	0.03	0.03	0.03	0.05	0.10	0.14	0.08	0.13	0.17	0.14	0.12	0.08	0.17
P_2O_5	0.26	0.12	0.12	0.11	0.13	0.19	0.25	0.21	0.30	0.24	0.25	0.27	0.18	0.19
total	99.58	100.04	100.06	99.17	100.25	99.33	99.87	99.38	99.64	99.85	99.65	99.70	99.91	99.41
mg#	53.8	66.6	66.5	66.7	63.8	60.2	56.0	59.3	50.3	57.5	53.9	51.5	58.5	58.5
Ba	9.1	2.9	3.1	2.7	4.0	7.7	9.0	6.7	9.3	10.5	9.7	8.4	6.3	6.7
Sr	121	105	106	103	102	113	122	114	110	142	120	121	98	110
Th	0.13	.07		0.04		0.11	0.07	0.09		0.17	0.16		0.08	0.07
U	0.21	.11		0.12		0.07	0.01	0.23			0.22		0.25	0.0
Ta	0.32	.12		0.08		0.23	0.32	0.13		0.40	0.28		0.23	0.26
Zr	200	90	92	84	101	139	185	155	230	173	186	202	133	145
Hf	5.58	2.14		2.36		3.46	4.38	3.74		4.30	4.78		3.40	3.59
Y	53.1	30.2	30.2	28.4	33.8	41.2	50.6	44.3	61.7	46.1	51.6	55.0	41.0	41.9
Sc	38.9	35.8	36	35.4	36.2	38.1	39.2	38.9	39	39.4	39.5	39.6	38.7	37.4
Ni	76	103	101	102	97	89	75	78	71	81	78	56	85	103
Cr	204	360	361	365	310	274	195	297	155	278	179	83	303	218
Co	39.2	39.7		39.9		39.9	38.1	37.3		38.4	39.0		40.3	41.1
V	379	252	254	249	279	321	368	329	411	348	396	400	344	342
Zn	95.4	70.4	68.8	73.7	73.8	85.2	97.2	80	98.9	90.4	99.9	98.1	87.7	91.4
Cu	52.8	74.3	72.8	74.4	72.1	70	58.2	65.4	50.4	61.7	55.0	55.3	63.7	57.1
La	6.52	1.9		2.14		4.27	5.34	4.54		5.71	5.71		3.85	4.82
Ce	21.5	9.2		9.1		15.3	17.4	15.0		19.5	18.6		12.8	12.5
Nd	21.9	7.8		6.6		13.2	15.2	15.1		17.5	19.2		15.9	12.9
Sm	6.60	2.94		3.05		4.47	5.63	4.73		5.24	5.96		4.35	5.08
Eu	2.20	1.14		1.12		1.61	1.81	1.59		1.76	2.03		1.45	1.57
Tb	1.63	.75		0.68		1.12	1.19	1.10		1.17	1.49		1.10	1.15
Yb	6.20	3.11		3.05		4.44	5.27	4.34		4.96	5.92		4.70	4.76
Lu	0.93	.42		0.47		0.64	0.80	0.66		0.79	0.80		0.63	0.76
Pb†		0.226												

† Pb analyses by isotope dilution.

Table III.6 Direct current plasma (DCP) and instrumental neutron activation analyses (INAA) of natural glass (cont.).

AAD (segments B5, B4, B3, & B2)

Sample	04-2	04-1	06-2	05-1	18-28	18-4	18-7	24-18	22-13	23-1	27-71	27-8	27-13	27-48	27-46	27-58	28-1	29-5	29-11	30-6	26-1
grp	a	b			a	b	c				a	b	c	d	e	e		a	b		
depth		3800		4400	4700		4800		3600	4000	3900			4100				4500	4500		3900	4900
km		12		48	74		19		70	94	111			170				188	220		234	288
SiO_2	49.29	49.80	50.55	50.19	50.58	50.90	51.48	50.92	50.45	50.57	51.06	50.65	50.69	51.00	50.23	50.3	50.95	51.08	50.94	50.96	50.46
TiO_2	1.35	1.44	1.37	1.34	1.12	1.26	1.47	1.24	0.97	1.04	1.15	1.22	1.26	1.32	1.43	1.40	1.29	1.20	1.32	1.21	1.34
Al_2O_3	16.28	15.55	15.80	15.96	16.56	16.55	15.80	16.51	16.79	16.26	16.10	16.40	15.95	16.36	17.19	17.21	15.92	16.09	16.48	16.16	16.20
Fe_2O_3	9.40	10.07	9.37	9.24	8.46	8.40	9.02	8.45	8.77	10.06	8.58	8.53	8.96	8.68	8.96	9.05	9.47	8.26	8.71	8.53	9.66
MnO	0.16	0.17	0.16	0.16	0.15	0.14	0.15	0.15	0.16	0.16	0.15	0.15	0.16	0.15	0.15	0.15	0.16	0.14	0.15	0.15	0.16
MgO	8.22	7.54	8.06	8.06	8.46	7.99	7.19	7.81	8.54	8.24	8.29	8.04	7.87	7.63	7.64	7.32	7.78	8.45	7.53	7.92	7.96
CaO	11.50	11.56	11.30	11.04	11.00	10.57	10.14	10.57	10.98	10.82	10.96	10.74	10.96	10.39	9.82	10.06	10.37	10.67	10.16	10.78	10.82
Na_2O	3.32	3.26	2.95	2.96	3.02	3.58	3.58	3.61	3.16	2.89	3.04	3.41	3.25	3.66	3.62	3.60	3.27	3.28	3.62	3.34	3.00
K_2O	0.05	0.13	0.07	0.12	0.09	0.11	0.25	0.14	0.08	0.07	0.10	0.13	0.12	0.19	0.64	0.56	0.11	0.17	0.19	0.15	0.09
P_2O_5	0.13	0.14	0.14	0.14	0.12	0.15	0.18	0.15	0.12	0.10	0.13	0.15	0.14	0.17	0.24	0.22	0.14	0.15	0.17	0.14	0.14
total	99.70	99.66	99.77	99.20	99.56	99.65	99.25	99.54	100.02	100.21	99.55	99.42	99.35	99.55	99.91	99.94	99.46	99.48	99.27	99.34	99.82
mg#	65.8	62.2	65.4	65.7	68.8	67.7	63.7	67.0	68.2	64.3	68.0	67.5	65.9	65.9	65.2	64.0	64.4	69.2	65.5	67.1	64.5
Ba	3.5	11.0	7.1	15.3	16.1	19.0	43.7	19.9	15.9	14.3	10.3	15.5	14.4	22.9	127.1	108.9	10.1	20.3	23.3	19.5	7.0
Sr	192	134	130	134	139	165	175	170	142	109	143	163	143	166	232	213	138	168	176	159	112
Th	0.03		0.05	0.26		0.15	0.23	0.17	0.16	0.15	0.10			0.32		0.88	0.11	0.16	0.30	0.15	0.10
U	0.33		0.14	0.18		0.14	0.45	3.76	0.08	0.11	0.29			0.52		1.90	0.31	0.70	0.34	0.31	0.35
Ta	0.11		0.15	0.21		0.24	0.36	0.27	0.16	0.14	0.10			0.22		0.81	0.17	0.32	0.27	0.17	0.23
Zr	111	110	106	111	95	107	131	111	81	73	89	105	101	119	139	122	102	104	122	99	100
Hf	2.52		2.59	2.86		2.52	2.92	2.59	1.83	1.82	2.07			2.84		2.97	2.53	2.30	2.63	2.19	2.77
Y	27.9	32.0	31.0	30.4	26.8	27.9	32.2	27.5	25.2	25.1	26.4	29.0	30.2	30.1	3	30.1	31.5	26.7	30.4	27.1	32.6
Sc	35.1	38.3	34.8	32.7	32.2	30.9	33.2	30.5	32.9	34.0	32.0	32.4	34.5	33.1	29.2	30.4	32.7	31.2	33.2	32.1	33.0
Ni	99	79	114	124	136	154	100	116	138	140	129	119	105	108	138	107	115	143	104	102	117
Cr	309	317	336	308	352	345	257	298	324	332	325	302	334	278	240	253	246	336	275	317	300
Co	39.5		37.5	36.9		34.1	33.8	35.6	38.8	41.8	36.0			34.3		34.2	36.9	35.1	33.6	35.2	39.7
V	226	265	257	259	229	228	256	223	207	193	230	228	257	234	216	214	239	219	228	218	250
Zn	71.2	72.0	67.8	68.6	60.6	65.8	66.8	60.5	63.2	75.2	61.1	7	64.8	68.5	66.9	64.1	67.8	62.4	66.6	64.7	70.3
Cu	76.0	89.8	64.1	62.0	65.0	62.0	58.7	65.0	75.7	82.5	57.9	56.9	59.4	58.2	57.0	56.0	58.2	56.4	55.1	64.3	55.0
La	3.97		3.45	4.10		4.10	6.09	4.46	3.25	2.40	3.53			4.99		9.43	3.73	4.32	5.54	4.34	3.31
Ce	12.5		11.4	11.4		13.3	16.0	13.8	9.5	7.2	10.8			12.6		21.3	10.3	11.6	14.3	11.7	11.2
Nd	12.4		8.9	10.7		11.3		12.1	7.4	5.9	8.9			13.1		13.4	9.6	10.4	12.1	10.7	9.9
Sm	3.39		3.43	3.37		3.32	3.94	3.45	2.57	2.39	3.00			3.59		3.62	3.45	3.11	3.77	3.29	3.74
Eu	1.24		1.23	1.21		1.21	1.37	1.22	0.97	0.93	1.09			1.31		1.30	1.23	1.14	1.27	1.13	1.29
Tb	0.77		0.78	0.76		0.66	0.84	0.77	0.58	0.61	0.71			0.75		0.80	0.79	0.70	0.78	0.66	0.95
Yb	2.95		3.11	3.16		2.64	3.03	2.76	2.56	2.57	2.77			3.12		2.99	3.29	2.53	2.89	2.71	3.28
Lu	0.44		0.47	0.48		0.40	0.53	0.44	0.40	0.40	0.41			0.52		0.45	0.50	0.42	0.50	0.41	0.51
Pb			0.358					0.550		0.275	0.414					0.808				0.496	

glass irradiated at the Oregon State University TRIGA reactor and spectra each sample was collected at three decay intervals to optimize the counting statistics for short, intermediate, and long-live radionuclides [Laul, 1979]. DCP analyses were completed by G. Eberhart at Lamont-Doherty Earth Observatory following procedures outlined in Klein et al.[1991] and Miller et al. [1992].

RESULTS

Axial Morphology

Sempéré et al.[1991] and Palmer et al. [1993] have presented detailed discussions of the diverse spreading axis morphology of the SEIR between 132°E and 123°E as a reflection of changing melting conditions beneath Zone A and AAD. A brief summary of their observations are given below.

The tectonics of the Zone A spreading system have been dominated by several episodes of rift propagation over the past 25 Ma [Vogt et al., 1984]. Presently, three in echelon propagating rift systems are migrating toward the AAD at rates roughly equal to the full spreading rate for this region (79-90 mm/yr) [Vogt et al, 1984; Sandwell and Smith, 1993]. Rift propagation is commonly occurs along spreading segments affected by excess melt production associated with hot spot volcanism (e.g., Galapagos and Juan de Fuca) [Sinton et al., 1983; Schilling et al., 1985; Hey et al., 1989]; but in the case of Zone A, rift propagation may be driven by gravitational forces resulting from an increase in axial depth toward the AAD [Phipps-Morgan et al., 1988]. A deficient melt supply relative to the intermediate spreading rate of AAD spreading segments may also be compensated by melt from more robust Zone A spreading centers resulting in sub-axial asthenospheric flow toward the AAD [Forsyth et al., 1987]. The large volume of melt reaching Zone A spreading centers is clearly evident from the broad axial high of the rift axis that persists even along the doomed rift segment (segment A1) and well into the Zone A ridge-transform intersection with the AAD (Fig. III.3a).

Figure III.3 SeaMARC bathymetry (200 m contours) of Zone A and AAD spreading centers: a) segments A1 and A2; b) segment B5; c) segment B4; d) segment B3; e) extensional basin within B2/B3 transform boundary. Dredge locations are designated as in Fig. 1. The locations of axial cross-sections for each spreading segment (Fig. 2) is represented by a black line.

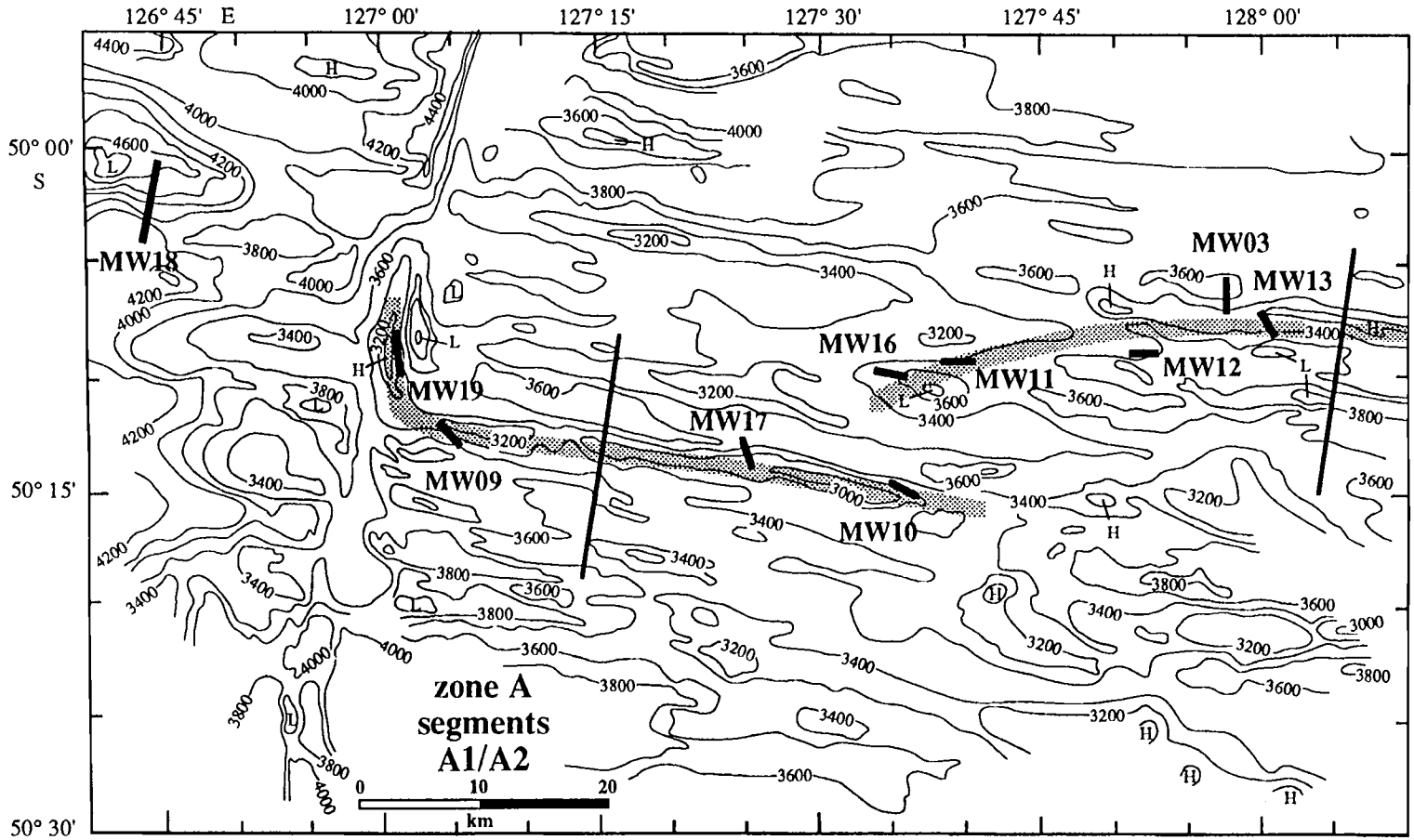

Figure III.3a

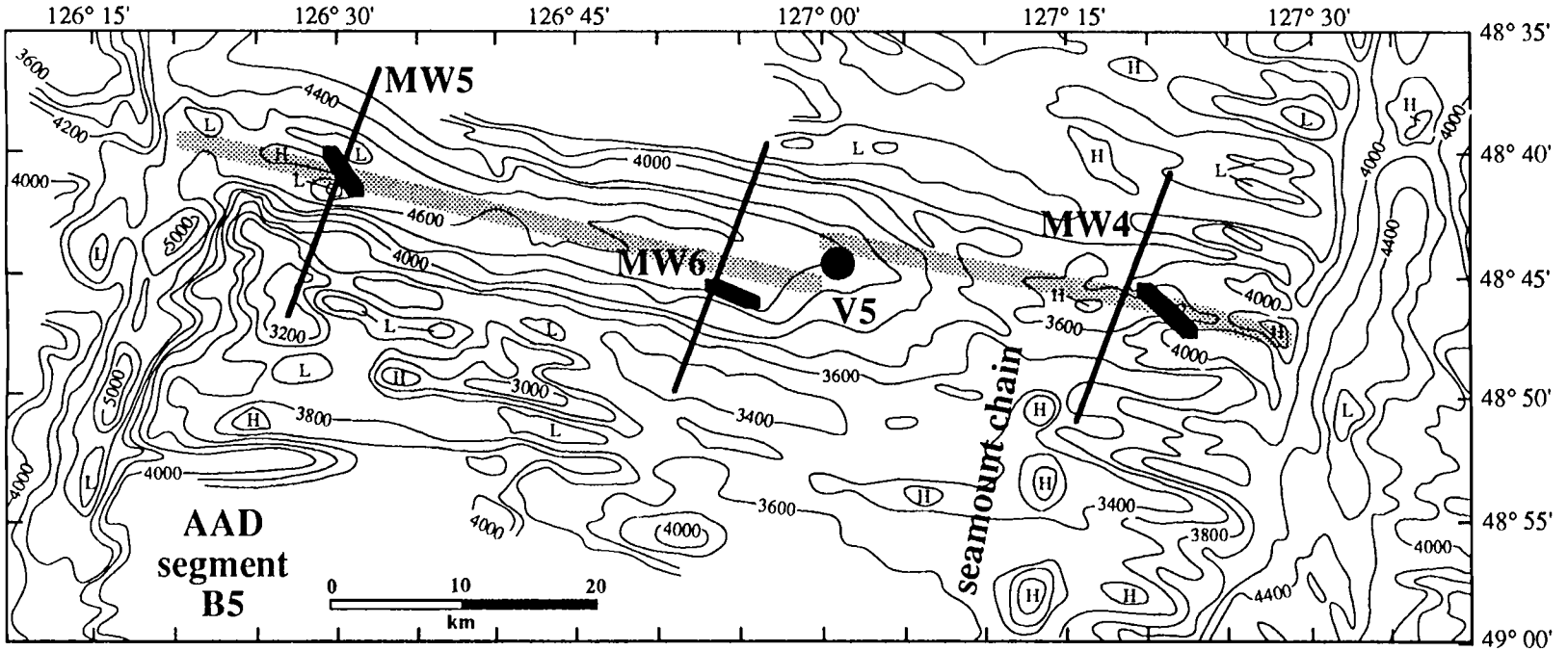

Figure III.3b

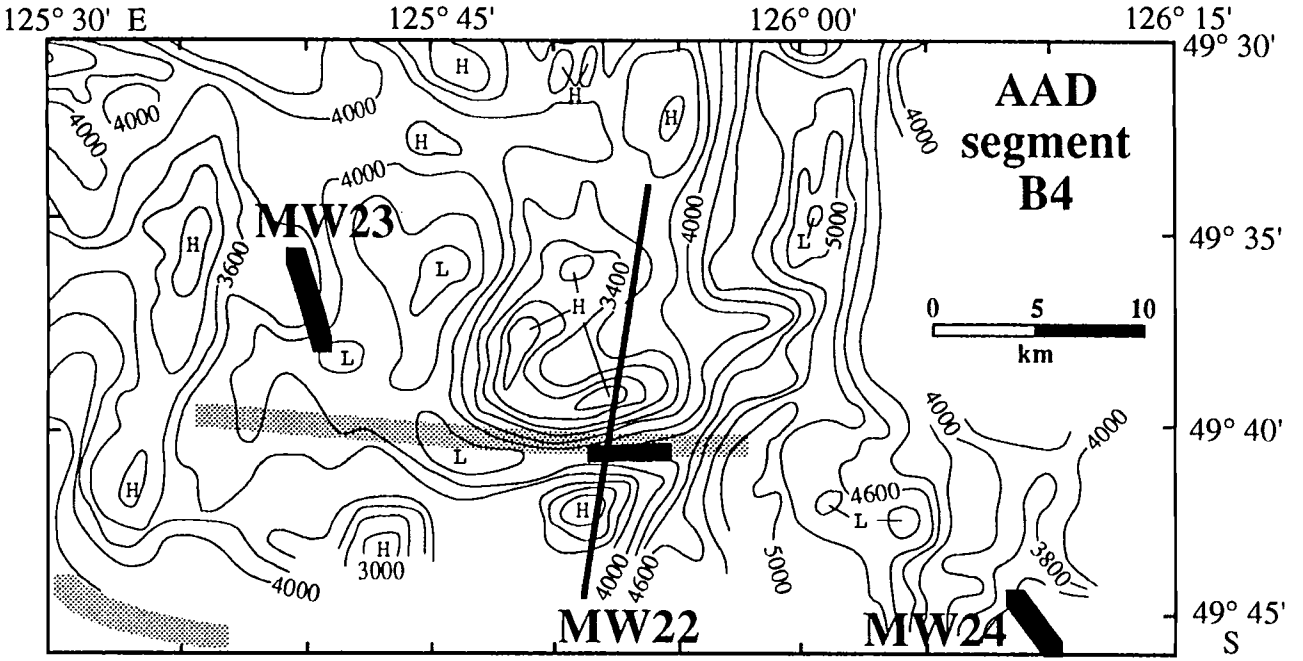

Figure III.3c

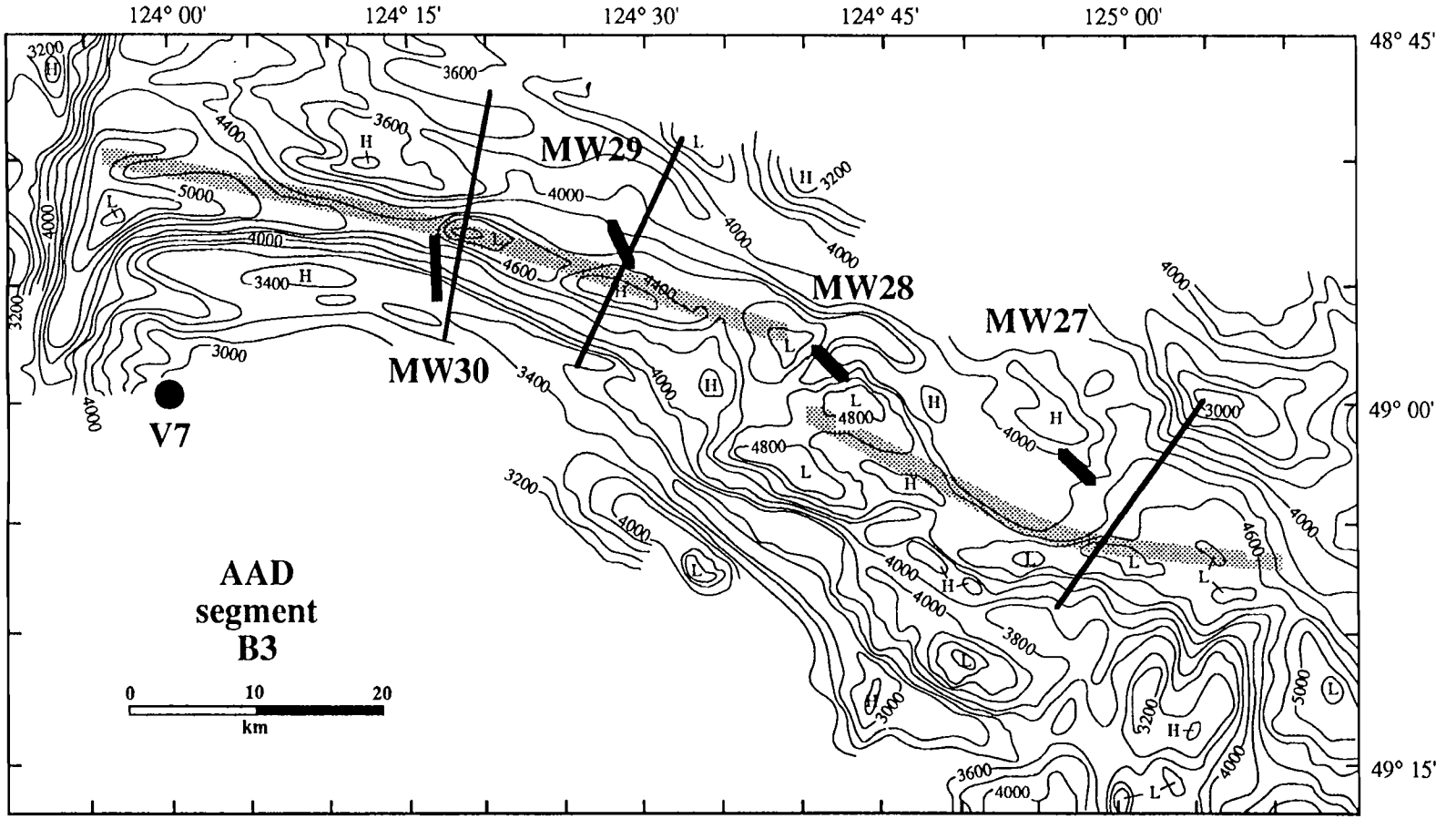

Figure III.3d

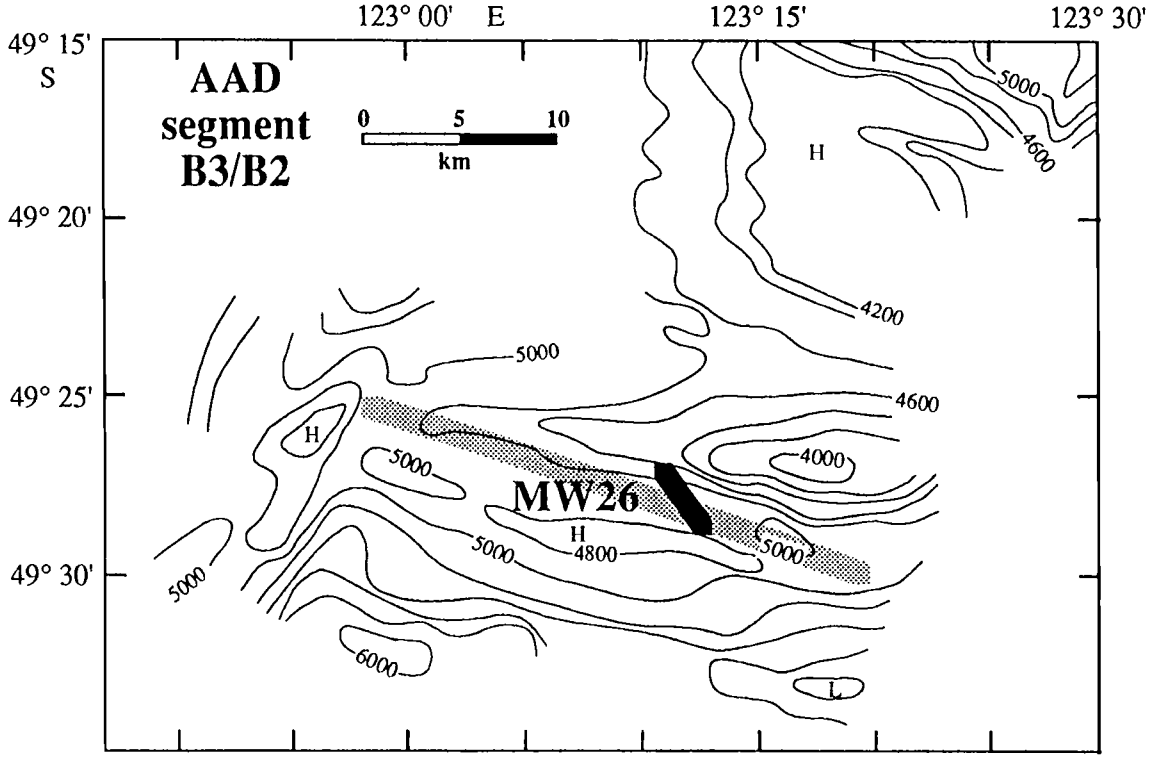

Figure III.3e

The transition from a Zone A-type axial rise morphology to an AAD-type axial rift valley morphology coincides with an abrupt deepening of the spreading axis east of a non-transform discontinuity along the B5 segment (Fig. III.3b). The eastern B5 segment (B5E) is partially inflated by a small axial seamount which is the youngest of a linear chain that extends south on the Antarctic plate. West of the B5 non-transform discontinuity, a 'typical' AAD axial valley appears. Typical AAD axial profiles show a 700-1200 m deep and 8-10 km wide rift valleys which are commonly at depths in excess of 4000 m, the most well developed examples being the B5E and B3 spreading segments (Fig. III.2; Fig. III.3b and Fig. III.3d).

The smaller B4 segment is considerably more tectonically complex and not as well defined as are B5 and B3 (Fig. III.3c). No clearly identifiable neovolcanic zone was detected in backscatter images of B4, and many off-axis, abyssal hills appear disoriented and atypical for normal, ridge-parallel spreading conditions. Several of these hills are unexpectedly shallow (3500-3000 m) relative to the deep spreading axis. In addition, a 3 km wide, 15 km long, 1000 m deep graben of B4E segment (neovolcanic zone?) terminates against a transform-parallel, 500 m high ridge. This rugged, unorganized seafloor terrain appears to result from poorly organized and/or amagmatic spreading. Similar bathymetric features appear on 3-4 Ma crust surrounding the off-axis dredge sites within the B5 segment.

Major Element Systematics

The diversity in spreading axis morphology is matched by the eruption of an equally diverse suite of MORB compositions within the AAD and Zone A (Fig. III.4). Zone A lavas include primitive basalts (8.2% MgO, 9.4% Fe_2O_3; MW16), highly differentiated FeTi basalts (15.2% Fe_2O_3, 2.9% TiO_2, 5.8% MgO; MW12 and MW03), and rare basaltic andesites (54.2% SiO_2, 4.1% MgO; MW13). Collectively, Zone A lavas define what appears to be a low-pressure, fractional crystallization sequence, similar to MORB from the

Figure III.4 Major element variations for DCP analyses of Zone A and AAD glasses. The DCP data of Klein et al. [1991] are also included in this figure. These data are from dredge locations that lie well out of our survey area, however, they complement our new results and offer a perspective which neither study could convey alone. Both data sets are directly comparable since all analyses were performed at the Lamont-Doherty DCP laboratory. One atmosphere fractional crystallization trends have been calculated for possible parental melt compositions from Zone A (MW17-26) and the AAD (MW29-5) using a modified version of MIXNFRAC (major element kd's based on experimental data appropriate for MORB suites only) [Nielsen, 1985]. None of the one atmosphere fractionation trends satisfy all the major element variations for either Zone A or AAD compositions. The B5 axial samples are outline by a shaded field. The circled question mark is the possible major element characteristics of an unsampled Zone A parental melt for the more evolved zone A samples.

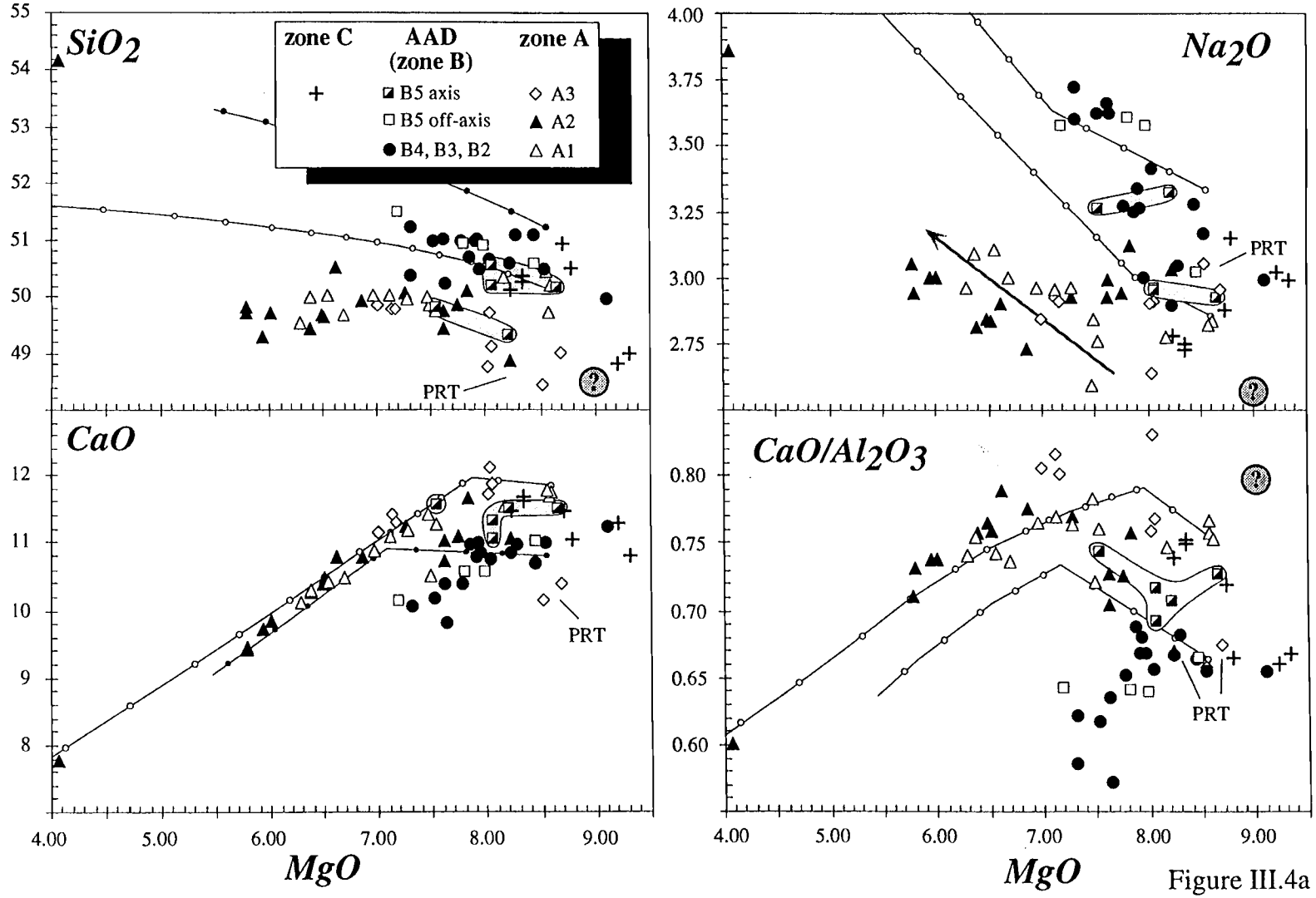

Figure III.4

Figure III.4a

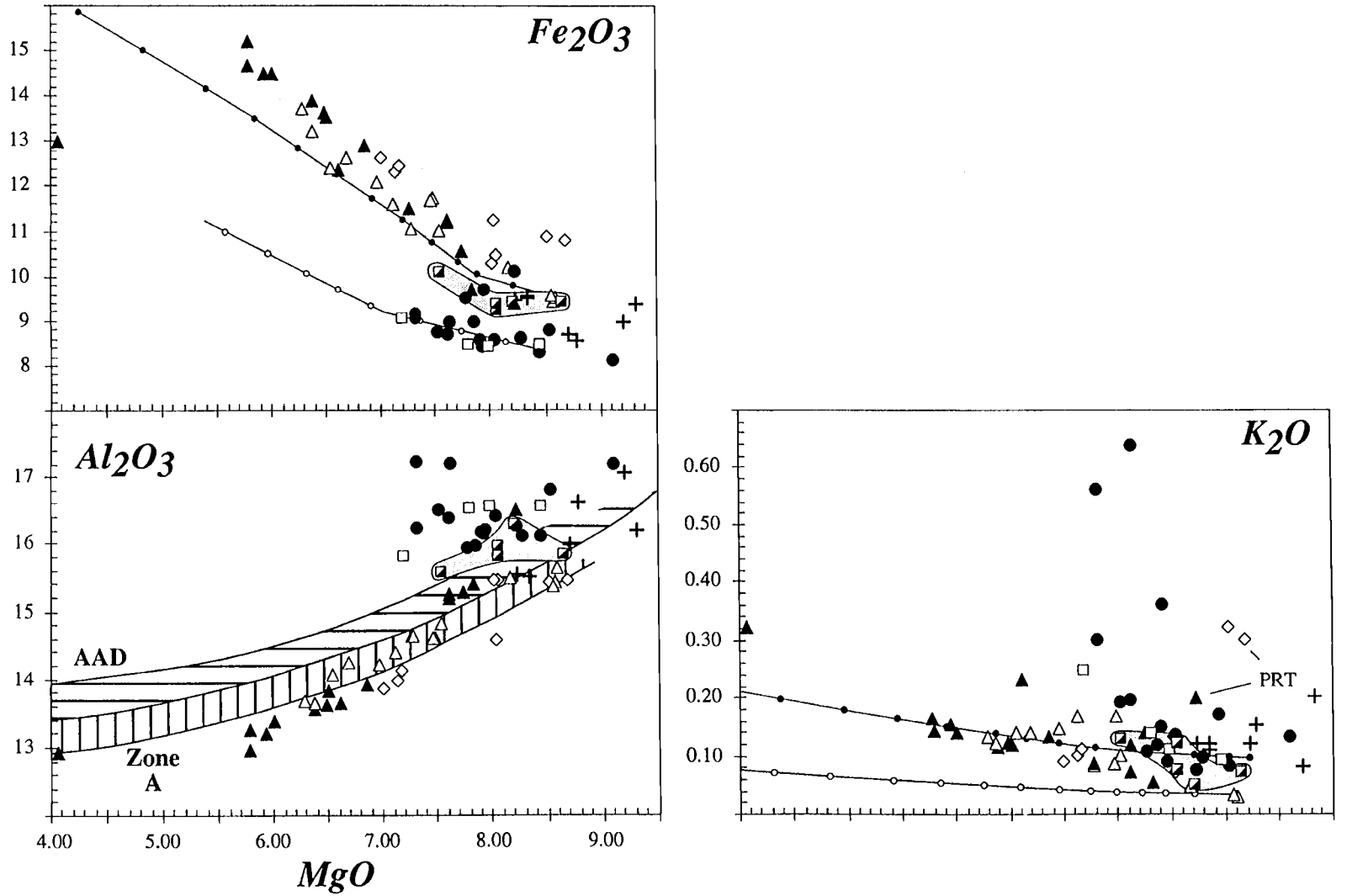

Figure III.4 (continued)

Galapagos spreading center [Christie and Sinton, 1981,1986; Sinton et al., 1983; Perfit and Fornari, 1983] and the East Pacific Rise [Bender et al., 1983; Langmuir et al, 1986]. Intra-dredge compositional variations typically cover a relatively restricted MgO range along this fractionation trend.

Systematic variations in MORB composition occur along the A2 spreading segment away from the 127.5 °E propagating rift tip similar to trends documented along the Galapagos 95° W propagating rift system [Christie and Sinton, 1981; 1986]. Rift tip lavas are relatively unfractionated and variable in major and trace element characteristics (i.e., several compositionally distinct groups). A short distance behind the 127.5° E rift tip (~30 km), extent of fractionation increases to a maximum resulting in the eruption of FeTi (MW12 and MW03) and andesitic basalt types (MW13; Fig. III.3a). Beyond the differentiation maximum, moderately evolved basalts were recovered, possibly reflecting the thermal stabilization of the underlying ridge mantle and the development of a magma system that homogenizes the basalt compositions reaching the spreading axis (e.g., MW01 and MW02) [Christie and Sinton, 1981, 1986].

In contrast to other propagating rift systems (e.g. Galapagos and Juan de Fuca) [Yonover, 1989; Sinton et al., 1983; Hey et al., 1989], the A1 doomed rift lavas cover a considerable fractionation range, nearly as great as that of the A2 propagating rift. In most respects, the low-pressure, fractional crystallization paths of A1 lavas are follow those of A2 lavas, particularly in Fe_2O_3 and TiO_2 content, although subtle differences do occur. Above 6.8 % MgO, A1 basalts tend to be higher in Al_2O_3 while below ~7.5% MgO they are higher in Na_2O and lower in CaO/Al_2O_3 (Fig. III.4). The most primitive A1 lavas (MW17, MgO~8.5 %) are slightly higher in MgO than the most primitive A2 lavas (MW16, MgO~8.3 %) and the most highly evolved A2 compositions are apparently absent from A1, although three locations along A2 recovered these evolved rock types. In addition, compositional variations are not systematic along the A1 segment. Nearly the entire compositional range of A1 lavas is present in a single dredge from the central portion

of this segment (MW17). Furthermore, the proximity of the AAD-A1 transform boundary appears to have little influence on the compositions of erupting lavas [Bender et al., 1984; Langmuir and Bender, 1984]. A broad axial high is maintained along the entire A1 segment and it curves into the AAD-Zone A transform domain.

Major element abundances and fractionation trends of AAD lavas are almost exclusive from those of Zone A. AAD lavas have lower Fe_2O_3, CaO, TiO_2, P_2O_5 and CaO/Al_2O_3, and higher Al_2O_3, Na_2O, and K_2O for any given MgO content. The AAD suite is also more primitive (i.e., most mg# $\leq$ 64), considerably more restricted in their MgO range, and consequently, displays a smaller range in Fe_2O_3 and TiO_2 (Fig. III.4). Conversely, variations in CaO/Al_2O_3, Na_2O and K_2O are significantly greater throughout the AAD, as well as within an individual AAD dredge when compared to Zone A. For example, nearly the entire CaO/Al_2O_3 range (.57-.69) of all AAD lavas is present at dredge site MW27. Furthermore, AAD lavas are among the highest SiO_2 MORB lavas known.

Propagating rift tip lavas of Zone A and B5 axial lavas of the AAD are noteworthy exceptions to the mutually exclusive major element ranges of the Zone A and AAD suites. These lavas are among the most primitive found within Zone A and have Na_2O and CaO/Al_2O_3 contents that overlap the AAD group, although more evolved rift tip lavas approach the Zone A range. The axial lavas from the B5 segment are compositional intermediate between the AAD and Zone A suites in all major element characteristics (Fig. III.4). Off-axis, the B5 composition have no transitional characters and are distinctly AAD-like in their characteristics. In fact, the B5 off-axis lavas cover the largest range in MgO and Fe_2O_3 contents found within the AAD, and therefore, represent the best approximation of a differentiation trend for this group of lavas.

Trace Element Systematics

Rare earth element (REE) abundances of Zone A lavas are remarkably uniform; their chondrite normalized patterns are generally sub-parallel, with total REE abundance

Figure III.5 Chondrite normalized REE patterns for the AAD and Zone A basaltic glass samples. Normalizing values are average ordinary chondrite of Ma et al. [1981].

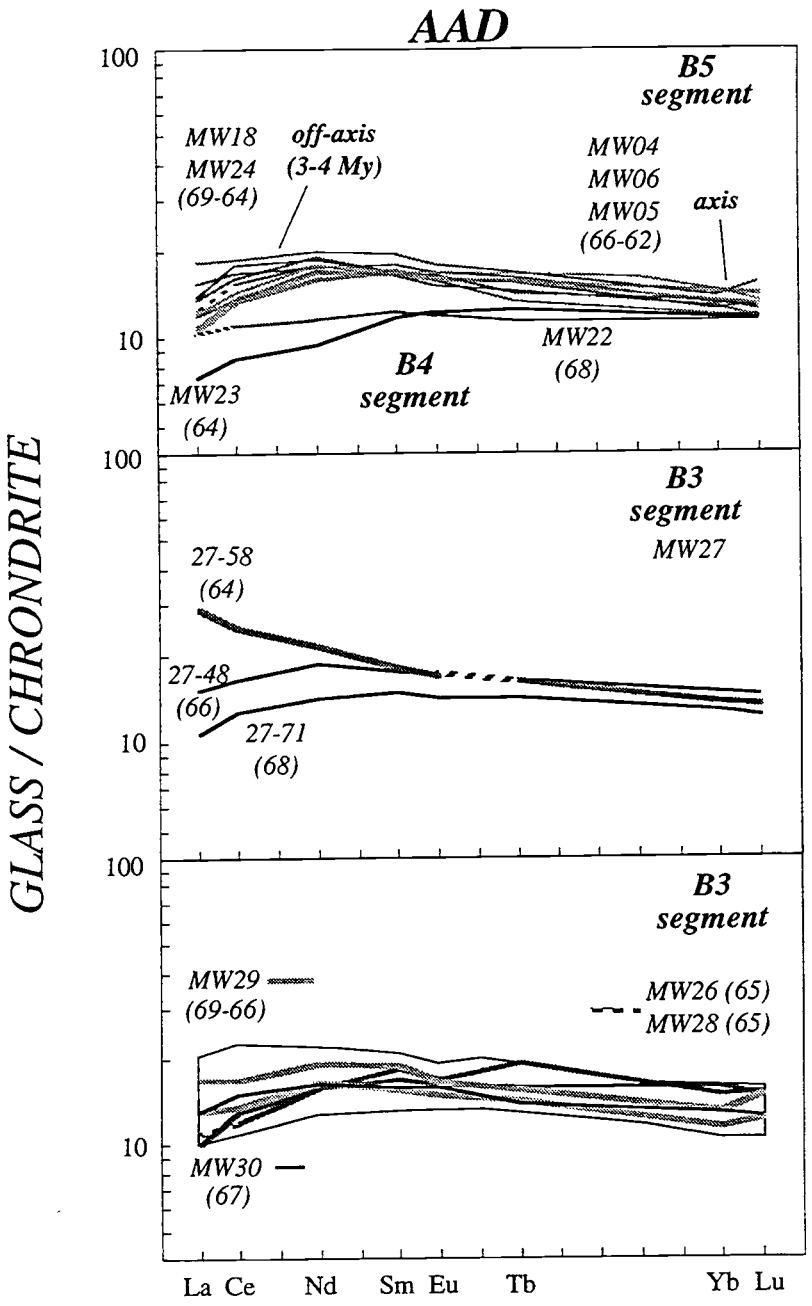
AAD
GLASS / CHRONDRITE
100
10
B5 segment
MW18
MW24
(69-64)
off-axis
(3-4 My)
MW04
MW06
MW05
(66-62)
axis
MW22
(68)
B4 segment
MW23
(64)
B3 segment
MW27
27-58
(64)
27-48
(66)
27-71
(68)
B3 segment
MW29
(69-66)
MW26 (65)
MW28 (65)
MW30
(67)
La Ce Nd Sm Eu Tb Yb Lu

Figure III.5

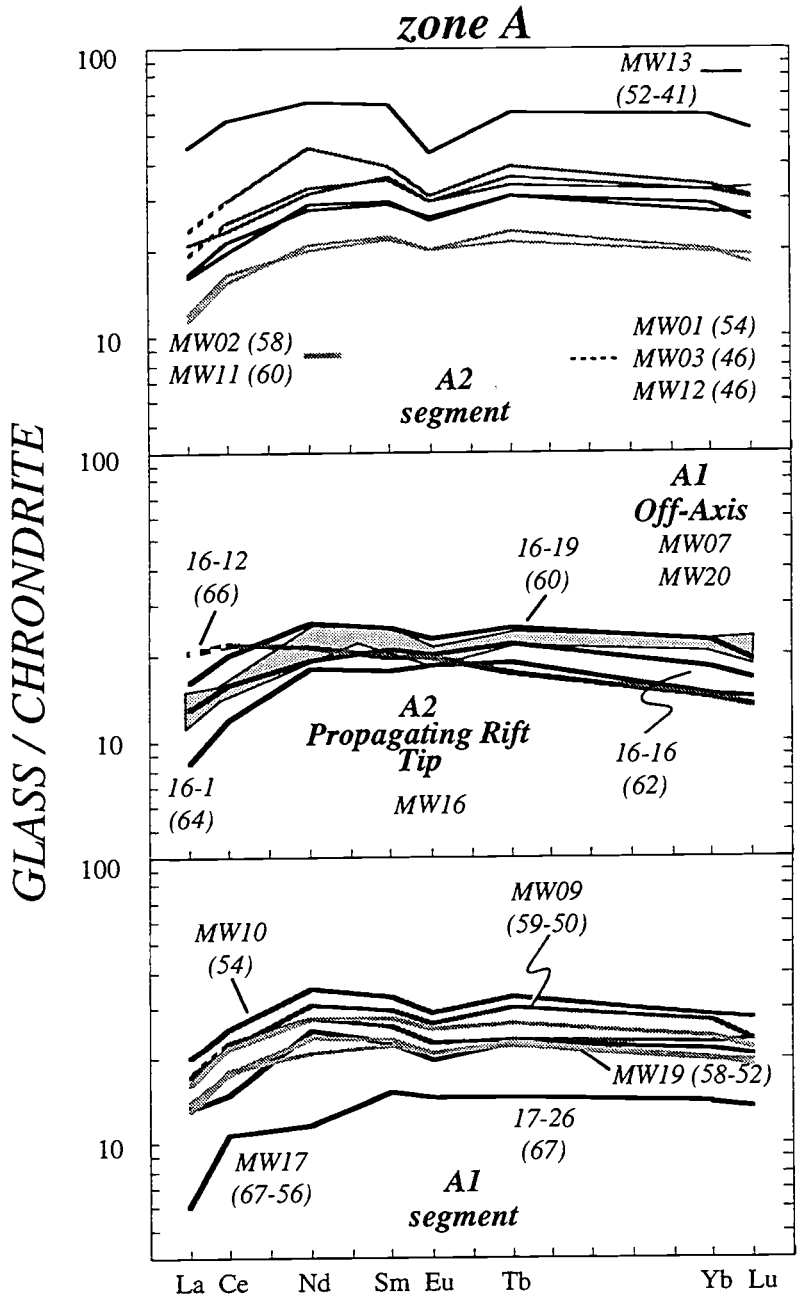

Figure III.5 (continued)

increasing with degree of fractionation. Zone A REE patterns are distinctively convex-up from La to Sm with middle REE values slightly higher than heavy REE values (Fig. III.5). Evolved lavas show Eu depletions that increase with fractionation, reflecting increasing removal of plagioclase. The most primitive Zone A basalts (e.g. MW17 and MW16) lack Eu depletions. The least evolved Zone A composition not recovered at a propagating rift tip (MW17-26) is the only primitive lava with a REE pattern similar to more evolved Zone A basalts. Primitive propagating rift tip lavas (MW16-12 and V1) have light REE enriched patterns that cross cut more typical Zone A patterns. These rift tip lavas are the same ones with high Na_2O and low CaO/Al_2O_3 contents that overlap AAD compositions. In addition, both light REE depleted and enriched patterns (La_n/Sm_n of .50 and 1.06, respectively; 'n' denotes chondrite normalized) can be found at the propagating rift tip, although the isotopic characteristics of these lavas are indistinguishable [Pyle et al., 1992]. Despite the distinctive REE systematics of the propagating rift tip lavas, depletion of La relative to Ce is universal feature of Zone A lavas, and by inference, their mantle source.

AAD lavas are typically lower in total REE content than most Zone A basalts and total REE abundance appears unrelated to degree of fractionation. Crossing REE patterns are frequently observed within and between AAD spreading segments, unlike the uniform and sub-parallel REE patterns displayed by normal Zone A lavas (i.e., away from propagating rift tips). Like Zone A, AAD lavas are commonly light REE depleted, but differ in their flat to slightly convex-up curvature between La and Sm and in their consistently lower heavy REE contents. The B4 lavas have the most light REE depleted patterns and the lowest total REE abundances, but these lavas are not the most primitive AAD composition.

Zone A and the AAD lavas distinct in the abundance and diversity with other trace elements as well (Fig. III.6). Concentrations of some highly incompatible elements, such as Ba and Th, are generally higher within the AAD, but La shows no distinctive characteristics. Moderately incompatible elements such as Zr, Yb, and Y are consistently higher in Zone A and display a greater range in variability than AAD lavas. Compatible

Figure III.6 Along-axis variations of selected highly incompatible, moderately incompatible, and compatible trace element abundances.

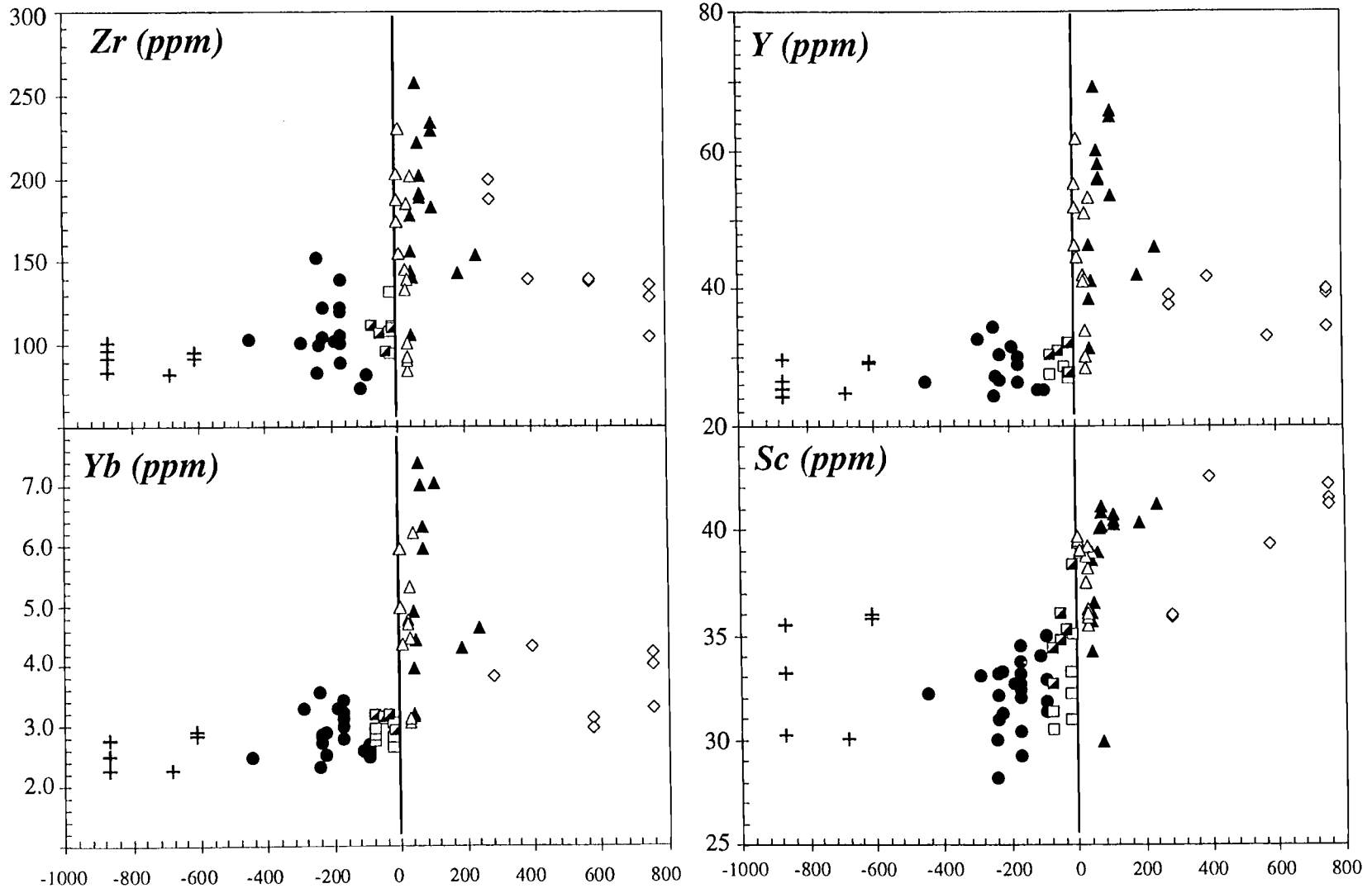
Zr (ppm)
Y (ppm)
Yb (ppm)
Sc (ppm)
300
250
200
150
100
80
60
40
20
7.0
6.0
5.0
4.0
3.0
2.0
40
35
30
25
-1000
-800
-600
-400
-200
0
200
400
600
800

Figure III.6

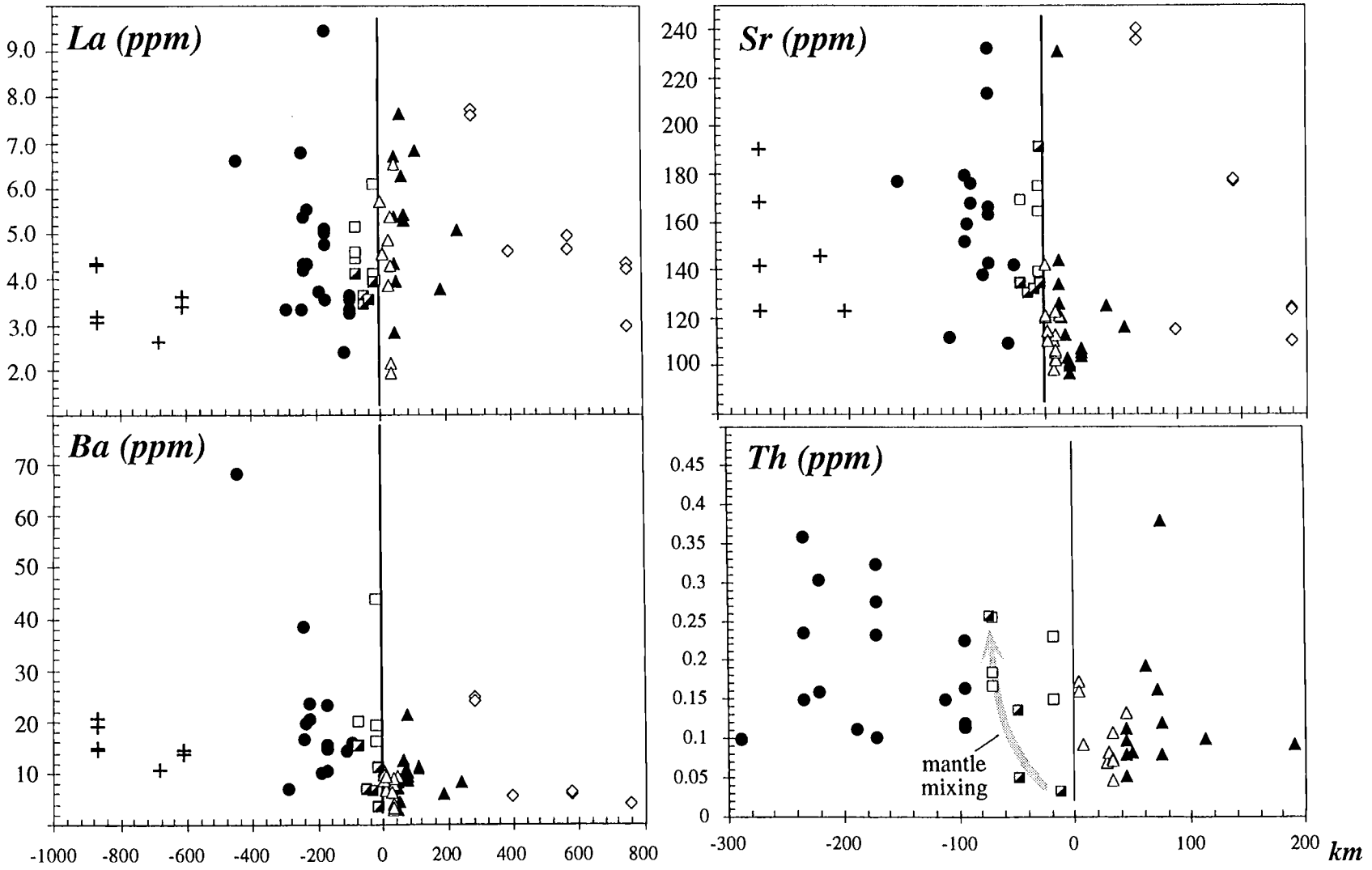

Figure III.6 (continued)

elements, such as Sc, are consistently higher in Zone A. The diversity of Sc is also higher in AAD lavas, but Cr is more variable in Zone A. These chemically coherent sets of trace element appear to show conflicting behavior between the AAD and Zone A MORB suites.

DISCUSSION

The Global Context

An incredible difference in the major element, trace element and isotopic composition exists between the AAD and Zone A MORB suites. These compositional contrasts are closely related to axial depth and axial morphology. Klein and Langmuir [1987] recognized a correlation between MORB major element composition and spreading axis depth on a global scale which they attributed to variations in mantle temperature. Mantle temperatures are estimated to decrease by approximately 100° C between Zone A and the AAD [Forsyth, 1993; West et al., 1994]. Since spreading rate is uniform throughout this region, mantle temperature controls melt production and mantle upwelling beneath Zone A and the AAD. Melt production and differentiation has resulted in two very distinct MORB suites. The geochemical contrasts between Zone A and the AAD suggest that mantle is processed through these two mantle temperature regimes very differently.

Mantle temperature dictates the pressure at which upwelling mantle intersects the solidus [Klein and Langmuir, 1987; McKenzie and Bickle, 1988], and therefore, the pressure interval over which melting occurs (i.e., the height of the melting column). The amount of melt extracted from the melting column during upwelling controls the bulk composition of MORB lavas [Klein and Langmuir, 1987; 1989; Plank and Langmuir, 1992]. As the height of the melting column increases with mantle temperature, melting increases, the thickness of oceanic crust increases, the density of the mantle residue decreases , and axial depth decreases [Oxburgh and Parmentier, 1977; Klein and Langmuir, 1987; 1989; McKenzie and Bickle, 1988; Langmuir et al., 1993].

To facilitate global comparisons of MORB compositions, Klein and Langmuir [1987; 1989] introduced low-pressure, fractionation corrected Na_2O ($Na_{8.0}$) and FeO_t ($Fe_{8.0}$)

parameters (i.e., Na_2O and FeO back calculated to an MgO content of 8.0 wt. %). $Na_{8.0}$ and $Fe_{8.0}$ proxy for degree of melting and mean depth of melting, respectively [Klein and Langmuir, 1987; 1989]. Compared to Zone A, and MORB in general, AAD lavas are high in Na_2O, high in SiO_2, and low in FeO. In addition, axial depth variations between the AAD and Zone A spreading segments (3000 m-4800 m) cover a considerable range of the total variation in MOR depths. As a result, the AAD and Zone A compositions cover nearly two-thirds of the global variation in $Na_{8.0}$ and $Fe_{8.0}$ (Fig. III.7).

Within Zone A, there is a regular increase in $Na_{8.0}$ and decrease in $Fe_{8.0}$ as depth increases from segment A2 to segment A1. A similar $Na_{8.0}$-$Fe_{8.0}$ trend is lacking in AAD lavas, but the few AAD lavas that show a negative, $Na_{8.0}$-$Fe_{8.0}$ 'global trend', are higher in $Na_{8.0}$ for any given $Fe_{8.0}$ value. The regional increase in $Na_{8.0}$ and decrease in $Fe_{8.0}$ from segment A2 through segment B3, suggests a regional decrease in the degree of melting (high $Na_{8.0}$) and decrease in the mean depth of melting (high $Fe_{8.0}$) toward the AAD. By inference, the major element systematics imply a progressive decrease in the height of the melting column (i.e., a decrease in the pressure interval over which mantle melting occurs), as a result of a progressive decrease in mantle temperature from Zone A to the AAD.

Zone A propagating rift lavas define a positive $Na_{8.0}$-$Fe_{8.0}$ correlations that are nearly orthogonal to the 'global' trend, resembling 'local' trends observed in many Mid-Atlantic Ridge MORB suites but absent from East Pacific Rise MORB [Batiza et al., 1988; Klein and Langmuir, 1989; Niu and Batiza, 1991]. 'Local-trend' systematics also dominate the AAD $Na_{8.0}$-$Fe_{8.0}$ relationships, particularly within segment B3. These 'local' trends have been interpreted as resulting from incomplete aggregation of melt produced in the mantle melting column and extraction of these melts from various depths within the melt column [Klein and Langmuir, 1989]. A component of high-pressure crystal fractionation may also contribute to the 'local trends' [Kinzler and Grove, 1991]. Since propagating rift tip and AAD lavas show similar $Na_{8.0}$ - $Fe_{8.0}$ "local-trend" correlations, melt extraction in these

Figure III.7 Variations of $Na_{8.0}$ versus $Fe_{8.0}$ and $Ti_{8.0}$ for AAD and Zone A lavas. Fractionation corrections of Na_20 to 8.0% MgO are calculated using the method of Plank and Langmuir [1992]. Fractionation corrections for Fe_2O_3 are based on a regression of the Zone A and AAD glass compositions with > 8.0% MgO presented in the paper (see Fig. III.4). The resulting fractionation corrections are $Fe_{8.0}=Fe_2O_3+1.923$ * (MgO-8.0) for the Zone A suite and $Fe_{8.0}=Fe_2O_3+0.691$ * (MgO-8.0) for the AAD suite. The $Fe_{8.0}$ formulations outlined here do not modify the interpretations obtained using conventional corrections slopes of m=1.664 for Zone A and m=.924 for AAD (note .924 is the mid-Cayman Rise regression and should be appropriate for the AAD suite) [Klein and Langmuir, 1989]. However, the conventional fractionation corrections increase the scatter on the diagram and amplify "local-trend" relationships. $Ti_{8.0}$ values are calculated using conventional algorithms. No corrections have been applied to samples with greater than 8.0% MgO.

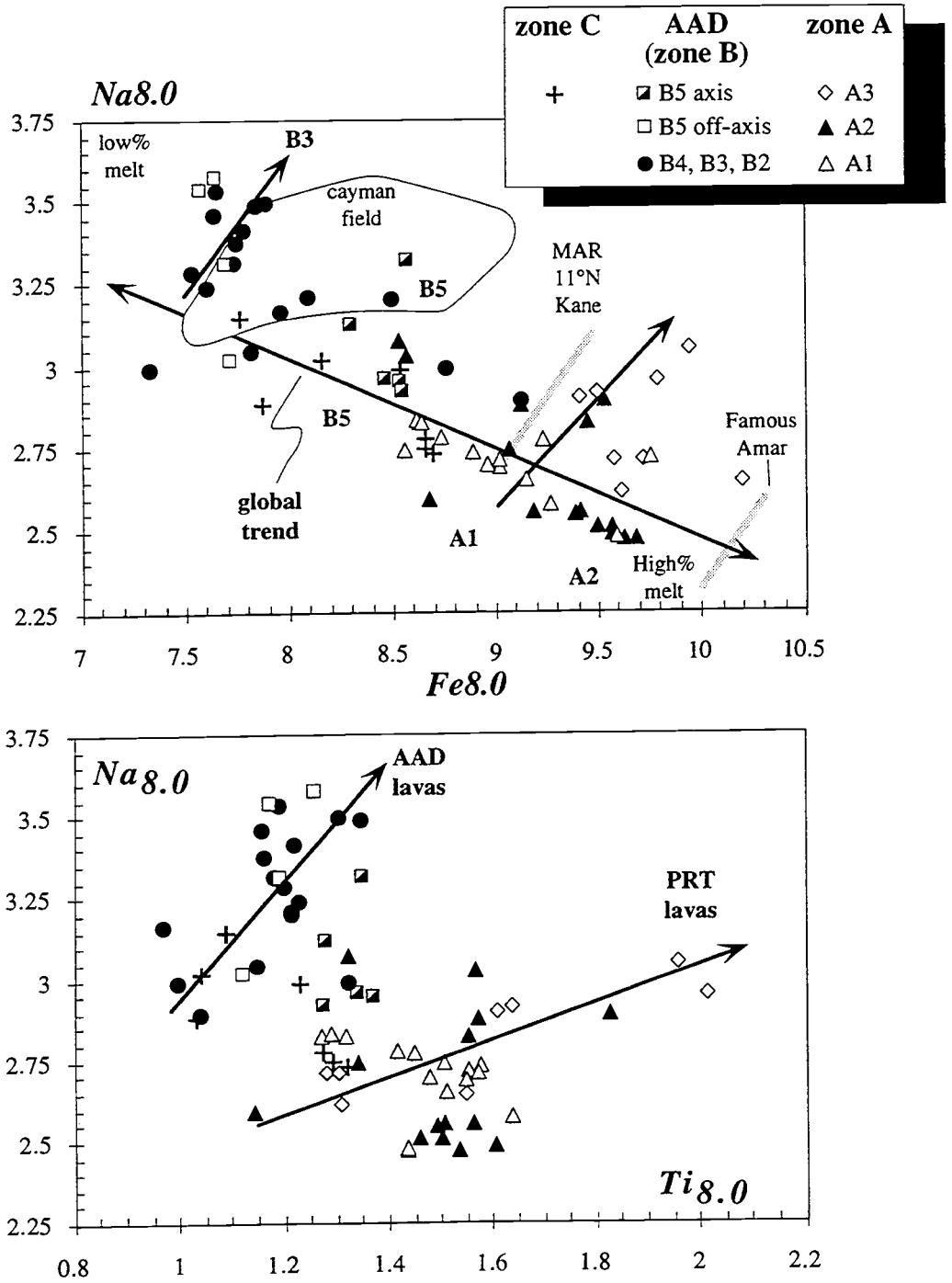
zone C
AAD (zone B)
zone A
+
B5 axis
B5 off-axis
B4, B3, B2
A3
A2
A1
Na8.0
low% melt
B3
cayman field
B5
MAR 11°N Kane
B5
global trend
A1
A2
Famous Amar
High% melt
Fe8.0
AAD lavas
PRT lavas
Ti8.0

Figure III.7

environments appears to be similar. Melts are generated and quickly erupt to the surface without encountering melts from other parts of the melting column. The variety in REE patterns for lavas from these environments supports this conclusion.

Niu and Batiza [1991] extended the fractionation correction concept to other major elements and derived formulations to quantify MORB composition to physical parameters controlling melt generation within the mantle. Applying these formulations to the AAD and Zone A data, the relative differences in the melt regimes can be assessed (Table III.7). Melts within the AAD melting column traverses a more restricted pressure interval, although the final pressure of equilibration is higher and the mean pressure of melting is lower than for Zone A melts. Zone A melts are generated over a much greater depth interval, with the final pressure of equilibration being lower and the mean pressure of melting being higher than that of the AAD. The values of P_o appear to be a fairly good estimate of the base of the melt column, however, the high final melt pressures (P_f) seem unusually high, possibly an artifact of the decompression melting model. The high P_f estimates might imply that decompression melting of a single mantle source composition does not occur within an individual melting column, particularly if the melting column spans a considerable pressure range.

Table III.7

	$Na_{8.0}$	$Fe_{8.0}$	$Si_{8.0}$	$Ca_{8.0}$	$Al_{8.0}$	P_o (kb)	P_f (kb)	F (%)	T_o (C°)	T_f (C°)
Zone A	2.75	10.5	49.5	11.5	15.2	20.4	14.0	16.7	1413	1291
AAD	3.50	8.5	51.0	10.5	16.2	9.7	8.2	11.2	1283	1225

Estimated $X_{8.0}$ values have been visually determined (not calculated) from MgO variation diagrams (Fig.III.4) and represent an 'average' composition for each region at ~8.0% MgO. The actual values depend on several assumptions including the experiments used to parameterize the model (Niu and Batiza, 1991) and the starting mantle composition (in this case MPY-40; Falloon et al., 1987). The relative differences are much more important than the actual values.

Parental Melts and Differentiation

Direct comparison of primitive MORB compositions is the rationale behind correcting MORB to an 'unfractionated' MgO value of 8.0 %. The identification Zone A and AAD primary or parental melts, and their differentiation trends is useful for understanding the melting processes leading to their formation. Glasses with greater than 8.0 % MgO were recovered from both the AAD and Zone A allowing a straight forward comparison of primitive melt characteristics within each region. A modified version of the one atmosphere fractionation model of Nielsen [1985] (Fig. III.4) and the pseudoternary projection of Grove et al.[1992] (Fig. III.8) have been used to evaluate potential parental melts and fractionation histories.

The primitive nature of the AAD MORB suite as a whole, suggests that only olivine removal has affected their compositions. Several AAD glasses could be considered parental but no evidence exists to suggest one parent is common to the entire AAD suite. The diversity of the AAD lavas cannot have been produced by any conceivable low pressure fractionation trend, as is clear from large variations in CaO/Al_2O_3 and Na_2O at constant MgO values and a wide array of AAD REE patterns. Projection from plagioclase suggests that AAD lavas last equilibrated between 2-6 kb in the mantle, never reaching a low pressure ol-pl-cpx cotectic (Fig. III.8). Position within the plagioclase projection is unrelated to mg#, suggesting that high pressure fractionation is not a significant process in the differentiation of AAD lavas, although a limited influence can not be entirely ruled out for samples from dredge MW18.

Variations in CaO/Al_2O_3 between .70 and .80 over a wide range in MgO, and the sub-parallel REE patterns of Zone A lavas, indicate low-pressure fractionation is a major factor in the differentiation of this MORB suite. Several high-MgO, zone A glasses were evaluated as possible parental melts, although none of these 'parental' compositions satisfy all of the major element variations by one-atmosphere fractional crystallization modelling (Fig. III.4). MW17-26 is the most likely high-MgO parent since its REE patterns most

closely resemble those of more evolved zone A lavas. The modelled one atmosphere fractionation path of MW17-26 predicts slightly lower Fe_2O_3 and TiO_2, and considerably higher Na_2O and SiO_2 than is observed in evolved Zone A lavas. High Na_2O and low CaO/Al_2O_3 is a persistent problem if primitive Zone A are indeed parental to more evolved Zone A compositions. Similar discrepancies between predicted fractionation trends of primitive zone A lavas and their evolved counterparts are observed irrespective of the low pressure fractionation model (e.g., Nielsen [1985], Weaver and Langmuir [1990]) This is somewhat unexpected given the coherent, 'low' pressure fractionation appearance of the major element data and the REE pattern similarities between MW17-26 and evolved Zone A basalts.

If only Zone A data with <7.5% MgO are considered, one atmosphere trends would suggest that these lavas are derived from a parent(s) lower in Na_2O, and possibly SiO_2, and higher in CaO/Al_2O_3 than any of the primitive lavas in our data set. The failure to reproduce the Zone A trends by one atmosphere fractionation may be partially related to a poorly tuned set of major element partition coefficients for this suite of basalts [Langmuir et al., 1993]. MORB differentiation is sensitive to bulk composition [Kinzler and Grove, 1992; Longi and Pan, 1988; Longi, 1989] and constraining the one atmosphere fractionation trends for primitive Zone A samples requires low pressure experiments which have not been completed. Alternatively, the evolved Zone A lavas may have been produced from the primitive Zone A lavas by fractionated at slightly elevated pressures [Grove et al., 1993].

Calculated ol-plag-cpx cotectics for different pressures are shown in Figure III. 8. The Zone A data are offset from a one atmosphere cotectic to pressures of 1-2 kb using the parameters outlined by Grove et al. [1993] for plagioclase lherzolite. The propagating rift lavas are shifted toward a slightly higher pressure ol-pl-cpx cotectic (~3-4 kb). To check these calculated cotectics, experimentally produced, one atmosphere glass compositions

Figure III.8 Projection of AAD and zone A glasses compositions within the ol-cpx-plag-q pseudoternary using the projection parameters outline in Grove et al., [1992]. The microprobe chemical groups are used for these projections (Tables III.2 and III.3). The shaded field on these projections shows one atmosphere, experimentally produced glass compositions representing several MORB suites (note: not all of the glass data used to construct this field are multiply saturated) [Walker et al., 1979; Juster et al., 1989; Grove et al., 1990; Grove and Juster, 1989; Tormey et al., 1987; Grove and Byran, 1983]. The experimental field roughly parallel the zone A data trend, although shifted away from the ol apex. The calculated cotectics and the raw experimental data indicate slightly elevated pressures of fractionation for Zone A lavas. Small open circle are the probe data of Klein et al. [1991] from the AAD, Zone A and Zone C. Chemical group MW23 is designated because it plots near a 4 phase saturated melting point suggesting it might be a primary melt. The low mg# (i.e., 64) for MW23 suggests it is not a primary composition.

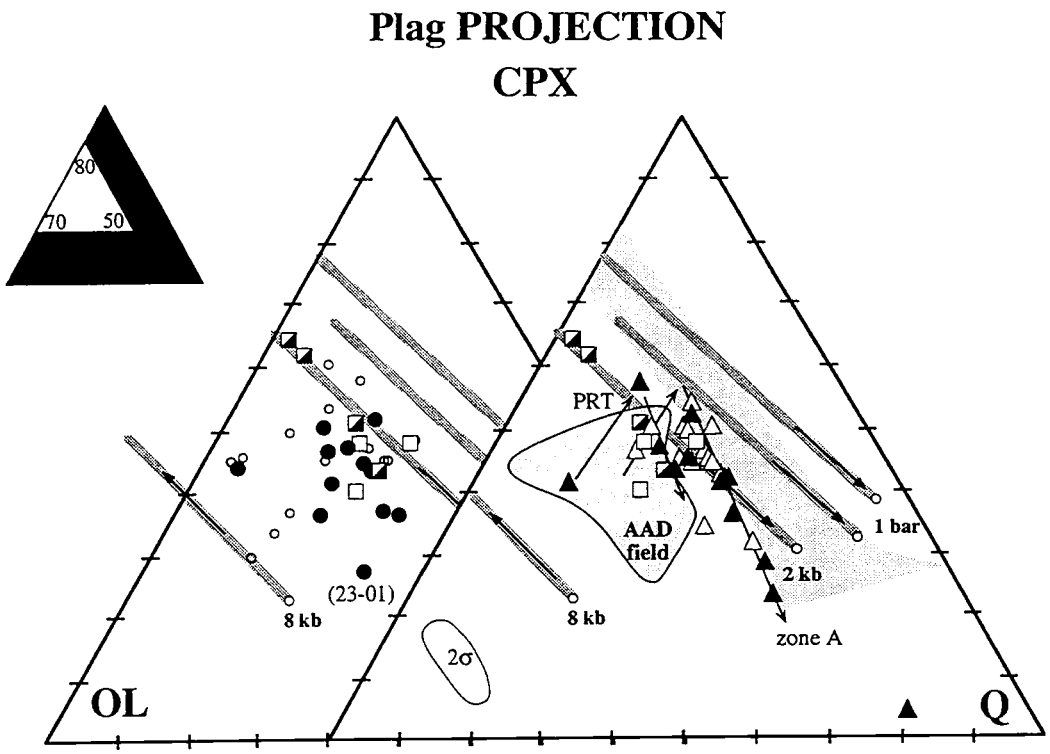
Plag PROJECTION
CPX
80
70
50
PRT
AAD
field
1 bar
2 kb
zone A
(23-01)
8 kb
8 kb
2σ
OL
Q

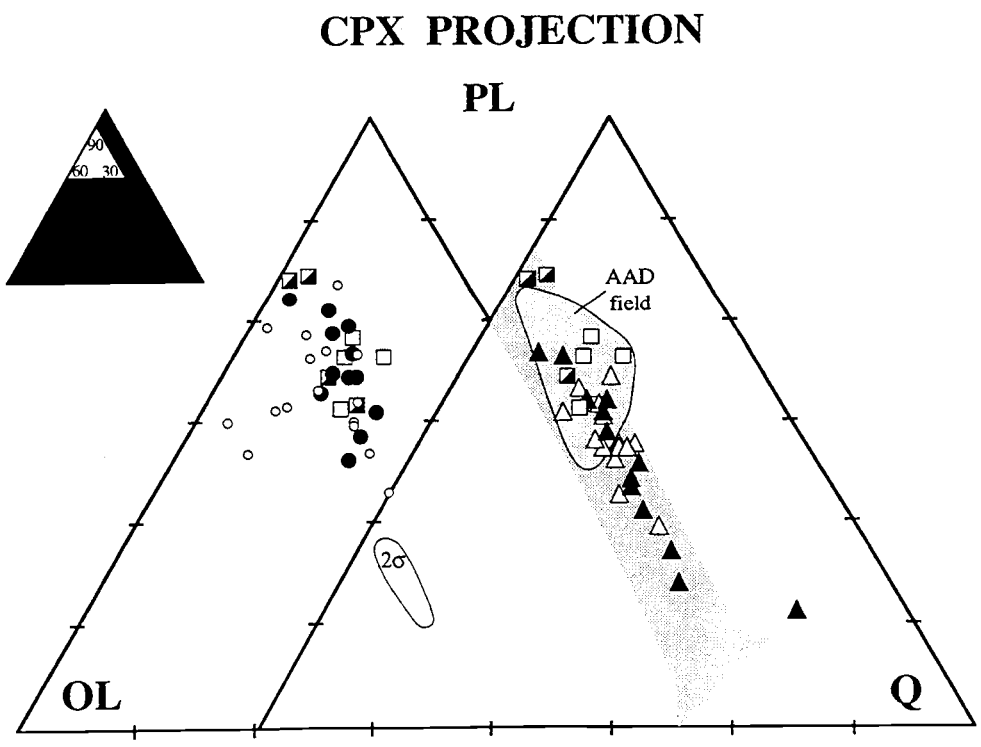
CPX PROJECTION
PL
90
60
30
AAD
field
2σ
OL
Q

Figure III.8

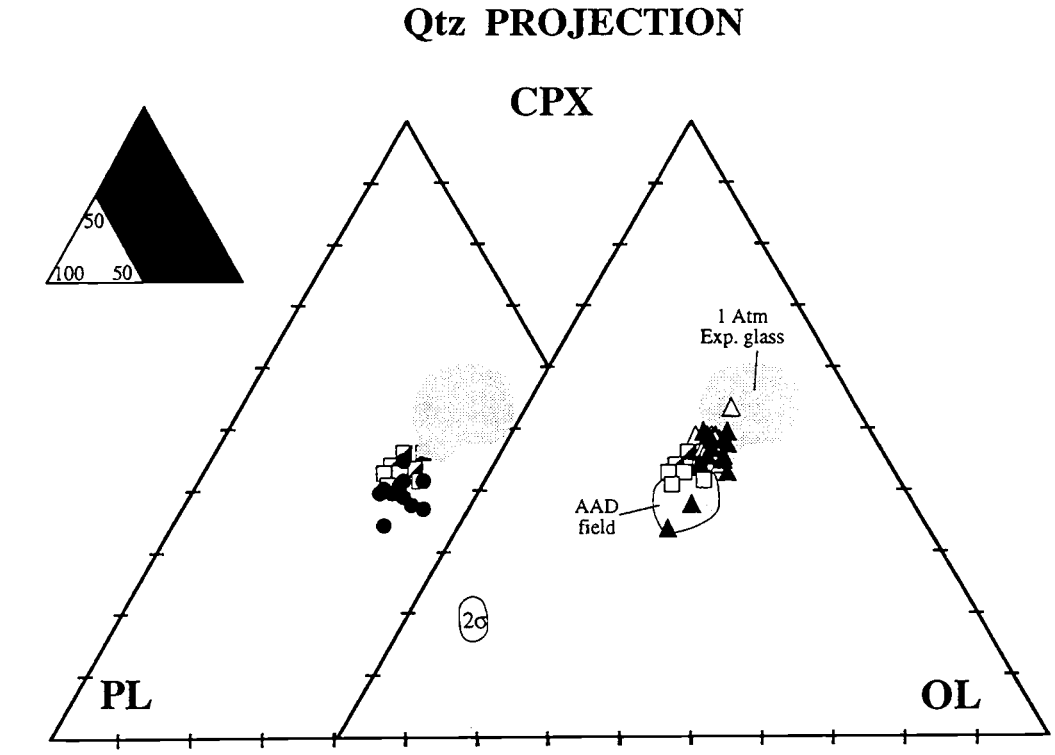

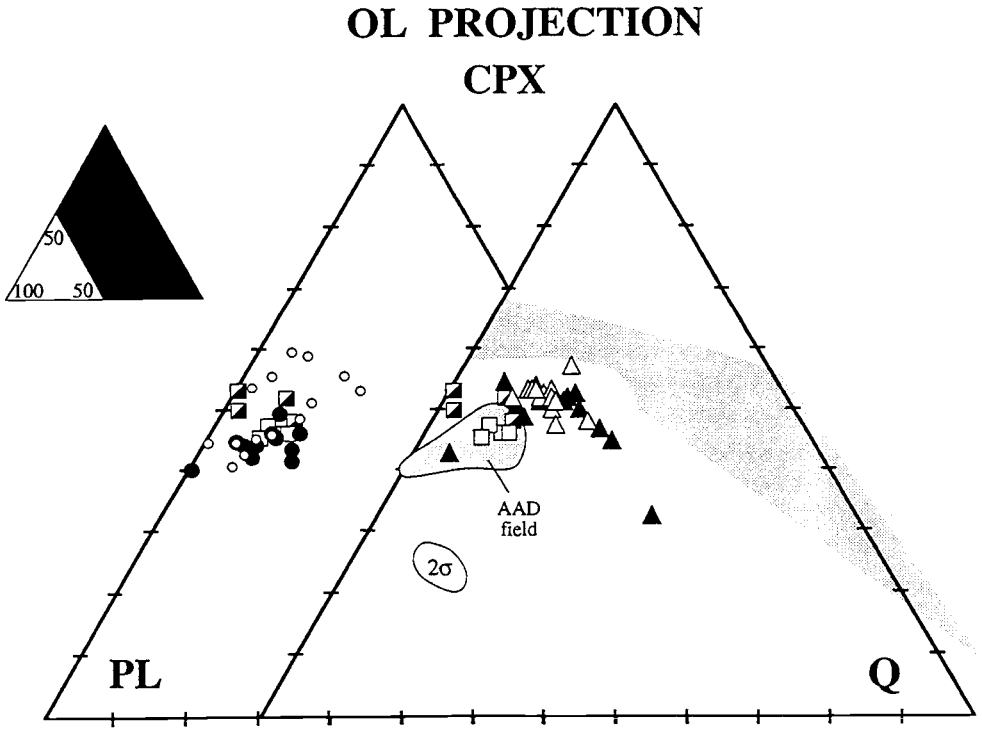

Figure III.8 (continued)

from several studies are shown by a gray shaded field. Comparison of the Zone A glass data with calculated cotectics and experimental data trends seems to indicate that the fractionation for Zone A lavas occur elevated pressures, in the range of 1-2 kb.

An unexpected trend toward increasing pressure with fractionation is shown by the Zone A data, cross-cutting the calculated ol-pl-cpx cotectics (note that the experimental data show a similar cross cutting trend). From these projections and cotectics we infer that the highly evolved FeTi basalts and andesites of the AAD differentiate at pressures greater than 2 kb, equivalent to the base of 6 km crust. Whether andesitic and FeTi basalts are actually derived from pressures greater than 2 kb or whether the cotectic calculation is not calibrated to this suite of samples is not clear. Qualitatively, the Zone A lavas have differentiated at 'low' pressure and the propagating rift samples appear to define a slightly higher pressure ol-pl-cpx cotectic. The models do not permit better constraints.

Melting and Morphology

The differences between the AAD and Zone A are similar in magnitude to those that exist between the Mid-Atlantic Ridge and the East Pacific Rise. Since contrasts between the AAD and Zone A occur at a uniform spreading rate, the composition of basalts and the morphology of the spreading axis must directly reflect differences in magma supply caused by differences in mantle temperature.

The propagating rift lavas of Zone A are low in CaO/Al_2O_3, high in Na_2O, and have enriched incompatible element contents, closely comparable to those of AAD lavas and distinct from the rest of Zone A. Propagating rift tips are commonly expressed as axial deeps ahead of the more mature sections of the spreading axis, reflecting decreased melt supply. On a very local scale, melting conditions beneath the rift tip may be broadly equivalent to the conditions beneath the more extensive axial valleys of the AAD, reflecting melt generation within relatively cool mantle.

Of the AAD spreading segment surveyed, the B4 segment is unusual. The chaotic seafloor morphology (see previous description) strongly suggests that the spreading "axis"

is ephemeral and not a steady-state feature. Relative to lavas from other AAD segments, B4 lavas are lower in TiO_2, Na_2O, K_2O, and P_2O_5, and they are distinctly light REE depleted. These chemical characteristics suggest that B4 lavas are derived by greater extents melting of a homogeneous AAD mantle and/or from a more depleted part of a heterogeneous mantle. Morphologic evidence, especially the occurrence of volcanic ridges perpendicular to the spreading axis, suggests localized and intermittent eruptions of large magma volumes. Thus, accretion along segment B4 appears to be dominated by intermittent eruption of high-degree melts.

The transition from the high magma supply regime of Zone A to the low magma supply regime of the AAD is reflected by the abrupt increase in axial depth and the development of an axial valley along the B5 spreading axis. Similarly, axial lavas from Zone B5 are transitional between those of Zone A and those of the AAD in almost every geochemical parameter. Off-axis, B5 lavas do not show these transitional characteristics, suggesting that the underlying mantle has evolved toward Zone A-like conditions over the last 4 m.y. For instance, B5 axial lavas have the lower La_n/Sm_n and higher heavy REE contents typical of Zone A lavas, but B5 off-axis lavas have the higher La_n/Sm_n and lower heavy REE contents typical of other AAD lavas (Fig. III.5). The isotopic systematics of the B5 lavas record a change from an 'Indian' mantle source (off-axis) to a 'Pacific' mantle source (axis) [Pyle et al., 1992] suggesting the rare earth element contrasts between off-axis and axis compositions may be partially related to a change in mantle source. In some instances, trace element variations within the AAD can be correlated to isotopic variability, however, systematic major element variations occur with changes in seafloor morphology. Detailed bathymetric coverage is incomplete, but it appears that the seafloor terrain near the off-axis dredge sites more closely resembles the chaotic terrain of Zone B4 than the organized, ridge parallel morphology closer to the present B5 spreading axis. These contrasts in morphology, coupled with the compositional changes, strongly imply an evolution of in the underlying mantle thermal regime beneath the B5 spreading segment

over the last 4 m.y. These differences are consistent with a relative increase in the amount of melt being delivered to the B5 spreading axis during this same period.

Upper Mantle Sources

To understand how melting is influencing compositional differences between Zone A and the AAD, chemical signatures inherent in the isotopically defined Pacific and Indian Ocean upper mantle reservoirs must be evaluated. Klein et al. [1991] noted a correlation between high Ba/K ratios and the 'Indian' Ocean upper mantle isotopic signature. Similar correlations exist for Ba/Zr, Ba/La, Th/La, and other ratios of highly or moderately incompatible elements involving Ba or Th (Fig. III.9). These ratios coincide exactly with the transition between Indian Ocean and Pacific Ocean upper mantle isotopic signatures within segment B5, both along-axis and off-axis. These correlations do not, however, imply that high Ba/Zr, Ba/La etc are unique or definitive of "Indian-type" mantle as defined isotopically. Lavas from the Zone A propagating rift tips also have high Ba/Zr and Ba/La ratios overlapping values found within the AAD. These trace element ratios should reflect the trace element signature of the mantle source even at low degrees of melting. The similarity of AAD and Zone A propagating rift tip lavas in these trace element ratios strongly suggests that a common mantle component is present beneath both regions, differing only in its time integrated Sr, Nd, and Pb isotope systematics.

Partial melting and low pressure fractionation trends can be distinguished using variations of Ce_n/Yb_n with Ce_n (Fig.III.10a). In Figure III.10a, low degree melts from Zone A propagating rift tips have high Ce_n/Yb_n ratios at high $(Ce)_n$ contents that are identical to low degree melts from the AAD. At the other extreme, high degree melts from the AAD (MW27-71 and MW23-1) and Zone A (MW17-13) have Ce_n/Yb_n ratios (.69 and .73) and low Ce_n values (8.4 and 10.5) that overlap. Therefore, lavas from both the AAD and Zone A lie along the same partial melting trend defined by increasing Ce_n/Yb_n ratios with increasing Ce_n values. These melting systematics suggest mantle sources with similar REE characteristics. Zone A lavas that have experienced shallow fractionation retain the

Figure. III.9 Along-axis variations in incompatible element ratios. Ba/La, Th/La, and Ba/Zr ratios closely follow the isotopic boundary, but the Zone A propagating rift tip lavas invariably overlap with the AAD data. The transitional lavas erupted at the B5 spreading axis are enclosed in a gray field. These trace element relationships indicate that the AAD and Zone A lavas tap a very similar mantle source that differs only in its Sr, Nd, and Pb isotopic composition.

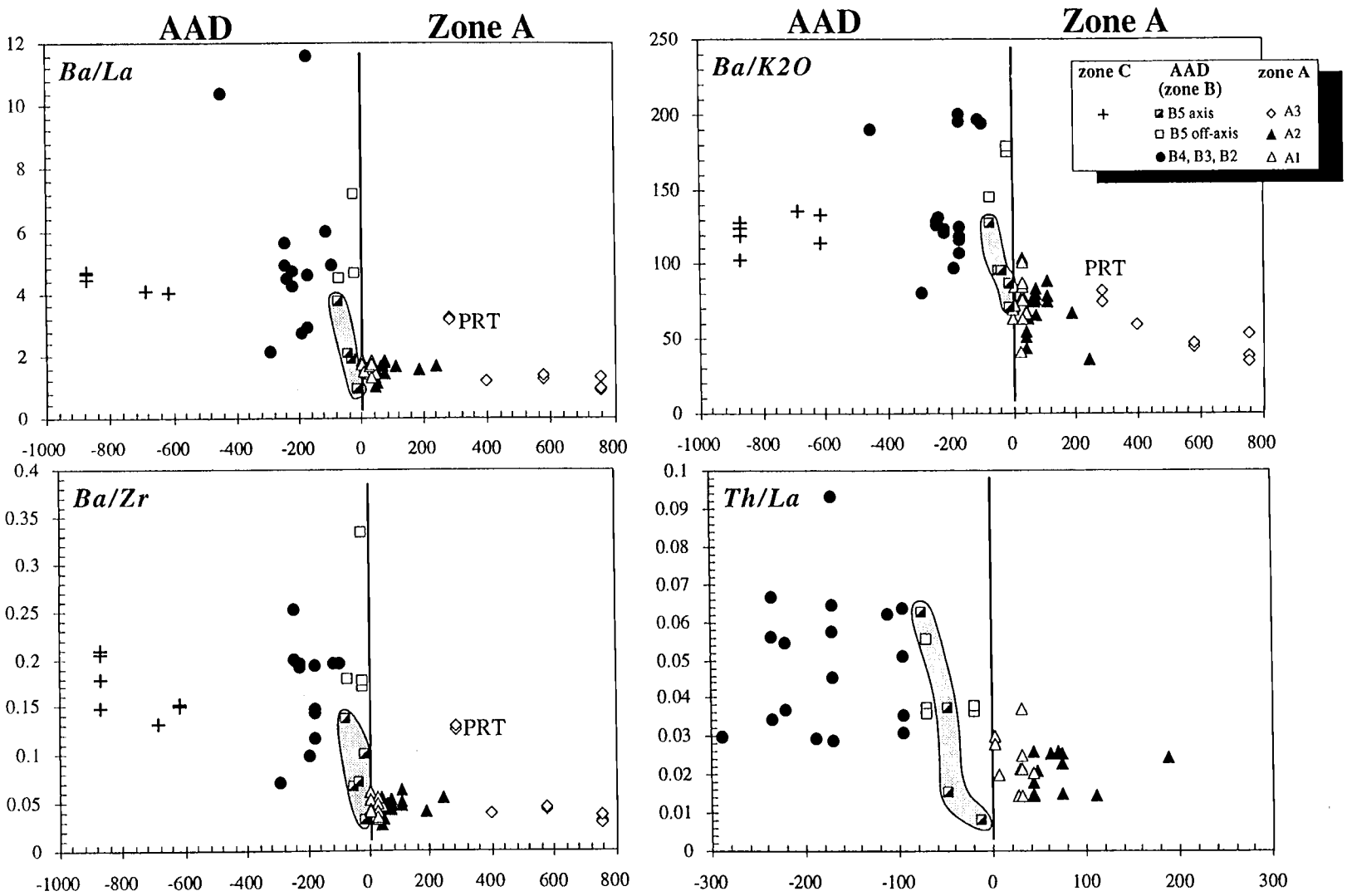
AAD
Zone A
Ba/La
PRT
AAD
Zone A
Ba/K2O
zone C
AAD (zone B)
zone A
B5 axis
B5 off-axis
B4, B3, B2
A3
A2
A1
PRT
Ba/Zr
PRT
Th/La

Figure III.9

Figure III.10 a) Ce_n/Yb_n - Ce_n diagram showing that the AAD lavas and the Zone A propagating rift lavas define a trend consistent with variations in partial melting. Other Zone A lavas show considerable variations in Ce_n but very little variation in Ce_n/Yb_n values. The low trajectory Zone A trend is indicative of low pressure differentiation which results in increasing total REE concentration but little fractionation the light rare earth elements from the heavy rare earth elements (i.e., small Ce_n/Yb_n variations). b) Zr/Y - Zr diagram illustrating source, partial melting, and differentiation characteristics of AAD and Zone A. The AAD MORB suite is dominated by partial melting, whereas the Zone A MORB suite is dominated by low pressure fractional crystallization. The arrows indicate general trends and are not regressed through the data.

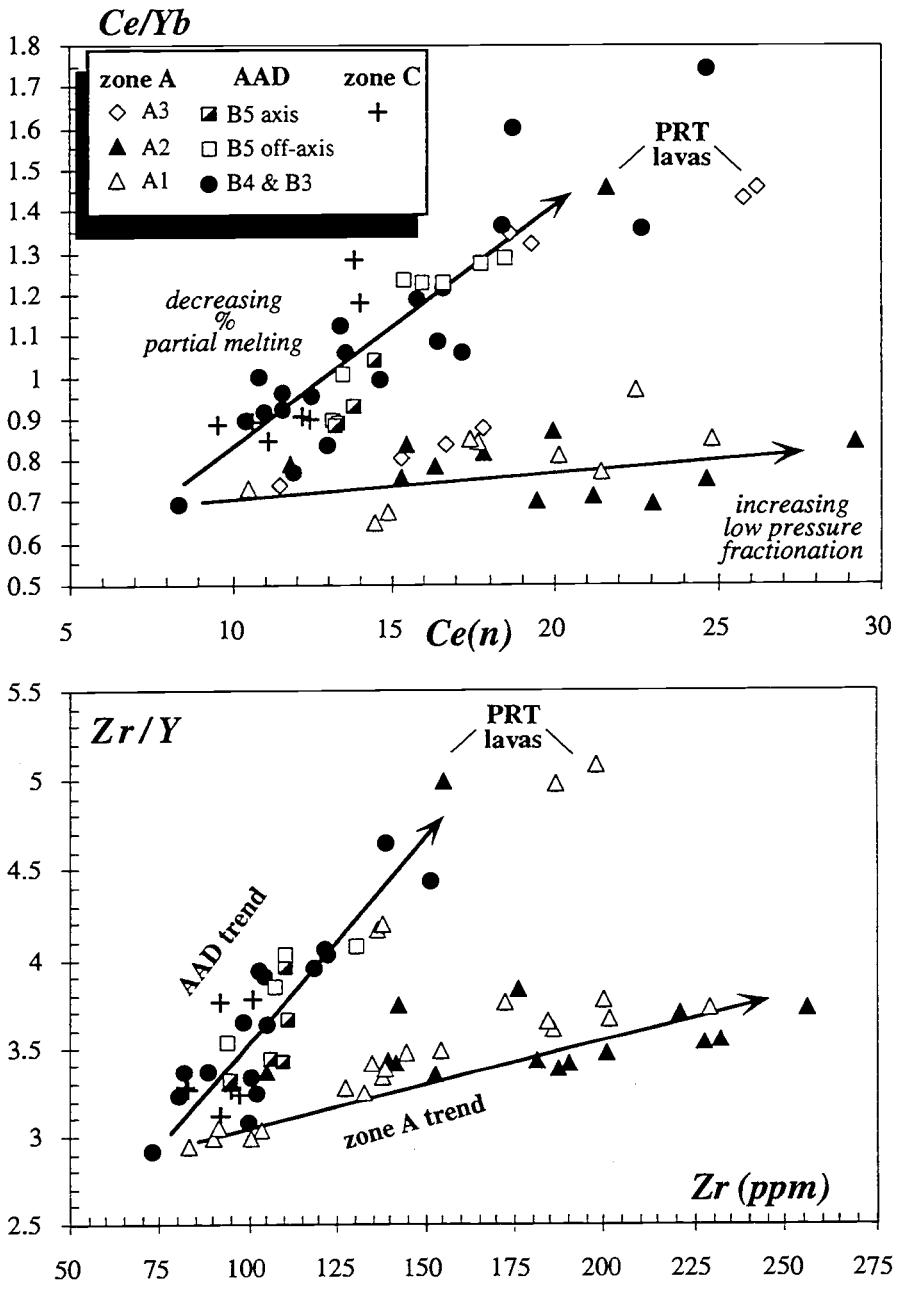

Figure III.10

high degree melt, low Ce_n/Yb_n signature with increasing Ce_n content. Similar behavior of Zr/Y relative to Zr is observed (Fig.III.10b). Again, these trace element characteristics suggest a common mantle source lies beneath both Zone A and the AAD.

The CaO/Al_2O_3 and Na_2O contents of propagating rift tip lavas vary within the range of the AAD suite, but Fe_2O_3, TiO_2 and P_2O_5 are typical of other Zone A basalts. One feature of the rift tip lavas distinct from both the AAD suite, and other Zone A lavas, is their very low SiO_2 abundances. Experimental data show that SiO_2 contents of MORB liquids increase with increasing pressure of melt generation [Jacques and Green, 1980; Falloon et al., 1988; Klein and Langmuir, 1989]. The lower SiO_2 contents of propagating rift tip lavas (~48.5%) relative to AAD lavas (~51.4%) imply that propagating rift tip lavas are derived from greater pressures. On the other hand, trace element enrichments in propagating rift tip lavas indicate low degrees of melting.. This combination of low SiO_2 and low degree melting, suggests that rift tip melts are derived from the deeper parts of a large melting column. If this is true, then the trace element signatures (e.g., Ba/Zr, Ba/La) that are common to both Zone A and the AAD, are associated with the most fertile (i.e, earliest melting) source material. This material, rich in basaltic components such as clinopyroxene is present at the base of the melting column, albeit at different depths, beneath both the AAD and Zone A.

Previous studies of the AAD and surrounding spreading centers have concluded that, relative to Zone A lavas, AAD lavas are produced by lower degrees of melting, resulting from lower mantle temperatures and lower initial pressures of melting [Anderson et al., 1980; Klein and Langmuir, 1987; Klein et al., 1991]. All else being equal, however, low degrees of melting, as inferred from high $Na_{8.0}$ values, should produce high concentrations of mildly to highly incompatible trace elements in AAD lavas. The higher, or equal, concentration of moderately incompatible elements (e.g., heavy REE, Zr, Hf, TiO_2) in Zone A lavas relative to those of the AAD, and the more complex variations in highly incompatible element concentrations (e.g., La; Fig. III.6) suggest the opposite. These

relationships hold if only the most primitive AAD and Zone A lavas are considered. Differences in partial melting cannot reproduce the observed trace element variations from a single, homogeneous mantle composition, complicating the simple model of decreased mantle melting from Zone A to the AAD.

To reconcile similarities in trace element signatures between Zone A and the AAD with major element variations that indicate regional variations in partial melting two options available; 1) The mantle source can be selectively enriched or depleted in trace element constituents to satisfy the major element constraints on mantle melting. This option requires a Zone A mantle higher in mildly incompatible elements such as heavy REE, Zr, Y, Sc, Hf, and Ti, but lower in Sr and lower in highly incompatible elements such as Ba and Th. 2) Assume a homogeneous trace element signature for the mantle source of both the AAD and Zone A, but vary the modal mineralogy of the mantle, thus affecting the mobility of key trace elements during melting. The first option is somewhat adhoc. The second suggestion is explored below.

Variable Mantle Mode

Assuming that the greatest proportion of mantle melting occurs in the pressure interval of spinel lherzolite stability, clinopyroxene (cpx) is the major melting phase and host for many trace constituents. As the modal proportion of cpx declines, the mantle becomes increasingly refractory. Partition coefficients of heavy REE are high for cpx (i.e., Yb kds ~.5; range .3-1.0) [Frey et al., 1978; Green and Pearson, 1985; Johnson et al., 1990; Hart and Dunn, 1993] and consequently, variations in this mineral should control the heavy REE concentration of melts generated at mantle pressures below garnet stability. The compatibility of Sc in cpx (cpx/melt ~1-3; Nielsen et al., 1992) makes this element useful for monitoring cpx during melting. Sc will slowly increase as melting increases until cpx is completely consumed, at which point mantle melting is likely to cease [e.g., Hess, 1993].

Sc variations are shown in Figure III.11 with $Si_{8.0}$ and Zr/Y. As in many other variations diagrams, the AAD and Zone A glass suites are compositionally distinct, but more remarkably, these geochemical parameters differentiate the propagating rift tip lavas from the AAD suite and from one another. There is a systematic decline in Sc in lavas from A3 through B3, reflecting the decreasing extent of melting required by many major element parameters. The $Si_{8.0}$ and Sc values are negatively correlated and the systematics along this trend is geographically related to position along the SEIR (Fig. III.11a). The A3 and A2 lavas (the easternmost samples in this MORB suite) are the highest in Sc and lowest in $Si_{8.0}$. Sc decreases and $Si_{8.0}$ increases in SEIR MORB toward the AAD and this correlation is preserved at the dredge scale within B5. The Zone A rift tip lavas define positive Sc-$Si_{8.0}$ trends orthogonal to the region trend. $Si_{8.0}$ reflects mean depth of melting as does $Fe_{8.0}$ [Klein and Langmuir, 1989], but Sc and $Na_{8.0}$ values should vary in opposite directions with melting. With this in mind, the negative $Si_{8.0}$-Sc correlations could be interpreted as are $Na_{8.0}$-$Fe_{8.0}$ relationships; a progressively shrinking melt column from Zone A toward the AAD. Likewise, the positive $Si_{8.0}$-Sc trends reflect rapid removal of low degree melts from deeper parts of the melt column (i.e., local trends). However, geochemical distinctions between the AAD and Zone A, as well as within Zone A, are more clearly defined. Partial melting trends are overprinted on a regional decline in Sc and increase in $Si_{8.0}$ toward the AAD. Variations in Zr/Y against Sc (Fig. III.11b) show many of the details outlined by the Si8.0-Sc diagram. Low degree melting in both the AAD and Zone A produce nearly identical Zr/Y ratios (4.5-5.0), but the variations in Sc are too large to be produced by melting alone. The sub-parallel, linear Zr/Y-Sc trends across this diagram suggest that compositional and/or mineralogical variations in the mantle source is required to explain the Sc data.

Melting curves have been calculated using common primitive mantle Zr (11.2 ppm) and Y (4.55 ppm) estimates [Sun and McDonough, 1989], but a relatively high mantle Sc

Figure III.11 $SiO_{8.0}$-Sc and Zr/Y-Zr variations diagrams. On both diagrams there is a regular transition from zone A segment A3 through AAD B3 and propagating rift lava are distinct from each other as well as from AAD lava compositions. These trends have been modelled by varying the modal mineralogy of the mantle. Initial starting composition of Zr (11.2 ppm) and Y (4.55 ppm) are primitive mantle compositions of Sun and McDonough [1989]. The Sc starting composition (18 ppm) is necessarily higher than most primitive mantle estimates (c.f., 14.9 ppm; [Hofmann, 1988]) to obtain the observed range in Sc content for zone A and AAD glasses. The melting reaction for spinel lherzolite from Kinzler and Grove [1992] was used to calculate the curves (melting proportions: Ol-.30:Opx .40:Cpx .82:Sp .08). Each tick mark along the curves represent .5% melting increments. Three mantle compositions are shown and indicate a higher content of cpx within the AAD. The partition coefficients have been estimated based on a comparison of published values (e.g., Kelemen et al., [1992]; Johnson et al., [1990]; Hart and Dunn, [1993]) with values calculated using BIGD [Nielsen, 1992]. Mineral compositions from peridotite melting experiments were used as input parameters for the BIGD program [Falloon et al., 1987; Falloon and Green, 1988].

Model partition coefficients:

element	Ol	Opx	Cpx	Sp
Y	.0035	.2	.4	.004
Zr	.01	.06	.2	.05
Sc	.23	1.5	2.8	1.3-.1

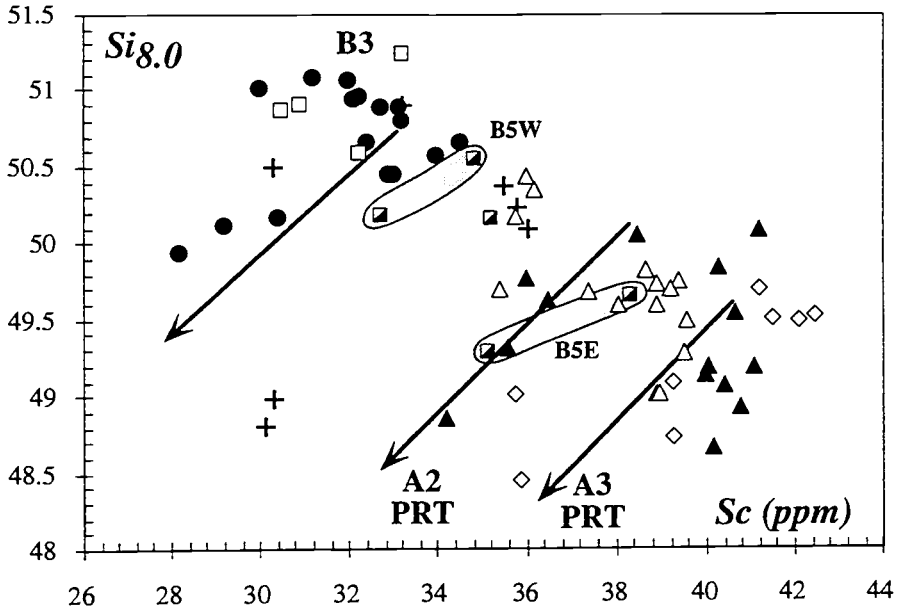

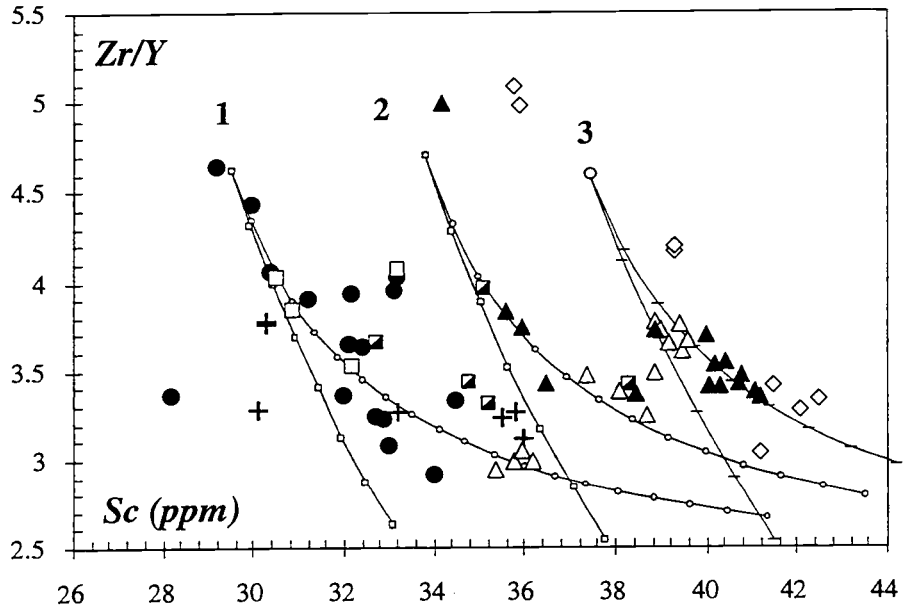

start composition
Zr=11.2
Y=4.55
Sc=18

melt reaction
ol -30
opx 40
cpx 82
sp 8

1	2	3
ol 75	ol 77	ol 79
opx 14	opx 16	opx 16
cpx 8	cpx 4	cpx 2
sp 3	sp 3	sp 3

Figure III.11

value (18 ppm) because published values (e.g., 14.9 ppm) [Hofmann, 1988] are too low to produce the observed MORB melt compositions by reasonable degrees of melting. Very low degrees of melting (<1%) maximize the fractionation of Zr from Y and produce the observed high Zr/Y ratios. Steep Zr/Y-Sc trends for both the AAD lavas and the Zone A propagating rift tips follow steep fractional melting curves while the trends for lavas from more 'mature' sections Zone A (i.e., higher melt flux zones with broad axial ridges) lie along batch melting curves. Clearly, no one melting model is sufficient to produce the entire range of data for the AAD and Zone A from a chemically homogeneous mantle source with uniform modal mineralogy. However, varying the modal proportion of cpx in mantle beneath the AAD and Zone A can reproduce the Zr/Y-Sc variations without resorting to modifying the trace element composition of the upper mantle.

A question that immediately leaps to mind is - Can the modal proportion of cpx be changed without affecting the trace element concentrations in the initial mantle starting composition? The answer to this question depends on one's concept of how mantle moves through the melt regime. The melt column model incrementally removes melt from mantle parcels that enter the base of the melting column and traverse the melt regime by adiabatic decompression [Klein and Langmuir, 1987; 1989; Plank and Langmuir, 1992]. All parcels begin melting with a common modal mineral composition and melts pooled from this process produce a range of MORB compositions by entering and exiting the melt regime at different pressures. If on the other hand, mantle parcels enter the melting column at different depths with different modal mineralogies, then the modal composition of the mantle is actually the mean of all mantle parcels which contribute to the melt. Such mean mantle mode is conceptually analogous to the mean depth of melting and mean pressure of melting which produce variations in $Na_{8.0}$ and $Fe_{8.0}$ [Klein and Langmuir, 1987; 1989]. For example, a deep melting column (high $Fe_{8.0}$ and low $Si_{8.0}$) produces high degrees of melting (low $Na_{8.0}$) beneath Zone A resulting in a more refractory residual mantle

composition than the shallower and smaller melting column of the AAD. Mantle entering the Zone A melt column at depths other than the base of the melt regime will be more depleted in basaltic components; the larger the melt column the greater the opportunity to incorporate more depleted mantle parcels. Beneath the AAD, a shallower melt column translates to lower degrees of melting, less depletion of the mantle and, in contrast to Zone A, mantle contributing to AAD melts will be less refractory relative to the total melt column (i.e., a higher modal proportion of cpx).

The melting models suggest that the AAD and Zone A Zr/Y-Sc relationships can be reproduced by varying the modal abundance of cpx in the mantle, although certain qualifications should be stated. The mantle modal mineralogies used for the melting calculations are quite refractory (10-2% cpx). These mineralogies were selected to bring the melting curves in line with AAD and Zone A data using the source composition outlined above. More fertile mantle compositions (i.e. higher in cpx) require higher Sc starting compositions because cpx buffers the amount of Sc released during melting. Also, most physical models of mantle flow involve laminar through the melt regime with flow lines that are initially vertical then turn from the upwelling regions. In a region with significant lateral (subaxial) mantle flow, such 2-D models may be inadequate and more complex 3-D models may, in some sense, allow more refractory mantle to enter the melt regime at shallow depths. We suggest this process must occur if, as seems probable, variations in mantle mineralogy are important in controlling the final melt trace element composition. The compositional affects of passive and dynamic mantle upwelling through the melt regime is an area of continued investigation.

Lu-Hf and Th-U isotope systematics indicate that MORB melting requires garnet as a residual mantle phase, implying that melting is initiated at depths >80 km [Salters and Hart, 1989; Beattie, 1993]. Both Sc and heavy rare earth elements have high partition coefficients for garnet and melting within the garnet stability field will buffer the abundance of these elements until garnet is no longer a residual phase. Until garnet is completely

consumed, increasing Sc and heavy rare earth element abundances will reflect increasing amounts of melting. Accepting that Zone A major element variations require a deeper melting column, a greater influence of garnet on Zone A melts might be predicted. If melting begins in the garnet stability field for Zone A lavas, but not for AAD lavas, then Sc and heavy rare earth element abundances would be expected to be lower, rather than higher in Zone A lavas. If residual garnet affects both the Zone A and AAD lavas, then garnet must be more depleted in the Zone A melt column, or completely consumed, relative to the AAD to produce a high heavy rare earth element signature in zone A lavas. Furthermore, a greater degree of light to heavy rare earth element fractionation might be expected if garnet played a large role. Initiating melting within the garnet stability field for both the AAD and Zone A would suggest very similar melt column configurations for both regions which is not apparent in the major element systematics of the two MORB suites. If melting begins at pressures of garnet stability for MORB in general, then decompression melting and the progressively depletion of a self-contained mantle diapir from these depths seems highly improbable. Whether a garnet bearing mantle is incorporated into a melting model or not, the modal mineralogy of mantle entering the melt regime beneath the ridge must vary between the AAD and Zone A.

CONCLUSIONS

The unusual diversity of MORB compositions and spreading axis morphologies, at a uniform spreading rate, are highly significant features of the SEIR in the vicinity of the AAD in terms of global accretionary processes. Magma processing after melt generation and prior to seafloor eruption appears to be fundamentally different between the AAD and Zone A, resulting two distinct MORB suites with different styles of differentiation. The broad axial rise of the Zone A segments suggests that relatively large volumes of melt are delivered to the neovolcanic zone. This 'excess' magma supply enables a low pressure magma system to develop, moderating the diversity of certain major and trace elements and allowing for extensive fractional crystallization. In general, Zone A melts are produced over a greater depth range within the melting column and pooled beneath the ridge. Within the AAD, the deep axial valleys suggest a 'deficient' magma supply. The primitive nature of AAD lavas suggests that little, if any, low pressure fractionation has modified their composition and, consequently, much of the chemical diversity within the AAD is due to melting within the mantle source. AAD lavas are produced over a more limited, shallower depth range and rapidly erupted at surface with little modification.

Contrasts in axial morphology and MORB composition between the AAD and Zone A vary together. Therefore, the geochemistry and morphology of the ridge is controlled by magma supply and magma supply is intimately tied to the underlying mantle temperature [Klein and Langmuir, 1987; 1991; Forsyth, 1992; Sempéré et al., 1991]. Higher mantle temperatures produce enough melt to create an axial rise morphology and sustain a well developed, low pressure magma system. The cooler mantle beneath the AAD does not allow low pressure fractionation and magma chemistry is controlled primarily by melting in the source. The average degree of melting and subsequent differentiation history of the AAD and Zone A MORB suites is tied to thermal energy available to create and maintain a shallow level magma system.

As concluded by previous studies, the major element characteristics of AAD lavas are consistent with lower degrees of partial melting at lower mean pressures of melting relative to Zone A lavas [Klein et al., 1991]. However, higher concentrations of moderately incompatible elements in Zone A lavas are inconsistent with the higher degrees of melting suggested by parameters such as $Na_{8.0}$. Therefore, differences in mantle melting beneath Zone A and the AAD cannot be the sole cause of the trace element contrasts between primitive melts from both regions.

A mantle source common to both the AAD and Zone A is suggested by trace element similarities between low degree melts throughout the region. In particular, the primitive Zone A propagating rift tip lavas share many trace element signatures of AAD lavas. The AAD and Zone A propagating rift lavas differ in their major element characteristics, suggesting that this common trace element signature is derived from deeper depths beneath the Zone A mantle. If melting is conceptualized as a column, then the fertile, undepleted base of this mantle melting column lies at a deeper depth below Zone A than it does below the AAD.

The condradictory melting information coveyed by the major and trace element variations between the AAD and Zone A can be reconciled by varying the modal mineralogy of the mantle source beneath these regions. The AAD mantle has a high proportion of cpx (i.e., more fertile), relative to the total melting column, than does Zone A mantle. This model satisfies major element requirements of decreasing melting toward the AAD, trace element signatures that indicate a common mantle source throughout the region, and trace element abundances that are higher than expected in Zone A. Lower modal cpx in the mantle beneath Zone A suggests incorporation of more depleted mantle at depths above the base of the melting column perhaps related to lateral mantle flow. This supposition follows from the similarity in trace element systematics of propagating rift tip and AAD lavas which indicate that fertile mantle exists beneath both regions, although it resides at higher pressures beneath Zone A. Alternatively, the mantle trace element composition must

be varied quite selectively in order to reconcile the trace element systematics with the major element systematics of the two MORB suites.

Chapter 4

Geochemistry and Geochronology of Ancient Southeast Indian and Southwest Pacific Seafloor

D. G. Pyle, D.M. Christie, J.J. Mahoney and R.A. Duncan

ABSTRACT

An isotopically defined boundary between the Pacific Ocean and Indian Ocean MORB presently exists at the center of the Southern Ocean between Australia and Antarctica within the Australian-Antarctic Discordance (AAD). Isotopic contrasts between axis and off-axis samples from the easternmost AAD spreading segment suggests that the boundary for these MORB sources has migrated westward at rate of ~25 mm/yr during the last 4 m.y. The trace element and Sr, Nd, Pb isotope analyses of DSDP samples from sites 264, 265, 266, 274, 278, 279A, 280A, 282, and 283, coupled with ^{40}Ar-^{39}Ar age determinations of selected samples, are presented to determine the regional pattern of mantle source and evaluate the large-scale migration of the isotopic boundary over the last 60 m.y.

The peripheral distribution of these DSDP sites to the Southern Ocean basin records important regional variations in upper mantle source composition, however, the large-scale westward flow of Pacific MORB mantle since rifting of the South Tasman Rise at ~40Ma cannot be resolved. DSDP basalts east of the South Tasman Rise have $^{87}Sr/^{86}Sr$ (0.7025-0.7029) and $^{206}Pb/^{204}Pb$ (18.80-19.48) characteristics that indicate a Pacific MORB-type mantle source beneath this region since seafloor spreading began in the Tasman Basin (~80 Ma). DSDP samples west of the AAD have Indian MORB-type, low $^{206}Pb/^{204}Pb$ and high $^{87}Sr/^{86}Sr$ characteristics. The South Tasman Rise basalts from DSDP sites 282 and 280A erupted between 60-69 Ma from an upper mantle source lower in $^{206}Pb/^{204}Pb$ than mantle farther east. Elevated $^{87}Sr/^{86}Sr$, $^{208}Pb/^{204}Pb$ and $^{207}Pb/^{204}Pb$ values indicate an Indian-type upper mantle source for site 280A, but site 282 basalt is borderline between Pacific-type and true Indian-type mantle in this region.

INTRODUCTION

The Australian-Antarctic Discordance (AAD)

In the center of the Southern Ocean between Australia and Antarctica lies the Australian-Antarctic Discordance (Fig. IV.1). The AAD has long been recognized as an unusual section of the global spreading system because of its deep axial bathymetry (4-5 km), rough (and in places chaotic) topography, low gravity signal, high upper mantle seismic wave velocities, and intermittent asymmetric spreading history [Weissel and Hayes, 1971, 1974; Forsyth et al., 1987; Marks et al., 1990; Sempéré et al., 1991; Palmer et al., 1991]. A history of multiple ridge propagation episodes towards the AAD from both the east and west suggests convergence of upper mantle towards this region [Vogt et al., 1984; Phipps-Morgan et al., 1988].

Coincident with the distinct geophysical features of the AAD is an equally distinct geochemical boundary between isotopically defined Indian Ocean-type and Pacific Ocean-type MORB [Klein et al., 1988]. All spreading axis samples dredged west of ~126° E have Indian Ocean MORB isotopic affinities and those dredged to the east have Pacific MORB isotopic affinities (Fig. IV.2). The isotopic boundary is defined by an abrupt decrease in $^{206}Pb/^{204}Pb$ and $^{208}Pb/^{204}Pb$, an increase in $^{87}Sr/^{86}Sr$ as the MORB source changes from Pacific Ocean-type to Indian Ocean-type mantle (Fig. IV.3). Its is accompanied by a more gradual declines in $^{207}Pb/^{204}Pb$ and $^{143}Nd/^{144}Nd$. The isotopic transition is unusually narrow, occurring over <40 km along-axis [Pyle et al., 1992]. Such a sharp boundary between two, ocean-basin scale upper mantle isotopic domains is unparalleled elsewhere in the mid-ocean ridge system.

Of equal, or even greater, significance has been the realization that the isotopic boundary between Indian MORB and Pacific MORB has not remained stationary. Isotopic contrasts between near-axis and off-axis samples from the easternmost AAD spreading segment require that the boundary has migrated westward at a minimum rate of ~25 mm/yr [Pyle et al., 1992]. Based on available data, we cannot determine whether the ~100 km

westward displacement of the isotopic boundary over the last 3-4 m.y. is a localized perturbation of an isotopic boundary which has always existed beneath the AAD, or part of a long-term, westward migration of Pacific MORB mantle since continental rifting opened a path for mantle outflow from a shrinking Pacific basin. In this latter case, the isotopic boundary has only recently arrived beneath the AAD. The nature of the isotopic boundary and its relationship to the mantle dynamics responsible for the AAD, remains a fundamental and lingering question.

The AAD depth anomaly stretches across the entire Southern Ocean basin, indicating that it has existed at least since continental rifting began at 96 Ma, and possibly since 300 Ma [Veevers, 1982; Mutter et al., 1985]. The V-shaped trace of the depth anomaly implies that it has migrated westward at ~15 mm/yr in the last 20 Ma, but remained centered on a northward migrating spreading center [Marks et al., 1992]. Furthermore, the depth anomaly cuts across the eastern transform boundary of the AAD (Fig. IV.2) and magnetic anomaly patterns suggest that the present, transform dominated morphology of the AAD developed only in the last 25 m.y. [Vogt et al., 1984]. The relationships between the depth anomaly, the present AAD transform boundaries, and the mantle dynamics responsible for these features remain unclear. What seems most apparent is the basic observation that both the depth anomaly and the isotopic boundary are moving westward, but probably not at the same rate.

DSDP Legs 28 and 29 recovered extrusive and shallow intrusive basaltic material from 10-80 Ma seafloor produced in a variety of tectonic settings east of the Kerguelen Plateau and west of the Macquarie Triple Junction (100° E to 180° E; Fig. IV.1). The locations of these DSDP sites peripheral to the Southern Ocean between Australia and Antarctica enable us to determine the positions and contributions of Indian Ocean, Pacific Ocean, and hot spot mantle sources beneath this region as seafloor spreading progressed. A geochemical and geochronological study of basaltic glass and whole rock samples from

Figure IV.1 Magnetic anomaly map of the Southeast Indian Ocean and Southwest Pacific Ocean [Cande et al., 1989] showing the DSDP Leg 28 and 29 sites that recovered layer 2 seafloor or volcanic material thought to be near basement. Major physiographic features discussed in text are outline by bathymetric contours above 3000 m. KP-Kerguelen Plateau; K Is.-Kerguelen Island; H Is.-Heard Island; A Is.-Amsterdam Island; SP Is.-St. Paul Island; BR-Broken Ridge; 90E-Ninetyeast Ridge; WB-Wharton Basin; NP-Naturaliste Plateau; AAD-Australian Antarctic Discordance; STR-South Tasman Rise; TS-Tasman Sea; NZ-New Zealand; M Is.-Macquarie Island; BI-Balleney Island; S Is.-Scott Island.

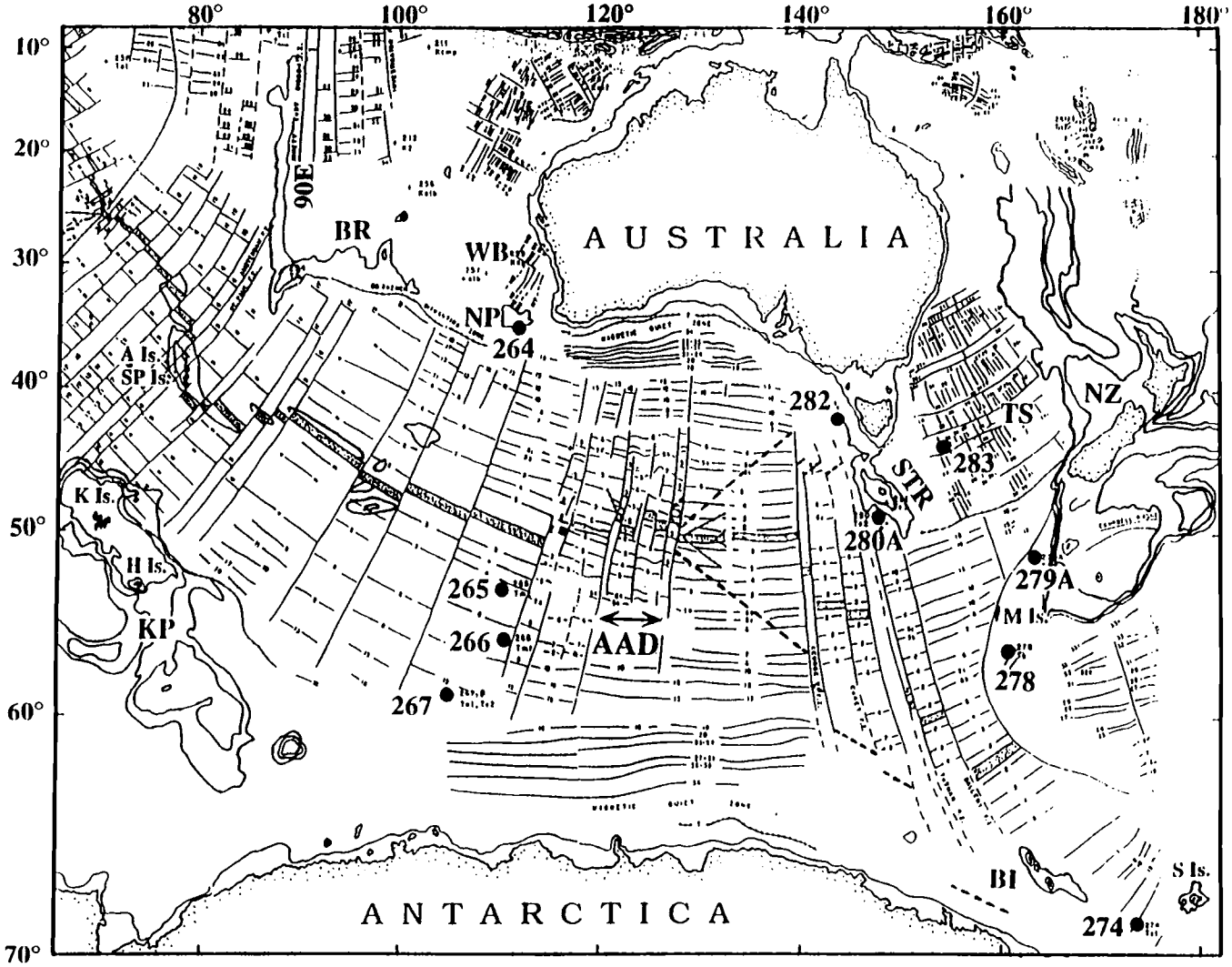
80°
100°
120°
140°
160°
180°
10°
20°
30°
40°
50°
60°
70°
90E
BR
WB
AUSTRALIA
NP
264
A Is.
SP Is.
K Is.
H Is.
KP
265
266
267
AAD
282
283
TS
NZ
STR
280A
279A
M Is.
278
BI
S Is.
274
ANTARCTICA

Figure IV.1

Figure IV.2 Schematic summary of the SEIR tectonics within the eastern AAD and western zone A. Filled circles are MW8801 and Vema dredge sites that have Indian MORB isotopic characteristics and open circles are those that have Pacific MORB isotopic characteristics. The isotopic boundary is presently near the transform boundary at 126° E. The grey line shows a hypothetical trace of the boundary assuming Pacific mantle migration began when the South Tasman Rise rifted.

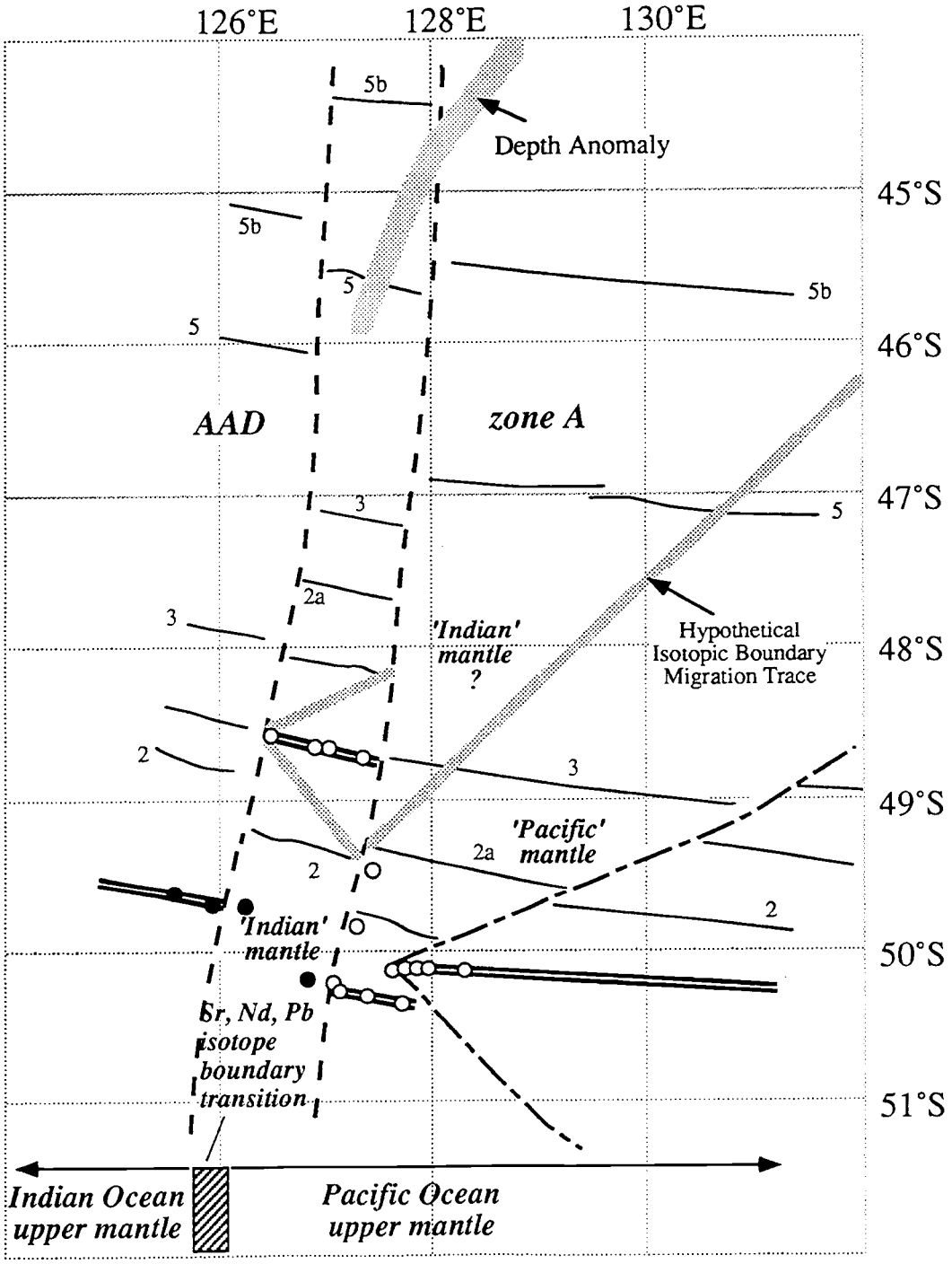
126°E
128°E
130°E
45°S
46°S
47°S
48°S
49°S
50°S
51°S
5b
Depth Anomaly
5
AAD
zone A
3
2a
'Indian' mantle ?
Hypothetical Isotopic Boundary Migration Trace
2
'Pacific' mantle
'Indian' mantle
Sr, Nd, Pb isotope boundary transition
Indian Ocean upper mantle
Pacific Ocean upper mantle

Figure IV.2

Figure IV.3 Along-axis profiles of isotopic ratios from the SEIR (115°-138°). Open symbols represent 'Pacific' group compositions and filled symbols represent 'Indian' group compositions [Klein et al., 1988; Pyle et al., 1992]. Filled squares with open circles in B5 are off-axis dredges. Horizontal axis is distance (km) from the eastern bounding transform of the AAD. The present location of the isotope boundary is at or close to the B4/B5 transform at 126° E. Vertical solid lines show the position of transforms and vertical dashed lines show axial non-transform discontinuities and propagating rift tips.

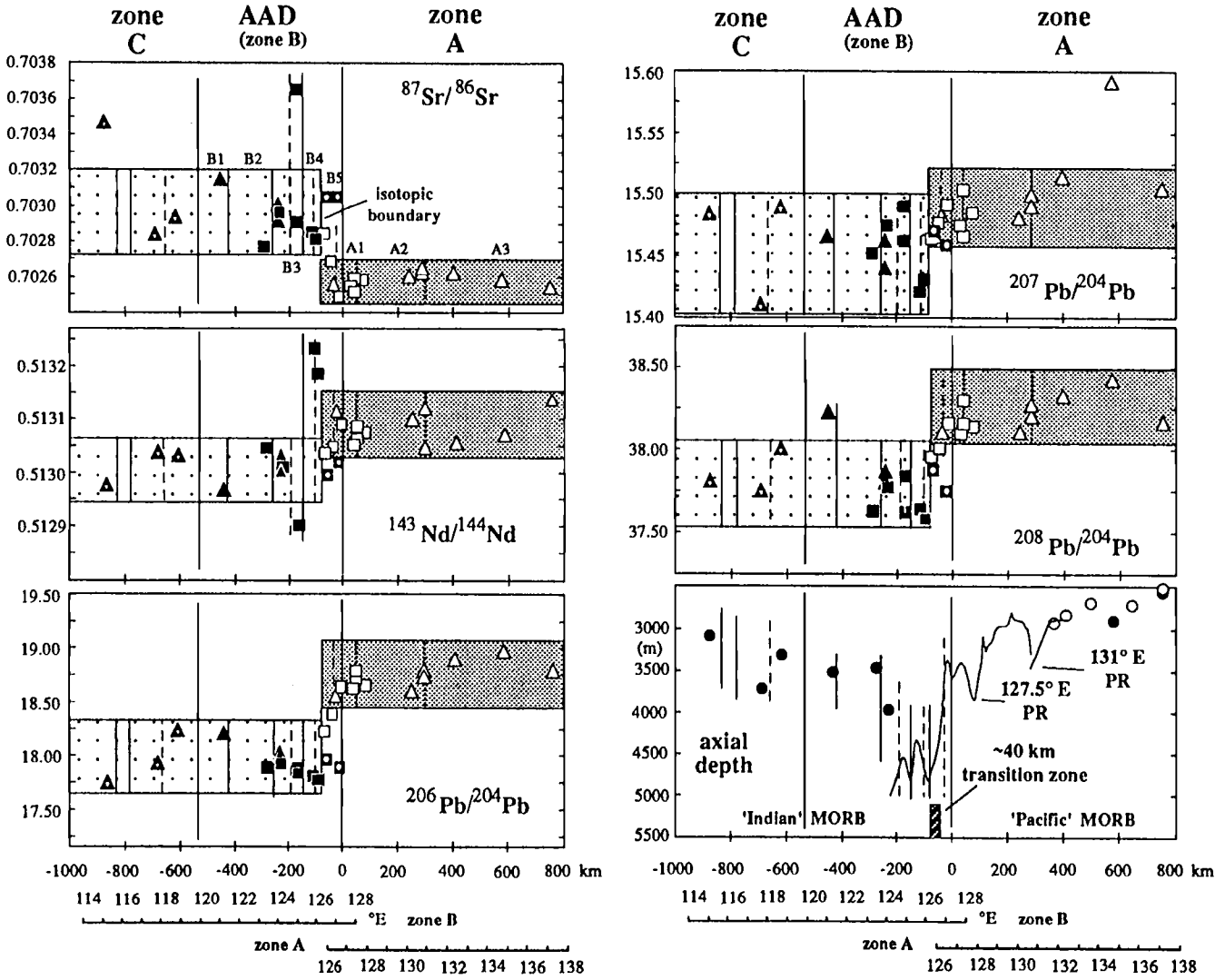
zone C
AAD (zone B)
zone A
$^{87}Sr/^{86}Sr$
B1
B2
B4
B5
B3
isotopic boundary
A1
A2
A3
$^{143}Nd/^{144}Nd$
$^{206}Pb/^{204}Pb$
$^{207}Pb/^{204}Pb$
$^{208}Pb/^{204}Pb$
axial depth
131° E PR
127.5° E PR
~40 km transition zone
'Indian' MORB
'Pacific' MORB
km
°E
zone B
zone A

Figure IV.3

DSDP Legs 28 and 29 is presented below to determine the regional implications for mantle flow in this region.

ANALYTICAL METHODS

Glass and whole rock samples from ten DSDP sites (Table IV.1) were analyzed for major and trace elements by combined microprobe, X-ray fluorescence spectrometry (XRF), and inductively coupled plasma mass spectrometry (ICP-MS). Petrographic descriptions of the core samples condensed from the DSDP Initial Reports volumes for Legs 28 and 29 are summarized in Appendix 1. All basalt core samples were trimmed, and sawn surfaces were ground on a lap wheel to remove contaminants, obtaining the freshest possible material. These rocks were crushed in ceramic jaw crusher, washed in Millipore filtered water, dried, and hand-picked to remove alteration veins and vug material. Whole rock powders were made using a tungsten carbide ring mill at Washington State University. All analyses are on splits of the same sample powder. Glass samples were crushed in a ceramic mortar, sieved to 30-mesh size fraction, and hand-picked to remove alteration and phenocryst phases.

The major element concentrations of all glass samples were determined using a Cameca SX-50, four-spectrometer electron-microprobe at Oregon State University. Each reported analysis represents the average of 5 spot analyses that have been normalized to standard BASL glass run along with the unknowns. Whole rock samples were analyzed for major and trace elements (Ni, Cr, Sc, V, Ba, Rb, Sr, Zr, Y, Nb, Ga, Cu, Zr) by XRF at Washington State University following standard methods (Tables IV.2, IV.3, IV.4).

Further trace element analyses were completed by ICP-MS using a Fisons PQ2+ PlasmaQuad at Oregon State University for Sc, V, Cr, Ni, Cu, Zn, Rb, Sr, Y, Zr, Nb, Cs, Ba, La,Ce, Pr, Nd, Sm, Eu, Gd, Tb, Dy, Ho, Er, Tm, Yb, Lu, Hf, Ta, Th, and U (Tables IV.2, IV.3, IV.4). The XRF and ICP-MS trace element results show good agreement except for low concentration elements (Table IV.5). At low concentrations, the ICP-MS values are assumed to be better (e.g., Rb, Ba).

Table IV.1 DSDP sites sampled for this study.

	Site	Latitude (S)	Longitude (E)	Magnetic Anomaly	~Age† (Ma)	Core Rec. (m)	Rec. %
LEG 28	264	34° 58.13'	112° 2.68'				
	265	53° 32.45'	109° 32.45'	5b	15	17	20
	266	56° 24.13'	110° 6.70'	6	23	14	14
	267	59° 15.74'	104° 29.30'	15	38	14	16
	274	68° 59.81'	173° 25.64'	13	36	6	34
LEG 29	278	56° 33.42'	160° 4.29'	12	33	11	50
	279A	51° 20.14'	162° 38.10'		23	5	70
	280A	48° 57.44'	147° 14.08'		?47	5	100
	282	42° 14.76'	143° 29.18'		?55	15	50
	283	43° 54.60'	154° 16.96'	31	69	4	43

† Kent and Gradstein (1986) magnetic anomaly time-scale

Table IV.2 Major and trace element composition of DSDP Leg 28 basaltic basement cores.

	DSDP 264	DSDP 265		DSDP 266		DSDP 267		DSDP 274	
core	264-15	265-17-01	265-18-01	266-23-01	266-23-01	267-07-01	267-07-01	274-44-02	274-45-02
interval	cc	61-63	41-49	pc. 5	76-82	78-82	61-64	88-93	110-114
split	w/r	glass	w/r	glass	w/r	glass	w/r	w/r	w/r
analysis	xrf	probe	xrf	probe	xrf	probe	xrf	xrf	xrf
SiO2	55.08	49.51	50.07	50.32	51.05	50.95	51.88	51.11	52.00
TiO2	1.53	1.63	1.58	2.18	2.28	1.31	1.32	1.71	2.01
Al2O3	17.32	16.67	17.14	13.92	14.77	14.62	15.80	17.82	17.05
FeOt	9.62	7.87	7.50	10.92	11.62	8.98	8.73	9.17	9.64
MnO	0.11	0.12	0.14	0.19	0.20	0.17	0.15	0.15	0.11
MgO	5.22	8.36	9.40	7.18	6.37	7.86	7.87	5.17	6.05
CaO	6.88	10.51	11.12	10.35	10.40	12.39	12.31	11.00	7.87
Na2O	3.00	3.27	3.45	2.96	3.11	2.63	2.95	3.35	3.40
K2O	1.17	0.60	0.64	0.25	0.35	0.13	0.31	0.12	1.27
P2O5	0.19	0.30	0.25	0.26	0.27	0.13	0.12	0.15	0.47
total	100.11	98.86	101.29	98.52	100.42	99.16	101.45	99.75	99.88
ICP-MS (ppm)									
Sc	27.9	33.3	29.2	42.7	38.8	42.9	41.4	46.8	38.4
V	215	232	186	372	336	292	260	361	267
Cr	116	325	303	285	201	296	259	222	207
Ni	19	187	268	118	90	79	78	96	62
Cu	16	50	54	54	56	70	77	97	73
Zn	90.9	81.4	79.9	109.3	110.8	75.2	75.5	94.5	102.5
Rb	20.2	9.2	7.2	4.2	4.5	1.5	4.8	1.2	23.3
Sr	205	297	257	150	129	130	126	128	235
Y	25	29	25	50	49	27	29	31	43
Zr	120	139	112	165	149	77	81	103	148
Nb	7.2	14.4	13.2	7.8	8.0	3.4	3.8	6.9	27.9
Cs	0.10	0.11	0.44	0.06	0.09	0.02	0.19	0.05	0.67
Ba	307	104	97	45	47	16	12	19	99
La	19.47	9.91	8.60	7.50	7.34	3.34	3.16	4.54	21.40
Ce	43.52	24.14	20.49	22.13	20.80	10.41	9.74	13.32	43.15
Pr	5.13	3.24	2.77	3.44	3.27	1.66	1.57	2.06	5.27
Nd	20.78	14.69	12.80	17.58	17.34	9.26	8.71	10.84	22.48
Sm	4.81	3.96	3.41	5.50	5.42	3.15	2.95	3.56	5.42
Eu	1.53	1.41	1.23	1.73	1.64	1.15	1.06	1.25	1.76
Gd	5.09	4.37	3.92	6.48	6.04	3.76	3.50	4.25	6.00
Tb	0.81	0.75	0.67	1.20	1.14	0.73	0.65	0.78	1.03
Dy	4.79	4.63	4.04	7.78	7.49	4.56	4.29	5.21	6.46
Ho	0.91	0.93	0.83	1.68	1.60	0.96	0.90	1.12	1.38
Er	2.51	2.75	2.49	4.94	4.71	2.98	2.74	3.25	4.05
Tm	0.36	0.41	0.37	0.78	0.74	0.45	0.42	0.50	0.62
Yb	2.10	2.55	2.22	4.79	4.53	2.76	2.58	3.10	3.68
Lu	0.30	0.38	0.34	0.71	0.67	0.41	0.39	0.45	0.55
Hf	3.25	2.86	2.41	4.16	3.88	2.03	1.91	2.58	3.80
Ta	0.53	0.91	2.79	0.48	0.87	0.19	1.02	0.56	2.02
Th	3.72	1.03	1.34	0.64	0.46	0.16	0.18	0.39	1.67
U	0.42	0.31	0.35	0.17	0.17	0.08	0.07	0.23	0.53
Pb*		0.700		0.689		0.401			

*** isotope dilution analysis**

Table IV.3 Major and trace element composition of DSDP Leg 29 basaltic basement cores.

	DSDP 278		DSDP 279A	DSDP 280A	DSDP 282		DSDP 283
core	278-35-02	278-35-03	279-13-02	280-23-02	282-20-02	282-20-01	283-18-01
interval	64-67	112-117	48-54	106-110	80-85	107-113	135-138
split	glass	w/r	w/r	w/r	glass	w/r	w/r
analysis	probe	xrf	xrf	xrf	probe	xrf	xrf
SiO2	49.89	50.43	50.95	48.68	48.65	50.18	49.20
TiO2	1.01	0.91	1.42	0.90	1.48	1.50	1.85
Al2O3	15.44	18.19	15.66	19.04	16.27	17.83	17.75
FeOt	8.23	7.24	9.49	8.50	8.83	9.18	10.20
MnO	0.15	0.13	0.14	0.10	0.14	0.16	0.21
MgO	8.73	7.96	8.36	10.47	8.13	5.86	8.18
CaO	13.39	13.29	11.50	7.65	11.95	11.75	6.67
Na2O	2.31	2.46	3.01	3.13	3.11	3.51	3.56
K2O	0.10	0.18	0.22	0.07	0.09	0.19	0.76
P2O5	0.10	0.08	0.16	0.06	0.13	0.12	0.19
total	99.35	100.87	100.91	98.59	98.78	100.29	98.57
ICP-MS (ppm)							
Sc	40.9	33.3	42.0	36.8	35.4		46.2
V	252	197	316	213	207		319
Cr	430	317	178	293	266		261
Ni	140	115	69	159	152		59
Cu	100	76	59	122	53		60
Zn	69.8	55.1	72.9	65.8	70.0		92.1
Rb	1.8	3.1	3.9	1.2	4.2		12.4
Sr	125	125	160	90	162		177
Y	21	20	23	18	30		24
Zr	62	59	80	45	101		117
Nb	3.7	3.6	12.5	1.5	3.1		7.4
Cs	0.02	0.27	0.06	0.22	0.24		0.25
Ba	15	8	65	20	12		34
La	3.05	2.52	7.17	1.23	3.13		5.23
Ce	8.70	7.56	17.54	4.19	10.88		14.76
Pr	1.39	1.16	2.37	0.69	1.83		2.13
Nd	6.99	6.30	11.75	4.22	10.00		10.79
Sm	2.26	2.07	3.22	1.58	3.24		3.20
Eu	0.85	0.80	1.20	0.69	1.21		1.21
Gd	2.71	2.59	3.74	2.17	3.82		3.62
Tb	0.51	0.49	0.67	0.43	0.70		0.67
Dy	3.31	3.06	4.18	2.98	4.66		4.23
Ho	0.69	0.64	0.88	0.65	0.98		0.88
Er	2.12	2.02	2.64	2.03	2.90		2.63
Tm	0.33	0.30	0.41	0.33	0.45		0.40
Yb	2.02	1.81	2.43	2.16	2.73		2.58
Lu	0.31	0.28	0.38	0.33	0.40		0.38
Hf	1.48	1.35	2.23	1.25	2.29		2.87
Ta	0.18	0.24	0.80	0.16	0.22		0.46
Th	0.16	0.18	0.71	0.15	0.15		0.41
U	0.08	0.07	0.23	0.04	0.05		0.18
Pb*	0.250				0.423		

*** isotope dilution analysis**

Table IV.4 Major and trace element composition of dredge samples recovered near the Southeast Indian Ridge.

	MW8801	zone A		AAD		
dredge	MW07-01	MW20-01	MW17-26	MW23-01	MW26-01	MW27-71
area	off-axis	off-axis	axis	axis	axis	axis
split	glass	glass	glass	glass	glass	glass
analysis	probe	probe	probe	probe	probe	probe
SiO2	50.14	50.87	50.62	51.34	51.1	52.39
TiO2	1.89	2.03	1.36	1.12	1.4	1.20
Al2O3	14.17	14.53	15.49	16.26	15.55	16.24
FeOt	10.18	10.41	8.44	9.18	8.52	7.56
MnO	0.17	0.17	0.15	0.13	0.17	0.15
MgO	7.32	7.25	8.37	7.71	7.88	8.10
CaO	11.64	10.61	11.54	10.86	10.95	11.10
Na2O	2.52	2.79	2.93	2.87	2.94	2.95
K2O	0.09	0.11	0.03	0.10	0.07	0.10
P2O5	0.14	0.22	0.15	0.15	0.18	0.17
total	98.26	98.99	99.08	99.72	98.76	99.96
ICP-MS (ppm)						
Sc	38.7	37.4	38.4	37.4	36.0	34.4
V	344	342	292	228	283	260
Cr	303	218	427	380	348	371
Ni	85	103	105	157	119	129
Cu	64	57	76	88	56	58
Zn	87.7	91.4	69.4	73.8	77.9	63.7
Rb	22.0	15.0	0.6	1.4	0.9	1.0
Sr	98	110	118	103	112	142
Y	41	42	27	23	32	26
Zr	133	145	79	61	96	84
Nb			1.2	2.4	2.1	2.4
Cs			0.01	0.02	0.02	0.02
Ba	6	7	3	17	9	12
La	3.85	4.82	1.91	2.06	3.06	3.13
Ce	12.80	12.50	8.05	6.89	11.06	10.46
Pr			1.41	1.10	1.84	1.69
Nd	15.90	12.90	8.91	6.51	10.57	9.41
Sm	4.35	5.08	3.09	2.39	3.73	3.05
Eu	1.45	1.57	1.19	0.95	1.34	1.15
Gd			3.87	3.05	4.38	3.69
Tb	1.10	1.15	0.77	0.60	0.87	0.69
Dy			4.86	4.03	5.66	4.45
Ho			1.01	0.90	1.20	0.96
Er			3.06	2.58	3.56	2.87
Tm			0.49	0.41	0.53	0.45
Yb	4.70	4.76	2.88	2.53	3.35	2.66
Lu	0.63	0.76	0.43	0.38	0.52	0.40
Hf	3.40	3.59	2.22	1.79	2.77	2.16
Ta	0.23	0.26	0.08	0.15	0.15	0.16
Th	0.08	0.07	0.07	0.14	0.14	0.14
U			0.02	0.04	0.05	0.05
Pb*			0.226	0.275		0.414

* isotope dilution analysis

Table IV.5 Duplicate analyses of whole rock powder splits by XRF and ICP-MS.

sample	Sc		V		Cr		Ni		Cu		Zn	
w/r	ICP	XRF	ICP	XRF	ICP	XRF	ICP	XRF	ICP	XRF	ICP	XRF
264-15-cc	28	30	215	239	116	90	20	10	16	57	87	117
265-18-01	29	29	186	206	303	431	268	273	54	90	80	82
266-23-01	39	42	336	362	201	205	90	74	56	89	111	121
267-07-01	41	44	260	277	259	267	78	67	77	115	75	88
278-35-03	33	34	197	217	317	358	115	107	76	116	55	66
282-20-01	35	42	207	238	266	340	152	155	53	123	70	91
279-13-02	42	43	316	294	178	126	69	59	74	120	73	81
280-23-02	37	41	213	234	293	284	113	161	122	183	67	89
283-18-01	46	51	319	338	261	251	59	55	60	119	92	113
274-44-02	47	49	361	327	222	202	96	85	97	153	95	113
274-45-02	38	43	267	303	207	222	62	54	73	131	102	120

sample	Rb		Sr		Y		Zr		Nb		Ba	
w/r	ICP	XRF	ICP	XRF	ICP	XRF	ICP	XRF	ICP	XRF	ICP	XRF
264-15-cc	20.3	19	205	210	24.6	30	111	148	7.2	8	311	292
265-18-01	7.2	8	257	283	25.3	27	112	121	13.2	13.4	97	65
266-23-01	4.4	5	129	140	49.2	50	149	154	8.0	8.9	46	17
267-07-01	4.7	4	126	132	28.7	29	81	80	3.8	3.1	11	0
278-35-03	3.0	3	125	131	20.1	21	59	62	3.6	4.3	6	0
282-20-01	4.1	3	162	176	29.9	32	101	102	3.1	3.3	11	0
279-13-02	3.9	6	166	164	20.2	24	80	87	12.1	12.1	56	
280-23-02	1.1	2	90	101	14.4	19	45	54	1.5	2.4	20	6
283-18-01	12.5	14	177	191	23.7	26	117	117	7.4	9.2	33	27
274-44-02	1.1	0	128	134	31.4	36	103	104	6.9	8.8	18	0
274-45-02	23.6	25	235	274	42.7	44	148	149	27.9	26.6	98	75

Sample solutions for ICP-MS were prepared with ~60-80 mg splits of glass and whole powders dissolved in tightly capped, 15 ml Savillex teflon beakers with ~800 µl of a HF:HNO3 acid mixture (1:3) heated at ~80° C overnight. Upon dissolution, beakers were uncapped and samples were dried on a hot plate to drive-off HF. Following drydown, the powders were then taken up once in 6N HCl and twice in 4N HNO3, each dissolution step followed by an intervening drying step, to break down fluorosilicate precipitates. The final dried powder was dissolved in 10 ml of 2N HNO3, from which a further 1:5 dilution was prepared to run on the ICP-MS. A multiple, 20 ppb internal spike of Be, In, and Bi was added to each sample to correct for machine drift. Unknown element abundances were determined using linear regression curves based on dissolved USGS rock standards (BIR-1, BHVO-1, BCR-1, and W-1) processed along with the samples.

Sr, Nd, and Pb isotope analyses were performed on fresh glasses from DSDP sites 265, 266, 267, 278, and 282 and two off-axis dredge samples recovered directly east of the AAD (Table IV.6 and IV.7). Core samples without glass were subjected to a sequential leaching procedure to remove alteration [Mahoney, 1987]. This leaching method differs from conventional warm acid techniques by being considerably more intense. A coarsely powdered sample (200-800 mg) is leached in 4N to 6N ultra-pure HCl and agitated ultrasonically for 20 minutes. The acid (clouded from the dissolution of alteration material) is removed from the remaining solid and the procedure is repeated until the acid remains clear during the leaching step. At this point, the final solid is removed, rinsed with ultra-pure water and dried, leaving typically 10% to 40% of the original powered volume, depending on the extent of alteration. The leached powder is essentially composed of well-crystallized plagioclase and clinopyroxene with very little, if any altered material [Mahoney, 1987]. Isotope dilution analysis of Nd, Sm, Sr, Rb, and Pb were determined on DSDP glass and leached whole rock powders, but not on dredge glasses recovered near the SEIR.

Selected whole rock sample ages were determined by ^{40}Ar-^{39}Ar incremental heating in order to clearly establish space-time relationships of the mantle sources in this region

Table IV.6 Sr, Nd, and Pb isotope ratios composition of DSDP Leg 28 cores.

DSDP Leg 28 Cores

DSDP site	**264**	**265**	**266**	**267**	**274**	**274**
core	15	17-01	23-1	07-01	44-02	45-02
interval	cc	61-63	pc. 5	78-82	88-93	110-114
split	lchd w/r	glass	glass	glass	lchd w/r	lchd w/r
206Pb/204Pb	18.076	18.080	18.100	17.992	18.800	19.484
(±)		0.007	0.010	0.007	0.005	0.003
207Pb/204Pb	15.677	15.497	15.479	15.489	15.499	15.590
(±)		0.006	0.009	0.007	0.005	0.003
Δ **7/4**	22.7	4.6	2.6	4.8	-3.0	-1.3
208Pb/204Pb	39.175	37.999	37.991	37.855	38.466	39.248
(±)		0.017	0.021	0.018	0.011	0.007
Δ **8/4**	169.4	51.3	48.1	47.6	11.0	6.5
87Sr/86Sr	0.713434	0.703490	0.703083	0.703039	0.702696	0.702890
(±)	0.000016	0.000013		0.000017	0.000015	0.000017
Δ **Sr**						
143Nd/144Nd	0.511828	0.512893				
(±)	0.000010	0.000012				
ε **Nd**	-15.8	4.9				
Pb (ppm)	5.558	0.700	0.689	0.401	0.250	0.458
(±)					0.0002	
Sr (ppm)	262.7	221.5			145.1	293.2
(±)						
Rb (ppm)	25.263	5.631				
(±)						
Nd (ppm)	7.786	11.562				
(±)	0.0012					
Sm (ppm)						
(±)						

†Nd, Sr and Pb isotopic values are not age corrected. $\varepsilon_{Nd}(T)=0$ corresponds to $^{143}Nd/^{144}Nd=0.512640$. Isotopic fractionation corrections are $^{148}NdO/^{144}NdO=0.242436$ ($^{148}Nd/^{144}Nd=0.241572$), $^{86}Sr/^{88}Sr=0.1194$; Pb isotopes are corrected for fractionation using NBS 981 standard values of Todt et al. [1984]. Data reported relative to $^{143}Nd/^{144}Nd=0.511850$ for La Jolla Nd, and $^{87}Sr/^{86}Sr=0.71024$ for NBS 987 Sr standard. Within-run errors are less than or equal to the total ranges measured for La Jolla Nd (±0.000012; 0.2 ε units), NBS 987 Sr (±0.000024), and NBS 981 Pb ($^{206}Pb/^{204}Pb$, ±0.010; $^{207}Pb/^{204}Pb$, ±0.011; $^{208}Pb/^{204}Pb$, ±0.038). Estimated uncertainties of isotope dilution analyses are <0.2% for Nd and Sm, <0.5% for Sr, ~1.0% for Rb, and <1.0% for Pb. Total procedural blanks are <20 picograms for Nd, <120 picograms Sr, and 5-30 picograms for Pb.

Table IV.7 Sr, Nd, and Pb isotope ratios composition of DSDP Leg 29 cores and SEIR dredge samples.

	DSDP Leg 29 Cores					SEIR Dredge	
DSDP site	**278**	**282**	**279A**	**280A**	**283**	**MW8801**	
core	35-02	20-02	13-02	23-02	18-01	MW07-01	MW20-01
interval	64-67	80-85	48-54	106-110	135-138	dredge	dredge
split	glass	glass	lchd w/r	lchd w/r	lchd w/r	glass	glass
206Pb/204Pb	18.808	18.488	19.072	18.656	18.843	18.633	18.609
(±)	0.008	0.011	0.008	0.004	0.006	0.006	0.005
207Pb/204Pb	15.529	15.495	15.549	15.606	15.565	15.496	15.490
(±)	0.007	0.010	0.006	0.004	0.005	0.006	0.004
Δ **7/4**	-0.1	0.0	-0.9	9.3	3.1	-1.5	-1.8
208Pb/204Pb	38.427	38.104	38.757	38.683	38.542	38.220	38.180
(±)	0.019	0.025	0.016	0.011	0.012	0.014	0.011
Δ **8/4**	6.1	12.5	7.2	50.1	13.4	6.6	5.5
87Sr/86Sr	0.702511	0.702606	0.702679	0.703110	0.702620	0.702602	0.702590
(±)				0.000017		0.000017	0.000014
Δ **Sr**							
143Nd/144Nd							
(±)							
ε **Nd**							
Pb (ppm)	0.249	0.423	0.114	0.373	0.337	NA	NA
(±)							
Sr (ppm)							
(±)							
Rb (ppm)							
(±)							
Nd (ppm)							
(±)							
Sm (ppm)							
(±)							

Table IV.8 ^{40}Ar-^{39}Ar plateau and isochron age from DSDP Legs 28 and 29, Southeast Indian Ocean and Southwest Pacific Ocean.

Sample	type†	Plateau Age (Ma)	%Ar (% of total)	Isochron Age (Ma)	$^{40}Ar/^{36}Ar$ intercept
264-15-CC	clastic	100.6 ± 1.2	55	99.6 ± 0.5	325.8 ± 54.8
267-07-01	basement	23.4 ± 0.8	100	23.3 ± 3.1	296.9 ± 7.9
274-44-02	clastic	67.5 ± 3.2	49	69.6 ± 5.7	295.1 ± 6.5
278-35-03	basement	23.7 ± 5.8	43	46.8 ± 5.9	288.3 ± 19.6
279A-13-02	basement	14.7 ± 1.6	73	13.9 ± 1.0	296.9 ± 0.8
280A-23-02	clastic	64.2 ± 3.3	86	69.5 ± 2.2	294.6 ± 2.2
282-20-01	basement	59.2 ± 2.0	52	62.8 ± 4.8	293.2 ± 26.3

† Clastic denotes basalt sampled from breccias on the surface or slighly above true layer 2 seafloor, whereas basement is considered actual oceanic crust.

(Table IV.8). Rock chips 0.5-1 mm in size were irradiated for 6-8 hours in the core of the Oregon State University TRIGA reactor and conversion of ^{39}K to ^{39}Ar by neutron capture monitored with a hornblende standard Mmhb-1 (520.4±1.7 Ma) [Samson and Alexander, 1987]. Five to eight incremental heating steps were conducted depending on the amount of gas available. The Ar composition of gas at each step was measured mass spectrometrically with an AEI-MS10S instrument at the OSU College of Oceanography rare gas laboratory.

Seawater-alteration of primary igneous phases (olivine, pyroxene, feldspar, oxides, and glass) to clays, zeolites, celadonite, and calcite causes a loss of radiogenic ^{40}Ar and an addition of K to seafloor basalts, resulting in conventional K-Ar ages that are younger than the true crystallization age. The ^{40}Ar-^{39}Ar incremental heating method [Merrihue and Turner, 1966; Dalrymple et al., 1981; McDougall and Harrison, 1988] has been used successfully to date slightly to moderately altered seafloor basalts [e.g. Duncan and Hargraves, 1990], flood basalt provinces [Duncan and Pyle, 1988] and oceanic basalt plateau provinces [e.g. Mahoney et al., 1992]. This technique uses a fast neutron flux to produce ^{39}Ar from ^{39}K. Incremental heating of the sample under vacuum allows extraction of parent (^{39}Ar representing K) and daughter (^{40}Ar) isotopes from discrete temperature-steps. Alteration phases are less retentive of Ar owing to their open crystal structure, so Ar diffuses out of them at low temperatures. Much of the excess K resides on grain boundaries, vesicles, and cracks and ^{39}Ar formed from it will be lost from the sample during irradiation. The remaining igneous phases outgas at higher temperatures, and their Ar isotopic compositions reflect the crystallization age of the sample.

RESULTS

Age of Volcanism

Tracing the compositional contributions of various mantle sources through time requires age constraints on volcanic activity. Previously, basement age estimates for DSDP Legs 28 and 29 have been based on magnetic anomaly ages and/or overlying sediment

ages. We have obtained more precise age estimates, for selected samples by ^{40}Ar-^{39}Ar incremental heating.

DSDP sites 264, 265, 266, and 267 lie on the western margin of the Southern Ocean between Australia and Antarctica (Fig.IV.1) and range in age from ~15 to 100 m.y. At site 264, a volcaniclastic sequence of basaltic andesite to rhyolite clasts was encountered beneath Cenomanian-Santonian chalks on the southern Naturaliste Plateau [Ford, 1975], which may be either a small remnant of continental crust and/or a flood basalt plateau related to the Kerguelen hot spot [Mahoney et al., 1994]. The apparent age spectrum of a basaltic andesite clast from this site produced a plateau between 99-102 Ma (100.6±1.2 Ma) and a concordant isochron age of 99.6±1.2 Ma (Fig. IV.4); volcanism slightly younger than Kerguelen Plateau basalts (109-118 Ma) [LeClaire et al., 1987; Whitechurch et al., 1992] and slightly older than Broken Ridge basalts (88-89 Ma) [Duncan, 1991].

Sites 265, 266 and 267 recovered systematically older crust from the Antarctic plate along a transect roughly normal to the SEIR between 105°-110° E (Fig. IV.1). Magnetic anomalies indicate seafloor ages of 14 Ma (A5), 25 Ma (A7), and 35 Ma (A13), respectively [Hayes and Frakes, 1975; Vogt et al., 1984]. Layer 2 oceanic crust was penetrated at sites 267 and 265, but site 266 recovered intermixed basalt and sediment resulting from eruption into soft sediment slightly above basement [Ford, 1975]. Since seafloor at site 267 was generated during the earliest stages of rapid seafloor spreading in this region, its age was determined by ^{40}Ar-^{39}Ar analysis. The plateau and isochron age are concordant (23.4±0.8 Ma and 23.3± 3.1 Ma, respectively; Fig. IV.4) but younger than the magnetic anomalies would suggest, overlapping the magnetic anomaly age estimate of site 266. In the absence further ^{40}Ar-^{39}Ar work, sites 267, 266, and 265 are tentatively interpreted to sample seafloor of progressively decreasing age.

East of the AAD, seafloor ages at DSDP sites range from ~13-70 m.y. The oldest seafloor appears to be associated with seafloor spreading in the Tasman Basin (site 283;

Figure IV.4 Apparent age spectrum (plateau) and companion $^{36}Ar/^{40}Ar$-$^{39}Ar/^{40}Ar$ isochron diagrams for samples from a) Naturaliste Plateau and the Southeast Indian Ridge; b) Western continental margin of Tasmania and South Tasman Rise; c) Macquarie Ridge and Emerald Basin; d) Balleny Basin. Open squares on isochron plots represent data omitted from the isochron age calculation.

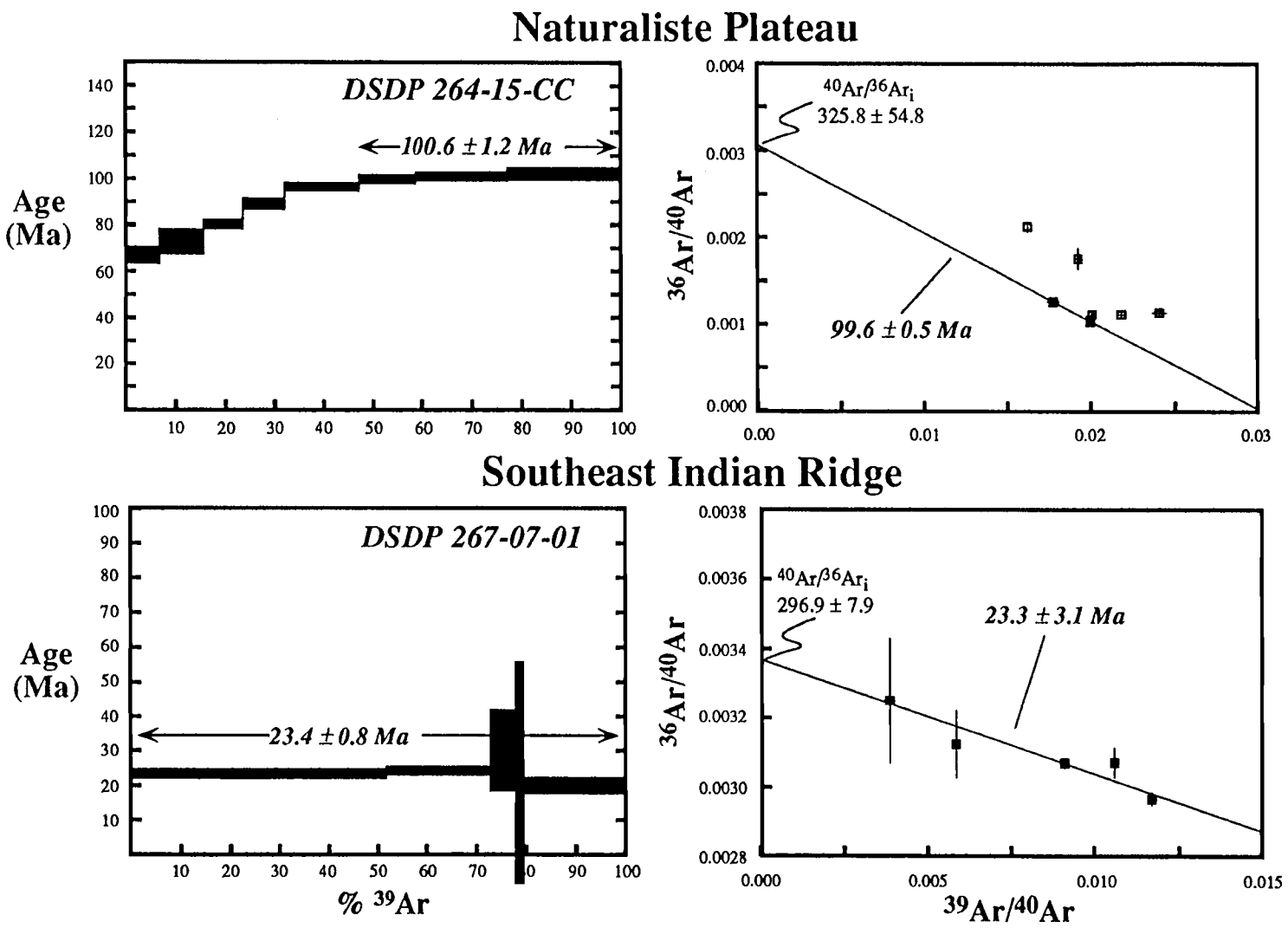
Naturaliste Plateau
DSDP 264-15-CC
←100.6 ± 1.2 Ma→
Age (Ma)
140
120
100
80
60
40
20
10 20 30 40 50 60 70 80 90 100
0.004
0.003
0.002
0.001
0.000
$^{36}Ar/^{40}Ar$
$^{40}Ar/^{36}Ar_i$
325.8 ± 54.8
99.6 ± 0.5 Ma
0.00 0.01 0.02 0.03
Southeast Indian Ridge
DSDP 267-07-01
Age (Ma)
100
90
80
70
60
50
40
30
20
10
23.4 ± 0.8 Ma
10 20 30 40 50 60 70 90 100
% ^{39}Ar
0.0038
0.0036
0.0034
0.0032
0.0030
0.0028
$^{36}Ar/^{40}Ar$
$^{40}Ar/^{36}Ar_i$
296.9 ± 7.9
23.3 ± 3.1 Ma
0.000 0.005 0.010 0.015
$^{39}Ar/^{40}Ar$

Figure IV.4a

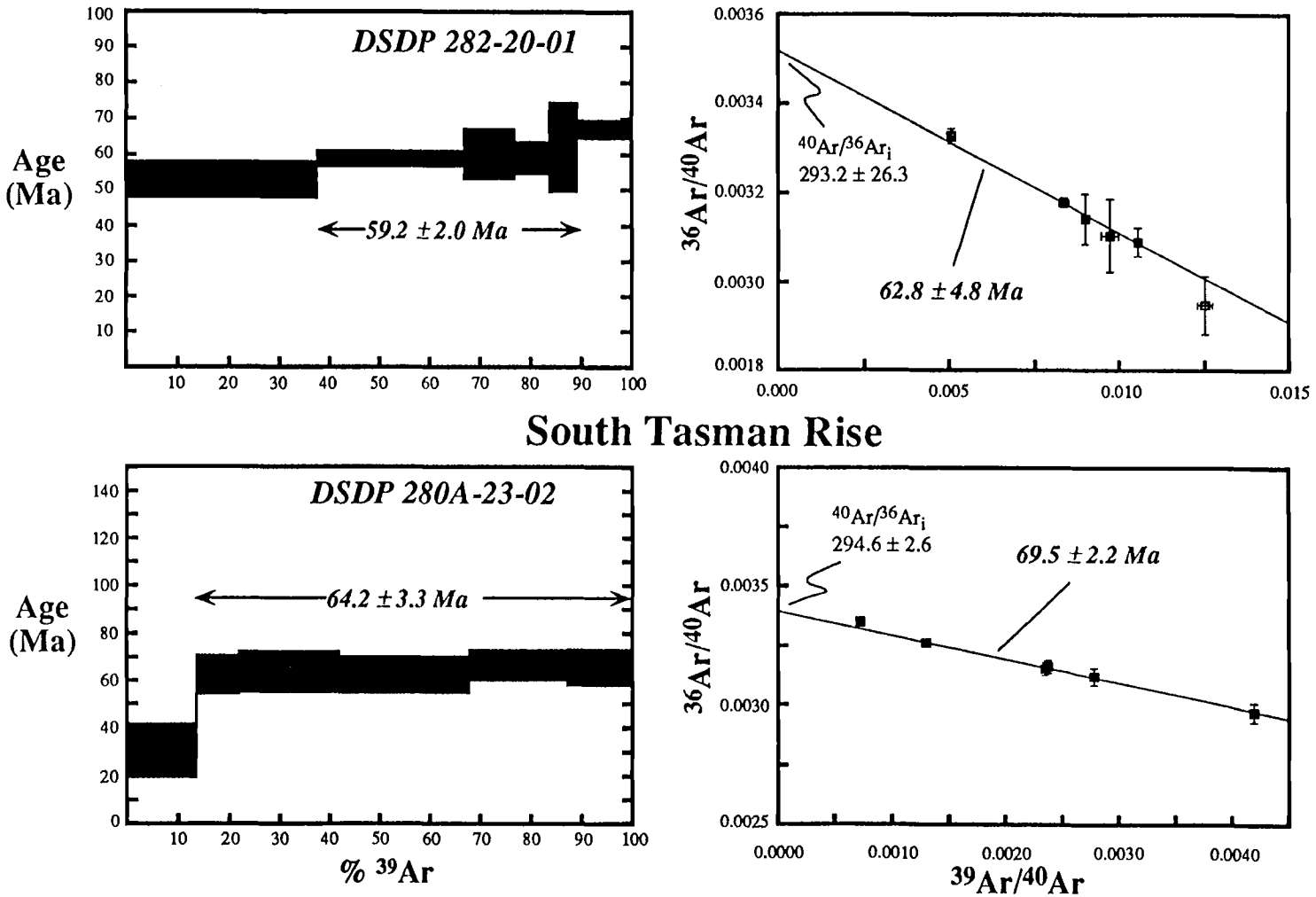
Western Tasmania Continental Margin
DSDP 282-20-01
Age (Ma)
59.2 ±2.0 Ma
$^{40}Ar/^{36}Ar_i$
293.2 ± 26.3
62.8 ±4.8 Ma
$^{36}Ar/^{40}Ar$
South Tasman Rise
DSDP 280A-23-02
64.2 ±3.3 Ma
$^{40}Ar/^{36}Ar_i$
294.6 ± 2.6
69.5 ±2.2 Ma
% ^{39}Ar
$^{39}Ar/^{40}Ar$

Figure IV.4b

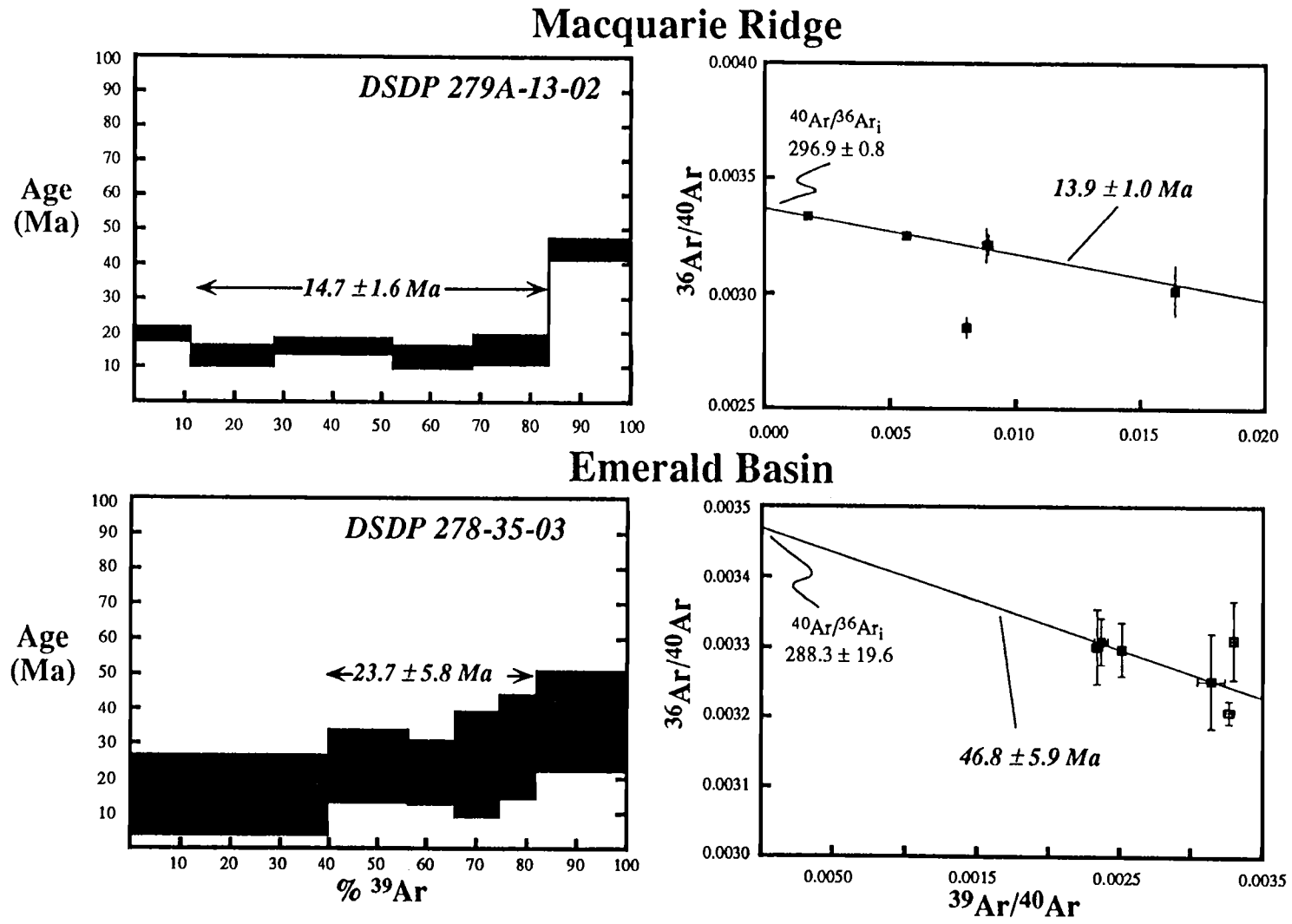
Macquarie Ridge
DSDP 279A-13-02
Age (Ma)
14.7 ±1.6 Ma
40Ar/36Ari
296.9 ± 0.8
13.9 ± 1.0 Ma
36Ar/40Ar
Emerald Basin
DSDP 278-35-03
Age (Ma)
23.7 ± 5.8 Ma
% 39Ar
40Ar/36Ari
288.3 ± 19.6
46.8 ± 5.9 Ma
36Ar/40Ar
39Ar/40Ar

Figure IV.4c

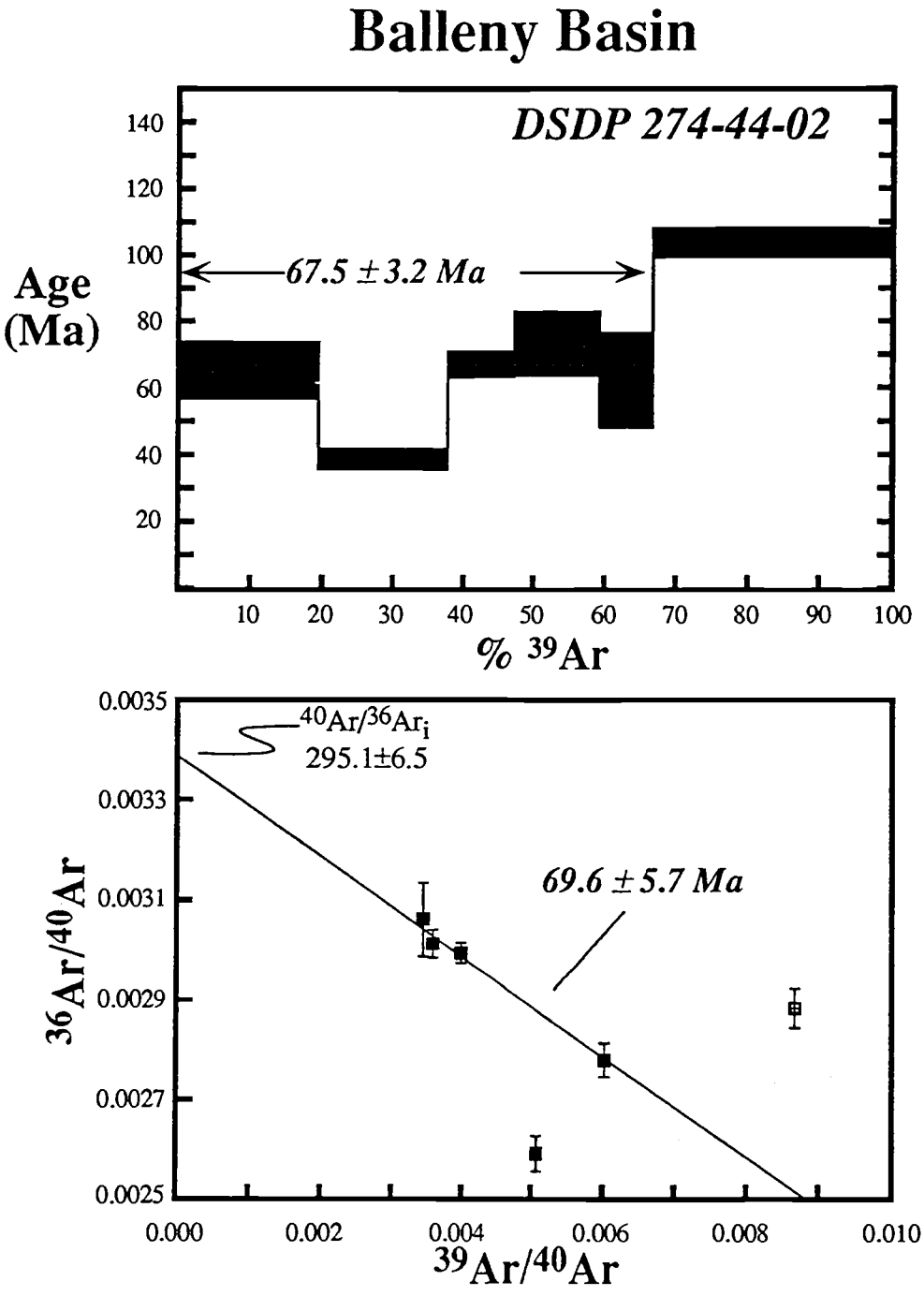
Balleny Basin
DSDP 274-44-02
Age (Ma)
140
120
100
80
60
40
20
67.5 ±3.2 Ma
10
20
30
40
50
60
70
80
90
100
% 39Ar
0.0035
0.0033
0.0031
0.0029
0.0027
0.0025
40Ar/36Ari
295.1±6.5
69.6 ±5.7 Ma
36Ar/40Ar
0.000
0.002
0.004
0.006
0.008
0.010
39Ar/40Ar

Figure IV.4d

A31, ~69 Ma), but equally old volcanism is indicated by the ^{40}Ar-^{39}Ar systematics of basalts from sites 280A and 282 along the western margin of Tasmania and the South Tasman Rise (Fig. IV.5). Massive, pillowed, and brecciated basalts were recovered at site 282 and site 280A encountered three massive basaltic layers separated by baked sediment [Overshine et al., 1974]. Samples from these continental margin sites have isochron ages older than plateau age estimates, but still within error. Comparisons of apparent plateau or isochron ages show that the age of site 280A basalts (69.5±2.2 Ma) overlapped or slightly preceded those at site 282 (62.8±4.8). The ^{40}Ar-^{39}Ar basalt age at site 280A is significantly older than surrounding mid-Eocene sediments (~55 Ma) [Leg 29 Shipboard Scientific Party, 1975]. In this case, the anomalously old age might indicate excess argon trapped during emplacement of the site 280A intrusion, but the initial $^{40}Ar/^{36}Ar$ value (294.6± 2.2) is near the atmospheric value (295.5) suggesting that this is not a problem.

Concordant plateau (14.7±1.6 Ma) and isochron (13.9±1.0 Ma) ages for seafloor at site 279A are slightly older than crust exposed farther south on Macquarie Island (11.5-9.7 Ma) [Duncan and Varne, 1988]. Presumably, both were derived from a common spreading center to the south. Recognized anomalies in the Emerald Basin are A12 and A13 (~34 Ma) and Oligocene sediment directly overlies basement [Overshine et al., 1974]. The plateau age estimate of 23.7±5.8 Ma for site 278 basalt is consistent with the magnetic anomalies and sediment cover, but the isochron age is believed to be unreasonably high (Fig. IV.5).

Balleny Basin site 274 is located on southwest Pacific seafloor older than A13 (36-39 Ma). Two geochemically distinct groups were sampled from this core. The most chemically enriched sample is celadonite-rich tuff, unsuitable for dating, although a young age is suspected based on chemical similarities to Balleny Island basalts (see below). The apparent age spectrum for a holocrystalline basalt clast from this core produced a plateau at 67.5±5.7 Ma (step two is unexplainably low) and an isochron age of 69.6±5.7 Ma. These ages are considerably older than A13 (~36 Ma), but younger than the oldest recognized

anomalies in this region (i.e., A 34, ~84 Ma) [Mayes et al., 1990]. Site 274 apparently contains both older, MORB-like seafloor and younger volcanic products of Balleny Island. The volcanic section in the core was originally interpreted as a flow breccia [Ford, 1975], but the ages and chemistry are more consistent with a volcanic debris flow.

Major Element Variations

With one exception, the basalts of DSDP Legs 28 and 29 basalts have major element compositions typical of basalts erupted in an ocean basin setting. The exception is the Naturaliste Plateau basaltic andesite (DSDP 264). The major element systematics of the basalts are complicated by alteration of whole-rock samples and the wide geographical distribution of sample sites. Although there can be no direct petrogenetic relationships among these widely dispersed basalts, some general observations are offered for perspective (Fig. IV.7).

West of the AAD, glass samples from sites 267, 266, and 265 show a progressive decline in CaO/Al_2O_3 (~.85 to .60) with decreasing age; considerable variability despite the relative restricted section of the SEIR. To the east, a simple mid-ocean spreading origin for all the DSDP basalts is less clear. Basalts erupted along the continental margin of Tasmania (282), the South Tasman Rise (280A), and the Tasman Sea (238) are relatively primitive (10.5 to 8.0% MgO), showing a large range in CaO/Al_2O_3 (.38 to .88). The low CaO/Al_2O_3 of whole rock samples undoubtedly reflects their pervasive alteration. DSDP 278, 279A, and 280A basalts are low in TiO_2 and similar to SEIR basalts in the vicinity of AAD [Pyle and Christie, 1994]. Some of the major element variations east of the AAD reflect different tectonic settings, but variations of TiO_2 and FeO_t at relatively high MgO contents for SEIR basalts west of the AAD reflect change melting and/or source conditions beneath the ridge.

Figure IV.5 Major element variations of DSDP Leg 28 and Leg 29 samples. Glass (denoted by cross behind symbol) and whole rock samples from the same site are connected by lines. Two chemically distinct samples from the Balleny basin (site 274) are enclosed with a field.

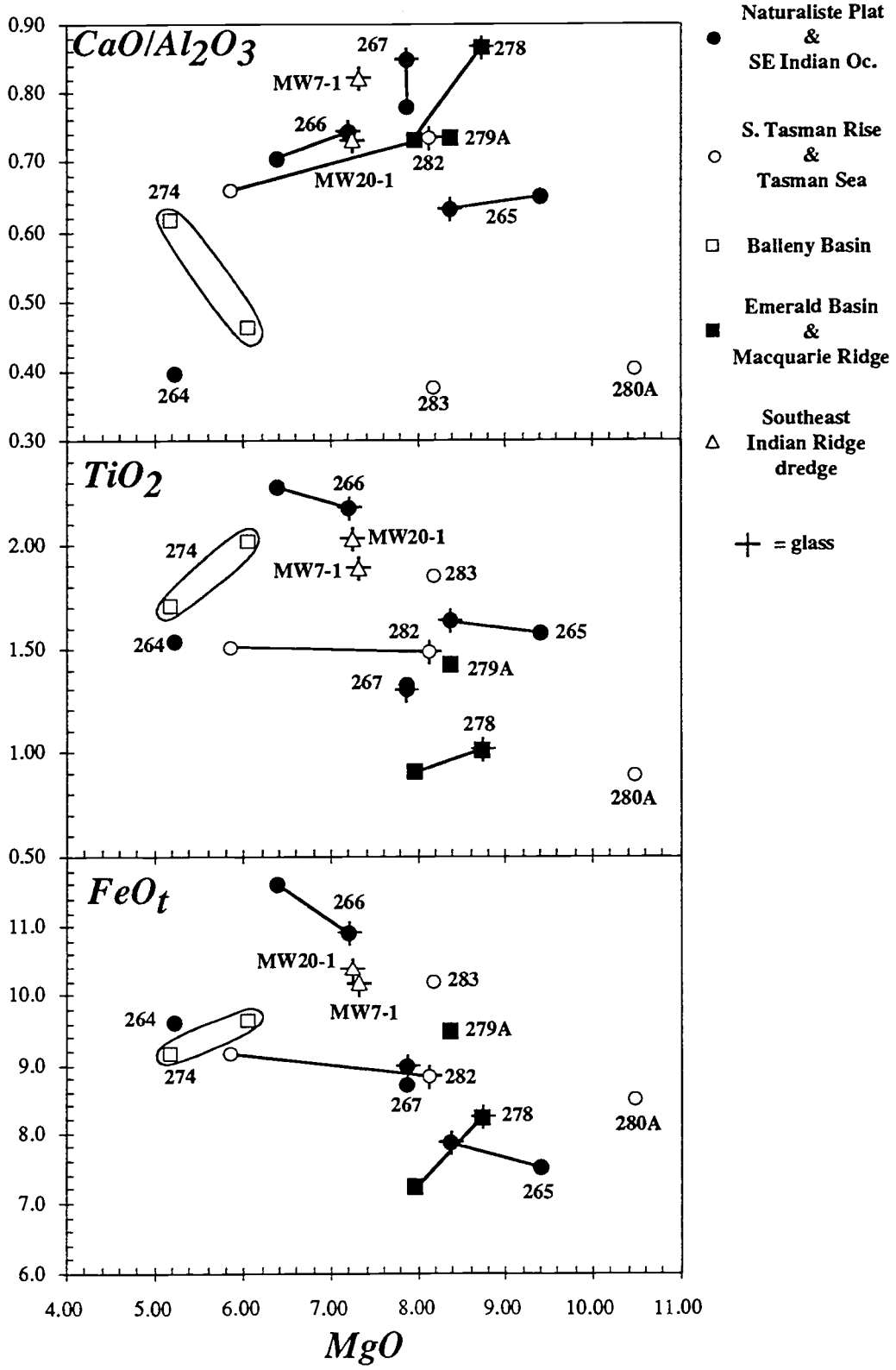
CaO/Al2O3
TiO2
FeOt
MgO
0.90
0.80
0.70
0.60
0.50
0.40
0.30
2.00
1.50
1.00
0.50
11.0
10.0
9.0
8.0
7.0
6.0
4.00
5.00
6.00
7.00
8.00
9.00
10.00
11.00
267
278
MW7-1
266
279A
282
MW20-1
274
265
264
283
280A
MW20-1
MW7-1
283
279A
MW7-1
Naturaliste Plat & SE Indian Oc.
S. Tasman Rise & Tasman Sea
Balleny Basin
Emerald Basin & Macquarie Ridge
Southeast Indian Ridge dredge
= glass

Figure IV.5

Trace Element and Isotope Variations

For the DSDP basalts from ~110° E west of the AAD, rare earth element patterns evolve from light rare earth depleted to light rare earth enriched (Fig. IV.6) with decreasing age. Highly incompatible elements, as well as $^{87}Sr/^{86}Sr$, $^{207}Pb/^{204}Pb$, and $^{208}Pb/^{204}Pb$ increase with the rare earth element fractionations indicating variations in the mantle source composition (Fig. IV.7-IV.10).

The Naturaliste Plateau (DSDP 264) basaltic andesite is light rare earth element enriched and distinctly depleted in Ta and Nb relative to Th and La when compared to primitive mantle (Fig. IV.6 and IV.7). Unusually high $^{87}Sr/^{86}Sr$, $^{208}Pb/^{204}Pb$, and $^{207}Pb/^{204}Pb$ at low $^{206}Pb/^{204}Pb$ values clearly implies that volcanism here is not compositionally related to normal seafloor spreading or hot spot volcanism(Fig. IV 8-IV.10). A more likely source for the Naturaliste Plateau basaltic andesite is subcontinental lithospheric source, not asthenospheric mantle.

East of the AAD, trace element and isotopic systematics require contributions from a variety of mantle sources. The compositional influence of the Balleny plume can be detected in Balleny Basin (DSDP 274-45) and Macquarie Ridge basalts (DSDP 279A). Both of these basalts have light rare earth enriched patterns and broad, convex-up primitive mantle spider diagram patterns (Fig. IV.6). The enriched Balleny Basin tuff is high in $^{206}Pb/^{204}Pb$ and $^{86}Sr/^{86}Sr$, with values nearly identical to Balleny Island compositions (Fig. IV. 8-IV.10) [Hart, 1984; Lanyon et al., 1993]. The Macquarie Ridge basalt (site 279A) shows less of a Balleny hot spot influence, but it is enriched compared to other DSDP samples in the region. The Macquarie Ridge basalt is similar to Macquarie Island basalts, suggesting a common upper mantle MORB source, slightly contaminated by the Balleny plume (Fig.IV.6-IV.10) [Griffith and Varne, 1980; Lanyon et al., 1993].

The other Southeast Pacific basalts also appear to have been derived from a depleted MORB mantle source. The Emerald Basin (site 278) and Balleny Basin (DSDP

Figure IV.6 Rare earth element patterns for DSDP Leg 28 and Leg 29 glass and whole rock samples. Normalizing values are those of Boyonton [1984] for 'average' ordinary achondrites. The gray field represents the range of SEIR AAD glass samples analyzed in this study and the black solid line is the most depleted SEIR MORB glass (MW17-26) recovered from Zone A (see Table IV.4).

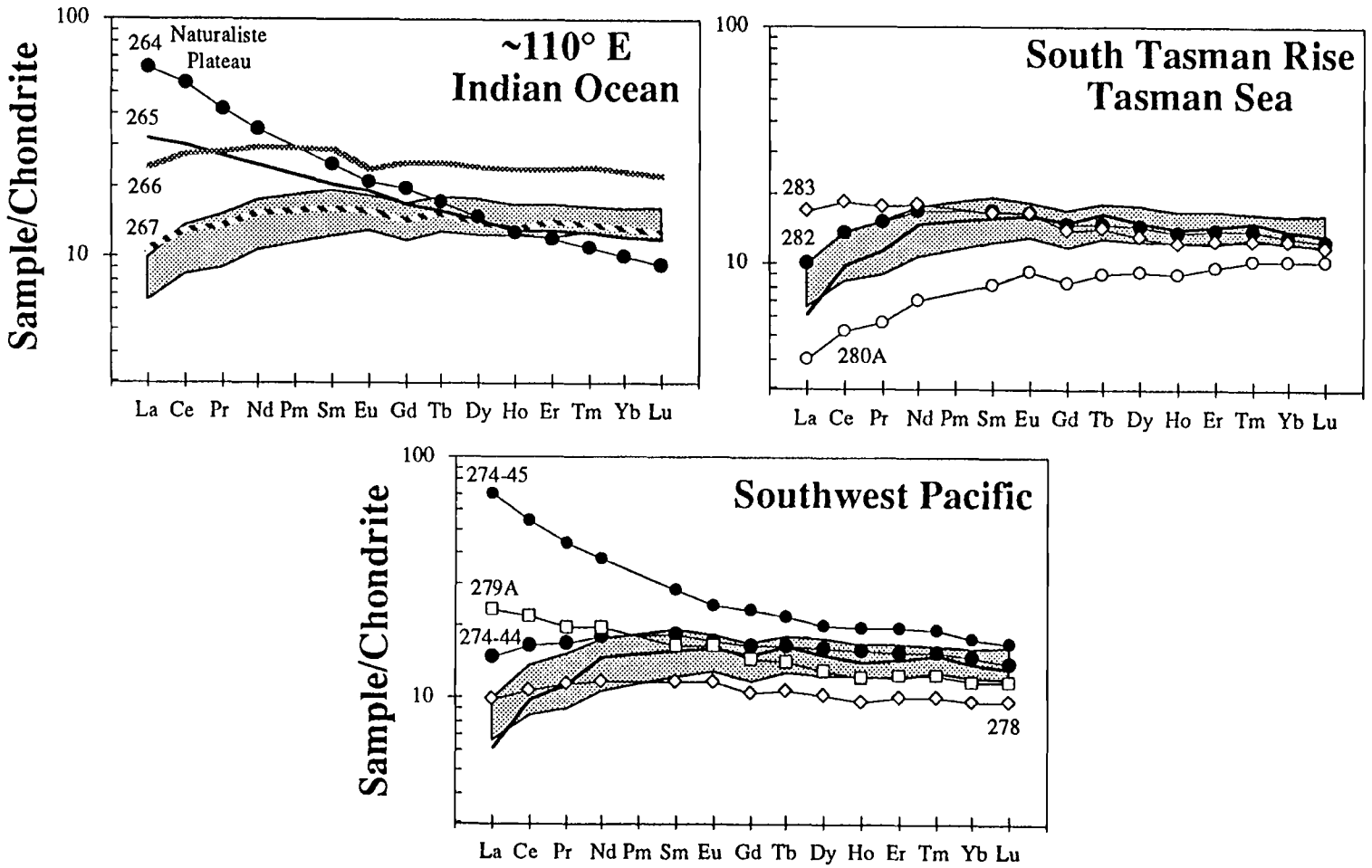
Sample/Chondrite
100
10
264 Naturaliste Plateau
265
266
267
~110° E
Indian Ocean
La Ce Pr Nd Pm Sm Eu Gd Tb Dy Ho Er Tm Yb Lu
South Tasman Rise
Tasman Sea
283
282
280A
274-45
279A
274-44
278
Southwest Pacific

Figure IV.6

Figure IV.7 Primitive mantle normalized spider diagrams for DSDP Leg 28 and Leg 29 samples. Normalizing values are those of Sun and McDonough [1989]. Shaded field in upper left plot shows the approximate range of SEIR MORB with an Indian Ocean isotopic signature from the present AAD ridge axis. The shaded field in other diagrams covers the range of SEIR MORB with a Pacific Ocean isotopic signature from off-axis samples within Zone A (i.e., MW20-01 and MW07-01). The unlabeled dark black line in upper right and lower diagrams is the primitive mantle normalized pattern of MW17-26.

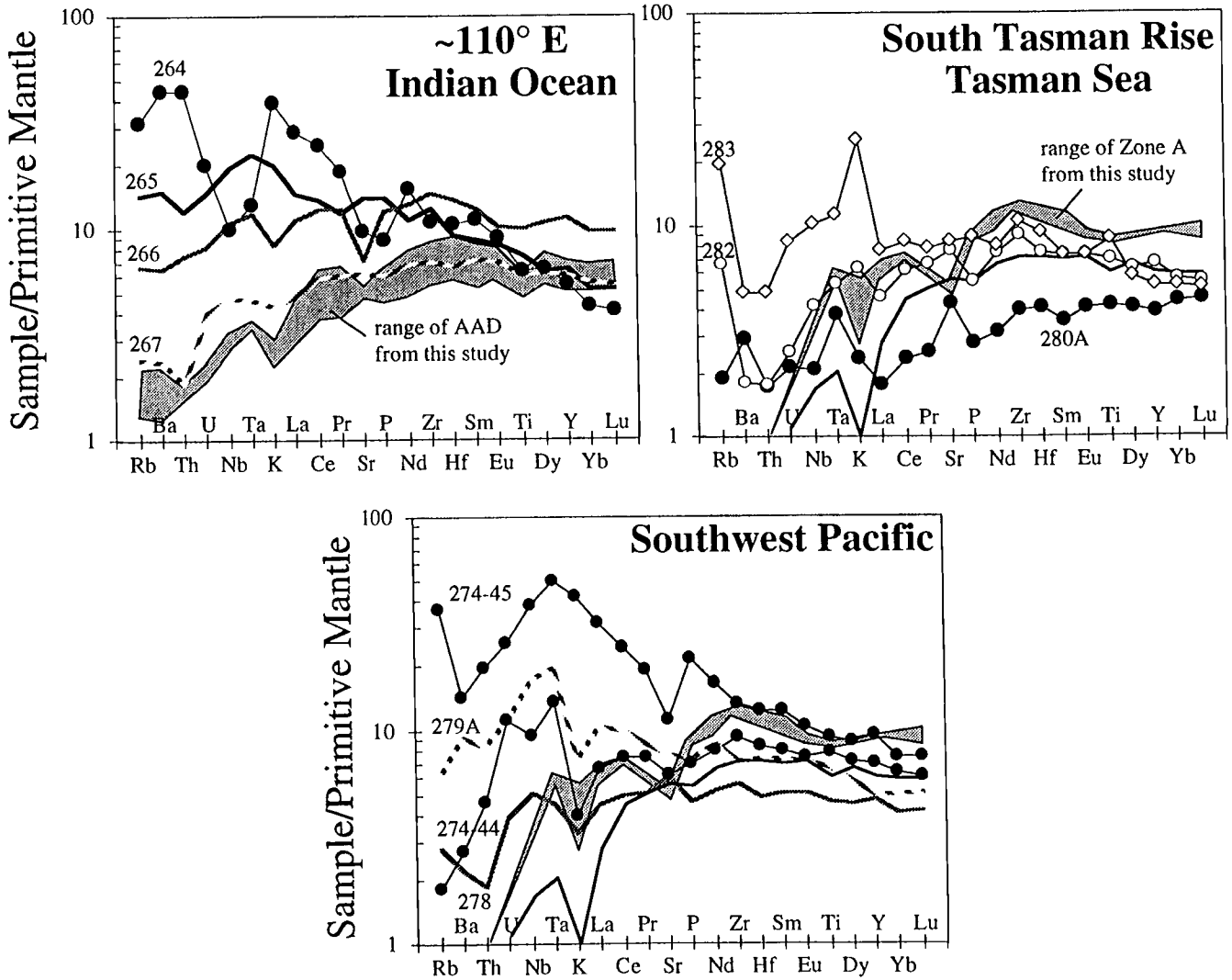
~110° E
Indian Ocean
South Tasman Rise
Tasman Sea
Southwest Pacific
Sample/Primitive Mantle
100
10
1
264
265
266
267
range of AAD
from this study
283
282
280A
range of Zone A
from this study
274-45
279A
274/44
278
Ba U Ta La Pr P Zr Sm Ti Y Lu
Rb Th Nb K Ce Sr Nd Hf Eu Dy Yb

Figure IV.7

Figure IV.8 $^{87}Sr/^{86}Sr$-$^{206}Pb/^{204}Pb$ variations for Leg 28 and 29 DSDP basement samples. Indian Ocean MORB has higher $^{87}Sr/^{86}Sr$, lower $^{143}Nd/^{144}Nd$, and high $^{208}Pb/^{204}Pb$, $^{207}Pb/^{204}Pb$ ratios at a given $^{206}Pb/^{204}Pb$ value compared to Pacific and North Atlantic MORB [e.g., Subbarao and Hedge, 1973; Hedge et al., 1973; Dupre and Allègre, 1983; Hamelin et al., 1985; Hamelin and Allègre, 1985; Hart, 1984; Michard et al., 1986; Price et al., 1986; Dosso et al., 1988; Klein et al., 1988; Mahoney et al., 1989]. Also shown are the Pacific MORB (Zone A, striped field) and Indian MORB (AAD, stippled field) groups from vicinity of the AAD. Hot spot and plateau compositions surrounding this region are labeled: K-Kerguelen; H-Heard; St. P-St. Paul; Am-Amsterdam; NP-Naturaliste Plateau; Ba-Balleny; Indian Ocean hotspot fields. Data for Kerguelen Plateau and Broken Ridge dredges, as well as fields for Naturaliste Plateau dredges and Kerguelen Plateau ODP sites taken from Mahoney et al.[1994] and references therein.

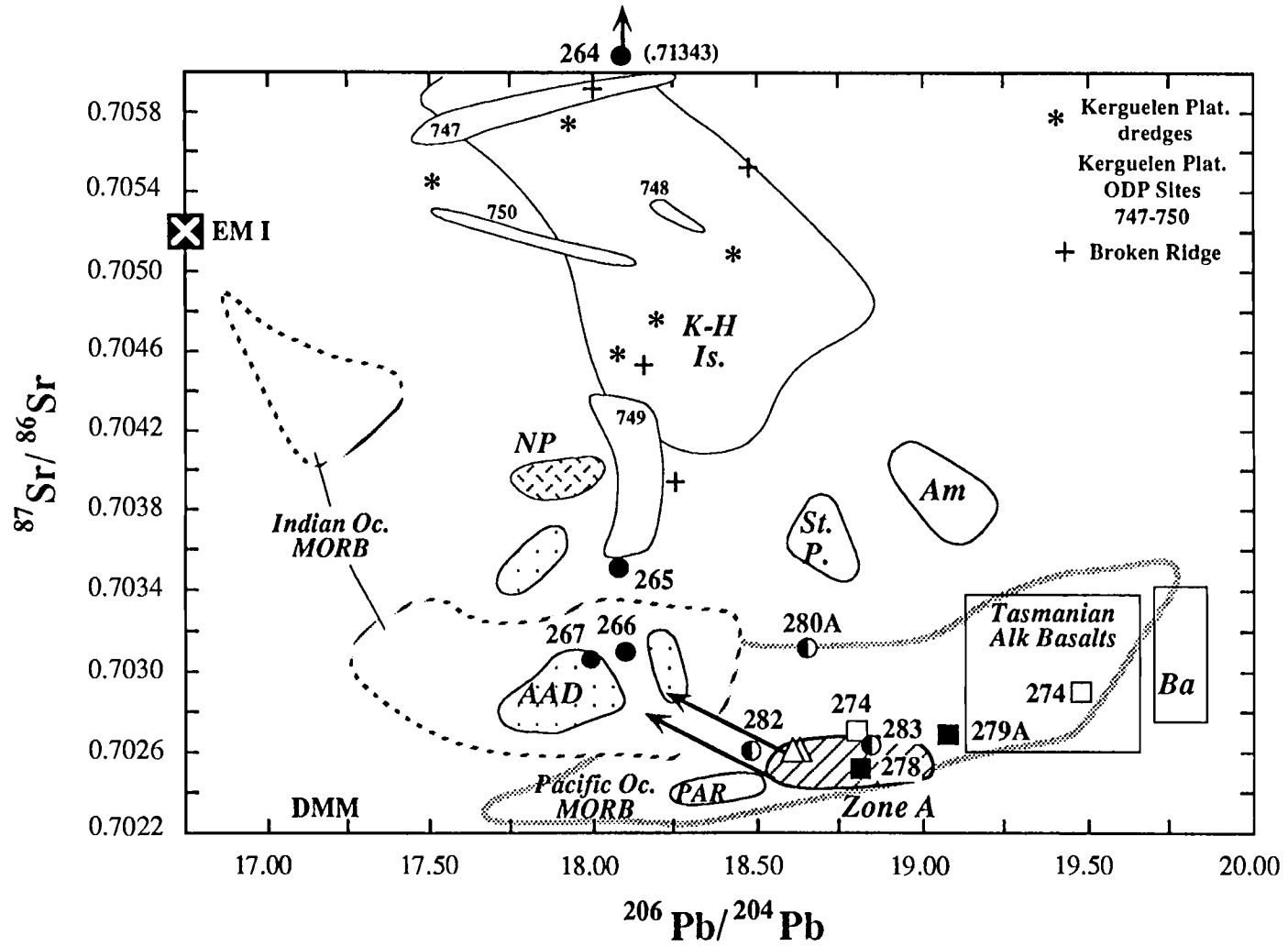
264 (.71343)
0.7058
0.7054
0.7050
0.7046
0.7042
0.7038
0.7034
0.7030
0.7026
0.7022
87Sr/86Sr
17.00
17.50
18.00
18.50
19.00
19.50
20.00
206 Pb/204 Pb
EM I
747
748
750
749
K-H Is.
NP
Indian Oc. MORB
St. P.
Am
265
267
266
280A
AAD
Tasmanian Alk Basalts
274
Ba
282
283
279A
278
Pacific Oc. MORB
PAR
Zone A
DMM
Kerguelen Plat. dredges
Kerguelen Plat. ODP Sites 747-750
Broken Ridge

Figure IV.8

Figure IV.9 $^{208}Pb/^{204}Pb$-$^{206}Pb/^{204}Pb$ variations for Leg 28 and 29 DSDP basement samples. The dark line across the diagram is the Northern Hemisphere Reference Line (the average isotopic composition of oceanic basalts in the northern hemisphere) [Hart, 1986]. Δ 8/4 and Δ 7/4 are calculated relative to this line. Fields and references as in Figure IV.8.

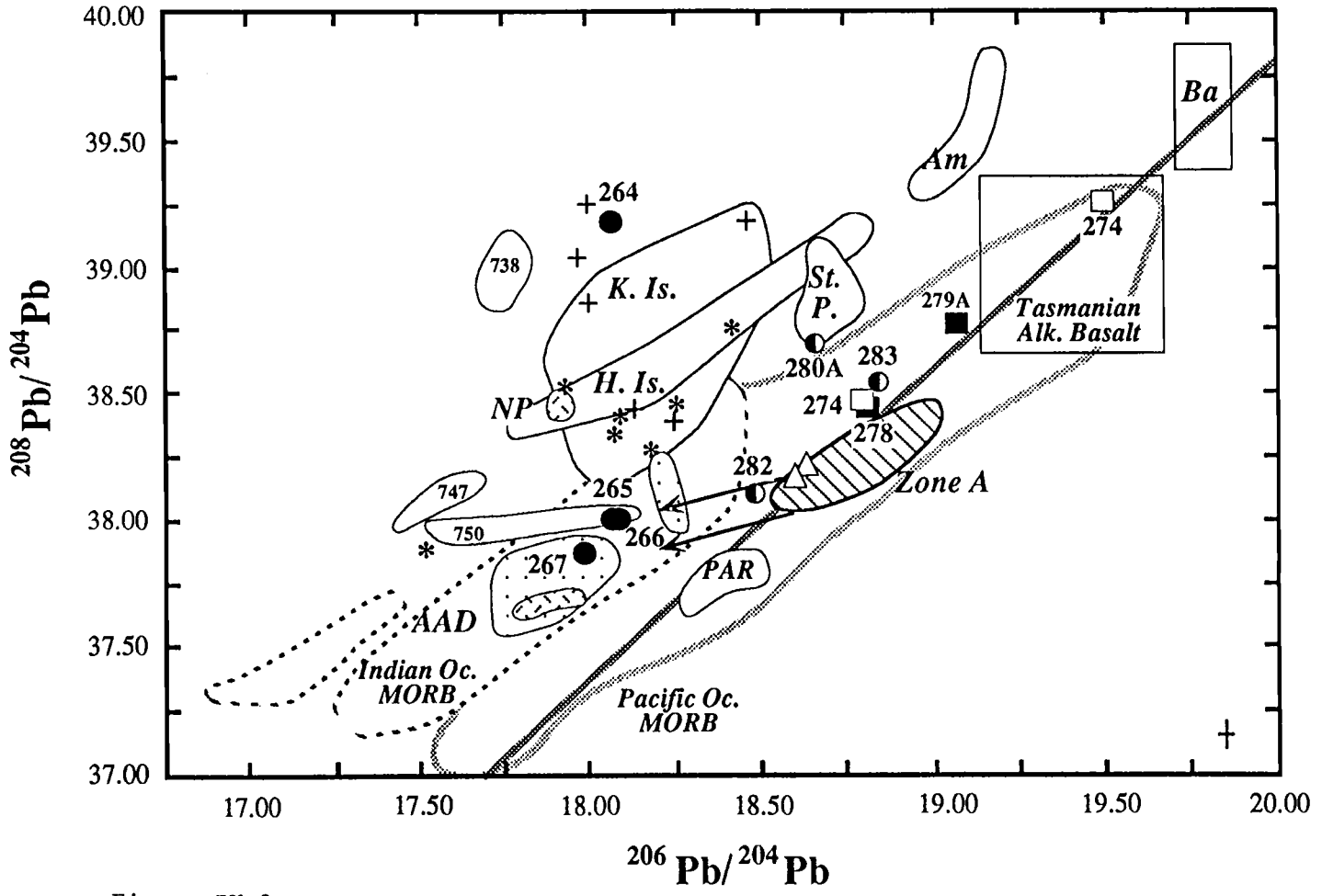
40.00
39.50
39.00
38.50
38.00
37.50
37.00
17.00
17.50
18.00
18.50
19.00
19.50
20.00
$^{208}Pb/^{204}Pb$
$^{206}Pb/^{204}Pb$
Ba
Am
264
738
K. Is.
St.
P.
274
279A
Tasmanian
Alk. Basalt
280A
283
NP
H. Is.
274
278
282
Zone A
265
747
750
266
267
PAR
AAD
Indian Oc.
MORB
Pacific Oc.
MORB

Figure IV.9

Figure IV.10 $^{207}Pb/^{204}Pb$-$^{206}Pb/^{204}Pb$ variations for Leg 28 and 29 DSDP basement samples. Fields and references as in Figure IV.8.

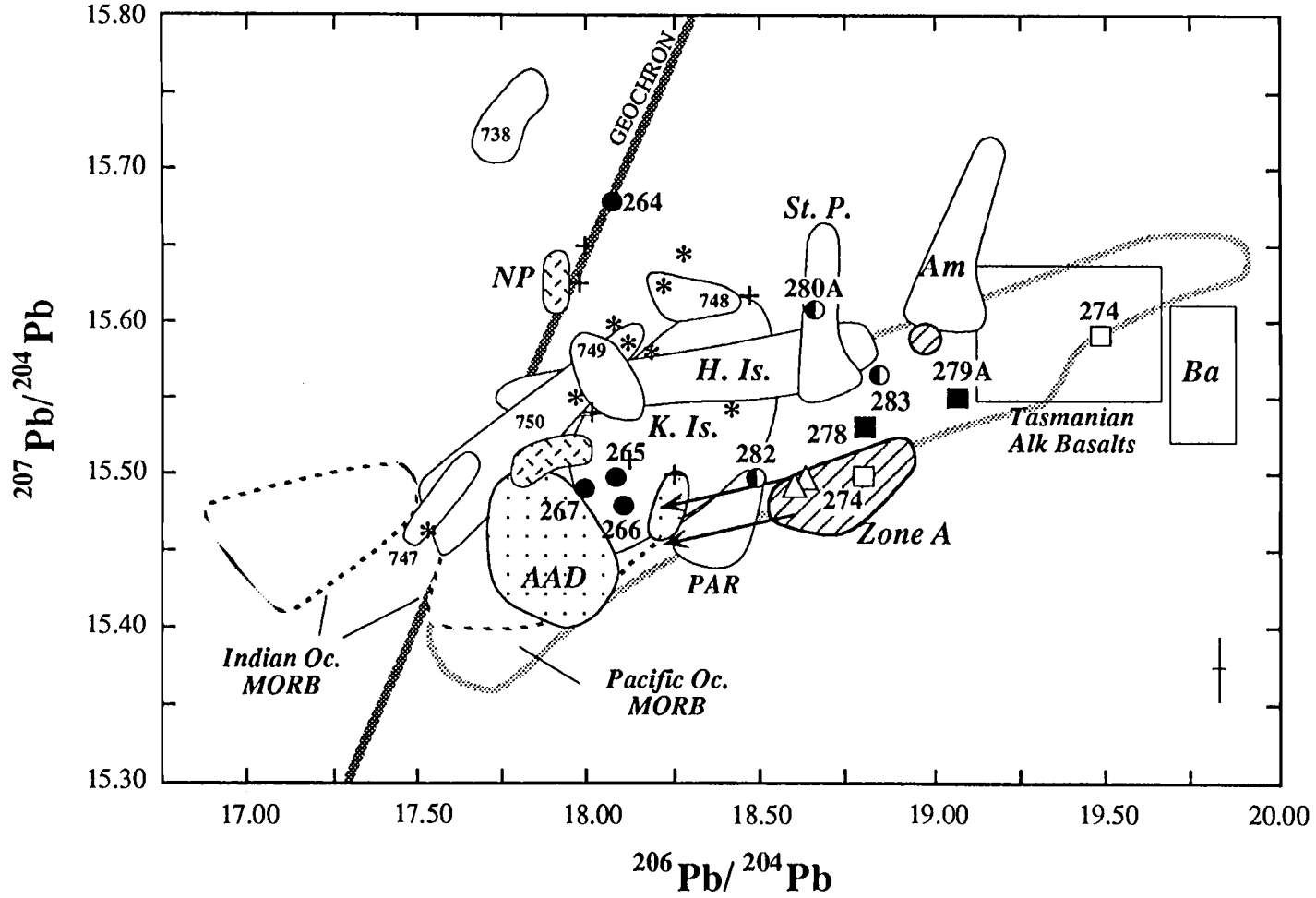
15.80
15.70
15.60
15.50
15.40
15.30
17.00
17.50
18.00
18.50
19.00
19.50
20.00
$^{207}Pb/^{204}Pb$
$^{206}Pb/^{204}Pb$
GEOCHRON
738
264
NP
St. P.
Am
280A
748
274
749
H. Is.
279A
Ba
283
750
K. Is.
278
Tasmanian
Alk Basalts
265
282
267
266
274
Zone A
747
AAD
PAR
Indian Oc.
MORB
Pacific Oc.
MORB

Figure IV.10

274-44) basalts have sub-parallel, flat to slightly depleted rare earth element patterns [c.f., Schilling and Ridley, 1974]. The convex-up curvature between La and Sm is similar to present day MORB from east of the AAD. Isotopically, these basalts fall within or near the fields defined by Pacific-type MORB east of the AAD (i.e., Zone A), but they have slightly higher $^{208}Pb/^{204}Pb$ and $^{207}Pb/^{204}Pb$ values (Fig. IV.7-IV.10).

The trace element systematics of basalts surrounding the South Tasman Rise indicate a source comparable to or slightly more depleted that the MORB source beneath the Balleny and Emerald Basins. The rare earth element pattern of DSDP 282 basalt resembles those of SEIR basalts from east of the AAD ($La_n/Sm_n<1$, $Sm_n/Yb_n>1$, and $Ce_n/Yb_n \sim 1$). By contrast, DSDP 280A basalt is unique in being exceptionally light rare earth depleted ($La_n/Sm_n=.49$, $Ce_n/Yb_n=.50$). Isotopically, DSDP 283 basalt have $^{87}Sr/^{86}Sr$ and $^{206}Pb/^{204}Pb$ values typical of other Pacific Ocean-type compositions but higher $^{208}Pb/^{204}Pb$ and $^{207}Pb/^{204}Pb$ values. Basalts from the western margin of Tasmania (site 282) and South Tasman Rise (site 280A) lie outside the Pacific Ocean isotopic fields for this region primarily because of low $^{206}Pb/^{204}Pb$ values. In addition, high $^{87}Sr/^{86}Sr$, $^{208}Pb/^{204}Pb$, and $^{207}Pb/^{204}Pb$ values relative to the $^{206}Pb/^{204}Pb$ composition suggests Indian Ocean-type source for DSDP 280A basalt.

DISCUSSION

Continental rifting and opening of an ocean basin requires flow of sub-oceanic asthenosphere into a region previously occupied by sub-continental lithosphere. Filling this upper mantle 'gap' could conceivably be accomplished by mantle upwelling from beneath and/or by lateral migration of asthenosphere along the ridge axis. Qualitatively, this process can be assessed by tracing the regional distribution of upper mantle sources in the Southern Ocean as Australia and Antarctic drifted apart. In this region, four distinct mantle sources can be traced isotopically: the Kerguelen plume (mixed EMI and EMII-type) [Weis et al., 1992; Weis et al., 1993], the Balleny plume (HIMU-type) [Lanyon et al., 1993], Pacific Ocean upper mantle, and Indian Ocean upper mantle (terminology of Zindler

and Hart [1986]). Alvarez [1990] proposed that upper mantle flow may be contained or obstructed by the roots of continents that reach hundreds of kilometers into the upper mantle. Similarly, excess volcanism associated with hot spots and large oceanic plateaus may promote upper mantle flow. Several bathymetric features in the southeast Indian and southwest Pacific Ocean are related either to continental remnants embedded in the upper mantle (e.g., South Tasman Rise and Naturaliste Plateau) or to oceanic flood basalts provinces (e.g., Kerguelen Plateau). The relative positions of continental material and hot spot activity through time are important for understanding their influence on upper mantle migration during the opening of this Southern Ocean basin. Reconstruction for the opening of the Southern Ocean between Australia and Antarctica are shown in Figure IV.11.

Regional Plate Motions

Continental rifting between Australia and Antarctica began between 110-90 Ma and propagated from west to east, culminating a period of extension (>300 km) that began at ~160 Ma [Powell et al., 1988]. Contemporaneous with continental rifting are the earliest manifestations of the Kerguelen hotspot recorded by extensive flood basalt volcanism in western Australia (Bunbury Basalts, 121-105 Ma) and northeastern India (Rajmahal Traps, 115-108 Ma) [Playford et al., 1976; Baksi et al., 1987; Morgan, 1981; Mahoney et al., 1983; Duncan and Richards, 1991]. Seafloor spreading between Australia and Antarctica began at ~96 Ma [Veevers, 1986] and progressed in two phases. An early slow spreading phase occurred from 84 Ma (anomaly 34) through 43 Ma (anomaly 18) [Cande and Mutter, 1982]. During this slow spreading phase, the eastern part of Broken Ridge and the northeastern Kerguelen Plateau were constructed by a Kerguelen hotspot centered on or near the SEIR [Leclaire et al., 1987; Schlich and Wise, 1988]. At A18 time, spreading ceased in what is now known as the Wharton basin, and a second, faster spreading phase (>60 mm/yr full rate) began between Australia and Antarctica and continues to the present

Figure IV.11 Tectonic reconstruction of the Southeast Indian Ocean and Southwest Pacific Ocean at A) 66 Ma, B) 57.5 Ma, C) 44 Ma, D) 37 Ma, E) 20.6 Ma, F) 10 Ma [Veevers et al., 1984]. The appearance of seafloor sampled by the DSDP sites in this study are shown based on their magnetic anomaly age estimates. The South Tasman Rise was rifted at ~40 Ma, shortly before spreading rates in this Southern Ocean basin increased from an initial slow spreading phase.

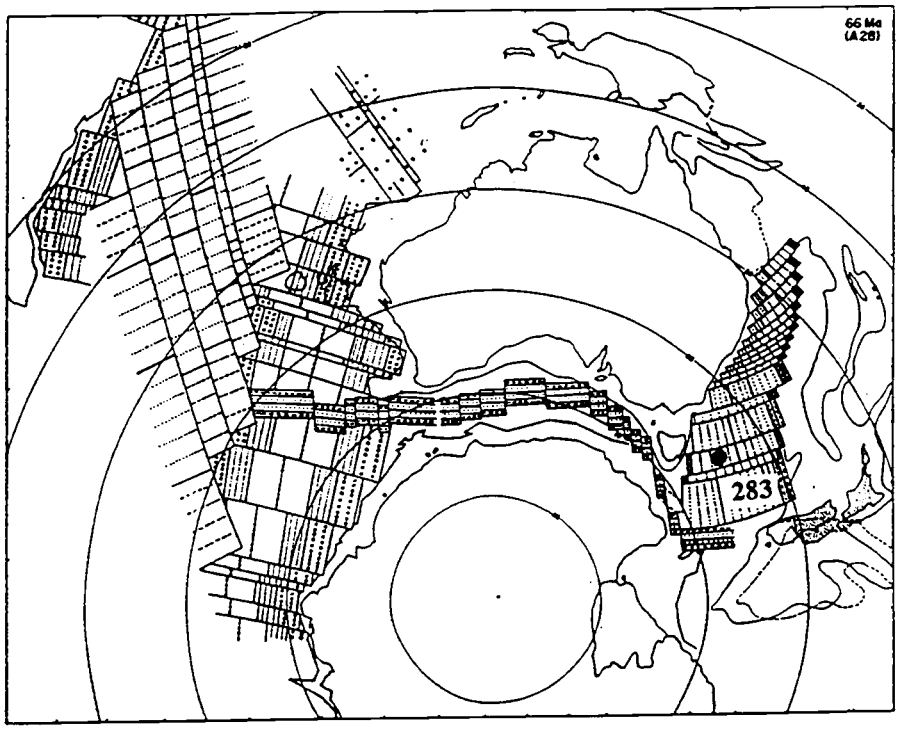

A 66 Ma (A28): continued rapid spreading east of India, and slow spreading south of Australia. Rapid spreading in Tasman Basin, involving ridge-jumps to Australia and asymmetrical spreading.

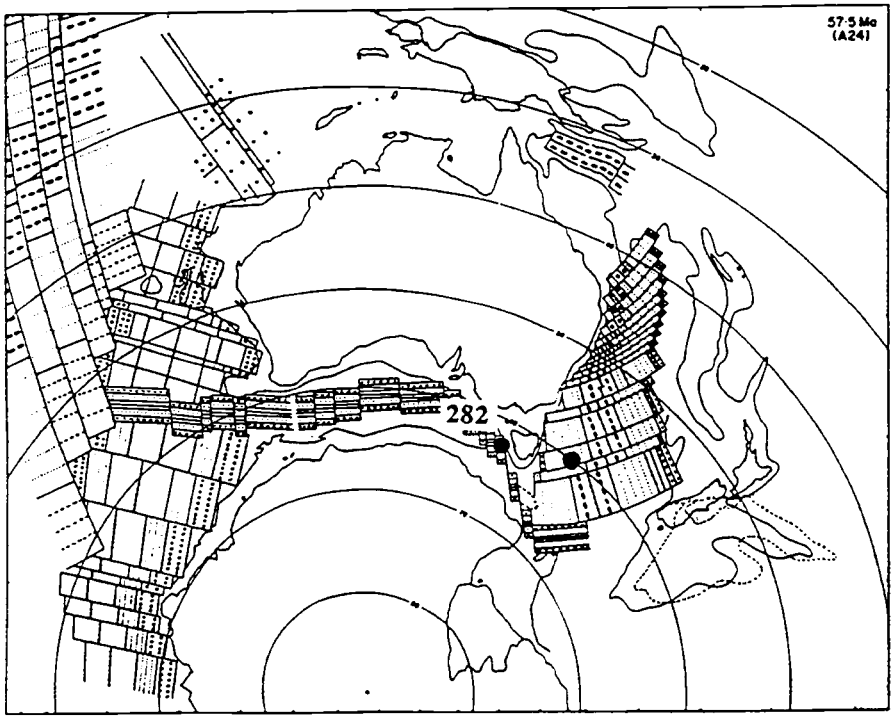

B 57.5 Ma (A24): continued rapid spreading east of India; end of spreading south-east of Australia; beginning and end of spreading between north-east Australia and the Papuan Peninsula; and continued slow spreading between Australia and Antarctica. Frame of map shifted eastward to show New Zealand.

Figure IV.11A, B

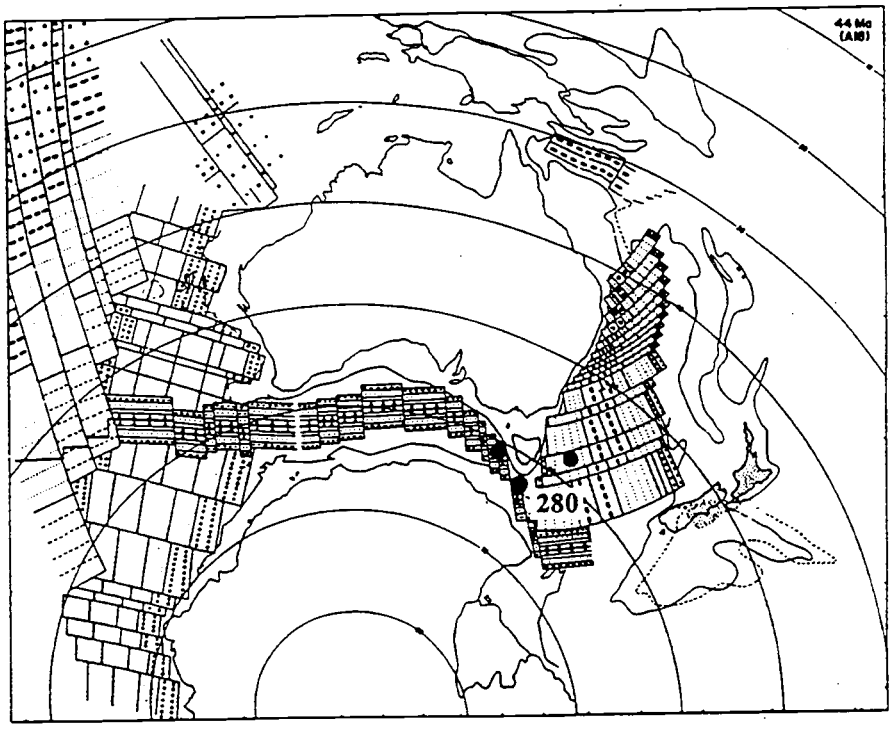

C 44 Ma (A18): final phase of spreading south-east of India, and continued slow spreading between Australia and Antarctica; westward propagation of South-east Indian Ocean Ridge.

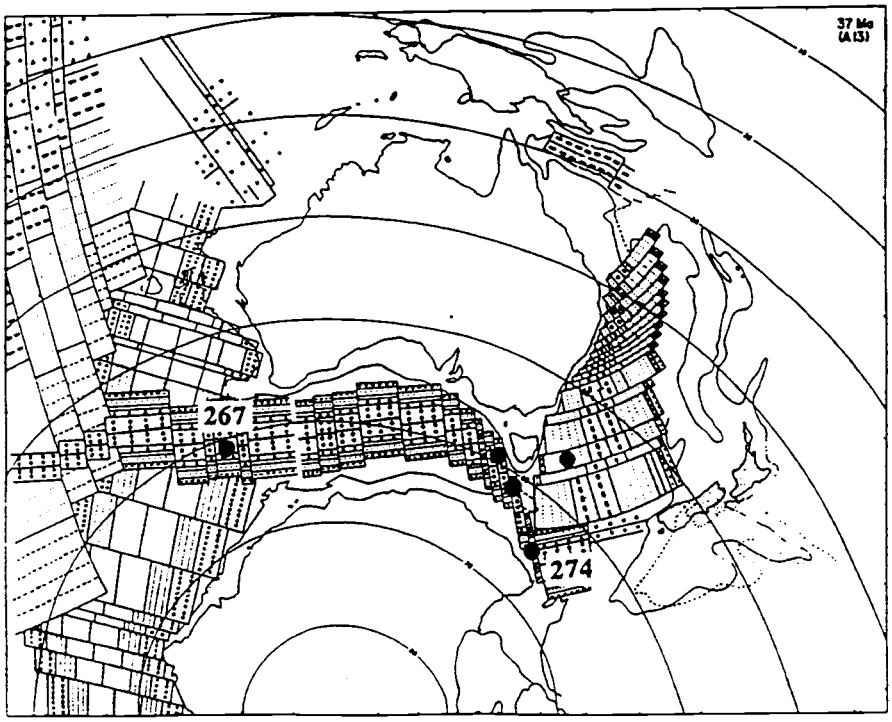

D 37 Ma (A13): rapid spreading between Australia and Antarctica and to the west.

Figure IV.11C, D

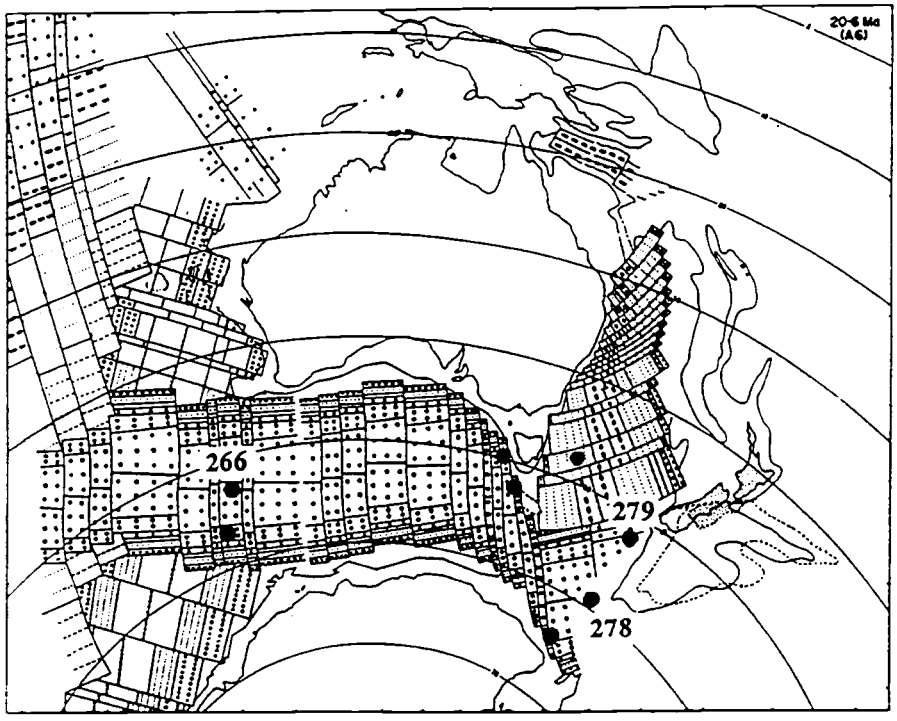

E 20.6 Ma (A6): continued rapid spreading between Australia and Antarctica, and to the west.

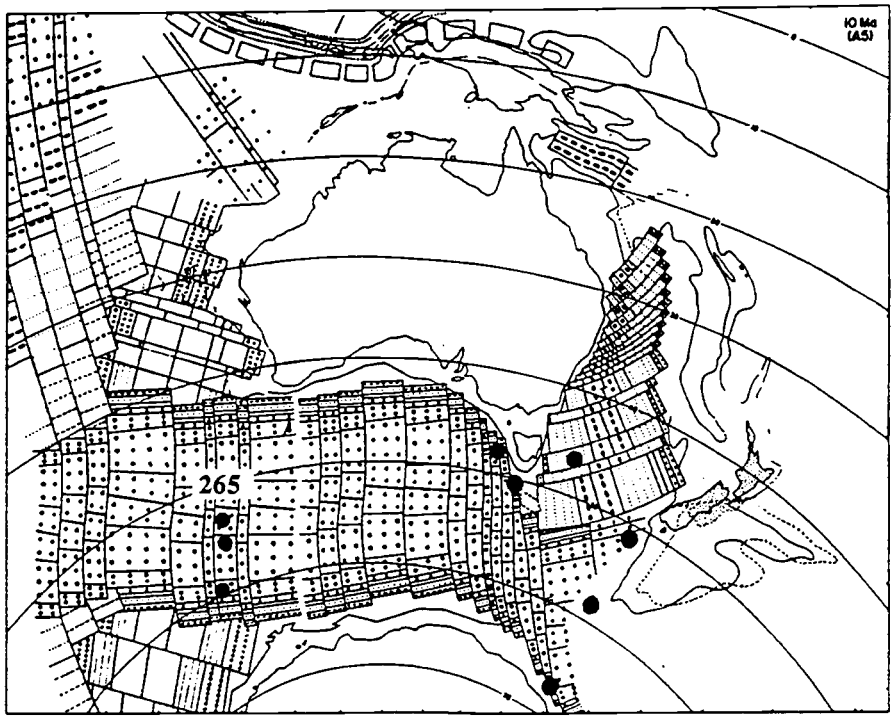

F 10 Ma (A5): continued rapid spreading between Australia and Antarctica, and to the west. Final adjustment of distended South Tasman Rise. Appearance in north of leading edge of Sundaland (dotted pattern) and Pacific Plates with an outer non-volcanic arc (blocks) and an inner arc (broken lines).

Figure IV.11E, F

(~74 mm/yr) [Vogt et al., 1984; Royer and Sandwell, 1989]. This new spreading axis eventually split off the Broken Ridge Plateau from the Kerguelen Plateau between A18 and A13 [Royer and Sandwell, 1989], establishing the present configuration of the SEIR (Fig. IV.4). Throughout this period, the Kerguelen hot spot was very active and presumably imparted a significant compositional contribution to the upper mantle in this region.

East of the AAD, the early, slow spreading between Australia and Antarctica coincided with spreading in the Tasman Sea from ~A34 to A24 (55 Ma) and spreading along the Pacific-Antarctic Ridge [Veevers et al., 1984; Hayes and Ringis, 1973; Weissel and Hayes, 1977; Mayes et al., 1990]. The Tasman Sea and the Pacific-Antarctic spreading systems may have been contiguous until A24, after which Tasman Basin spreading ceased and transform motion along the Macquarie Ridge progressively offset the two spreading systems [Weissel et al., 1977; Stock and Molnar, 1987]. Transform motion along Macquarie Ridge since the Miocene and the migration of the SEIR away from Antarctica have produced a series of short spreading segments offset by large transforms that translate the Pacific-Antarctic Ridge north to join the SEIR. The final separation of Australia and Antarctica, marked by rifting of the South Tasman Rise, is not well constrained but presumably occurred between A18 and A13 (42-36 Ma) [Royer and Sandwell, 1989; Hinz et al., unpub. manuscript]. Circum-Antarctic deep water circulation remained blocked by the South Tasman Rise until late Oligocene (~30 Ma) [Leg 29 Shipboard Scientific Party, 1975]. The effectiveness of this small continental fragment as a barrier to upper mantle flow is unknown. Assuming Pacific mantle has been migrating at a steady 25 mm/yr migration rate, the South Tasman Rise and the position of the isotopic boundary coincide at 50 Ma, slightly before the estimated rifting event.

Unlike the Kerguelen-SEIR system, hot spot activity in the Southeast Pacific is not closely associated with spreading ridges. The Tasmantid and Lord Howe volcanic chains in the Tasman Sea are age-progressive along the eastern Australian continent [e.g., McDougall and Duncan, 1988; Eggins et al., 1991]. The oldest known volcanoes directly

associated with these hotspots are ~40 Ma, although plate motion models suggest volcanism in northeast Australia at 80 Ma may be related to these hot spot tracks [Johnson, 1989]. The Balleny hotspot track stretches across the Southern Ocean basin from Tasmania to the Antarctic continental margin [Lanyon et al., 1993]. Volcanic activity in this group began at ~36 Ma and continues to the present in the Balleny Islands [Duncan, 1981]. Of these eastern hot spots, only Balleny has encountered a spreading ridge as it moved from the Australian Plate to the Antarctic Plate.

The transition from slow to fast spreading at A18 and rifting of the Kerguelen Plateau and the South Tasman Rise suggests that unobstructed upper mantle communication between the Indian and Pacific Ocean Basins has probably existed at least since A13 (i.e., for the last 36 m.y.).

Distribution of Mantle Sources

Volcanism on the Naturaliste Plateau and Kerguelen hot spot activity are clearly related in space and time, but the chemical contrasts between their volcanic products indicate very different sources. The subcontinental-lithosphere-like isotopic signature of the basaltic andesite from the Naturaliste Plateau indicates that any Kerguelen hot spot influence at this site was primarily related to the plume's thermal effects rather than any material contribution [Mahoney et al., 1994].

The isotopic compositions of basaltic glasses from the DSDP sites near ~110° E are identical to those of present day AAD basalts, with some tendency towards enrichment with a Kerguelen-type contaminant [Michard et al., 1986; Dosso et al., 1988; Klein et al., 1988; Pyle et al. 1992]. Like all Indian-type MORB, they are lower in $^{206}Pb/^{204}Pb$ than nearby Pacific-type MORB. Basalts from the three sites display a progressive enrichment in $^{208}Pb/^{204}Pb$, $^{207}Pb/^{204}Pb$, and $^{87}Sr/^{86}Sr$ with decreasing seafloor age. This enrichment trend strongly suggests that Kerguelen hot spot material had not reached this section of the SEIR until after spreading rates had increased. Fast spreading may have initiated or enhanced the eastward dispersion of hot spot material between Australia and Antarctica,

possibly carried along with the ambient Indian MORB mantle matrix. It is surprising that the oldest drill sites did not encounter the most Kerguelen-like compositions because the ridge at this time should have been within the radius of a postulated, large, flattened Kerguelen plume head (~1000 km) [Griffiths and Campbell, 1990; Coffin and Eldholm, 1993; Mahoney et al., 1991].

East of the AAD, the older seafloor basalts from the Tasman Sea and the Balleny basin have isotopic affinities that clearly represent a 'Pacific' upper mantle source in the region at 65-70 Ma. More recent contamination of the upper mantle from the Balleny hotspot is evident in the Macquarie Ridge region, but Emerald basin basalts show no such influence. The trace element and isotopic signatures of these basalts are strong evidence for the presence of Pacific-type MORB mantle adjacent to the eastern margin of Gondwana before Australia and Antarctica rifted.

Volcanism surrounding the South Tasman Rise is of particular interest, because it may be associated with early rifting of this feature. Lanyon et al. [1993] suggested that the South Tasman Rise may actually be a volcanic plateau produced by excessive volcanism of the Balleny hot spot, rather than a remnant continental fragment. Their proposal is based on the compositional similarities of Tasmanian Tertiary alkalic basalts and Balleny hot spot lavas. If the South Tasman Rise is a continental fragment, some contribution of sub-continental, lithospheric material to the basalts, as observed at the Naturaliste Plateau (Site 264), might be expected. The highly depleted trace element signatures of the South Tasman Rise basalts suggest that such contamination has been insignificant. Neither do site 282, 280A, and 283 basalts display trace element or isotopic characteristics that would indicate a Balleny hot spot influence. These basalts appear to have been derived solely from depleted upper mantle MORB sources.

Whether the upper mantle source for South Tasman Rise volcanism is isotopically of Pacific-type or Indian-type depends on the criteria used to define these upper mantle reservoirs. The isotopic characteristics of Site 283 basalt are in line with other Pacific

MORB samples from the region (Fig. IV.8-IV.10). The $^{206}Pb/^{204}Pb$ values of 280A are also similar to Pacific-type MORB, but high $^{208}Pb/^{204}Pb$, $^{207}Pb/^{204}Pb$ and $^{87}Sr/^{86}Sr$ contents place this sample outside the Pacific MORB field and within the range of enriched Indian MORB and oceanic islands compositions. The isotopic composition of site 282 presents an interesting problem because it lies between the Indian and Pacific MORB fields, within the mixing field defined by AAD lavas near the present isotopic boundary (double arrows; Fig. IV.8-IV.10). Pacific-type MORB mantle beneath the SEIR, east of the AAD, is low in $^{87}Sr/^{86}Sr$, $^{208}Pb/^{204}Pb$ and $^{207}Pb/^{204}Pb$ at any given $^{206}Pb/^{204}Pb$, relative to the overall Pacific MORB field. Compared to Pacific-type MORB from the SEIR, and to ancient seafloor east of the South Tasman Rise, the source for site 282 basalt is transitional to Indian-type upper mantle. In fact, a compositional field encompassing both site 282 and 280A basalts always plots between the Indian and Pacific MORB groups from this region.

Mantle Flow

The primary evidence for westward migration of the Indian-Pacific isotopic boundary remains the difference in source composition between on- and off-axis samples from the easternmost AAD spreading segment [Pyle et al., 1992]. In addition, it seems likely that upper mantle flow toward the AAD has been associated with the several episodes of rift propagation and the westward displacement of the depth anomaly [Weissel and Hayes, 1974; Klein et al., 1988; Vogt and Johnson, 1973; Marks et al, 1990; 1991; Forsyth et al., 1987; Alvarez, 1982; 1990]. There are three ways in which the isotopic boundary may relate to the upper mantle dynamics of the region: 1) the boundary between Pacific and Indian MORB mantle may have always been located near the AAD, with small-scale, east-west fluctuations in its position; 2) the isotopic boundary may have migrated with the depth anomaly with small-scale fluctuations in mantle flow, causing variations in short-term apparent migration rates; 3) the isotopic boundary may have migrated westward, completely independently of the depth anomaly.

It does not seem likely that the isotope boundary remained stationary throughout the opening of the southeast Indian Ocean basin, since both 'Indian' and 'Pacific' sources (or at least some mixture of the two) are detectable in basalts from western margin of the South Tasman Rise. Similar reasoning can be used as evidence that the depth anomaly and the isotope boundary are decoupled. The depth anomaly intersects the Australian continent near 140° E, far to the west of the South Tasman Rise [Veevers, 1987]. If the depth anomaly and the isotope boundary resulted from the same process, then the South Tasman Rise basalts should have 'Pacific' MORB isotopic signatures.

Presently, the only geochemical evidence of mantle flow outside the AAD is the apparent eastward movement of Kerguelen hot spot contaminants down the SEIR after spreading rates increased between Australia and Antarctica. The DSDP sites east of the South Tasman Rise all have Pacific MORB isotopic signatures and the South Tasman Rise basalts have isotopic compositions that appear transitional between Pacific- and Indian-types. The essential samples for determining the long-term, westward migration of Pacific MORB mantle have yet to be collected. Samples of seafloor younger than 40 m.y. and located west of the South Tasman Rise will be critical for unraveling this problem.

CONCLUSIONS

1). Regional variations in isotopic signatures of basalts from DSDP sites throughout the region south of Australia show 'Pacific' mantle present on the eastern margin of Gondwana at least since the inception of seafloor spreading in the Tasman Sea and beneath westernmost Pacific-Antarctic ridge ~70 Ma (A34). This observation is consistent with, but not proof of, the postulated migration of Pacific mantle into the southeast Indian Ocean basin since rifting of the South Tasman Rise at ~45 Ma.

2). Isotopic and trace element variations along the SEIR between 100°E and 110°E suggest that eastward migration of Kerguelen hotspot-related mantle, toward the AAD, began with the initiation of rapid spreading, following rifting of Broken Ridge and the Kerguelen Plateau.

3). An episode of volcanism at sites 280A and 282, along the western margin of Tasmania, may be related to early rifting of the South Tasman Rise ~60-70 Ma. Basalts from these sites are resemble modern basalts from the vicinity of the AAD that are transitional between Pacific-type and Indian-type in their trace element and isotopic signatures. These transitional lavas may record the presence of Indian-type mantle at the easternmost end of the SEIR at that time.

BIBLIOGRAPHY

Abbey, S., An evaluation of USGS III, *Geostandards Newsletter, 6*, 47-49, 1982.

Altherr, R., F. Henjes-Kunst, and A. Baumann, Asthenosphere versus lithosphere as possible sources for basaltic magmas erupted during formation of the Red Sea: constraints from Sr, Pb, and Nd isotopes, *Earth and Planet. Sci. Lett., 96*, 269-286, 1990.

Alvarez, W., Geological evidence for the geographical pattern of mantle return flow and the driving mechanism of plate tectonics, *J. Geophys. Res., 87*, 6697-6710, 1982.

Alvarez, W., Geologic evidence for the plate driving mechanism: the continental undertow hypothesis and the Australian-Antarctic Discordance, *Tectonics, 9*, 1213-1220, 1990.

Anderson, D.L., T. Tanimoto and Y. Zhang, Plate Tectonics and Hotspots: The Third Dimension, *Science*, 256, 1645-1651, 1992.

Anderson, R.N., D.J. Sariosu, J.K. Weissel, and D.E. Hayes, The interrelation between variations in magnetic anomaly amplitudes and basalt magnetization and chemistry along the southeast Indian Ridge, *J. Geophys. Res., 85*, 3883-3898, 1980.

Baksi, A.K., T.R. Barman, D.K. Paul, and E. Farrar, Widespread early Cretaceous flood basalt volcanism in eastern India: Geochemical data from the Rajmahal-Bengal-Sylhet Traps, *Chem. Geol., 63*, 133-141, 1987.

Barling, J., and S.L. Goldstein, Extreme isotopic variation in Heard Island lavas and the nature of mantle reservoirs, *Nature, 348*, 59-62, 1990.

Beattie, P., Uranium-thorium disequilibria and partitioning on melting of garnet peridotite, *Nature, 363,* 63-65, 1993.

Bender, J.F., C.H. Langmuir, and G.N. Hanson, Petrogenesis of basalt glasses from the Tamayo region, East Pacific Rise, *J. Petrol., 25*, 213-254, 1984.

Bercovici, D., G. Schubert, and G.A. Glatzmaier, Three-dimensional spherical models of convection in the Earth's mantle, *Science, 244*, 950-955, 1989.

Byran, W.B., G. Thompson, and J.N. Ludden, Compositional variations in normal MORB from 22°-25° N; mid-Atlantic ridge and Kane Fracture Zone, *J. Geophys. Res., 86,* 11815-11836, 1981.

Cande, S.C., and J.C. Mutter, A revised identification of the oldest sea-floor spreading anomalies between Australia and Antarctica, *Earth and Planet. Sci. Lett., 58*, 151-160, 1982.

Cande, S.C., J.L. LaBrecque, R.L. Larson, W.C. Pitmann III, X. Golovchenko, and W.F. Haxby, Magnetic Lineations of the World's Ocean Basins (map), *American Association of Petroleum Geologists*, Tulsa, Oklahoma, 1989.

Christie, D.M., and J.M. Sinton, Evolution of abyssal lavas along propagating segments of the Galapagos spreading center, *Earth and Planet. Sci. Lett., 56*, 312-335, 1981.

Christie, D.M., and J.M. Sinton, Major element constraints on melting, differentiation and mixing of magmas from the Galapagos 95.5° W propagating rift system, *Contrib. Mineral. Petrol., 94*, 274-288, 1986.

Christie, D.M., D.G. Pyle, J.-C. Sempéré, J. Phipps-Morgan, and A. Shor, Petrologic and tectonic observations in and adjacent to the Australian-Antarctic Discordance (abstract), *EOS Trans. 69*, 1426, Fall AGU meeting, 1988.

Christie, D.M., D.G. Pyle, J.-C. Sempéré, and J. Palmer, Petrologic diversity, axial morphology and magma supply at the Australian-Antarctic Discordance (AAD), *EOS, 71*, 1388, 1990.

Cochran, J.R., Variations in subsidence rates along intermediate and fast spreading mid-ocean ridges, *Geophys. J. R. Astr. Soc., 87*, 421-454, 1986.

Coffin, M.F., and O. Eldholm, Scratching the surface: estimating dimensions of large igneous provinces, *Geology, 21*, 515-518.

Cordery, M.J., and J. Phipps-Morgan, Melting and mantle flow beneath a mid-ocean spreading center, *Earth and Planet. Sci. Lett., 111*, 493-516, 1992.

Dalrymple, G.B., E.C. Alexander, Jr., M.A. Lanphere, and G.P. Kraker, Irradiation of samples for $^{40}Ar/^{39}Ar$ dating using the Geological Survey TRIGA reactor, *U.S. Geol. Surv. Prof. Paper, 1179*, 1981.

Davis, A.S., and D.A. Clague, Geochemistry, mineralogy, and petrogenesis of basalt from the Gorda Ridge, *J. Geophys. Res., 92*, 10467-10483, 1987.

De Mets, C, R.G. Gordon, D.F. Argus, and S. Stein, Current plate motions, *Geophys. J. Int., 101*, 425-478, 1990.

Dosso, L., H. Bougault, P. Beuzart, J.-Y. Calvez, and J.-J. Joron, The geochemical structure of the South-East Indian Ridge, *Earth and Planet. Sci. Lett., 88*, 47-59, 1988.

Duncan, R.A., Hotspots in the southern oceans - An absolute frame of reference for motion of the Gondwana continents, *Tectonophysics, 74*, 29-42, 1981.

Duncan, R.A., Age distribution of volcanism along aseismic ridges in the eastern Indian Ocean, in Weissel, J., Peirce, J., Taylor, E., Alt, J., et al., ed., *Proc. Ocean Drilling Program, 121*, 507-517.

Duncan, R.A., and D.G. Pyle, Rapid eruption of the Deccan flood basalts at the Cretaceous/Tertiary boundary, *Nature, 333*, 841-843, 1988.

Duncan, R.A., and R.B. Hargraves, $^{40}Ar/^{39}Ar$ geochronology of basement rocks from the Mascarene Plateau, the Chagos Bank, and the Maldives Ridge, in R.A. Duncan, J. Backman, L.C. Peterson, eds., *Proc. Ocean Drilling Program, Scientific Results, 115*, 43-51, 1990.

Duncan, R.A., and M.A. Richards, Hotspots, mantle plumes, flood basalts, and true polar wander, *Reviews of Geophys., 29*, 31-50, 1991.

Duncan, R.A., and I. McDougall, Volcanic time-space relationships, in Johnson, R.W., ed., *Intraplate volcanism in eastern Australia and New Zealand,* Cambridge University Press, 43-54, 1989.

Dupré, B., and C.J. Allègre, Pb-Sr isotope variation in Indian Ocean basalts and mixing phenomena, *Nature, 303*, 142-146, 1983.

Dupré, B., G. Blanc, J. Boulègue, and C.J. Allègre, Metal remobilization at a spreading centre studied using lead isotopes, *Nature, 333*, 165-167, 1988.

Eggins, S.M., D.H. Green, and T.J. Falloon, The Tasmantid Seamounts: shallow melting and contamination of an EM1 mantle plume, *Earth and Planet. Sci. Letts., 107*, 448-462, 1991.

Falloon, T.J., D.H. Green, C.J. Hatton, and K.L. Harris, Anhydrous partial melting of a fertile and depleted peridotite from 2 to 30 kb and application to basalt petrogenesis, *J. Petrol., 29*, 1257-1282, 1988.

Falloon, T.J., and D.H. Green, Anhydrous partial melting of peridotite from 8 to 35 kb and the petrogenesis of MORB, *J. Petrol., Special Lithosphere Issue*, 379-414, 1987.

Ferguson, E.M., and E.M. Klein, Fresh basalts from the Pacific-Antarctic Ridge extend the Pacific geochemical province, *Nature, 366*, 330-333, 1993.

Ford, A.B., Antarctic deep-sea basalt, Southeast Indian Ocean and Balleny Basin, DSDP Leg 28, in D.E. Hayes, L.A. Frakes et al., *Initial Reports of the Deep Sea Drilling Project, 28*, Washington (U.S. Printing Office), 835-859, 1975.

Forsyth, D.W., Geophysical constraints on Mantle Flow and Melt generation Beneath Mid-Ocean Ridges, in J. Phipps-Morgan, D.K. Blackman, and J.M. Sinton, eds., *Mantle flow and melt generation at Mid-Ocean Ridges, Geophysical Monograph 71*, 1-65, 1993.

Forsyth, D.W., R.L. Ehrenbard, and S. Chapin, Anomalous upper mantle beneath the Australian-Antarctic Discordance, *Earth and Planet. Sci. Lett., 84*, 471-478, 1987.

Frey, F.A., D.H. Green, and S.D. Roy, Integrated models of basalt petrogenesis: a study of olivine tholeiites to olivine melilitites from southeastern Australia utilizing geochemical and experimental petrological data, *J. Petrol., 19*, 463-513, 1978.

Frey, F.A., N. Walker, D. Stakes, S.R. Hart, and R. Nielsen, Geochemical characteristics of basaltic glasses from the AMAR and FAMOUS axial valleys, Mid-Atlantic Ridge (36°-37° N): Petrogenetic implications, *Earth and Planet. Sci. Lett., 115*, 117-136, 1993.

Gallahan, W.E. and R.L. Nielsen, The partitioning of Sc, Y, and the rare earth elements between high-Ca pyroxene and natural mafic to intermediate lavas at 1 atmosphere, *Geochim. Cosmochim. Acta, 56*, 2387-2404, 1992.

Govindaraju, K., 1989 compilation of working values and sample description for 272 geostandards, *Geostandards Newsletter, 13*, 1-113, 1989.

Green, T.H., and N.J. Pearson, Rare earth element partitioning between clinopyroxene and silicate liquid at moderate to high pressure, *Contrib. Mineral. Petrol., 91*, 24-36, 1985.

Griffith, B.J., Igneous and metamorphic petrology of lavas and dykes of the Macquarie Island ophiolite complex, Ph.D. dissertation (unpub.), University of Tasmania, 1982.

Griffith, B.J., and R. Varne, The Macquarie Island Ophiolite complex: mid-Tertiary oceanic lithosphere from a major ocean basin, *Chem. Geol., 30.*, 285-308, 1980.

Griffiths, R.W., and I.H. Campbell, Stirring and structure in mantle starting plumes, *Earth Planet. Sci. Lett.*, 99, 66-78, 1990.

Grove, T.L., and W.B. Bryan, Fractionation of pyroxene-phyric MORB at low pressure: An experimental study, *Contrib. Mineral. Petrol., 84*, 293-309, 1983.

Grove, T.L., and T.C. Juster, Experimental investigations of low-Ca pyroxene stability and olivine-pyroxene-liquid equilibria at 1-atm in natural basaltic and andesitic liquids, *Contrib. Mineral. Petrol., 103*, 287-305, 1989.

Grove, T.L., R.J. Kinzler, and W.B. Bryan, Natural and experimental phase relationships of lavas from Serocki Volcano, in Detrick et al. eds., *Proc. Ocean. Drilling Program, Scientific Results, 106/109*, 9-17, 1990.

Grove, T.L., R.J. Kinzler, and W.B. Bryan, Fractionation of Mid-Ocean Ridge Basalt (MORB), in J. Phipps-Morgan, D.K. Blackman, and J.M. Sinton, eds., *Mantle flow and melt generation at Mid-Ocean Ridges, Geophysical Monograph 71*, 281-310, 1992.

Hamelin, B., and C.J. Allègre, Large-scale regional units in the depleted upper mantle revealed by an isotope study of the South-West Indian Ridge, *Nature, 315,* 196-199, 1983.

Hamelin, B., B. Dupré, and C.J. Allègre, Pb-Sr-Nd isotopic data of Indian Ocean ridges: new evidence of large-scale mapping of mantle heterogeneities, *Earth and Planet. Sci. Letts., 76*, 288-298, 1986.

Hart, S.R., A large-scale isotope anomaly in the Southern Hemisphere mantle, *Nature, 309*, 753-757, 1984.

Hart, S.R., J.-G. Schilling, and J.L. Powell, Basalts from Iceland and the Reykjanes Ridge: Sr isotopic geochemistry, *Nature, 246*, 104-107, 1973.

Hart, S.R., and A. Zindler, In search of a bulk-earth composition, *Chem. Geol., 57*, 247-267, 19xx.

Hart, S.R., and T. Dunn, Experimental cpx/melt partitioning of 24 trace elements, *Contrib. Mineral. Petrol., 113*, 1-8, 1993.

Hayes, D.E., Nature and implications of asymmetric sea-floor spreading - "Different rates for different plates", *Geol. Soc. Am. Bull., 87*, 994-1002, 1976.

Hayes, D.E., and J.R. Conolly, Morphology of the Southeast Indian Ridge, in D.E. Hayes, ed., *Antarctic Oceanology II: The Australian-New Zealand Sector, Antarctic Res. Ser., 19*, 125-145, AGU, 1972.

Hayes, D.E., and J. Ringis, Sea-floor spreading in the Tasman Sea, *Nature, 243*, 454-458, 1973.

Hayes, D.E., and L.A. Frakes, General synthesis, Deep Sea Drilling Project Leg 28, in Hayes and Frakes and others, eds., *Initial Reports of the Deep Sea Drilling Project, 28*, Washington (U.S. Government Printing Office), 919-942, 1975.

Hedge, C.E., R.A. Watkins, W. Hildreth, and W.P. Doering, $^{87}Sr/^{86}Sr$ ratios in basalts from islands in the Indian Ocean, *Earth and Planet. Sci. Lett., 21*, 29-34, 1973.

Hess, P.C., Phase equilibria constraints on the origin of ocean floor basalts, in J. Phipps-Morgan, D.K. Blackman, and J.M. Sinton, eds., *Mantle flow and melt generation at Mid-Ocean Ridges, Geophysical Monograph 71*, 67-102, 1993.

Hey, R.N., F.K. Duennebier, and W.J. Morgan, Progagating rifts on mid-ocean ridges, *J. Geophys. Res., 85*, 2647-2658, 1980.

Hey, R.N., M.C. Kleinrock, S.P. Miller, T.M. Atwater, and R.C. Searle, Sea Beam/Deep-Tow investigation of an active oceanic propagating rift system, Galapagos 95.5° W, *J. Geophys. Res., 91*, 3369-3393, 1986.

Hinz, K., M. Hemmerich, U. Salge, and O. Eiken, Structures in rift-basin sediments on the conjugate margins of Western Tasmania, South Tasman Rise and Ross Sea, Antarctica, (unpublished manuscript), 1991.

Hofmann, A.W., Chemical differentiation of the Earth: the relationship between mantle, continental crust, and oceanic crust, *Earth and Planet. Sci. Lett., 90*, 297-314, 1988.

Hofmann, A.W., and W.M. White, Mantle plumes from ancient oceanic crust, *Earth and Planet. Sci. Lett., 57*, 421-436, 1982.

Hofmann, A.W., and D.P. McKenzie, The destruction of geochemical heterogeneities by differential fluid motions during mantle convection, *Geophys. J. R. Astron. Soc., 82*, 163-206, 1985.

Ito, E., W.M. White, and C. Gopel, The O, Sr, Nd, and Pb isotope geochemistry of MORB, *Chem. Geol., 62*, 157-176, 1987.

Jacques, A.L, and D.H. Green, Anhydrous melting of peridotite at 0-15 kb pressure and the genesis of tholeiitic basalts, *Contrib. Mineral. Petrol., 73*, 287-310, 1980.

Johnson, B.D., C. McA. Powell, and J.J. Veevers, Early spreading history of the Indian Ocean between India and Australia, *Earth and Planet. Sci. Letts., 47*, 131-143, 1980.

Johnson, K.T.M., H.J.B. Dick, and N. Shimizu, Melting in the oceanic upper mantle: an ion microprobe study of diopsides in abyssal peridotites, *J. Geophys. Res., 95*, 2661-2678, 1990.

Johnson, R.W., Intraplate volcanism in Eastern Australia and New Zealand, *Cambridge University Press*, 1989.

Juster, T.C., T.L. Grove, and M.R. Perfit, Experimental constraints on the generation of FeTi basalts, andesites and rhyodacites at the Galapagos Spreading Center, 85° W and 95° W, *J. Geophys. Res., 94*, 9251-9274, 1989.

Karsten,J.L. and J.D. Delaney, Hot spot-ridge crest convergence in the Northeast Pacific, *J. Geophys. Res., 94*, 700-712, 1989.

Kent, D.V., and F.M. Gradstein, A Jurassic to recent chronology, in P.R. Vogt, and B.E. Tucholke, eds., *The western North Atlantic Region, Geol. Soc. Am., The Geology of North America, M*, Decade of North American Geology, 45-50, 1986.

Kelemen, P.B., R.J. Kinzler, K.T.M. Johnson, and A.J. Irving, High field strength element depletions in arc basalts due to mantle-magma interaction, *Nature, 345*, 521-525, 1990.

Kinzler, R.J., and T.L. Grove, Primary magmas of mid-ocean ridge basalts, 1: Experiments and methods, *J. Geophys. Res., 97*, 6885-6906, 1992a.

Kinzler, R.J., and T.L. Grove, Primary magmas of mid-ocean ridge basalts, 2: Applications, *J. Geophys. Res., 97*, 6907-6296, 1992b.

Kinzler, R.J., and T.L. Grove, Corrections, clarifications, and further discussions of the primary magmas of mid-ocean ridge basalts, 1 experiments and methods, and 2 applications, unpub. manuscript, 1993.

Klein, E.M., C.H. Langmuir, A. Zindler, H. Staudigel, and B. Hamelin, Isotope evidence of a mantle convection boundary at the Australian-Antarctic Discordance, *Nature, 333*, 623-629, 1980.

Klein, E.M., and C.H. Langmuir, Global correlations of ocean ridge basalt chemistry with axial depth and crustal thickness, *J. Geophys. Res., 92*, 8089-8115, 1987.

Klein, E.M., C.H. Langmuir, and H. Staudigel, Geochemistry of basalts from the Southeast Indian Ridge, 115°E-138°E, *J. Geophys. Res., 96*, 2089-2107, 1991.

Klein, E.M., C.H. Langmuir, A. Zindler, H. Staudigel, and B. Hamelin, Isotope evidence of a mantle convection boundary at the Australian-Antarctic discordance, *Nature, 333*, 623-629, 1988.

Klein, E.M., and C.H. Langmuir, Local versus global variations in ocean ridge basalt composition: A reply, *J. Geophys. Res., 94*, 4241-4252, 1989.

Klein, E.M., C.H. Langmuir, and H. Staudigel, Geochemisty of basalts from the Southeast Indian Ridge, 115°E-138°E, *J. Geophys. Res. 96*, 2089-2107, 1991.

Kostopoulos, D.K., Melting of the shallow upper mantle: A new perspective, *J. Petrol., 32*, 671-699, 1991.

Langmuir, C.H., J.F. Bender, and R. Batiza, Petrological and tectonic segmentation of the East Pacific Rise, 5°30'-14°30'N, *Nature, 322*, 422-429, 1986.

Langmuir, C.H., E.M. Klein, and T. Plank, Petrologic systematic of Mid-Ocean Ridge basalts: constraints on melt generation beneath ocean ridges, in J. Phipps-Morgan, D.K. Blackman, and J.M. Sinton, eds., *Mantle flow and melt generation at Mid-Ocean Ridges, Geophysical Monograph 71*, 183-280, 1993.

Lanyon, R., R. Varne, and A.J. Crawford, Tasmanian Tertiary basalts, the Balleny plume and opening of the Tasman Sea - southwest Pacific Ocean, *Geology*, X, x-x, 1993.

Laul, J.C., Neutron activation analysis of geological materials, *Atomic Energy Rev., 17*, 603-695, 1979.

Leclaire, L., Y. Bassias, M. Denis-Clocchiatti, H. Davies, I. Gautier, B. Gensous, P.-J. Giannesini, P. Patriat, J. Segoufin, M. Tesson, and J. Wannesson, Lower Cretaceous basalt and sediments from the Kerguelen Plateau, *Geo-Mar. Lett., 7*, 169-176, 1987.

Leg 29 Shipboard Scientific Party, Site 280, in J.P. Kennett, R.E. Houtz et al., *Initial Reports of the Deep Sea Drilling Project, 29*, Washington (U.S. Government Printing Office), 225-270, 1975.

Longi, J., Comparative liquidus equilibria of hypersthene-normative basalts at low pressures, *Am. Min., 76*, 785-800, 1991.

Longi, J., and V. Pan, A reconnaisance study of phase boundaries in low-alkali basaltic liquids, *J. Petrol., 29*, 115-147, 1988.

Ma, M.-S., J.C. Laul, and R.A. Schmitt, Complementary rare earth element patterns in unique achondrites, such as ALHA 77005 and shergottites, and in the Earth, *Proc. Lunar Planet. Sci. Conf., 12B*, 1349-1358, 1981.

Mahoney, J.J., An isotopic survey of Pacific Ocean Plateaus: Implications for their nature and origin, in Seamounts, Islands, and Atolls, in Keating, Fryer, Batiz, and Boehlert, eds., *J. Geophys. Res. Monogr., 43*, 207-220, 1987.

Mahoney, J.J., J.D. Macdougall, and G.W. Lugmair, Kerguelen hotspot source for Rajmahal Traps and Ninetyeast Ridge?, *Nature, 303*, 385-389, 1983.

Mahoney, J.J., J.H. Natland, W.M. White, R. Poreda, S.H. Bloomer, R.L. Fisher, and A.N. Baxter, Isotopic and geochemical provinces of the western Indian Ocean spreading centers, *J. Geophys. Res., 94*, 4033-4052, 1989.

Mahoney, J.J., C. Nicollet, and C. Dupuy, Madagascar basalts: tracking oceanic and continental sources, *Earth and Planet. Sci. Lett., 104*, 350-363, 1991.

Mahoney, J.J., M. Storey, R.A. Duncan, K.J. Spencer, and M. Pringle, Geochemistry and geochronology of Leg 130 basement lavas: Nature and origin of the Ontong Java Plateau, *Proc. Ocean Drilling Program, Scientific Reports, 130*, College Station, TX, submitted 11/91, 1992.

Mahoney, J.J., A.P. le Roex, Z. Peng, R.L. Fisher, and J.H. Natland, Western limits of the Indian MORB mantle and the origin of low $^{206}Pb/^{204}Pb$ MORB: Isotope systematics of the central Southwest Indian Ridge (17°-50°E), *J. Geophys. Res.*, in revision, 1992.

Mahoney, J.J., W.B. Jones, F.A. Frey, V.J.M. Salters, D.G. Pyle, and H.L. Davies, Geochemical characteristics of lavas from Broken Ridge, the Naturaliste Plateau and southernmost Kerguelen Plateau: early volcanism of the Kerguelen Hotspot, in Arndt, N., McDonough, W., and Shirey, S., eds., *Chemical evolution of the mantle,* submitted, 1994.

Marks, K.M., P.R. Vogt, and S.A. Hall, Residual depth anomalies and the origin of the Australian-Antarctic Discordance Zone, *J. Geophys. Res., 95*, 17325-17337, 1990.

Marks, K.M., D.T. Sandwell, P.R. Vogt, and S.A. Hall, Mantle downwelling beneath the Australian-Antarctic Discordance Zone: evidence from geoid height versus topography, *Earth and Planet Sci. Lett., 103*, 325-338, 1991.

Mayes, C.L., L.A. Lawver, and D.T. Sandwell, Tectonic history and new isochron chart of the South Pacific, *J. Geophys. Res., 95*, 8543-8567, 1990.

McDougall, I. and R.A. Duncan, Age progressive volcanism in the Tasmantid Seamounts, *Earth and Planet. Sci. Letts., 89*, 207-220, 1988.

McDougall, I. and T.M. Harrison, Geochronology and thermochronology by the $^{40}Ar/^{39}Ar$ method, 212 pg., *Oxford University Press*, New York, 1988.

Macdougall, J.D., and G.W. Lugmair, Extreme isotopic homogeneity among basalts from the southern East Pacific Rise: mantle or mixing effect?, *Nature, 313*, 209-211, 1985.

McKenzie, D., and M.J. Bickle, The volume and composition of melt generated by extension of the lithosphere, *J. Petrol., 29, 625-679*, 1988.

Melson, W.G., T.L. Vallier, T.L. Wright, G. Byerly, and J. Nelsen, Chemical diversity of abyssal volcanic glass erupted along Pacific, Atlantic, and Indian Ocean sea-floor spreading centers, in G.H. Sutton et al., eds., *Geophysics of the Pacific Ocean basin and its margins, Am. Geophys. Union*, 351-367, 1976.

Merrihue, C., and G. Turner, Potassium-argon dating by activation with fast neutrons, *J. Geophys. Res., 71*, 2852-2857, 1966.

Michard, A., R. Montigny, and R. Schlich, Geochemistry of the mantle beneath the Rodriguez Triple Junction and the South-East Indian Ridge, *Earth and Planet. Sci. Letts., 78*, 104-114, 1986.

Miller, D.M., C.H. Langmuir, S.L. Goldstein, and A.L. Franks, The importance of Parental Magma Compositions to Calc-Alkaline and Tholeiitic Evolution: Evidence from Umnak Island in the Aleutians, *J. Geophys. Res., 97*, 321-343, 1992.

Morgan, W.J., Hotspot tracks and the opening of the Atlantic and Indian Oceans, in C. Emiliani, ed., *The Sea, 7*, 443-487, John Wiley and Sons, New York, 1981.

Mutter, J.C., K.A. Hegarty, S.C. Cande, and J.K. Weissel, Breakup between Australia and Antarctica: a brief review in the light of new data, *Tectonophysics, 114*, 255-279, 1985.

Nielsen, R.L., EQUIL: a program for the modeling of low pressure differentiation processes in natural mafic magma bodies, *Computers and Geoscience, 11*, 531-546, 1985.

Nielsen, R.L., BIGD.FOR: a fortan program to calculate trace-element partition coefficients for natural mafic and intermediate composition magmas, *Computers & Geosci.*, pre-print, 1992.

Nielsen, R.L., W.E. Gallahan, and F. Newberger, Experimentally determined mineral-melt partition coefficients for Sc, Y and REE for olivine, orthopyroxene, pigeonite, magnetite and ilmenite, *Contrib. Mineral. Petrol., 110,* 488-499, 1992.

Niu, Y., and R. Batiza, An empirical method for calculating melting compositions produced beneath mid-ocean ridges: applications for axis and off-axis (seamounts) melting, *J. Geophys. Res., 96*, 21753-21777, 1991.

Overshine, A.T., G.R. Winkler, P.B. Andrews, and V.A. Gostin, Chemical analyses and minor element composition of Leg 29 basalts, in J.P. Kennett, R.E. Houtz et al., *Initial Reports of the Deep Sea Drilling Project, 29*, Washington (U.S. Government Printing Office), 1097-1102, 1974.

Oxburgh, E.R., and E.M. Parmentier, Compositional and density stratification in oceanic lithosphere - causes and consequences, *J. Geol. Soc. London, 133*, 343-355, 1977.

Palmer, J., J.-C. Sempéré, D.M. Christie, and J. Phipps-Morgan, Morphology and tectonic of the Australian-Antarctic Discordance between 123° E and 128° E, *Mar. Geophys. Res., 15*, 121-151, 1993.

Perfit, M.R., and D.J. Fornari, Geochemical studies of abyssal lavas recovered by DSRV Alvin from eastern Galapagos Rift, Inca Transform, and Ecuador Rift 2. Phase chemistry and crystallization history, *J. Geophys. Res., 88*, 10530-10550, 1983.

Phipps-Morgan, J., and E.M. Parmentier, Causes and rate-limiting mechanisms of ridge propagation: a fracture mechanism model, *J. Geophys. Res., 90*, 8603-8612, 1985.

Phipps-Morgan, J., E.M. Parmentier, and J. Linn, Mechanisms for the origin of mid-ocean ridge axial topography: Implications for the thermal and mechanical structure of accreting plate boundaries, *J. Geophys. Res., 92*, 12823-12836, 1987.

Phipps-Morgan, J., and D.W. Forsyth, Three-dimensional flow and temperature perturbations due to a transform offset: effects on oceanic crustal and upper mantle structure, *J. Geophys. Res., 93*, 2955-2966, 1988.

Phipps-Morgan, J., J.-C. Sempéré, D. Christie, and A. Shor, Propagating rifts along the Southeast Indian Ridge, *EOS, 69*, 1430, 1988.

Plank, T., and C.H. Langmuir, Effects of the melting regime on the composition of the oceanic crust, *J. Geophys. Res, 97*, 19749-19770, 1992.

Playford, P.E., A.E. Cockbain, and G.H. Low, Geology of the Perth Basin, Western Australia, *Geol. Surv. W. Austral. Bull., 124*, 311, 1976.

Powell, C.McA., S.R. Roots, and J.J. Veevers, Pre-breakup continental extension in East Gondwanaland and the early opening of the eastern Indian Ocean, *Tectonophysics, 155*, 261-283, 1988.

Price, R.C., A.K. Kennedy, M. Riggs-Sneeringer, and F.A. Frey, Geochemistry of basalts from the Indian Ocean triple junction: Implications for the generation and evolution of Indian Ocean ridge basalts, *Earth and Planet. Sci. Lett., 78*, 379-396, 1986.

Pyle, D.G., D.M. Christie, and J.J. Mahoney, Upper mantle flow in the Australian-Antarctica Discordance (abstract), *EOS, Trans., 71*, 1388, Fall AGU meeting, 1990.

Pyle, D.G., D.M. Christie, and J.J. Mahoney, Fine scale resolution of an isotopic boundary within the Australian-Antarctic Discordance, submitted *Earth and Planet. Sci. Letts.*, 1992.

Pyle, D.G., D.M. Christie and J.J. Mahoney, Resolving an isotopic boundary within the Australian-Antarctic Discordance, *Earth and Planet. Sci. Lett., 112*, 161-178, 1992.

Pyle, D.G., and D.M. Christie, Petrologic and tectonic diversity in the vicinity of the Australian-Antarctic Discordance, in prep., chapter 3, 1994.

Richards, M.A., R.A. Duncan, and V.E. Courtillot, Flood basalts and hotspot tracks: plume heads and tails, *Science, 246*, 103-107, 1989.

Rouland, D., S.H. Xu, and F. Schindele, Upper mantle structure in the Southeast Indian Ocean: A surface wave investigation, *Tectonophysics, 114*, 281-292, 1985.

Royer, J.-Y., and D.T. Sandwell, Evolution of the eastern Indian Ocean since the Late Cretaceous: Constraints from GEOSAT altimetry, *J. Geophys. Res., 94*, 13755-13782, 1989.

Salters, V.J.M., and S.R. Hart, The hafnium paradox and the role of garnet in the source of mid-ocean-ridge basalts, *Nature, 342*, 420-422, 1989.

Samson, S.D. and E.C. Alexander, Calibration of the interlaboratory $^{40}Ar/^{39}Ar$ dating standard, Mmhb-1, *Chem. Geol., 66*, 27-34, 1987.

Schilling, J-G., and W.I. Ridley, Volcanic rocks from DSDP Leg 29: Petrography and rare-earth abundances, in J.P. Kennett, R.E. Houtz et al., *Initial Reports of the Deep Sea Drilling Project, 29*, Washington (U.S. Government Printing Office), 1103-1107, 1974.

Schilling, J.-G., R.H. Kingsley, and J.D. Devine, Galapagos hot spot-spreading center system 1: Spatial petrological and geochemical variations (83°W-101°W), *J. Geophys. Res., 87*, 5593-5610, 1982.

Schilling, J.-G., R.H. Kingsley, B.B. Hanan, and B.L. McCully, Nd-Sr-Pb isotopic variations along the Gulf of Aden: Evidence for mantle plume-continental lithosphere interaction, *J. Geophys. Res.*,97, 10927-10966, 1992.

Schilling, J.-G., G. Thompson, R. Kingsley, and S. Humphris, Hotspot-migrating ridge interaction in the South Atlantic, *Nature, 313*, 187-191, 1985.

Schilling, J.-G., Fluxes and excess temperatures of mantle plumes inferred from their interaction with migrating mid-ocean ridges, *Naure, 352*, 397-403, 1991.

Schilling, J.-G., Upper mantle heterogeneities and dynamics, *Nature, 314*, 62-67, 1985.

Schlich, R., and S.W. Wise, *Proc. Ocean Drilling Program, Initial Reports, 120*, College Station, TX (Ocean Drilling Program), 1989.

Sempéré, J.-C., J. Palmer, D.M. Christie, J. Phipps-Morgan, and A.N. Shor, The Australian-Antarctic Discordance, *Geology, 19*, 429-432, 1991.

Sinton, J.M, and R.S. Detrick, Mid-ocean ridge magma chambers, *J. Geophys. Res,* 97, 197-216, 1992.

Sinton, J.M., D.S. Wilson, D.M. Christie, R.N. Hey, and J.R. Delaney, Petrologic consequences of rift propagation on oceanic spreading ridges, *Earth and Planet. Sci. Lett., 62*, 193-207, 1983.

Smith, M.C., M.R. Perfit, and .R. Jonasson, Petrology and geochemisry of basalts from the southern Juan de Fuca Ridge: Controls on the spatial and temporal evolution of MORB, *J. Geophys. Res.*, submitted, 1993.

Spencer, K.J., and J.J. Mahoney, Isotopic evidence for the origin of the Manihiki and Ontong Java oceanic plateaus, *Earth and Planet. Sci. Letts.*, submitted, 1991.

Stock, J., and P. Molnar, Uncertainties in the relative positions of the Australia, Antarctica, Lord Howe, and Pacific plates since the late Cretaceous, *J. Geophys. Res., 87*, 4697-4714, 1982.

Stock, J., and P. Molnar, Revised history of early Tertiary plate motion in the south-west Pacific, *Nature, 325*, 495-499, 1987.

Storey, M., A.D. Saunders, J. Tarney, P. Leat, M.F. Thirlwall, R.N. Thompson, M.A. Menzies, and G.F. Marriner, Geochemical evidence for plume-mantle interactions beneath Kerguelen and Heard Islands, Indian Ocean, *Nature, 336*, 371-374, 1988.

Storey, M., A.D. Saunders, J. Tarney, I.L. Gibson, M.J. Norry, M.F. Thirlwall, P. Leat, R.N. Thompson, and M.A. Menzies, Contamination of Indian Ocean asthenosphere by the Kerguelen-Heard mantle plume, *Nature, 338*, 574-576, 1989.

Subbarao, K.V., and C.E. Hedge, K, Rb, Sr and $^{87}Sr/^{86}Sr$ in rocks from the Mid-Indian Ocean Ridge, *Earth and Planet. Sci. Lett., 18*, 223-228, 1973.

Sun, S.-S., and W.F. McDonough, Chemical and isotopic systematics of oceanic basalts: implications for mantle composition and processes, in A.D. Saunders and M.J. Norry, eds., *Magmatism in the Ocean Basins, Geological Society Spec. Publ., 42*, 313-345, 1989.

Sun, S.-S., M. Tatsumoto, and J.G. Schilling, Mantle plume mixing along the Reykjanes ridge axis: lead isotope evidence, *Science, 190*, 143-147, 1975.

Todt, W., B. Dupré, and A.W. Hofmann, Pb isotope measurements using a multicollector: applications to standards and basalts, *Terra Cognita, 3*, 140, 1983.

Tormey, D.R., T.L. Grove, and W.B. Bryan, Experimental petrology of normal MORB near the Kane Fracture Zone: 22°-25° N, Mid-Atlantic Ridge, *Contrib. Mineral. Petrol., 96*, 121-139, 1987.

Veevers, J.J., Australian-Antarctic depression from the mid-ocean ridge to adjacent continents, *Nature, 295*, 315-317, 1982.

Veevers, J.J. and contributors, Phanerozoic earth history of Australia, 418 pg., *Oxford Geological Sci. Series 2*, Oxford University Press, New York, 1984.

Veevers, J.J., and Z.X. Li, Review of seafloor spreading around Australia, II: Marine magnetic anomaly modeling, *Aust. Jour. Earth Sci., 38*, 391-408, 1991.

Veevers, J.J., C. McA. Powell, and S.R. Roots, Review of seafloor spreading around Australia, I: Synthesis of the patterns of spreading, *Aust. Jour. Earth Sci., 38*, 373-389, 1991.

Vogt, P.R., and G.L. Johnson, A longitudinal seismic reflection profile of the Reykjanes Ridge, Part II: Implications for the mantle hot spot hypothesis, *Earth and Planet. Sci. Lett., 18*, 49-58, 1973.

Vogt, P.R., and G.L. Johnson, Transform faults and longitudinal flow below the midoceanic ridge, *J. Geophys. Res., 80*, 1399-1428, 1975.

Vogt, P.R., N.K. Cherkis, and G.A. Morgan, Project Investigator-I: evolution of the Australian-Antarctic Discordance from a detailed aeromagnetic study, in R.L. Oliver, P.R. James, and J. Jago, eds., *Antarctic Earth Science: Proceedings 4th International Symposium on Antarctic Earth Sciences, Canberra*, Australian Academy of Science, 1984.

Walker, D., T. Shibata, and S.E. DeLong, Abyssal tholeiites from the Oceanographer Fracture Zone, II: Phase equilibria and mixing, *Contrib. Mineral. Petrol., 70*, 111-125, 1979.

Weaver, J.S., and C.H. Langmuir, Calculation of phase equilibrium in mineral-melt systems, *Computers & Geoscience, 16*, 1-19, 1990.

Weissel, J.K., and D.E. Hayes, Asymmetric seafloor spreading south of Australia, *Nature, 231*, 518-522, 1971.

Weissel, J.K., and D.E. Hayes, Magnetic anomalies in the southeast Indian Ocean, in D.E. Hayes ed., *Antarctic Res. Ser., 19*, 165-196, AGU, Washington, D.C., 1972.

Weissel, J.K., and D.E. Hayes, The Australian-Antarctic Discordance: New results and implications, *J. Geophys. Res., 79*, 2579-2587, 1974.

Weissel, J.K., and D.E. Hayes, Evolution of the Tasman Sea reappraised, *Earth and Planet. Sci. Letts., 36*, 77-84, 1977.

Weissel, J.K., D.E. Hayes, and E.M. Herron, Plate tectonics synthesis: The displacements between Australia, New Zealand, and Antarctica since the late Cretaceous, *Marine Geol., 25*, 231-277, 1977.

Weis, D., W.M. White, F.A. Frey, R.A. Duncan, M.R. Fisk, J. Dehn, J. Ludden, The influence of mantle plumes in generation of Indian oceanic crust, in Duncan, R.A., et al., *Synthesis of results from scientific drilling in the Indian Ocean, Geophys. Monogr., 70*, 57-89, 1992.

Weis, D., F.A. Frey, H. Leyrit, and I. Gautier, Kerguelen archipelago revisited: geochemical and isotopic study of the Southeast Province lavas, *Earth and Planet. Sci. Lett., 118*, 101-119, 1993.

West, B.P., J.-C. Sempéré, D.G. Pyle, J. Phipps Morgan, and D. M. Christie, The importanc of mantle termperature in crustal accretion: evidence from the Australian-Antarctic Discordance and numerical modeling of mid-ocean ridge dynamics, Earth Planet. Sci. Lett., accepted, 1994.

White, W.M., A.W. Hofmann, and H. Puchelt, Isotope geochemistry of Pacific mid-ocean ridge basalt, *J. Geophy. Res., 92*, 4881-4893, 1987.

Wood, D.A., A variably veined suboceanic upper mantle - Genetic significance for mid-ocean ridge basalts from geochemical evidence, *Geology, 7*, 499-503, 1979.

Woodhouse, J.H., and A.M. Dziewonski, Mapping the upper mantle: Three-dimensional modeling of earth structures by inversion of seismic waveforms, *J. Geophys. Res., 89*, 5953-5986, 1984.

Zindler, A., and S.R. Hart, Chemical Geodynamics *Ann. Rev. Earth and Planet. Sci., 14*, 493-571, 1986.

APPENDICES

APPENDIX 1

DSDP Petrographic Summaries

DSDP Leg 28:

Site 265: pillowed surface flow with glassy and variolitic upper section becoming more crystalline downward; devitrified glass containing a few percent olivine microphenocrysts in a variolitic matrix of plumose plagioclase with translucent unidentified microcrystalline material; small vesicles and carbonate-filled amygdules less than 1% but increase in size and amount (<5%) downward; several small fragments of olivine-bearing, undevitrified glass indicate remains of pillow rim; down core basalts chiefly plagioclase normally zoned (An73-65) and lesser amounts of clinopyroxene with minor olivine; veinlets of calcite, chlorite, and zeolite cut the rock.

Site 266: recovery of basalt fragments with no evidence of pillow structure; mostly medium to dark gray devitrified glasses, one sample of fresh black glass; all samples are phenocryst free with a few percent vesicles filled with white calcite; rare thin veinlets are filled with calcite, smectite, translucent iron oxide, and zeolite(?)

Site 267: pillowed surface flow with glassy and variolitic upper section becoming more crystalline downward, some thin selvages of dark glass; plagioclase only phenocryst phase up to 10% of mode; small, poorly formed pyroxene rare; vesicles-amygdules (~5%)and veinlets filled with calcite, smectite, and/or zeolite.

Site 274: flow breccia of holocrystalline basalt with quench plagioclase and clinopyroxene in non-spherulitic matrix, no evidence of significant original glass component; fragments inferred to represent large blocks in a breccia rather than separate flow units; plagioclase is the only phenocrystic phase (1-3mm size), groundmass of plagioclase, clinopyroxene, and alteration; alteration variable from slight to highly altered with calcite, zeolite, chlorite and/or hydrous iron oxides

APPENDIX 1
(cont.)

DSDP Leg 29:

Site 278: upper portion of a pillow flow; plagioclase porphyritic (~20%) basalt, large plag phenocrysts zoned An64 core to An30 rims; groundmass plag An45 as fresh laths with interstitial, fibrous to skeletal pyroxene; euhedral olivine in fresh glass reported; vesicles are rare rimmed with brown devitrified glass and filled with mesostasis glass crystallized to subspherulitic intergrowths of pyroxene and titanomagnetite; abundant veinlets of sparry calcite, chalcedony, and micritic limestone cut basalt.

Site 279A: upper portion of a massive flow; vesicular to amygdaloidal, very fine grained plagioclase porphyritic basalt that grade downward into non-vesicular, non-porphyritic fine grained basalt; 50% of vesicles are unfilled with the remaining vesicles partly to completely filled with white calcite, chlorite, or a gray-blue zeolite(?); thin section description reports plagiclase (35%), anhedral pyroxene (30%), altered brown glass (25%), magnetite (10%), accessory minerals include calcite, chlorite, analcite (?), and an unidentified zeolite; groundmass plagiclase (52%), clinopyroxene (25%), mesostasis glass (20%), and titanomagnetite (2%); mesotasis altered to chlorite, epidote, zeolite with patches of brown biotite.

Site 280A: basalt intercalated with claystone and siltstone; intrusive origin with silicification, pyritization, and lithification of sediment; basalt apophyses are 2.0, 0.5, and 1.1 m thick; fresh clinopyroxene with some clorite replacement enclose small plagioclase laths; essentially aphyric with rare phenocrysts of plagioclase with sericitic alteration and occasional clots of olivine; rock cut by veins of calcite, antigorite, epidote, chlorite; more plagiclase and olivine phenocrysts reported in lowermost basalt layer with no calcite veining.

Site 282: altered pillow basalt or possibly broken pillow breccia and hyaloclastite; veins of calcite, chlorite, limonite pervade a highly fractured core; olivine pseudmorphed by serpentine with chrome spinel; thin section indicate subophitic intergrowths of zoned plagioclase and pyroxene with intergrown titanomagnetite in a devitrified groundmass; groundmass highly altered with pervasive calcite, brown iron oxide, and serpentine minerals.

APPENDIX 1
(cont.)

Site 283: pillow lava or broken pillow breccia, possible intrusive origin indicated only by a color change in the overlying sediment; upper 20 cm consists of rare altered feldspar laths (2%) in an altered groundmass of clay, zeolite and serpentine; lower 1.3 m dark greenish-gray amygdaloidal basalt (80%), calcite veins (15%), and dark fragments of serpentinized glass (5%); altered plagioclase laths (20%), partially altered olivine and pyroxene (30%), opaque minerals (10%), serpentine (?) after glass (10%), calcite (5%), and minor clay, serpentine, and zeolite reported in thin section.

APPENDIX 2

Analytical Method Comparison

Table 1. Microprobe accuracy and precision determined during this investigation.

	LDGO VG-2 mean (n=4)	sd	VG-2 rec	LDGO JDF D2 mean (n=334)	sd	JDF D2 rec	OSU JDF D2 mean (n=17)	sd	OSU BASL mean (n=70)	sd	BASL rec
SiO2	50.34	0.60	50.81	50.74	0.43	50.80	51.03	0.43	51.04	0.31	50.94
TiO2	1.87	0.02	1.85	1.93	0.03	1.93	1.88	0.10	3.99	0.21	4.06
Al2O3	13.95	0.06	14.06	13.84	0.20	13.80	13.90	0.25	12.54	0.12	12.49
FeO	11.38	0.13	11.84	11.85	0.23	12.17	12.06	0.32	13.29	0.20	13.30
MnO	0.20	0.02	0.22	0.21	0.03	0.22	0.20	0.04	0.21	0.04	0.15
MgO	6.83	0.07	6.71	6.60	0.20	6.83	6.78	0.66	5.04	0.09	5.08
CaO	10.97	0.06	11.12	10.68	0.24	10.80	10.87	0.51	9.33	0.09	9.30
Na2O	2.70	0.03	2.62	2.71	0.12	2.77	2.67	0.18	2.61	0.10	2.66
K2O	0.16	0.03	0.19	0.21	0.03	0.22	0.21	0.04	0.84	0.03	.82
P2O5	0.37	0.02	0.20	0.38	0.03	0.23	0.22	0.06	0.47	0.06	.38
total	98.78		99.62	99.15		99.77	99.83		99.36		99.18

Table 2. DCP accuracy and precision determined during this investigation.

	BHVO-1 mean (n=6)	BHVO-1 sd btw runs	BHVO-1 max sd replicates	BHVO-1 recommended†	
SiO2	49.86	.14	.25	49.94	.30
TiO2	2.72	.011	.021	2.71	.07
Al2O3	13.71	.05	.11	13.80	.23
Fe2O3	12.28	.03	.06	12.23	.15
MnO	0.17	.001	.001	0.168	.005
MgO	7.03	.021	.024	7.23	.22
CaO	11.42	.062	.138	11.40	.10
Na2O	2.36	.015	.013	2.26	.02
K2O	.54	.005	.007	.52	.01
P2O5	.28	.002	.002	.273	.02
total	100.34			100.53	
Sr	402.9	.1	.8	403	40
Ba	135.2	.3	1.4	139	10
Zn	97.3	3.3	2.0	105	5
Cu	144.0	.3	1.2	136	5
Ni	106.1	1.1	1.7	121	5
V	318.2	2.3	5.1	317	12
Sc	31.4	.2	.3	31.8	1
Cr	253.3	2.8	5.1	289	20
Zr	183.8	1.4	0.0	179	15
Y	27.8	.3	0.0	27.6	2

†Recommended values from Govindaraju [1989] and estimated 'confidence limits' from Abbey [1982].

APPENDIX 2 (continued)

Table 3. INAA accuracy and precision.

	BCR-1				BHVO-1				JDF D2				est. error
	mean	sd		rec	mean	sd		rec	mean	sd		rec	%
	INAA 1		INAA2		INAA1		INAA2		INAA1		INAA2		
Rb	62	7	54	47.2	20	5	19	11	16	7	15		20-60
U	1.66	.42	1.97	1.75	.29	.27	1.07	.42	.41	.26	.59		25-100
Th	5.84	.11	5.83	5.98	1.32	.10	1.32	1.08	.22	.06	.29		10-60
Ta	.91	.10	2.25	.81	1.53	.15	1.46	1.23	.71	.10	.68		10-40
Hf	4.85	.18	4.71	4.95	4.57	.16	4.36	4.38	4.21	.19	4.12		3-7
Co	39.9	.4	43.7	37	45.3	.5	50.6	45	62.1	.6	63.7		1-3
La	27.3	.5	43.9	24.9	16.1	.4	17.0	15.8	6.85	.20	7.01	6.98	3-7
Ce	54.6	1.2	53.2	53.7	41.3	1.1	39.8	39	16.1	1.1	16.4	18.8	3-9
Nd	30.7	2.5	29.5	28.8	28.2	2.1	29.2	25.2	16.2	2.8	15.6	15.0	7-20
Sm	6.49	.05	6.44	6.59	6.27	.05	6.12	6.2	5.11	.05	5.10	4.91	1-3
Eu	1.93	.05	1.95	1.95	2.12	.05	2.05	2.06	1.71	.05	1.70	1.65	2-5
Tb	.99	.06	1.02	1.05	.97	.06	.94	.96	1.39	.08	1.31		3-10
Yb	3.40	.16	4.06	3.38	2.19	.15	2.45	2.02	4.98	.19	5.33	5.08	2-10
Lu	.55	.03	.53	.51	.30	.03	.31	.29	.76	.02	.81	.75	3-7

APPENDIX 2 (continued)

Table 4
Comparison of duplicate ICP-MS and DCP/INAA results on splits of MW8801 basalt glass.

	MW17-26		MW23-01		MW26-01		MW27-71	
method	ICP-MS	DCP INAA	ICP-MS	DCP INAA	ICP-MS	DCP INAA	ICP-MS	DCP INAA
area type	zone A glass		AAD glass		AAD glass		AAD glass	
(ppm)								
Sc	38.4	35.8	37.4	34.0	36.0	33.0	34.4	32
V	292	252	228	193	283	250	260	230
Cr	427	360	380	332	348	300	371	325
Ni	105	103	157	140	119	117	129	129
Cu	76	74	88	83	56	55	58	57.9
Zn	69.4	70.4	73.8	75.2	77.9	70.3	63.7	61.1
Rb	0.6		1.4		0.9		1.0	
Sr	118	105	103	109	112	112	142	143
Y	27.3	30.2	23.2	25.1	32.4	32.6	26.0	26.4
Zr	79	90	61	73	96	100	84	89
Nb	1.2		2.4		2.1		2.4	
Cs	0.01		0.02		0.02		0.02	
Ba	3.3	2.9	16.6	14.3	8.6	7.0	12.1	10.3
La	1.91	1.90	2.06	2.40	3.06	3.31	3.13	3.53
Ce	8.05	9.20	6.89	7.20	11.06	11.20	10.46	10.80
Pr	1.41		1.10		1.84		1.69	
Nd	8.91	7.80	6.51	5.90	10.57	9.90	9.41	8.90
Sm	3.09	2.94	2.39	2.39	3.73	3.74	3.05	3.00
Eu	1.19	1.14	0.95	0.93	1.34	1.29	1.15	1.09
Gd	3.87		3.05		4.38		3.69	
Tb	0.77	0.75	0.60	0.61	0.87	0.95	0.69	0.71
Dy	4.86		4.03		5.66		4.45	
Ho	1.01		0.90		1.20		0.96	
Er	3.06		2.58		3.56		2.87	
Tm	0.49		0.41		0.53		0.45	
Yb	2.88	3.11	2.53	2.57	3.35	3.28	2.66	2.77
Lu	0.43	0.42	0.38	0.40	0.52	0.51	0.40	0.41
Hf	2.22	2.14	1.79	1.82	2.77	2.77	2.16	2.07
Ta	0.08	0.12	0.15	0.14	0.15	0.23	0.16	0.10
Th	0.07	0.07	0.14	0.15	0.14	0.10	0.14	0.10
U	0.02	0.11	0.04	0.11	0.05	0.35	0.05	0.29